

REC'D AUG 20 1953

(1600)

CONFIDENTIAL

Copy /  
RM SL53G20Source of Acquisition  
CASI Acquired

**NACA**  
**CLASSIFICATION CANCELLED**  
**RESEARCH MEMORANDUM**

for the

Bureau of Aeronautics, Department of the Navy  
AERODYNAMIC CHARACTERISTICS IN PITCH AND SIDESLIP AT  
HIGH SUBSONIC SPEEDS OF A 1/14-SCALE MODEL OF  
THE GRUMMAN XF10F AIRPLANE WITH WING  
SWEEPBACK OF  $42.5^{\circ}$   
TED NO. NACA DE 354

By Richard E. Kuhn and John W. Draper

Langley Aeronautical Laboratory  
Langley Field, Va.

**CLASSIFICATION CANCELLED**

*J. W. Crowley* 1/14/55  
CLASSIFIED DOCUMENT

This document contains information affecting the National Defense of the United States within the meaning of the espionage laws, Title 18, U.S.C., Secs. 793 and 794, the transmission or revelation of which in any manner to an unauthorized person is prohibited by law.

Status: **INACTIVE**

**NATIONAL ADVISORY COMMITTEE  
FOR AERONAUTICS**

WASHINGTON

AUG 18 1953

**FILE COPY**

To be returned to  
the files of the National  
Advisory Committee  
for Aeronautics  
Washington, D. C.

**CLASSIFICATION CANCELLED**

16

## NATIONAL ADVISORY COMMITTEE FOR AERONAUTICS

## RESEARCH MEMORANDUM

for the

Bureau of Aeronautics, Department of the Navy

AERODYNAMIC CHARACTERISTICS IN PITCH AND SIDESLIP AT

HIGH SUBSONIC SPEEDS OF A 1/14-SCALE MODEL OF

THE GRUMMAN XF10F AIRPLANE WITH WING

SWEEPBACK OF  $42.5^\circ$ 

TED NO. NACA DE 354

By Richard E. Kuhn and John W. Draper

## SUMMARY

An investigation has been made at high subsonic speeds of the aerodynamic characteristics in pitch and sideslip of a 1/14-scale model of the Grumman XF10F airplane with a wing sweepback angle of  $42.5^\circ$ . The longitudinal stability characteristics (with the horizontal tail fixed) indicate a pitch-up near the stall; however, this was somewhat alleviated by the addition of fins to the side of the fuselage below the horizontal tail. The original model configuration became directionally unstable for small sideslip angles at Mach numbers above 0.8; however, the instability was eliminated by several different modifications.

## INTRODUCTION

The results of a free-flight test of a 1/7-scale rocket-powered model of the Grumman XF10F-1 airplane (ref. 1) indicated the possibility of a deterioration of the directional stability at high subsonic speeds. Therefore, at the request of the Bureau of Aeronautics, Department of the Navy, an investigation of a 1/14-scale sting-mounted model was made in the Langley high-speed 7- by 10-foot tunnel to study the problem in more detail and to investigate means for correcting the condition.

The tests were designed primarily to investigate the lateral and directional stability characteristics of the configuration with a limited investigation of the longitudinal stability characteristics. The tests covered a Mach number range from 0.40 to 0.94, which corresponds to a Reynolds number range from  $2.0 \times 10^6$  to  $3.4 \times 10^6$ . In order to expedite the issuance of the results, the data are presented with only a limited discussion and analysis.

#### COEFFICIENTS AND SYMBOLS

The stability system of axes used in presentation of the data, together with an indication of the positive forces, moments, and angles are presented in figure 1. All moments are referred to the center of gravity located at 25.4 percent M.A.C. as shown in figure 2.

$C_L$	lift coefficient, Lift/qS
$C_D$	drag coefficient, Drag/qS
$C_m$	pitching-moment coefficient, Pitching moment/qS $\bar{c}$
$C_l$	rolling-moment coefficient, Rolling moment/qSb
$C_n$	yawing-moment coefficient, Yawing moment/qSb
$C_Y$	lateral-force coefficient, Lateral force/qS
q	free-stream dynamic pressure, $\frac{\rho V^2}{2}$ , lb/sq ft
$\rho$	mass density of air, slugs/cu ft
V	free-stream velocity, ft/sec
S	wing area, sq ft
W/S	wing loading, lb/sq ft
b	wing span, ft
$\bar{c}$	mean aerodynamic chord, ft
M	Mach number

R Reynolds number, based on mean aerodynamic chord

$\alpha$  angle of attack, deg

$\beta$  angle of sideslip, deg

$\delta$  control deflection, deg

$$C_{l_\beta} = \frac{\partial C_l}{\partial \beta}$$

$$C_{n_\beta} = \frac{\partial C_n}{\partial \beta}$$

$$C_{Y_\beta} = \frac{\partial C_Y}{\partial \beta}$$

$$C_{L_\alpha} = \frac{\partial C_L}{\partial \alpha}$$

$$C_{m_\alpha} = \frac{\partial C_m}{\partial \alpha}$$

$$C_{mC_L} = \frac{\partial C_m}{\partial C_L}$$

$l$  longitudinal distance from center of gravity, parallel to fuselage reference line, ft

$h$  height above fuselage reference line, ft

$\epsilon$  angle of downwash, deg

$\sigma$  angle of sidewash, deg

$A$  aspect ratio

$A_e$  effective aspect ratio

$Z_w/d$  ratio of wing height (perpendicular distance from fuselage center line to wing chord plane, positive when wing is above fuselage) to maximum diameter of fuselage

$C_{m_{it}}$  pitching-moment effectiveness of horizontal tail, per degree

$i_t$  incidence of horizontal-tail assembly, deg

### MODEL AND APPARATUS

A three-view drawing of the model as tested is shown in figure 2. Sketches of the modifications to the model as tested are shown in figure 3. The model differed from the airplane in that the side air inlets were closed and faired into the nose of the model. There was no internal flow in the model. Also, the airplane has a free-floating horizontal tail which is controlled by the small canard surface. The pilot's controls are linked to the canard through a spring tab arrangement. For the model used in the present investigation (in order to expedite construction), the horizontal tail was set at predetermined angles which were suggested by the manufacturer.

The model was constructed by the Langley model shops and was of composite construction. The wings, vertical tail, fuselage, and tail boom were constructed using steel cores to carry the loads and covered with wood, Paraplex, and Fiberglas to give the desired contour. The horizontal tail surfaces were cut from solid brass stock. The incidence of the stabilizer, boom, and canard surfaces was varied by the use of interchangeable incidence blocks while the deflection of the stabilizer flap was changed by bending the web-type support member at the hinge line. The horizontal-tail assembly was tested at two altitudes ( $0^\circ$  and  $-4^\circ$  angle of incidence) which were obtained by setting the angle of incidence of the individual components of the assembly as follows:

Horizontal-tail assembly, $i_t$	$0^\circ$	$-4^\circ$
Boom	$0^\circ$	$-4^\circ$ nose down from model ref. line
Stabilizer	$0^\circ$	$-4^\circ$ nose down from model ref. line
Stabilizer flap	$0^\circ$	$-4^\circ$ trailing edge up from stabilizer
Canard	$0^\circ$	$-10^\circ$ nose down from boom ref. line
Canard tab	$0^\circ$	$0^\circ$ from canard

The model was tested on the sting-type support system as shown in figure 4. With this support system the model can be remotely operated through a  $28^\circ$  angle range in the plane of the support strut. By utilization of couplings in the sting behind the model, the model can be rolled through  $90^\circ$  so that either the angle of attack  $\alpha$  or the angle of sideslip  $\beta$  can be the remotely controlled variable. With the wings horizontal (perpendicular to the plane of the support strut), the couplings

can be used to support the model at angles of sideslip of  $2^\circ$ ,  $-2^\circ$ , and  $6^\circ$  while the model is tested through an angle-of-attack range. Forces and moments on the model were measured by an electric strain-gage balance system mounted in the model.

### TESTS AND CORRECTIONS

The tests were made in the Langley high-speed 7- by 10-foot tunnel through a Mach number range from approximately 0.40 to 0.94 which corresponds to the test Reynolds numbers shown in figure 5. The size of the model used caused the tunnel to choke at a corrected Mach number of about 0.95. The blocking corrections which were applied were determined by the method of reference 2.

The jet-boundary corrections which were applied to the angle of attack, drag coefficients, and pitching-moment coefficients were determined by the method of reference 3. The corrections to lateral force, yawing moment, and rolling moment were computed and were found to be negligible. The angle of attack and angle of sideslip have been corrected for the deflection of the balance and sting-support system under load. The drag data have been adjusted to correspond to a pressure at the base of the fuselage equal to free-stream static pressure. For this correction, the base pressure was determined by measuring the pressure inside the fuselage at a point 9 inches forward of the base.

Tare tests were not made for this investigation but previous experience has indicated that, for a configuration in which the vertical tail does not extend beyond the fuselage base, the effect of the sting support is negligible for all components except pitching moment and drag. For the configuration involved here, however, it is possible that a small tare to the directional stability may be present. No pitching moment tares were applied. However, the pitching moment tare would take the form of a change in trim as a result of a change in flow angle at the tail surface, and does not appreciably change the stability. This flow-angle change has been estimated to be of the order of  $1^\circ$  or less. No correction for drag tare was determined or applied to the data; however, experience has indicated the possibility of a drag tare which would tend to increase the drag values presented.

## PRESENTATION OF RESULTS AND DISCUSSION

The results of the investigation are presented in the following figures:

	Figures
Aerodynamic characteristics in pitch:	
Basic data -	
Original configuration . . . . .	6 to 10
Effect of modifications . . . . .	11 to 16
Summary data -	
Lift-curve slopes . . . . .	17
Longitudinal stability data . . . . .	18 to 23
Pitching moment due to sideslip . . . . .	24
Drag data . . . . .	25 to 30
Aerodynamic characteristics in sideslip:	
Basic data -	
Original configuration . . . . .	31
Modifications . . . . .	32 to 34
Summary data -	
Stability derivatives, $\alpha = 0^\circ$	
Low-speed and high-speed data . . . . .	35
Original configuration . . . . .	36
Modifications . . . . .	37 to 40
Effect of stabilizer incidence . . . . .	39 (a)
Effect of rocket booster and large ventral fin . . . . .	41
Stability derivatives, $\alpha = -4^\circ$ to $14^\circ$ . . . . .	42
Effect of wing sidewash or vertical-tail efficiency . . . . .	43
Effective aspect ratio of vertical tail . . . . .	44 to 45
Center of pressure of vertical-tail contribution . . . . .	46 to 47
Unsteady force characteristics of the model . . . . .	48

The following system was used in identifying the components for all modifications tested:

F	Fuselage alone
WF	Wing and fuselage
WV	Wing, fuselage, and vertical tail
FVH	Fuselage, vertical tail, and horizontal tail
FV	Fuselage and vertical tail
WVH	Complete model: Wing, fuselage, vertical tail, and horizontal tail

The results are presented without detailed analysis or discussion. Only a few points of interest, which have come to the attention of the

authors during the reduction and assembly of these data, will be presented here.

### Aerodynamic Characteristics in Pitch

Lift characteristics.- It is of interest to note that, for the configuration, with the external stores installed (modification 12), the large "bucket" in the variation of lift-curve slope with Mach number (fig. 17) occurs at Mach numbers at which a perceptible decrease in the angle of attack for zero lift occurs (fig. 15). This may indicate a tendency toward choking of the flow in the channel between the pylon and the fuselage.

Pitching-moment characteristics.- The Grumman XF10F airplane has a free-floating tail, while the model used in this investigation was tested with the horizontal-tail assembly at fixed incidence settings. However, although not exactly representative of the airplane, some general comparisons concerning the longitudinal stability can be made.

The effects of a change of horizontal-tail incidence from  $0^\circ$  to  $-4^\circ$  were investigated and the results are presented in figure 18 for two configurations. The differences between the results for the two configurations probably are a result of difficulties experienced in setting the angle of the stabilizer flap, which was bent into position, and are probably not associated with the change of configuration.

The variation of pitching-moment coefficient with lift coefficient for the basic configuration (fig. 6) indicated a sharp pitch-up tendency at lift coefficients approaching the stall. This pitch-up is also present to a lesser extent in the horizontal tail-off data of figures 7 and 8. It is possible that the free-floating feature of the tail on the airplane will have a tendency to alleviate this pitch-up. Installation of the horizontal fuselage fins reduced the high-lift instability (compare figs. 6 and 11).

The pitching moment due to sideslip is presented in figure 24. At small angles the change in pitching-moment coefficient is insignificant. At the larger angles it amounts to about  $1^\circ$  to  $1.5^\circ$  of stabilizer displacement.

Drag characteristics.- Some difficulty was experienced during the routine tests in measuring the drag as accurately as desired by the regular test procedure. Because of this difficulty, special tests were run with the model at zero angle of attack and measurements of the drag made through the Mach number range. Care was taken to establish the correct Mach number and the time required for a test was short so that the balance zero drift was minimized in obtaining minimum drag data. The results of these tests are presented in figures 25 and 26. It can be noted that the



installation of the fuselage side fins (modification 8) had little effect on the Mach number at which drag began to rise appreciably whereas the deteriorating effect of the installation of the external wing stores (modification 12) is readily apparent.

The drag due to lift for the wing-fuselage at various Mach numbers is presented in figure 27. The deteriorating effects of Mach number are clearly shown, although up to about a lift coefficient of 0.2 the drag is about as low as predicted by theory. The increment of drag at zero angle of attack due to a  $4^\circ$  deflection of the stabilizer is presented in figure 28. This increment is large when compared with the expected induced drag due to the lift carried by the stabilizer and canard surface at this angle and is probably due to some bad flow characteristics in the juncture of the vertical tail and the horizontal tail.

The drag of the fuselage (fig. 26) appears high. When the drag coefficient is based on the fuselage surface area of 4.25 square feet it has a value of 0.0038 at low Mach number. Results obtained on a cleaner fuselage design (ref. 6), when based on the fuselage surface area, indicate a drag coefficient of only 0.0025.

The parameter  $\frac{\sqrt{C_L}}{C_D}$ , which is important for the range of jet-propelled aircraft (ref. 7), is presented in figure 29 for the basic configuration. This parameter is particularly sensitive to small changes in minimum drag and therefore it was necessary, for the preparation of this figure, to adjust the drag data of figure 6 to the minimum drag values shown in figure 25. The range parameter  $\frac{\sqrt{C_L}}{C_D} \frac{1}{\sqrt{\rho/2}}$  for level flight at sea level and at 40,000 feet is presented in figure 30. The advantages of cruising at altitude (larger values of  $\frac{\sqrt{C_L}}{C_D} \frac{1}{\sqrt{\rho/2}}$ ) are quite apparent.

#### Lateral Stability Characteristics

The investigation of the lateral stability characteristics showed that the basic model had low directional stability in the low Mach number range — becoming unstable at  $M = 0.80$  as shown in figures 31 and 36. Figure 35 shows the complete-model data of figure 36 extended into the lower speed range by tests of a 1/7-scale model (constructed as a rocket test vehicle) in the Langley 300 mph 7- by 10-foot tunnel. In breakdown tests (fig. 31) it was established that sidewash from the wing (fig. 43) caused a large reduction of directional stability and that the end-plate effect of the horizontal tail was greater than would be predicted by reference 9 (fig. 45).

The result of the modification tests (figs. 32 to 34 and 37 to 40) showed that several of the changes would reduce the nonlinearity of the yawing moment through  $\beta = 0^\circ$  and would increase the directional stability to a satisfactory value through the Mach number range. The vertical tail end plate (modification 13) and fuselage side fins (modification 11) proved to be satisfactory modifications and could probably be easily installed on the airplane. It is possible that increases in Reynolds number also would increase the directional stability of the airplane to a more satisfactory value.

Modifications 15 and 16 were tested in conjunction with the rocket-model test program. The large ventral fin was proposed to insure directional stability of the rocket-powered model while studying the longitudinal stability and also to serve as a means of rotating the principal axis of the rocket model to correspond to that of the airplane (ref. 1). The model was tested in the presence of a simulated rocket booster to determine if there were any interference effects of the booster on the model at booster separation.

Plots of the vertical-tail efficiency factor obtained by the method of reference 8 are presented in figure 43. The effective aspect ratios of the vertical tail for various configurations, obtained by the method of reference 9, are presented in figures 44 and 45. Figures 46 and 47 show the center-of-pressure location obtained from the equations

$$\frac{z}{b} = \frac{-(\Delta C_{n\beta})_{\text{Vertical tail}}}{\Delta(C_{Y\beta})_{\text{Vertical tail}}}$$

and

$$\frac{h}{b} = \frac{(\Delta C_{l\beta})_{\text{Vertical tail}}}{(\Delta C_{Y\beta})_{\text{Vertical tail}}}$$

A summary of the effects of the various modifications on directional stability is shown in table I.

#### INFORMATION RELATIVE TO BUFFETING

An effort has been made to obtain some information which might be of interest with regard to the possible buffeting characteristics of the airplane. The model-induced fluctuations of the balance readings have been


examined and a boundary of lift coefficient and Mach number above which severe fluctuations were encountered is presented in figure 48. These fluctuations were most severe in the drag data, probably because the drag balance was the most sensitive. They appear to be definitely model induced rather than tunnel induced and are probably a reflection of flow separation or turbulence on the model. It would be expected, therefore, that this boundary would show some relationship to the lift coefficient at which the first departure from the linear variation of the lift curve occurs. This comparison is presented in figure 48.

These fluctuations did not seriously affect the determination of average values of the forces at any angle of attack but are presented here because they may have some bearing on the buffet characteristics of the airplane.

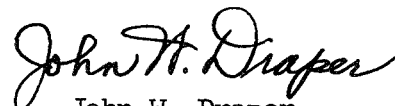
#### CONCLUDING REMARKS

An investigation of the aerodynamic characteristics in pitch and sideslip of a 1/14-scale model of the Grumman XF10F airplane in the swept-wing condition with the horizontal-tail assembly fixed indicates a pitch-up near the stall; however, this was somewhat alleviated by the addition of fins to the side of the fuselage below the horizontal tail. The original model configuration became directionally unstable for small sideslip angles at Mach numbers above 0.8; however, the instability was eliminated by several different modifications investigated, of which fuselage side fins and a vertical tail end plate may be the most practical.


Langley Aeronautical Laboratory,  
National Advisory Committee for Aeronautics,  
Langley Field, Va., June 30, 1953.



Richard E. Kuhn  
Aeronautical Engineer



John W. Draper  
Aeronautical Research Scientist

Approved: 

Thomas A. Harris  
Chief of Stability Research Division

mhg

## REFERENCES

1. Gardner, William N.: Preliminary Results Obtained From Flight Test of a 1/7-Scale Rocket-Powered Model of the Grumman XF10F Airplane Configuration in the Swept-Wing Condition. TED No. NACA DE 354. NACA RM SL52I25, Bur. Aero., 1952.
2. Herriot, John G.: Blockage Corrections for Three-Dimensional-Flow Closed-Throat Wind Tunnels, With Consideration of the Effect of Compressibility. NACA Rep. 995, 1950.
3. Gillis, Clarence L., Polhamus, Edward C., and Gray, Joseph L., Jr.: Charts for Determining Jet-Boundary Corrections for Complete Models in 7- by 10-Foot Closed Rectangular Wind Tunnels. NACA WR L-123, 1945. (Formerly NACA ARR L5G31.)
4. DeYoung, John: Theoretical Additional Span Loading Characteristics of Wings With Arbitrary Sweep, Aspect Ratio, and Taper Ratio. NACA TN 1491, 1947.
5. Fisher, Lewis R.: Approximate Corrections for the Effects of Compressibility on the Subsonic Stability Derivatives of Swept Wings. NACA TN 1854, 1949.
6. Kuhn, Richard E., and Wiggins, James W.: Wind-Tunnel Investigation of the Aerodynamic Characteristics in Pitch of Wing-Fuselage Combinations at High Subsonic Speeds. Aspect-Ratio Series. NACA RM L52A29, 1952.
7. Perkins, Courtland D., and Hage, Robert E.: Airplane Performance - Stability and Control. John Wiley & Sons, Inc., 1949.
8. Goodman, Alex: Effects of Wing Position and Horizontal-Tail Position on the Static Stability Characteristics of Models With Unswept and 45° Swept Back Surfaces With Some Reference to Mutual Interference. NACA TN 2504, 1951.
9. Brewer, Jack D., and Lichtenstein, Jacob H.: Effect of Horizontal Tail on Low-Speed Static Lateral Stability Characteristics of a Model Having 45° Sweptback Wing and Tail Surfaces. NACA TN 2010, 1950.

TABLE I

Summary of lateral stability characteristics of the complete model


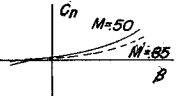
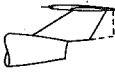


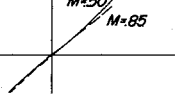

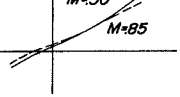

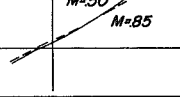

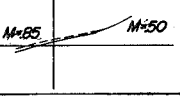

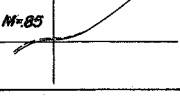

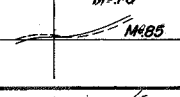

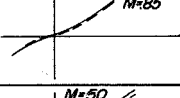

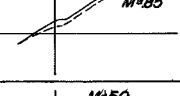

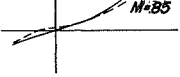

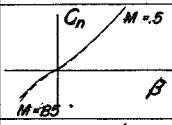

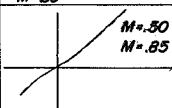

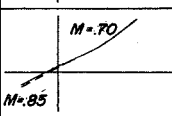

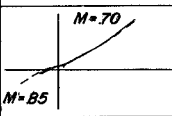

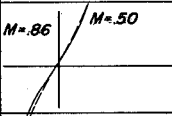
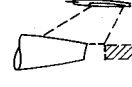
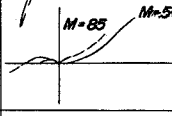

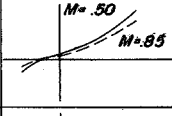
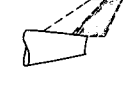
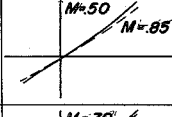
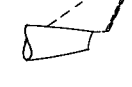
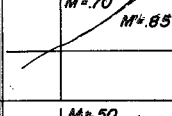

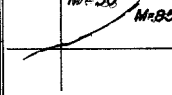
CONFIGURATION		$M=0.50, \alpha=0^\circ$			$M=0.85, \alpha=0^\circ$			Typical $C_n$ Curves	Figure Ref.
		$C_{n\beta}$	$C_{z\beta}$	$C_{y\beta}$	$C_{n\beta}$	$C_{z\beta}$	$C_{y\beta}$		
Basic Model		.0003	-.0016	-.0095	-.0001	-.0019	-.0100		31a, 36
I		.0012	-.0019	-.0109	.0009	-.0020	-.0110		32a, 37f
II		.0017	-.0020	-.0122	.0017	-.0024	-.0124		32b, 37d
III		.0010	-.0018	-.0110	.0010	-.0020	-.0115		32c, 37a,d
IV		.0011	-.0019	-.0117	.0011	-.0020	-.0121		32d, 37a
V		.0006	-.0017	-.0114	.0005	-.0018	-.0116		32e, 37b
VI		$M=0.70$ .0002	$M=0.70$ -.0018	$M=0.70$ -.0162	0	-.0020	-.0163		32f, 37c
VII		$M=0.70$ 0	$M=0.70$ -.0016	$M=0.70$ -.0093	-.0003	-.0016	-.0094		32g, 37e
VIII		.0008	-.0015	-.0110	.0005	-.0016	-.0110		32b, 39b
IX		.0011	-.0020	-.0110	.0009	-.0020	-.0106		32i, 37c
X		.0007	-.0020	-.0110	.0004	-.0023	-.0118		33a, 37f

TABLE I CONCLUDED

CONFIGURATION		$M=0.50, \alpha=0^\circ$			$M=0.85, \alpha=0^\circ$			Typical $C_n$ Curve	Figure Ref.
		$C_{n\beta}$	$C_{l\beta}$	$C_{y\beta}$	$C_{n\beta}$	$C_{l\beta}$	$C_{y\beta}$		
XI		.0015	-.0020	-.0134	.0014	-.0013	-.0151		34a, 39b
XII		.0015	-.0023	-.0151	.0015	-.0026	-.0150		34d, 39e
XIII		$M=.7$ .0012	$M=.7$ -.0023	$M=.7$ -.0130	.0011	-.0025	-.0130		34e, 40
XIV		$M=.7$ .0010	$M=.7$ -.0023	$M=.7$ -.0125	.0008	-.0027	-.0125		34f, 40
XV		.0044	-.0015	-.0216	.0044	-.0017	-.0224		34g, 41
XVI		$M=.7$ -.0001	$M=.7$ -.00175	$M=.7$ -.0105	-.0003	-.0021	-.0110		34h, 41
XVII	Sealed 	.0008	-.0021	-.0119	.0004	-.0023	-.0113		34i, 39f
XVIII		.0016	-.0024	-.0132	.0015	-.0025	-.0131		34j, 39g
XIX		$M=.7$ .0013	$M=.7$ -.0023	$M=.7$ -.0124	.0011	-.0025	-.0126		34l, 40
XX		.0007	-.0021	-.0116	.0005	-.0024	-.0124		34m, 40

NACA

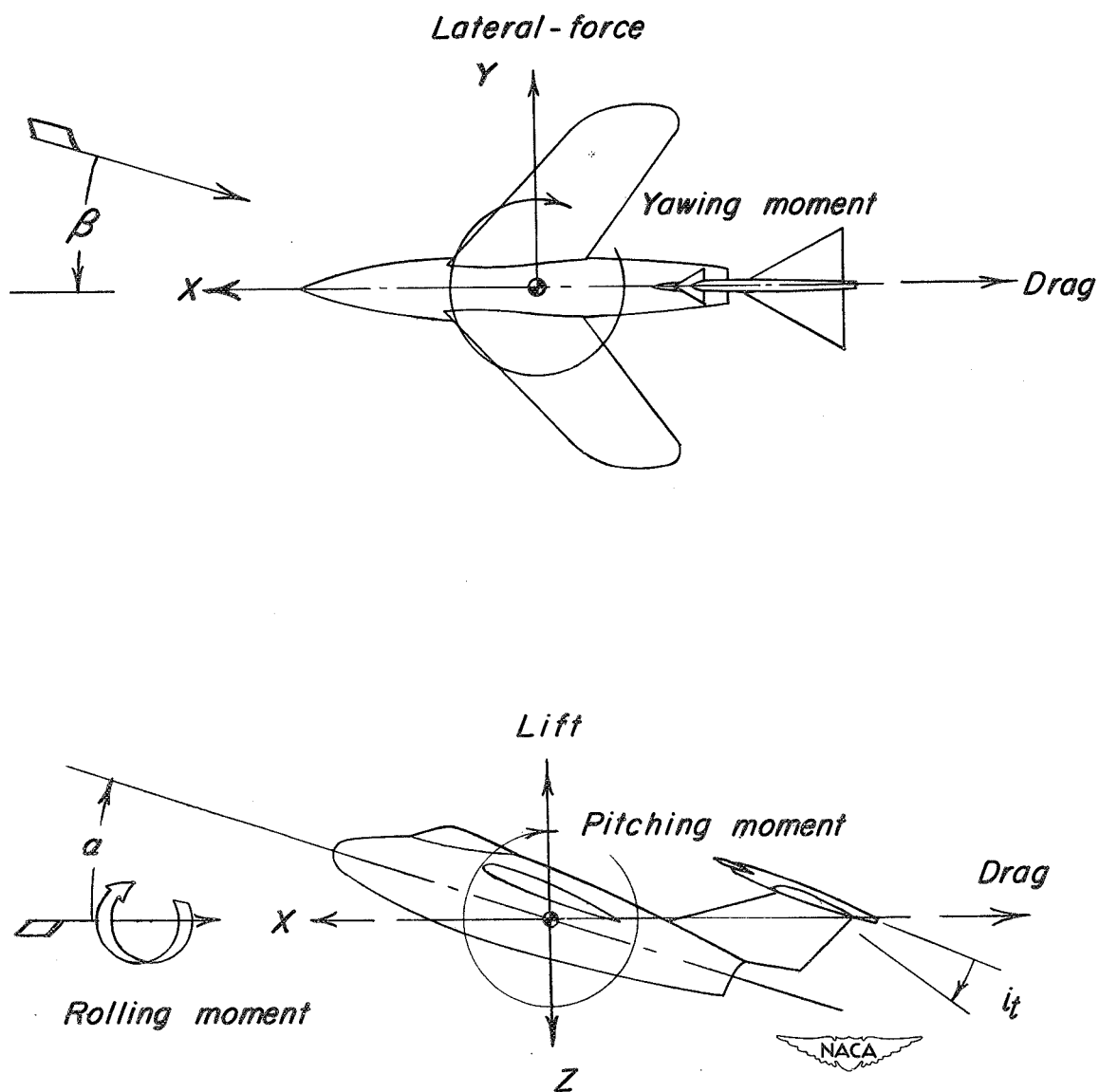


Figure 1.- Sketch showing positive direction of forces, moments, angles, and velocity.

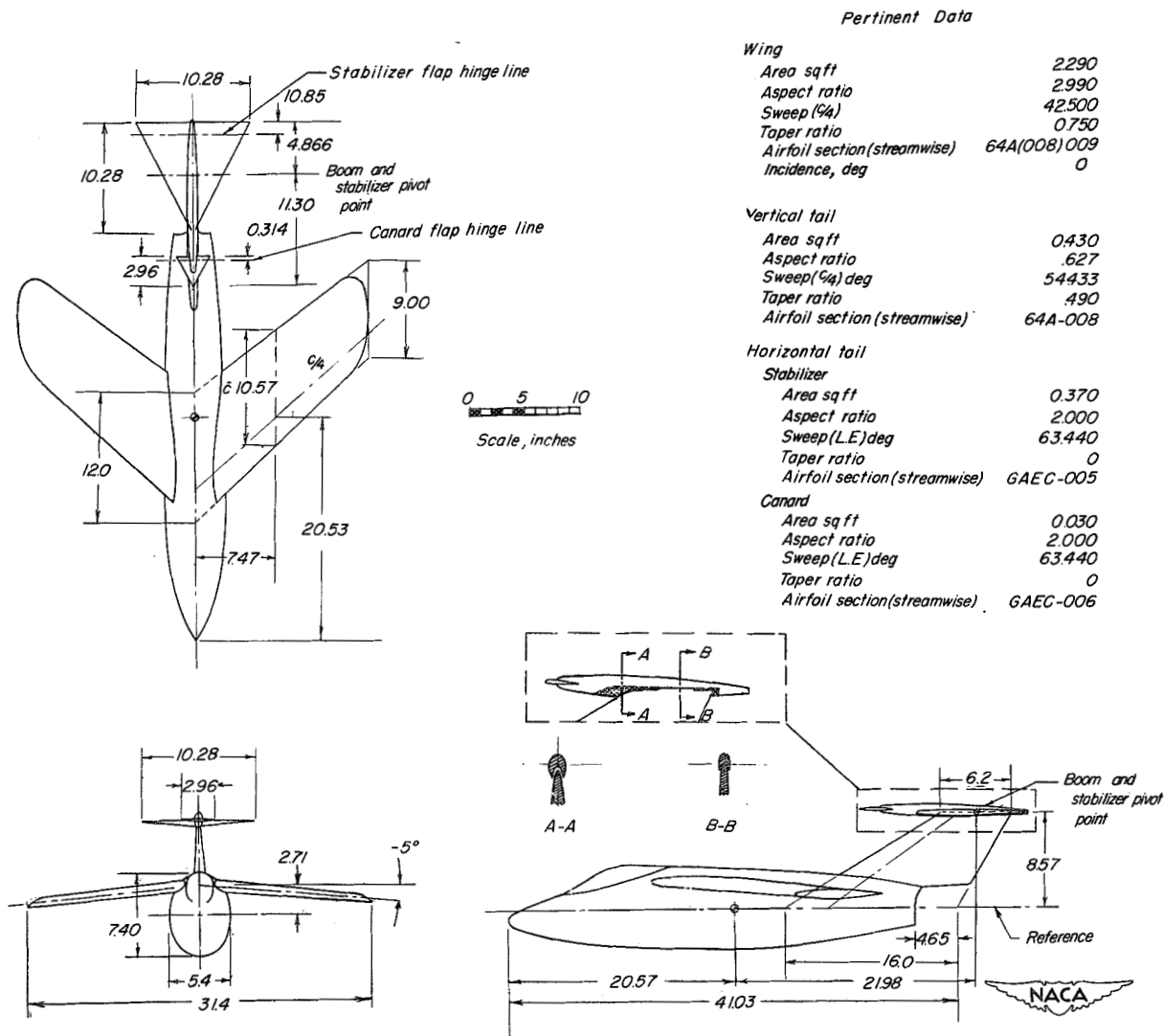
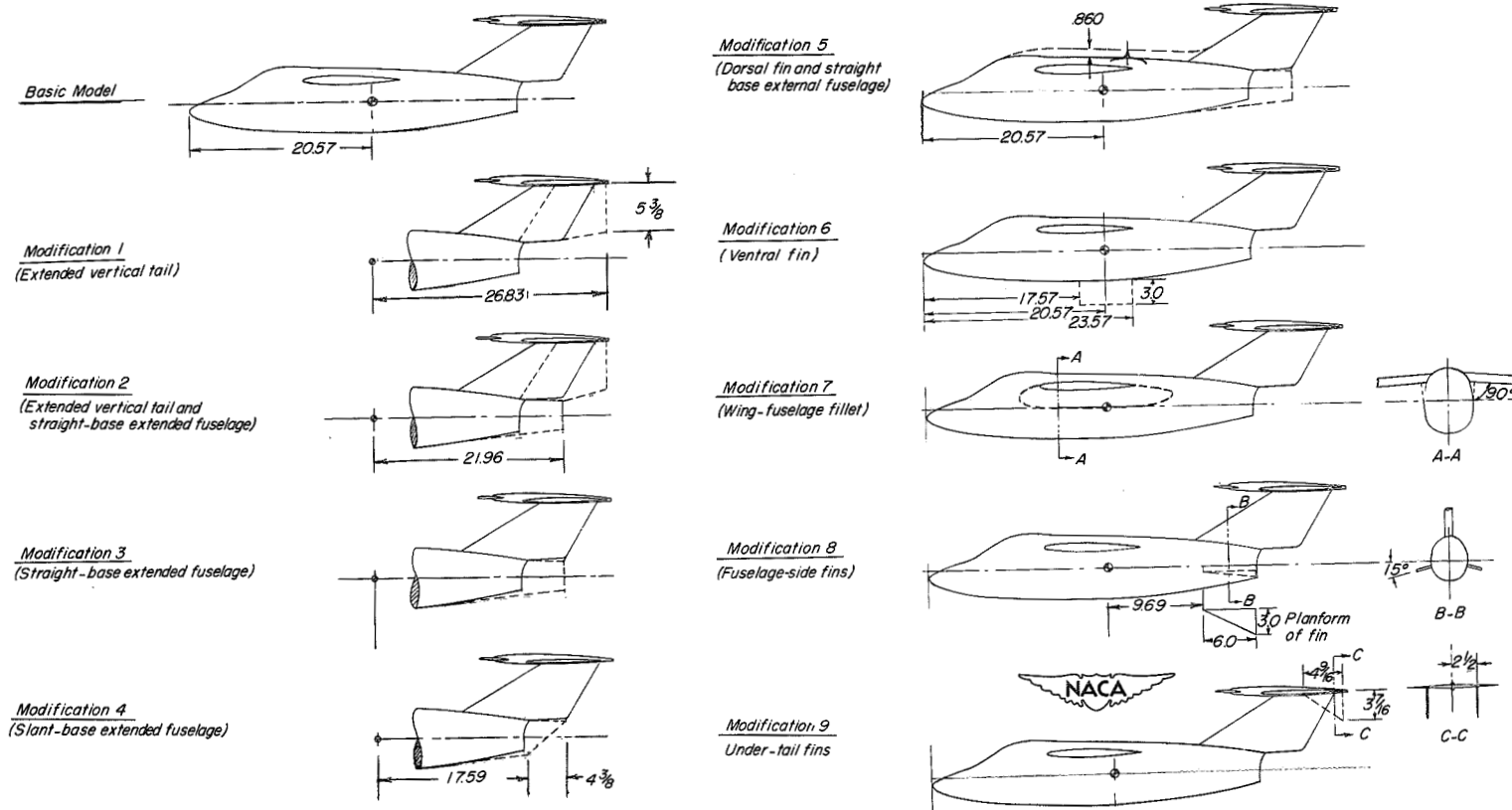


Figure 2.- 1/14-scale model of the XF10F airplane.

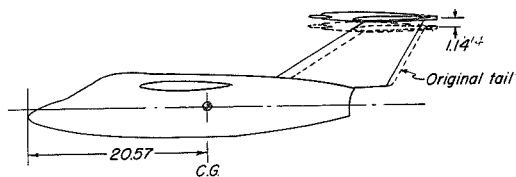




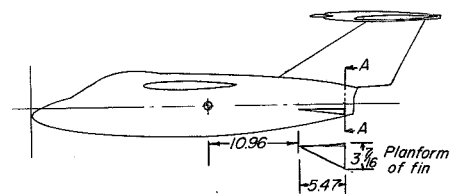
(a) Basic model and modifications 1 to 9.

Figure 3.- Sketches of modification to 1/14-scale XF10F model.

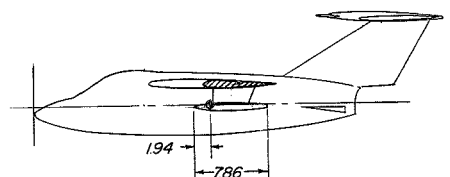
Modification 10  
(Enlarged vertical tail)



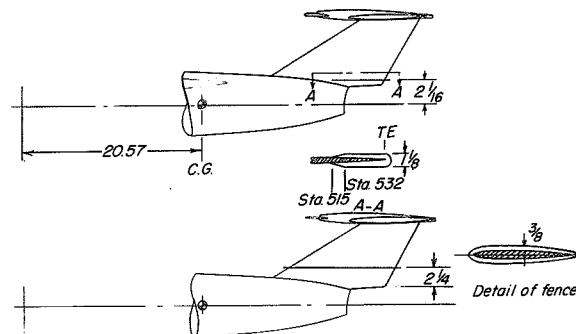
Modification 11  
(Modification 10 with modified fuselage fins)



Modification 12  
(Modification 11 with external wing stores)



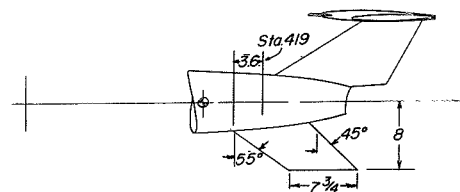
Modification 13  
(Modification 10 with jet deflection end plate)



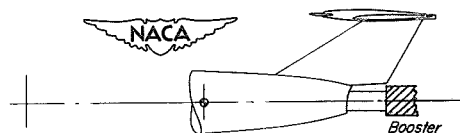
Modification 14  
(Modification 10 with vertical-tail fence)



Modification 15  
(Modification 10 with large ventral fin)

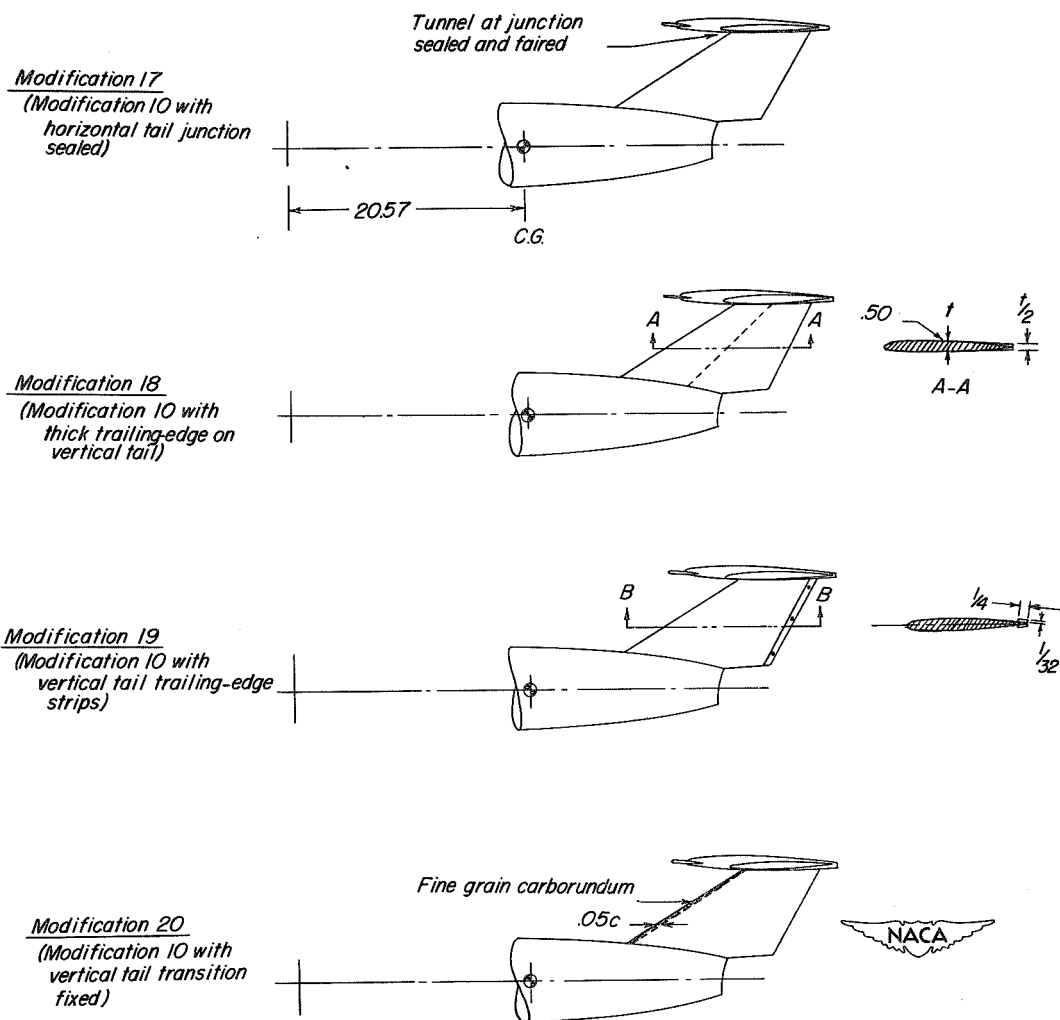


Modification 16  
(Modification 10 with rocket model booster simulated)



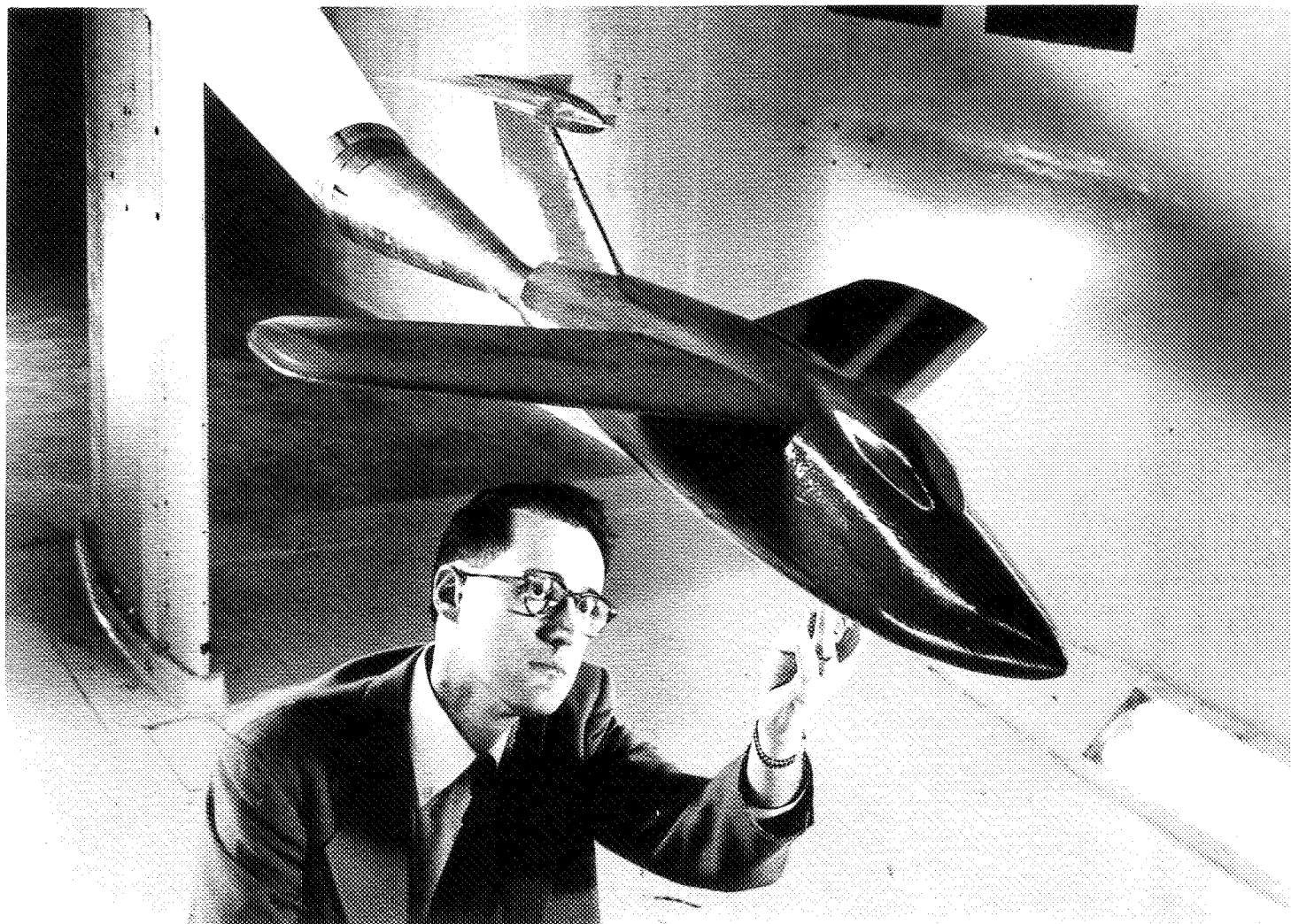
(b) Modifications 10 to 16.

Figure 3.- Continued.



(c) Modifications 17 to 20.

Figure 3.- Concluded.



L-75669

Figure 4.- Model mounted on sting balance in tunnel.

..  
..  
..  
..  
..

..



L-75671

Figure 4.- Concluded.

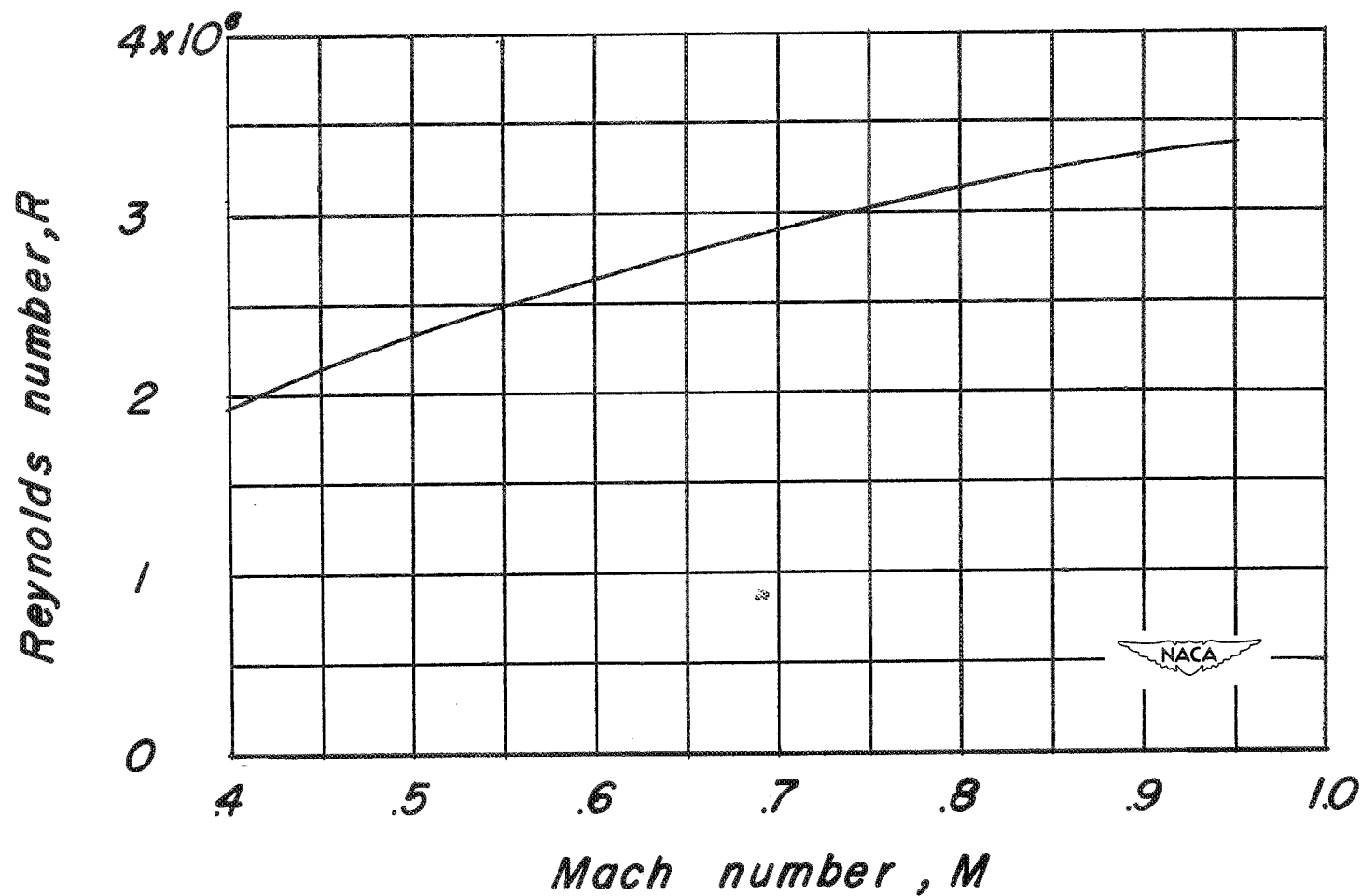
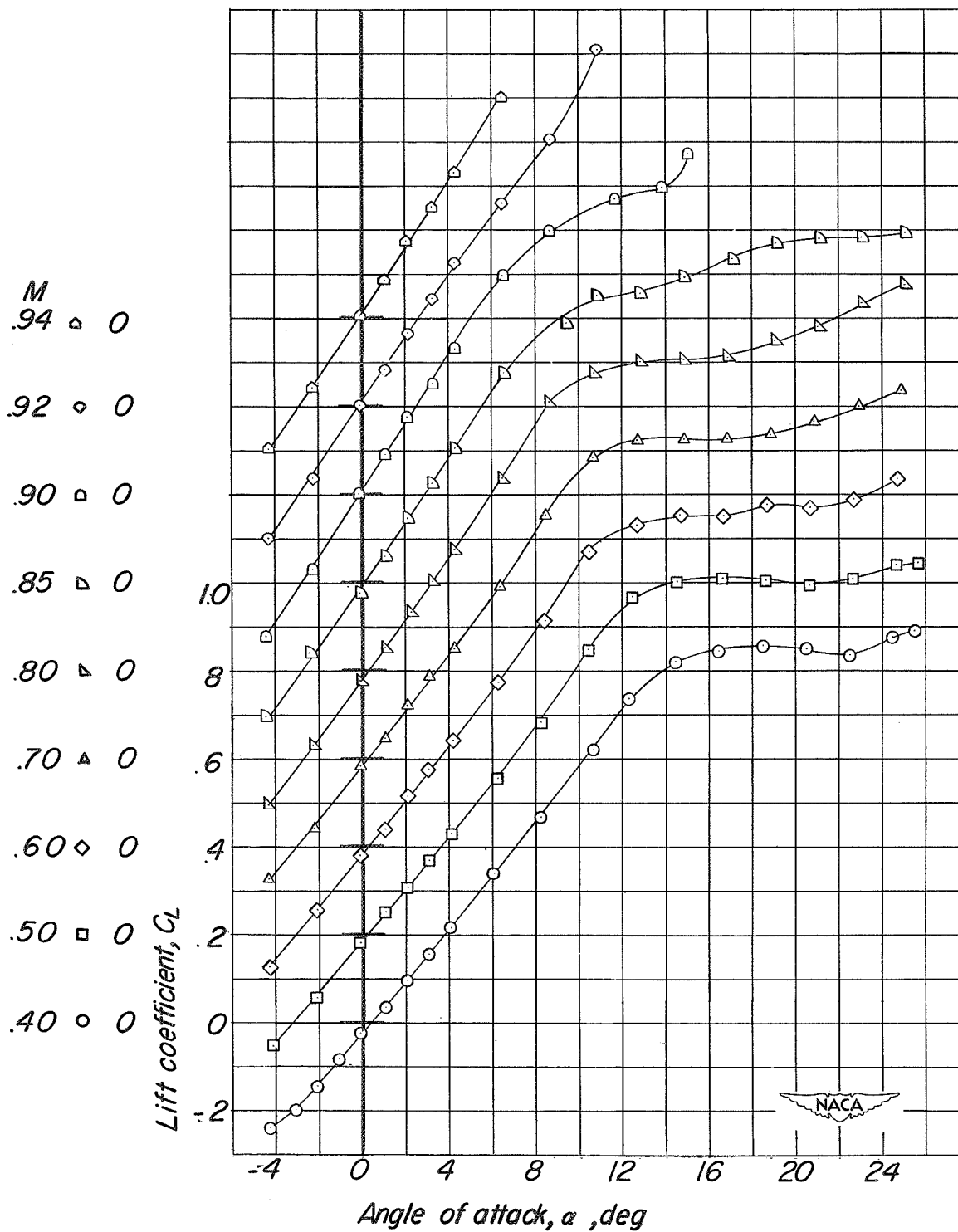
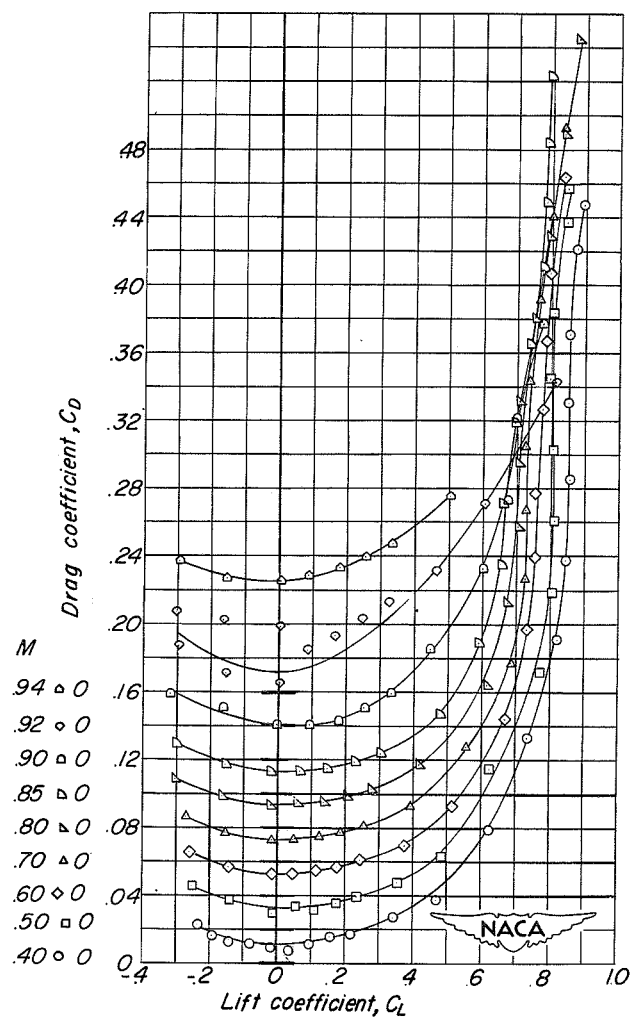
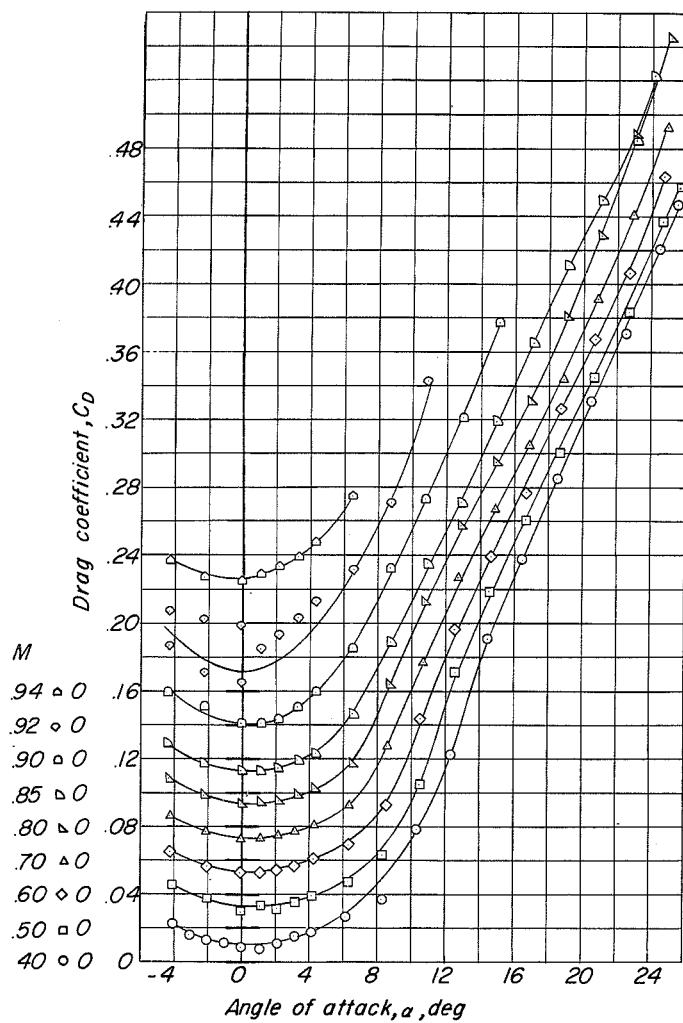


Figure 5.- Variation of Reynolds number with Mach number for tests of the 1/14-scale model of the XF10F airplane.



(a) Lift.

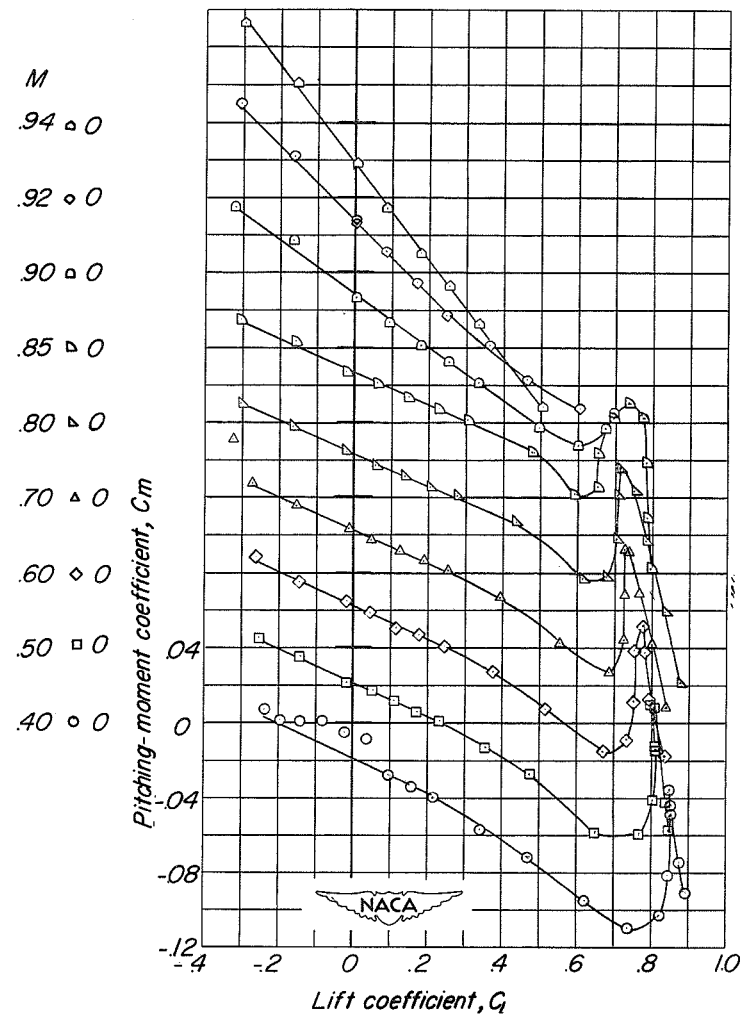
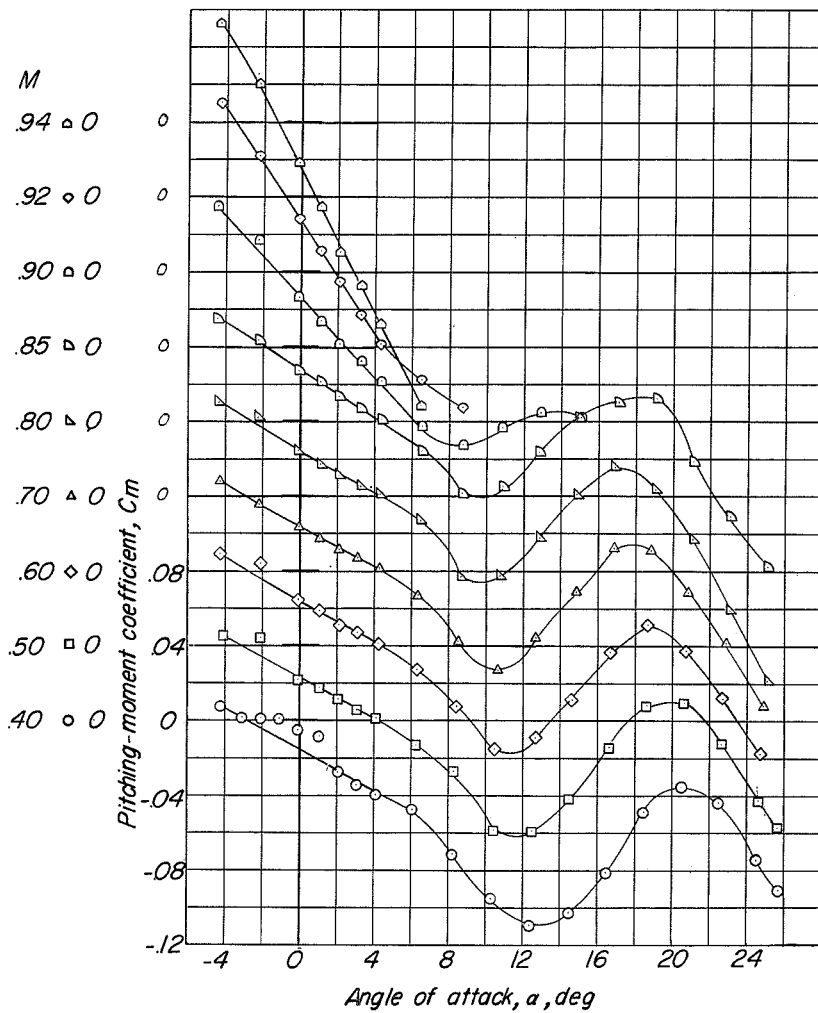
Figure 6.- Aerodynamic characteristics in pitch of the basic model.  
 $\beta = 0^\circ$ ;  $i_t = 0^\circ$ .



(b) Drag.

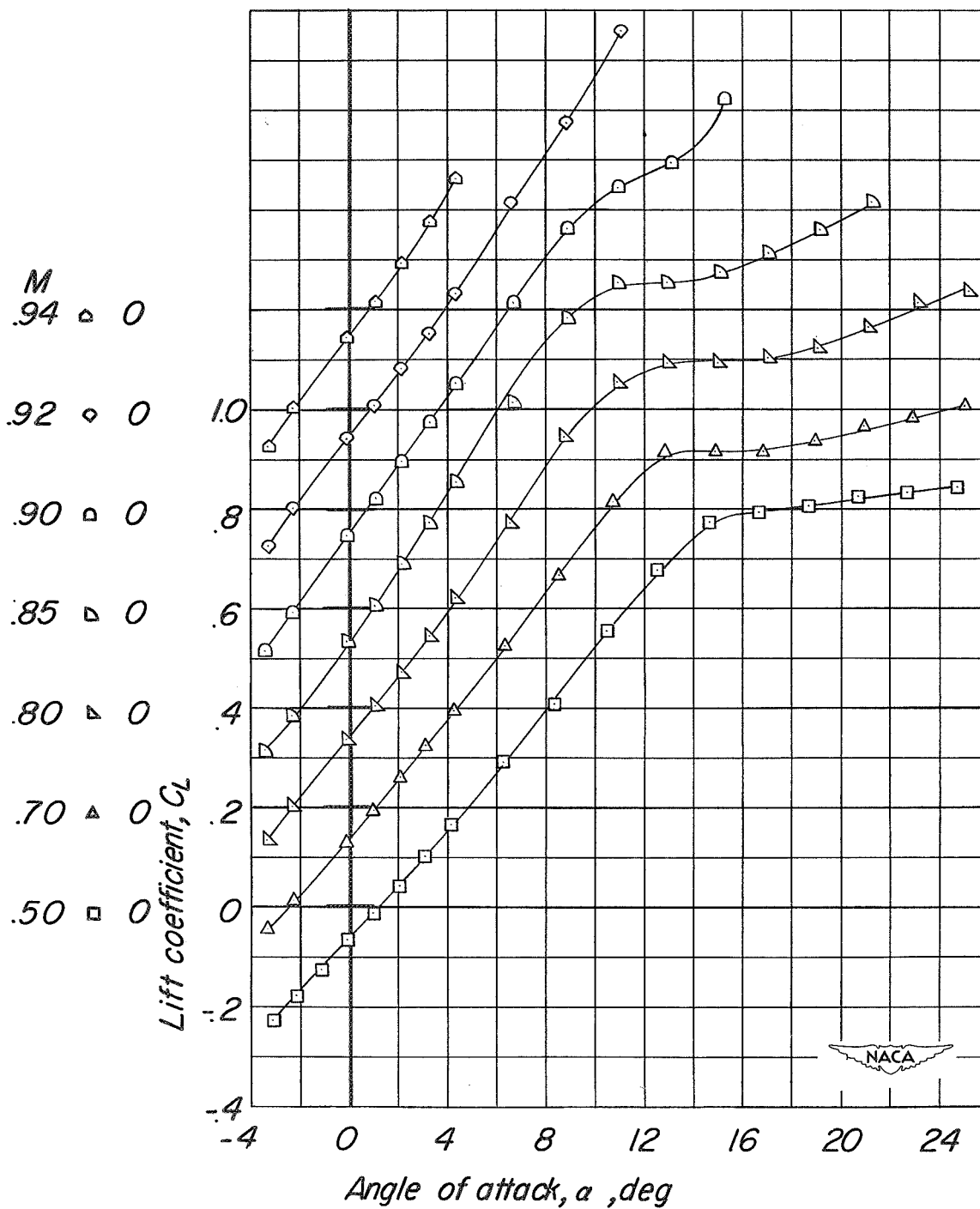
Figure 6.- Continued.





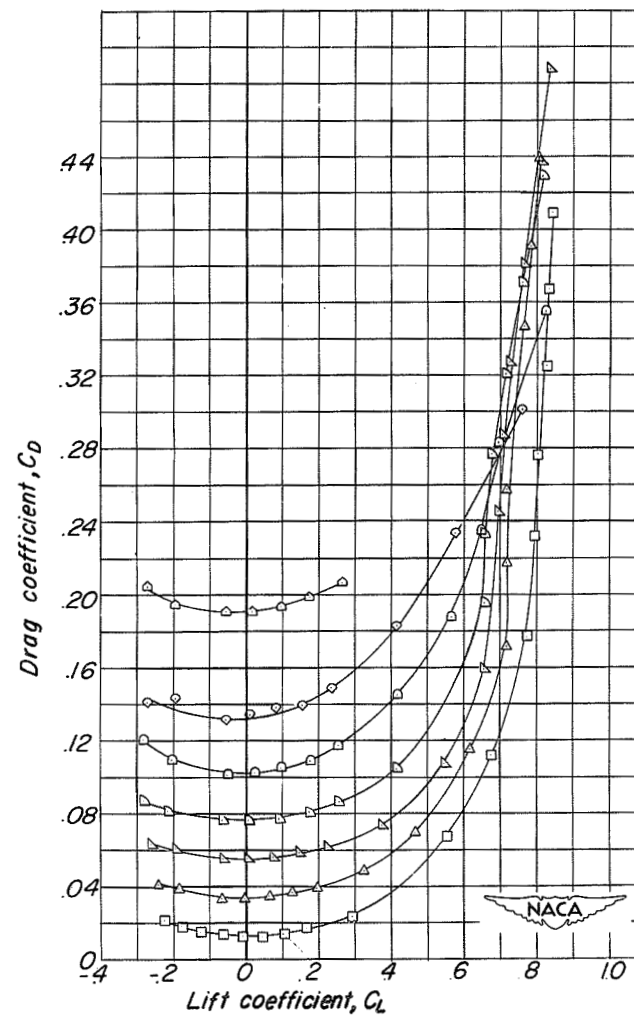
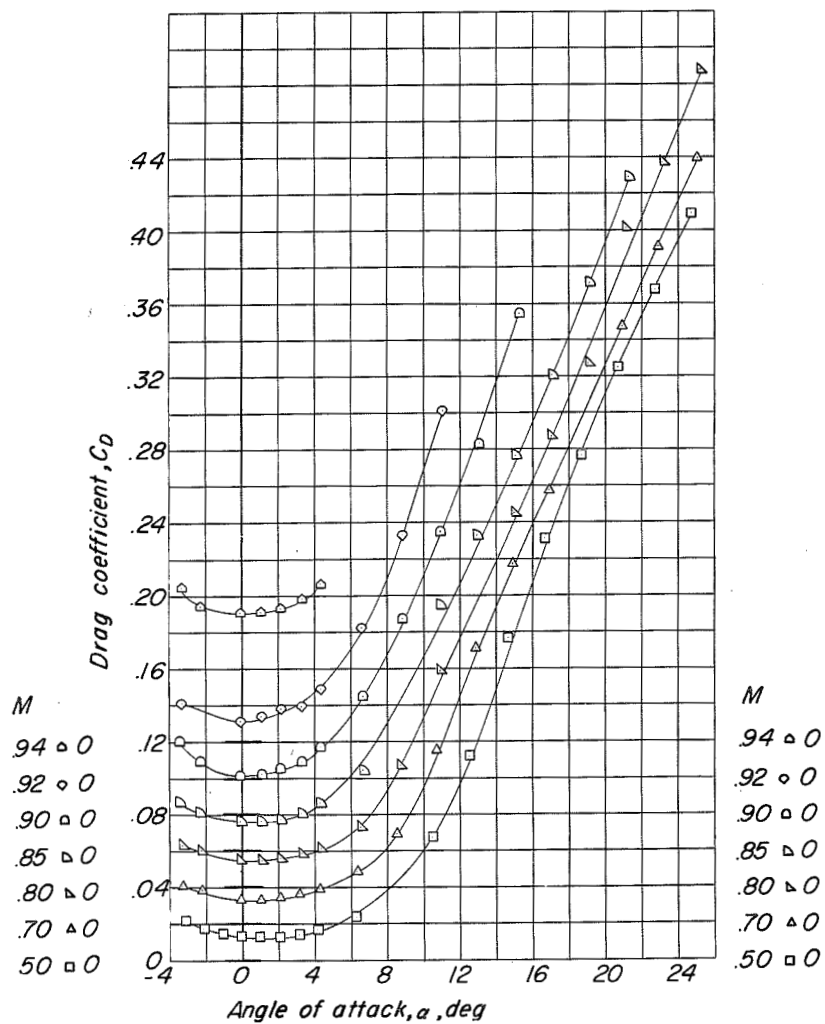
(c) Pitching moment.

Figure 6.- Concluded.



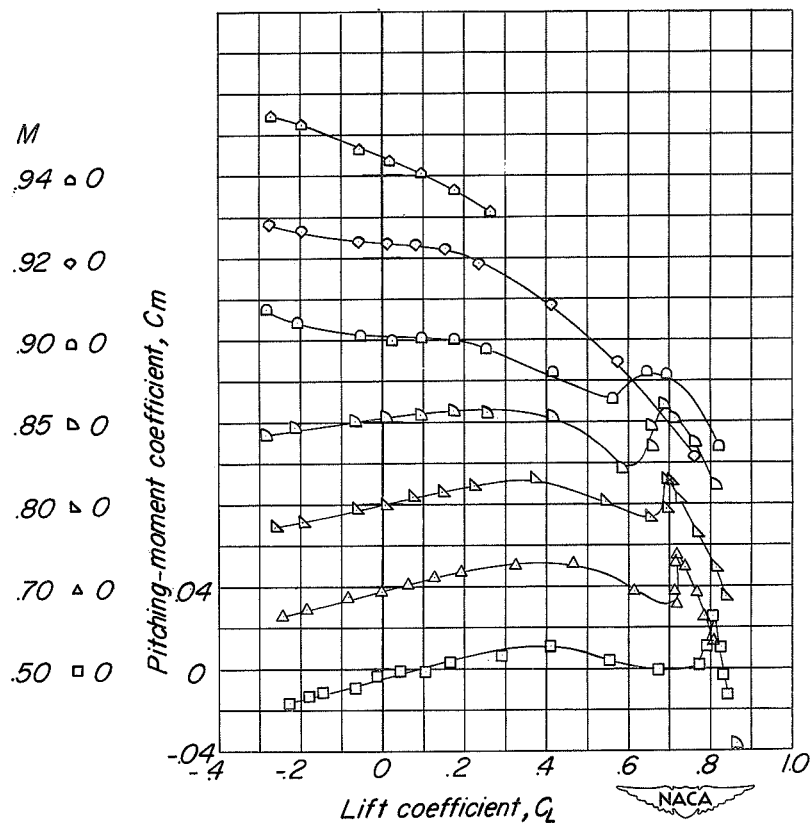
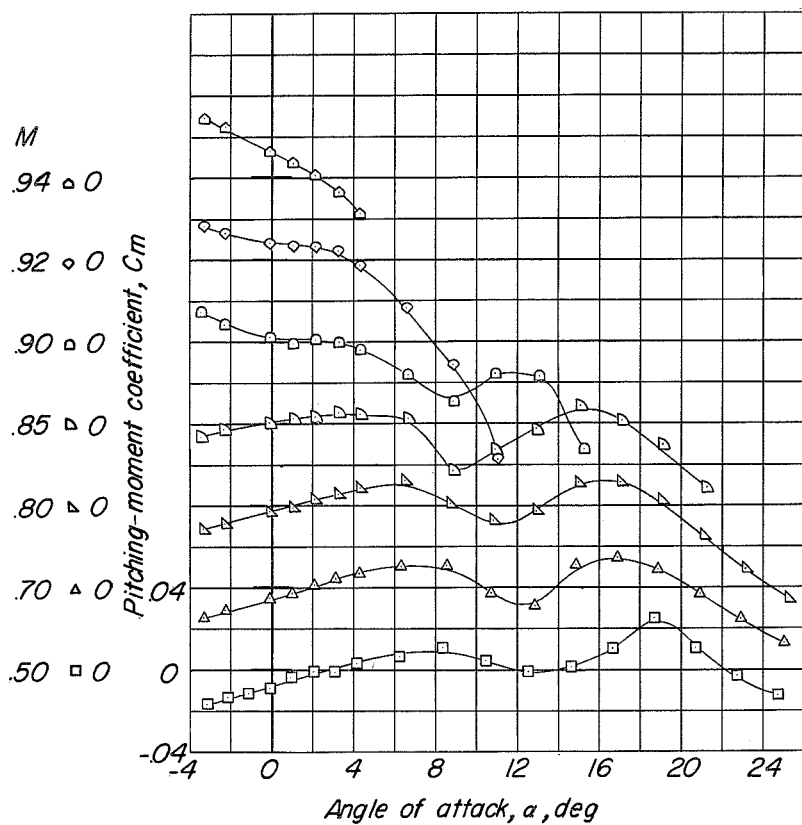
(a) Lift.

Figure 7.- Aerodynamic characteristics in pitch of the wing-fuselage-vertical tail of the basic model.  $\beta = 0^\circ$ .



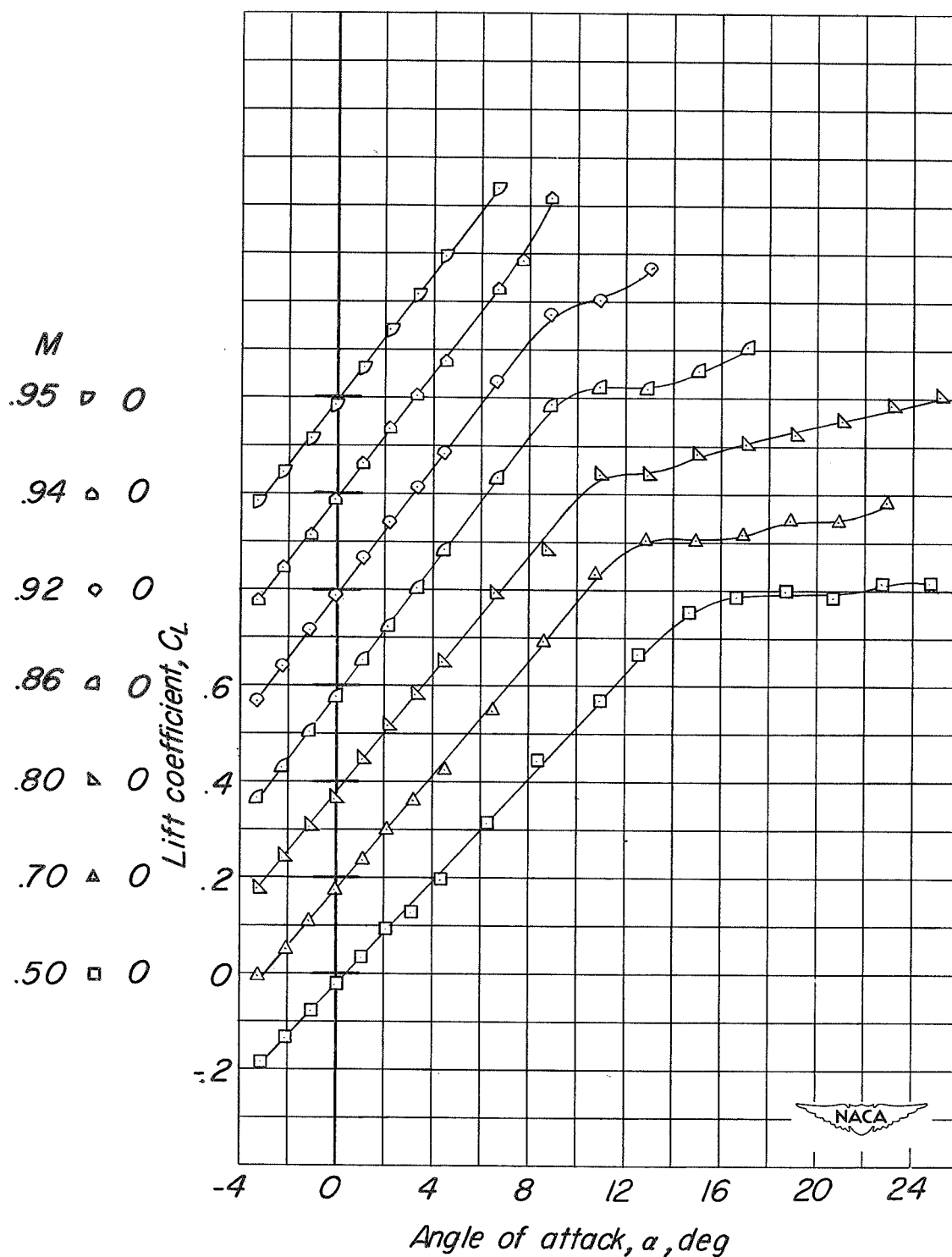
(b) Drag.

Figure 7.- Continued.



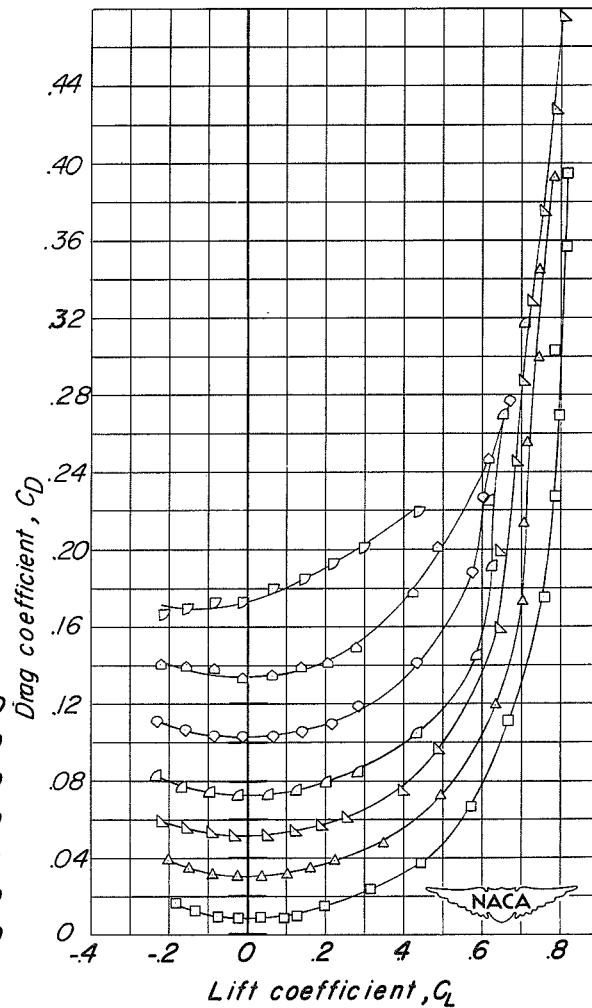
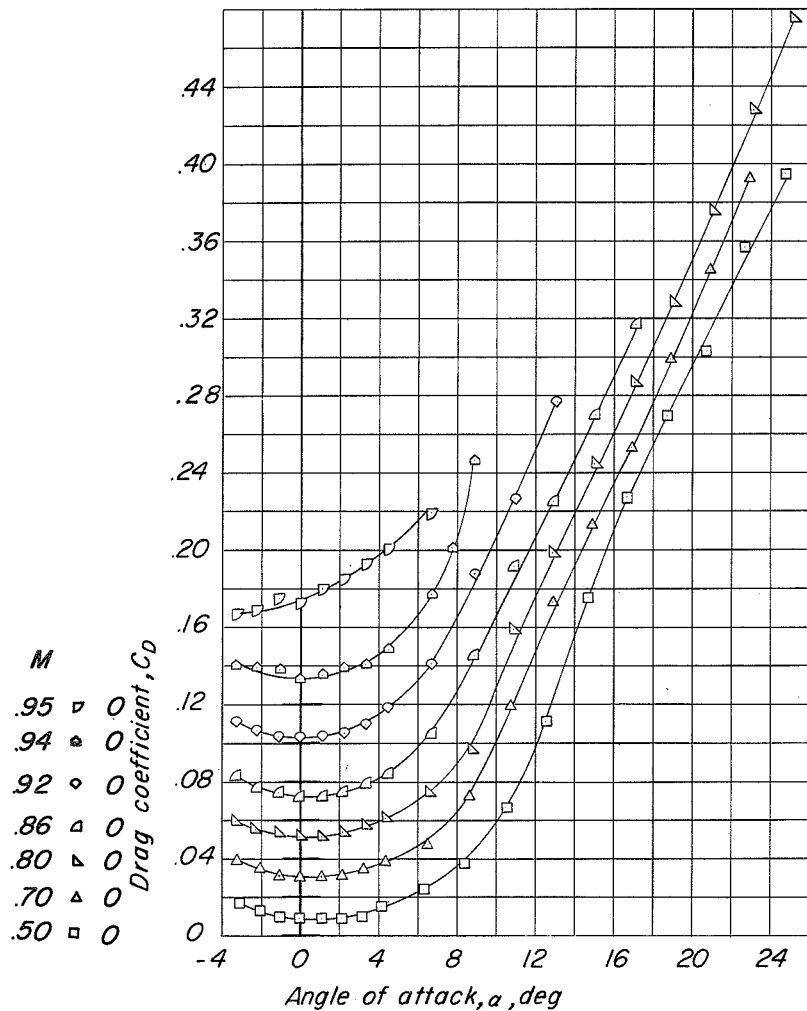
(c) Pitching moment.

Figure 7.- Concluded.



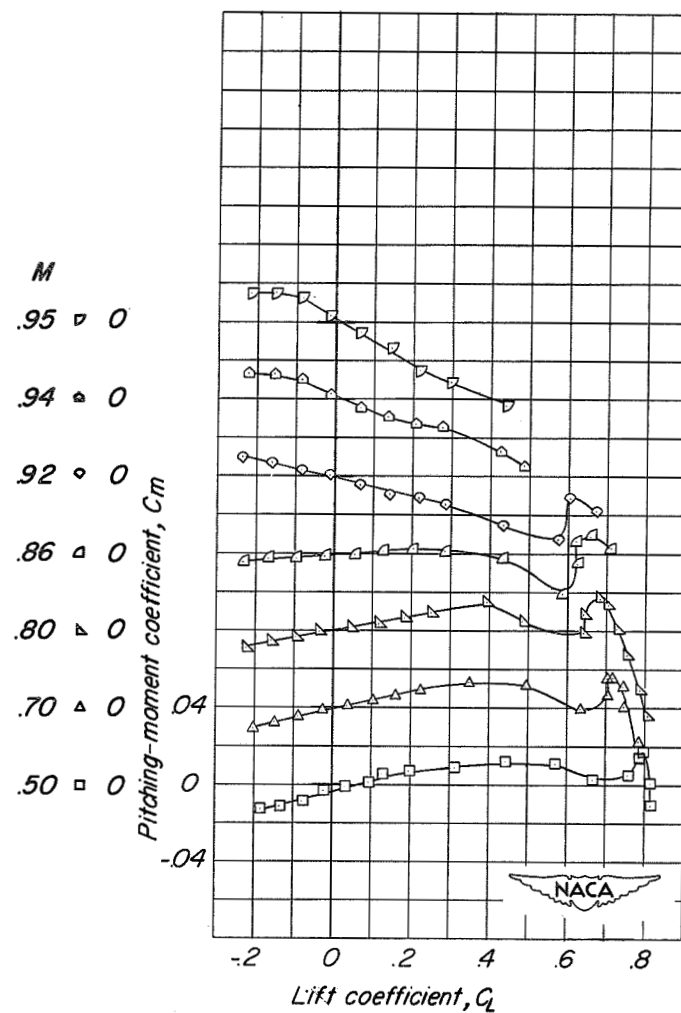
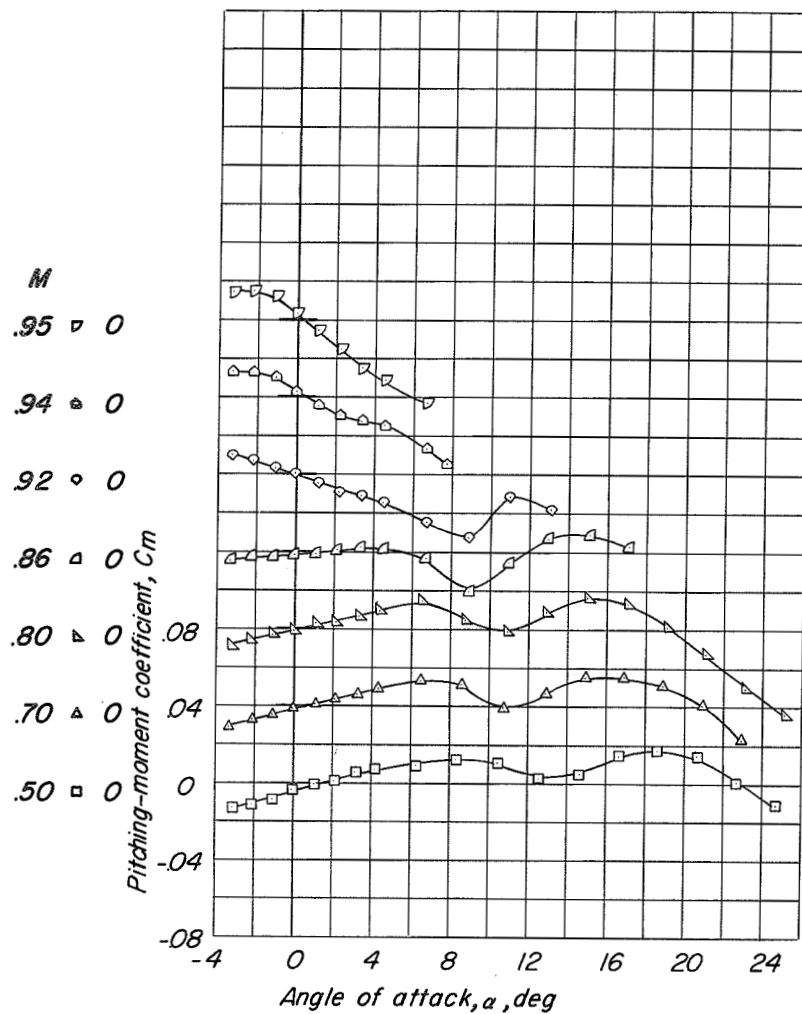
(a) Lift.

Figure 8.- Aerodynamic characteristics in pitch of the wing fuselage of the basic model.  $\beta = 0^\circ$ .



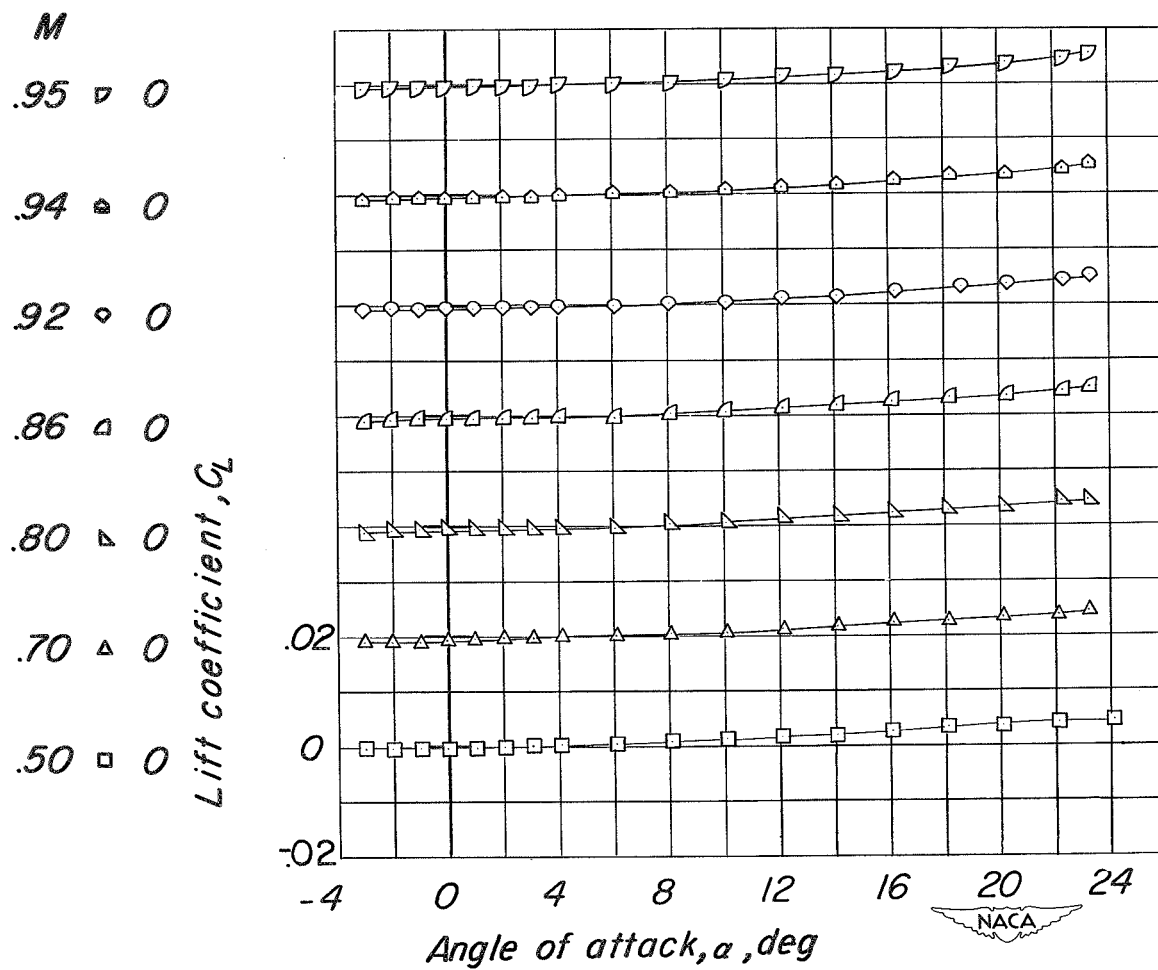
(b) Drag.

Figure 8.- Continued.



(c) Pitching moment.

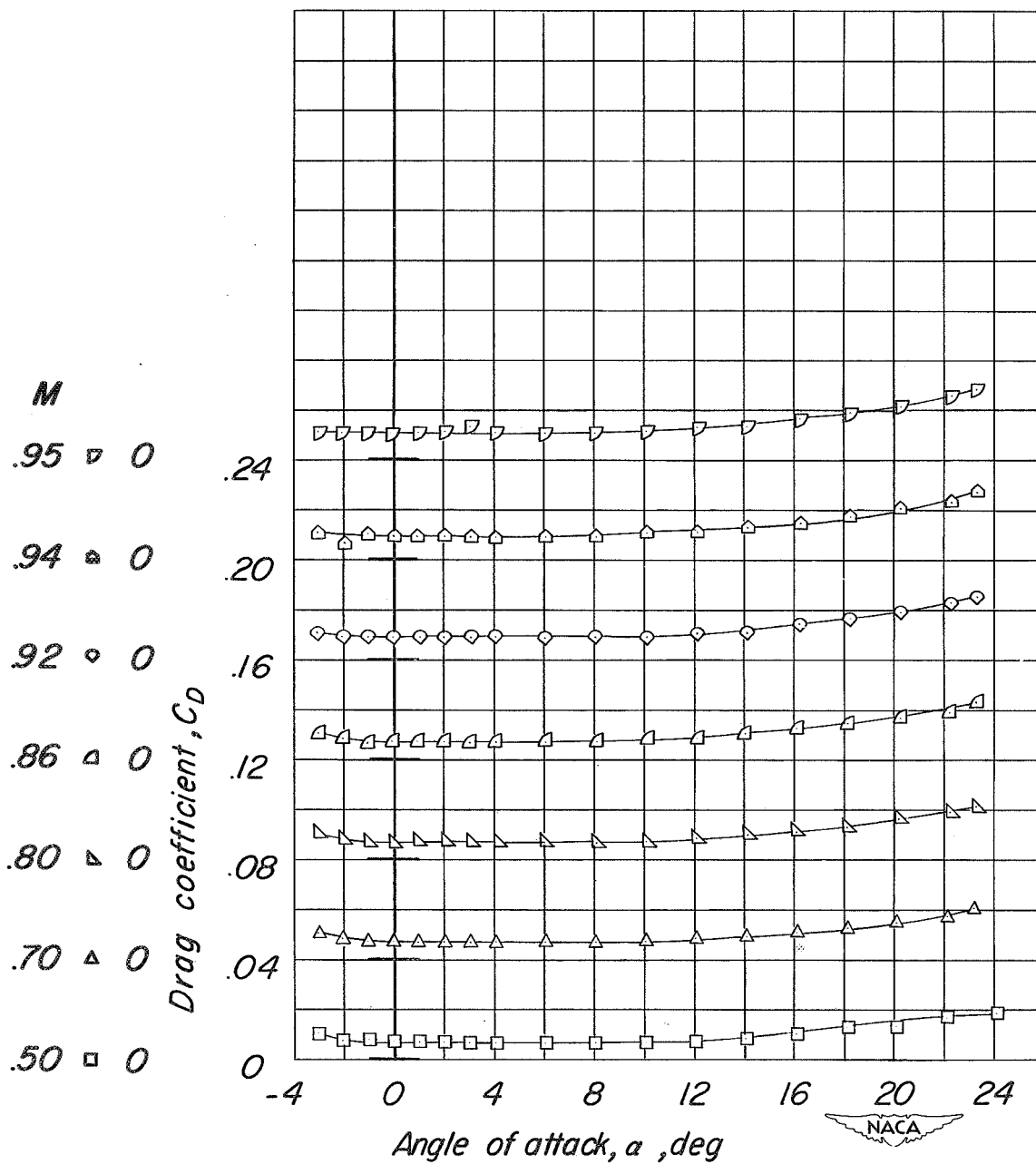
Figure 8.- Concluded.



(a) Lift.

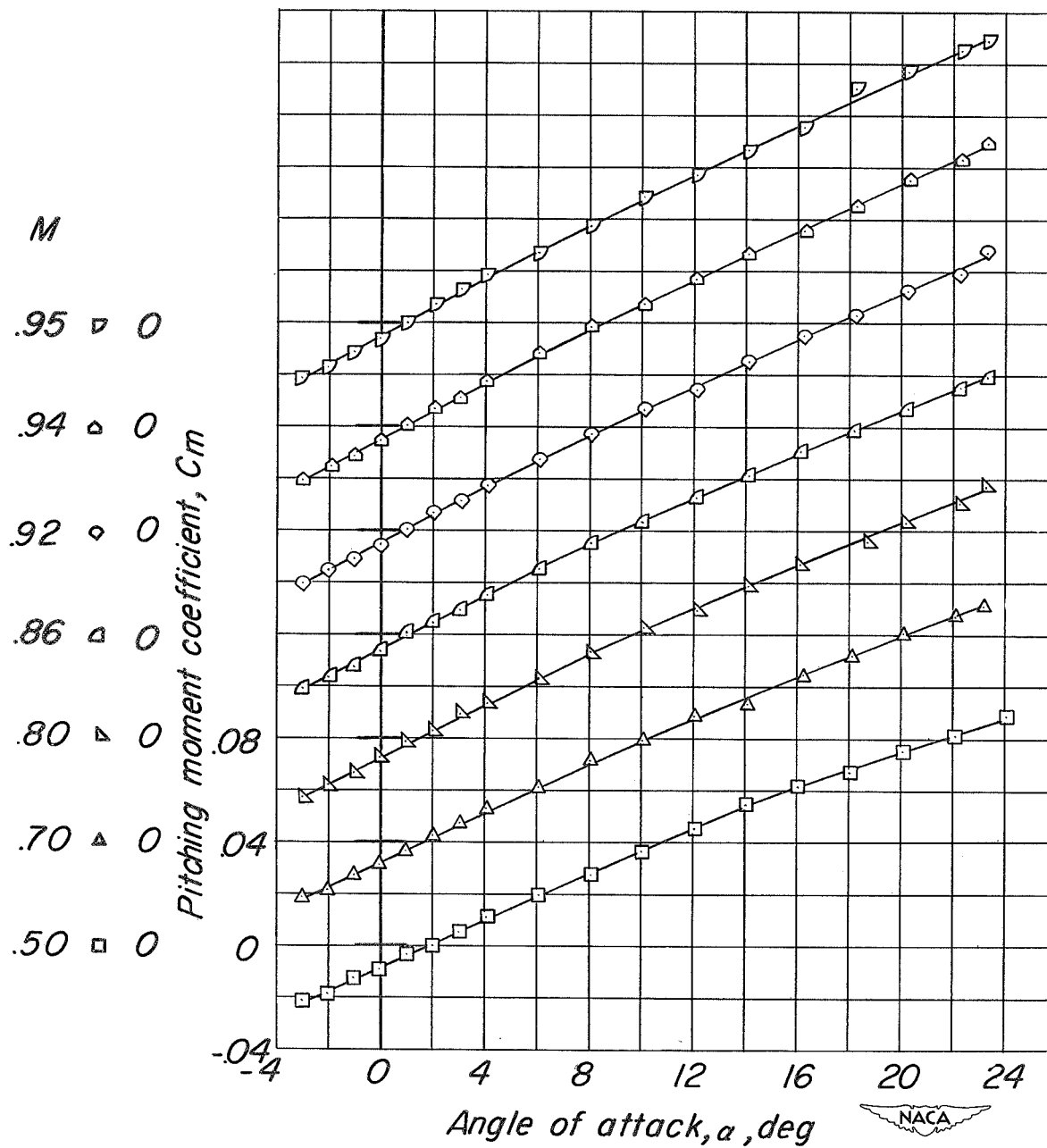
Figure 9.- Aerodynamic characteristics in pitch of the fuselage alone.  
 $\beta = 0^\circ$ .





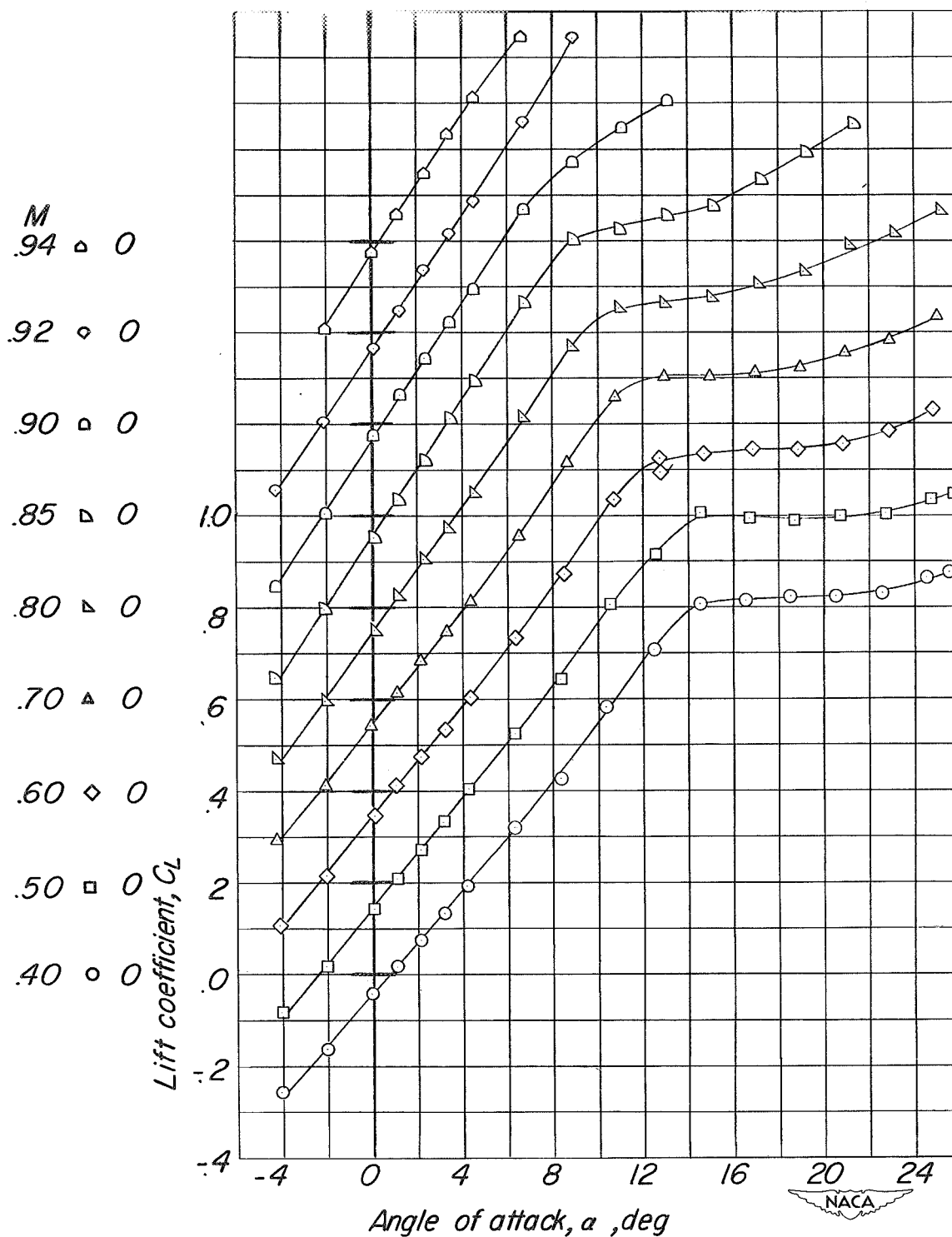
(b) Drag.

Figure 9.- Continued.



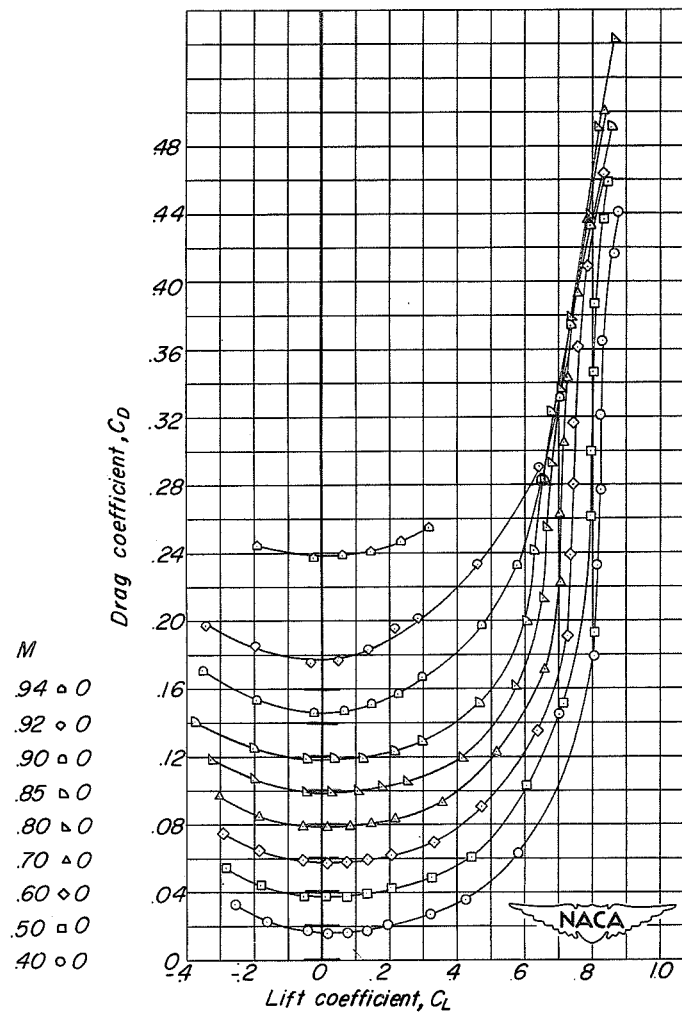
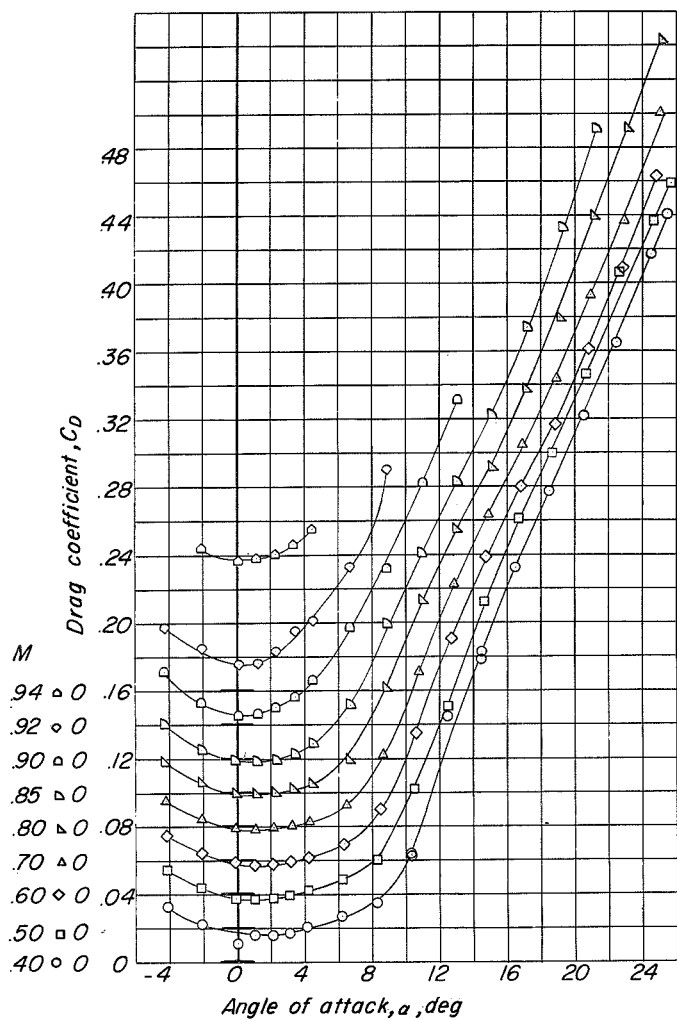
(c) Pitching moment.

Figure 9.- Concluded.



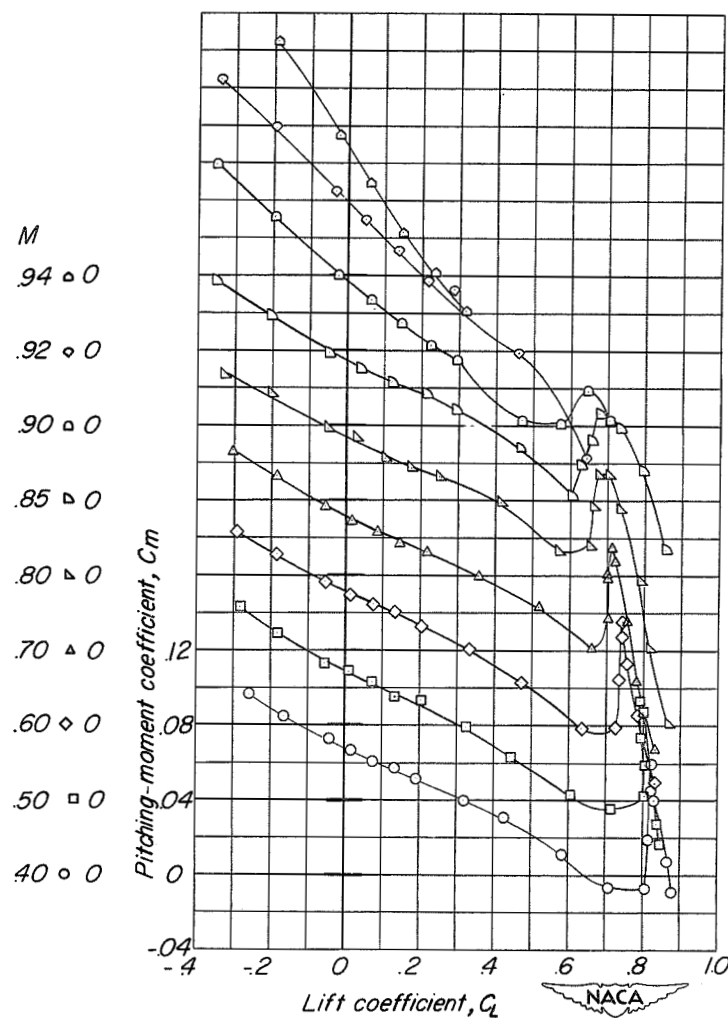
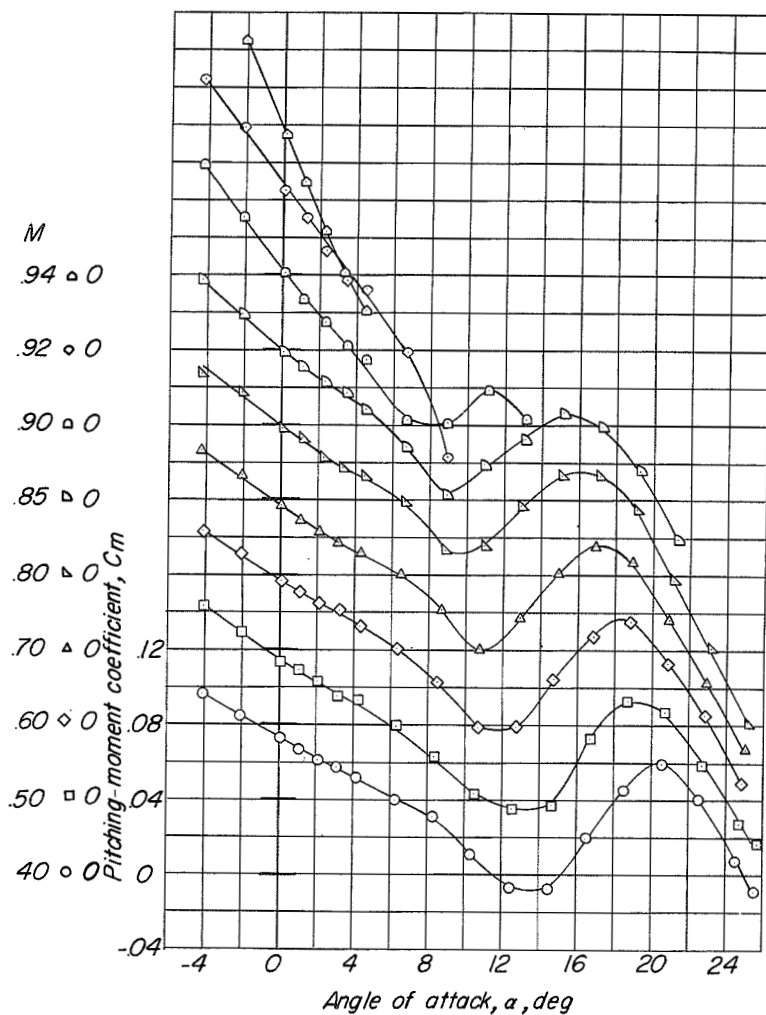
(a) Lift.

Figure 10.- Aerodynamic characteristics in pitch of the basic model.  
 $\beta = 0^\circ$ ;  $i_t = -4^\circ$ .



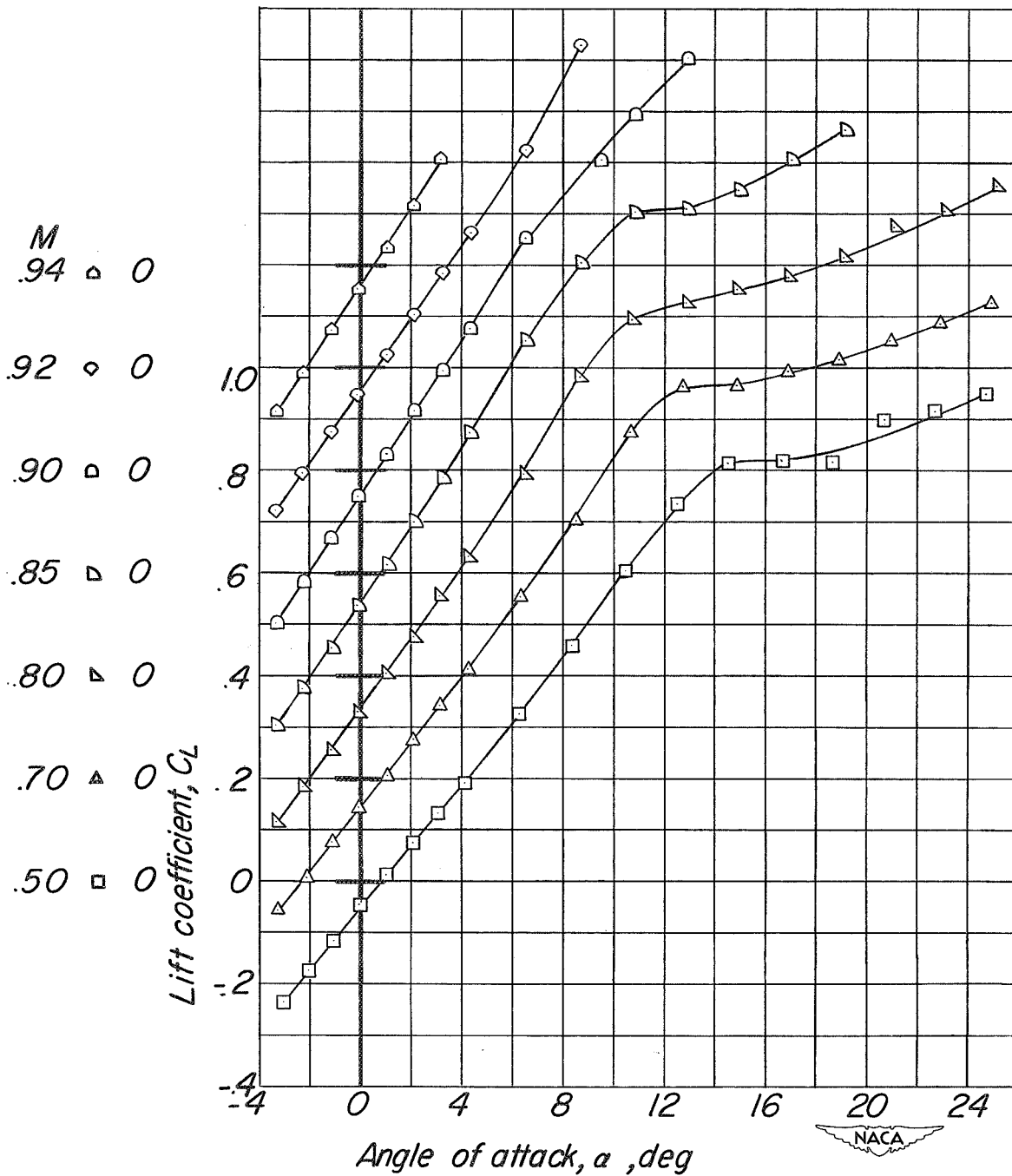
(b) Drag.

Figure 10.- Continued.



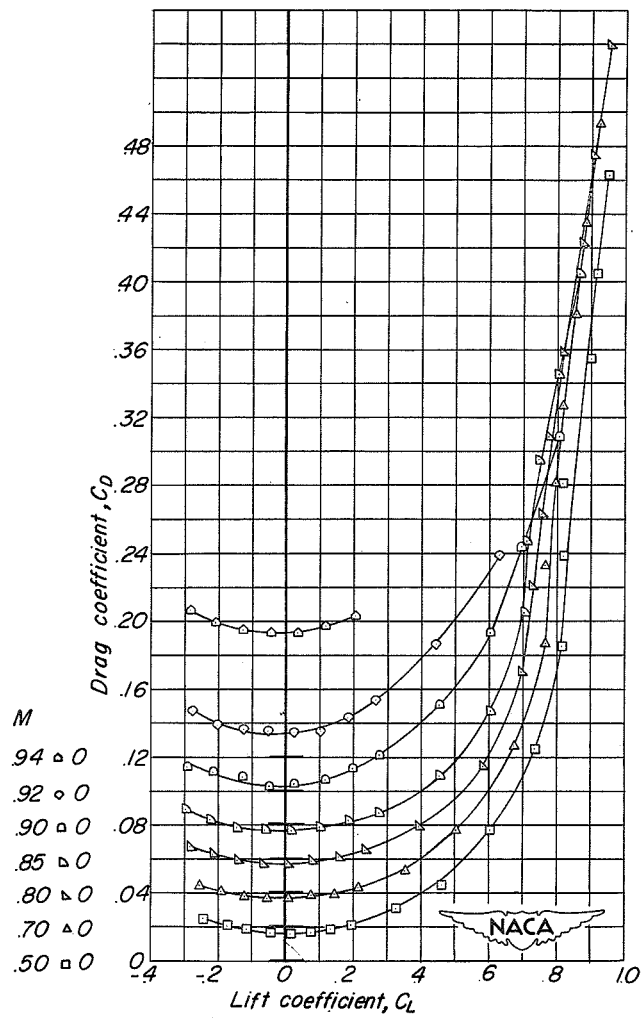
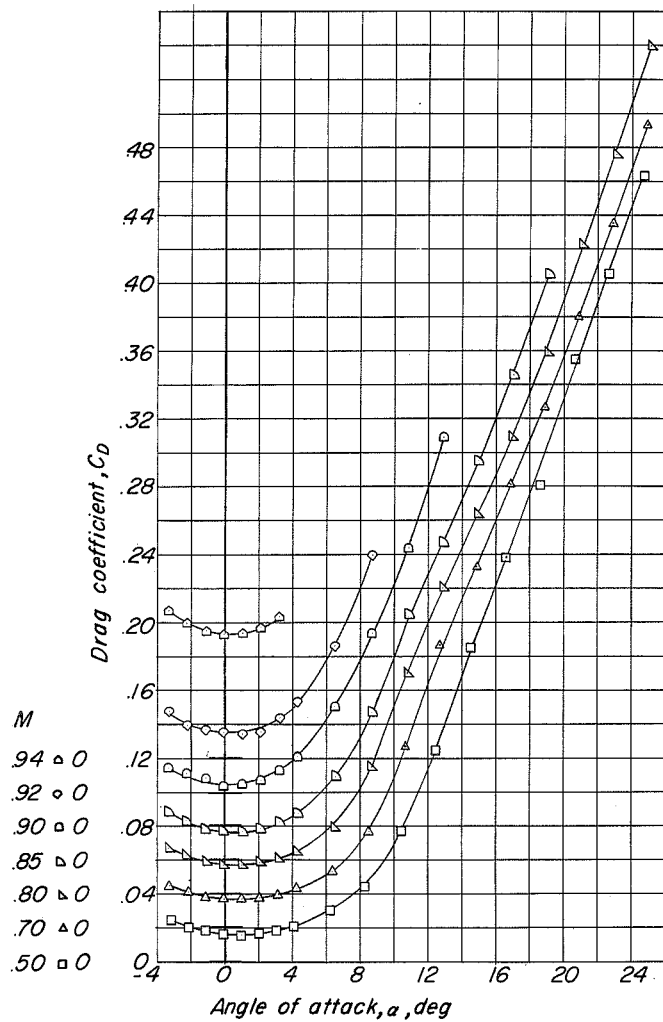
(c) Pitching moment.

Figure 10.- Concluded.



(a) Lift.

Figure 11.- Aerodynamic characteristics in pitch of the vertical-tail configuration with fuselage side fins (modification 8).  $\beta = 0^\circ$ ;  $i_t = 0^\circ$ .



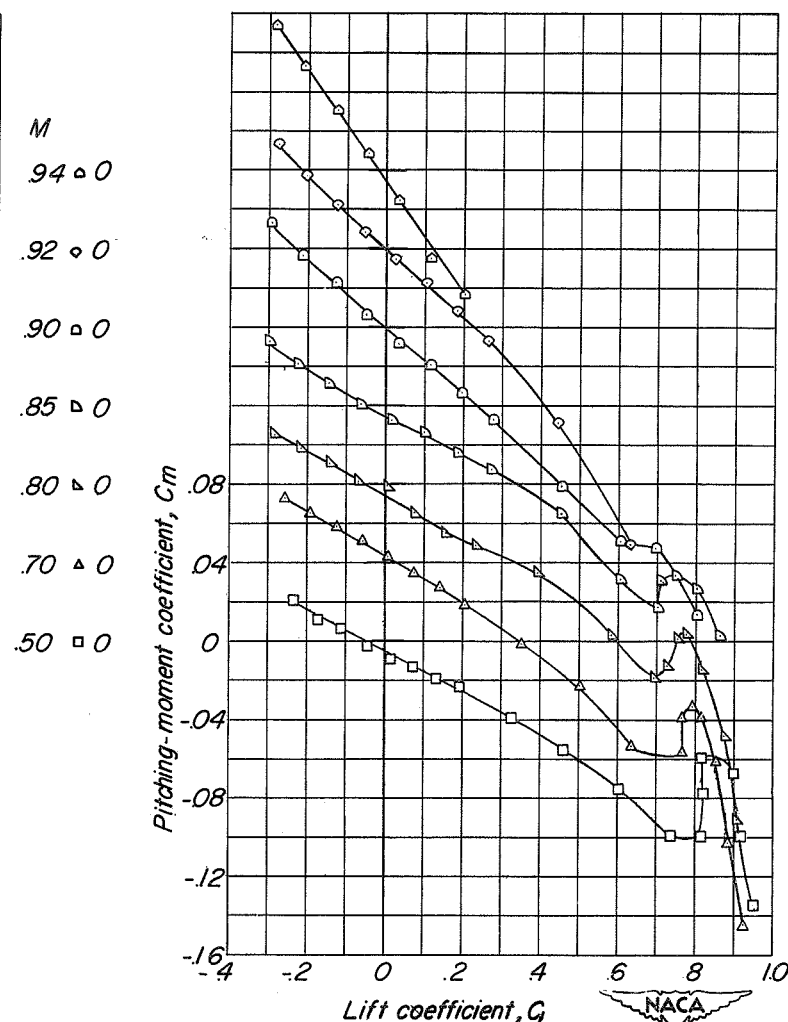
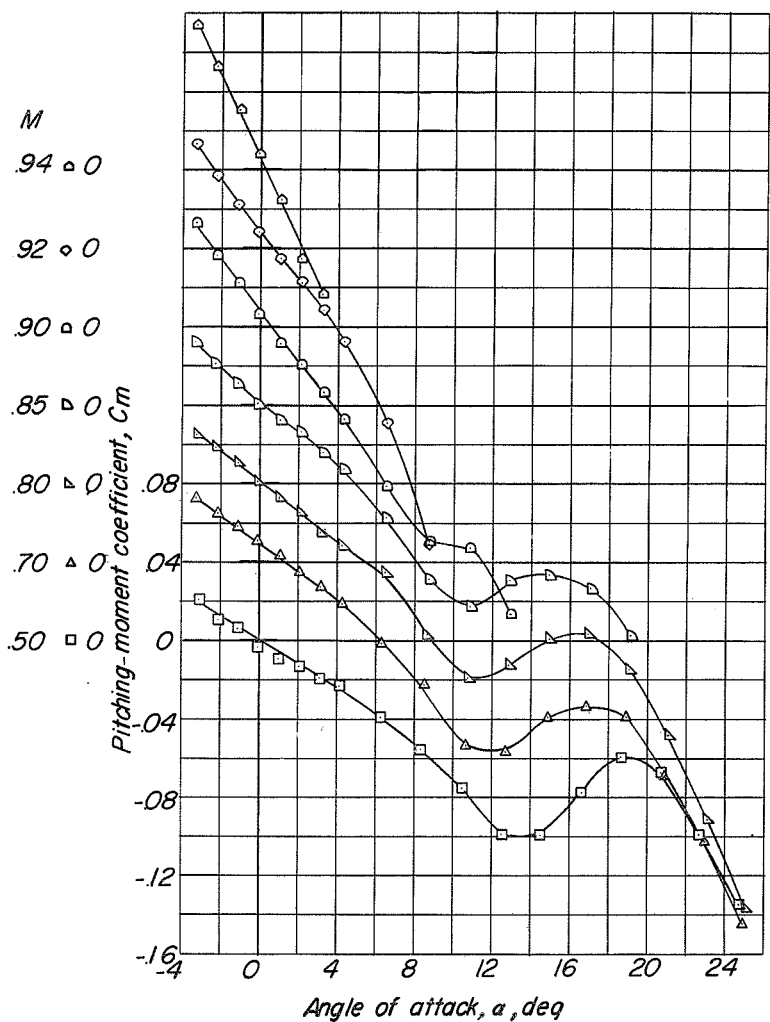
(b) Drag.

Figure 11.- Continued.

CONFIDENTIAL

NACA RM SL53G20

CONFIDENTIAL

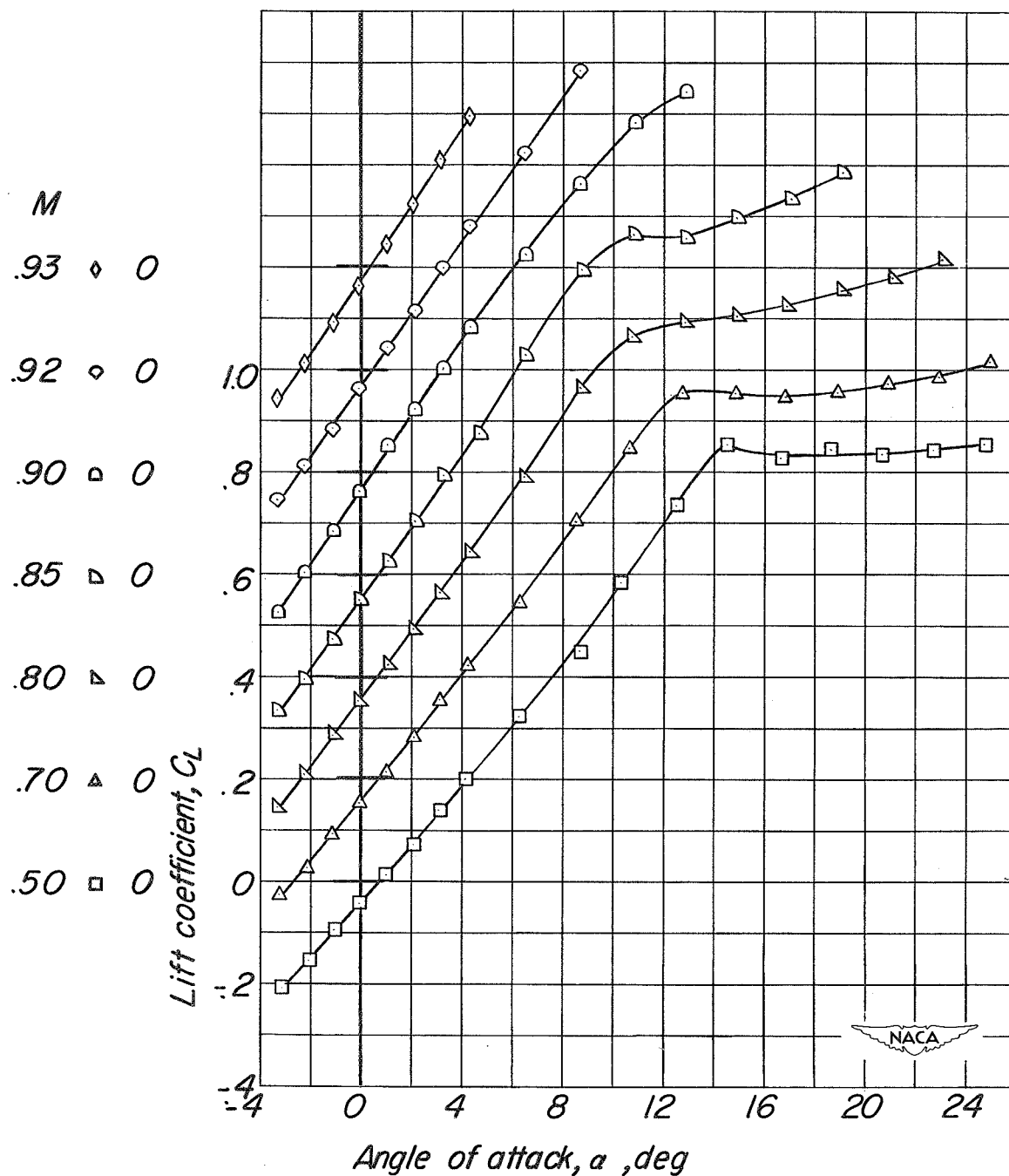


(c) Pitching moment.

Figure 11.- Concluded.

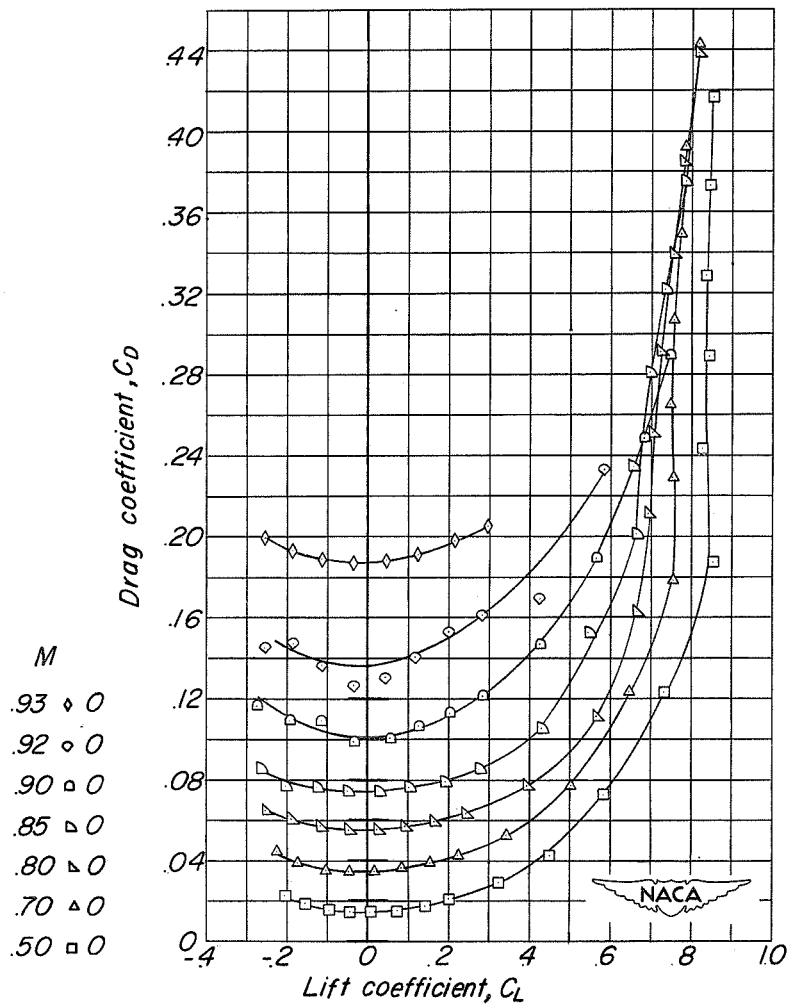
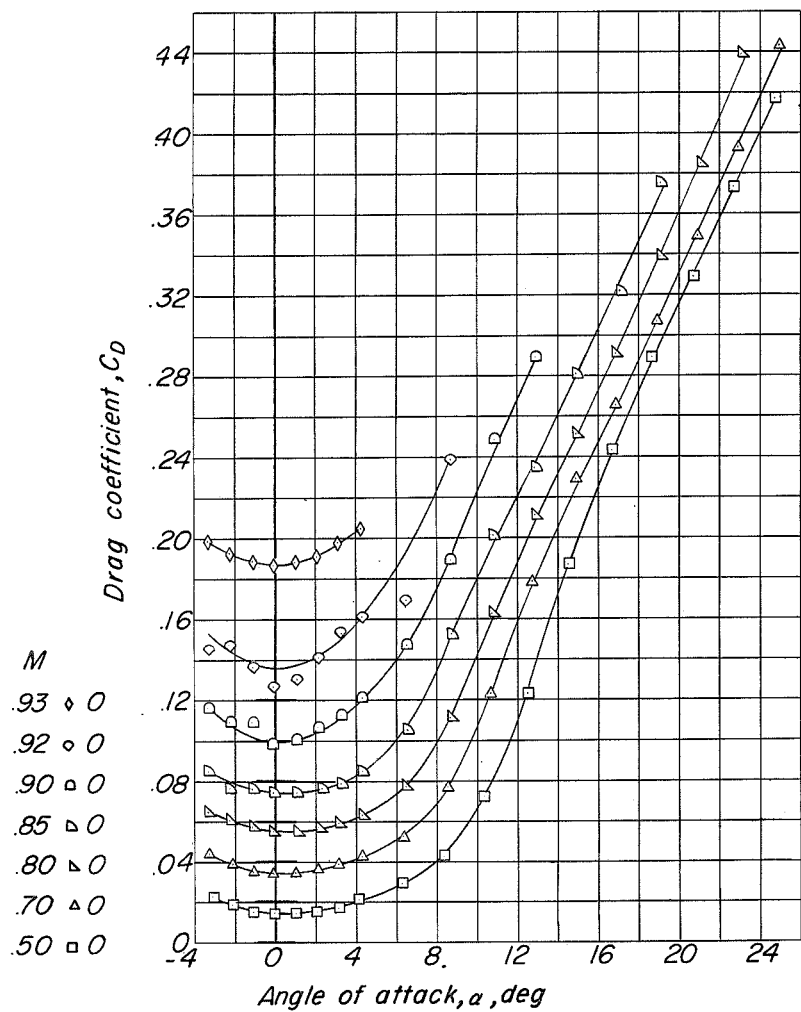
CONFIDENTIAL





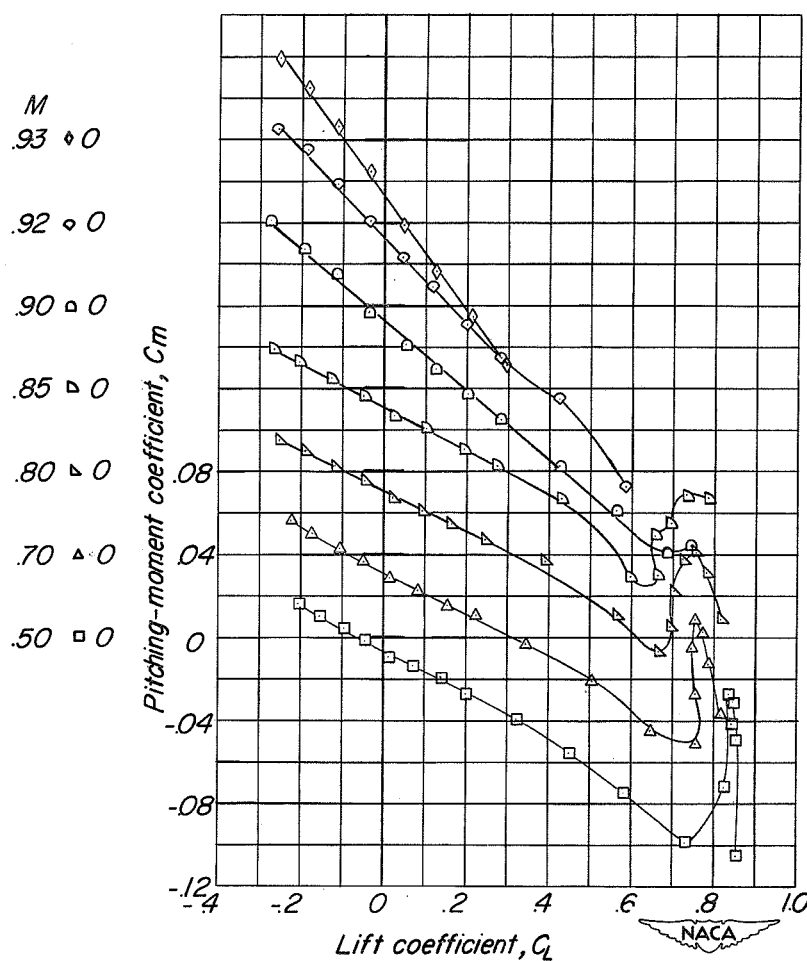
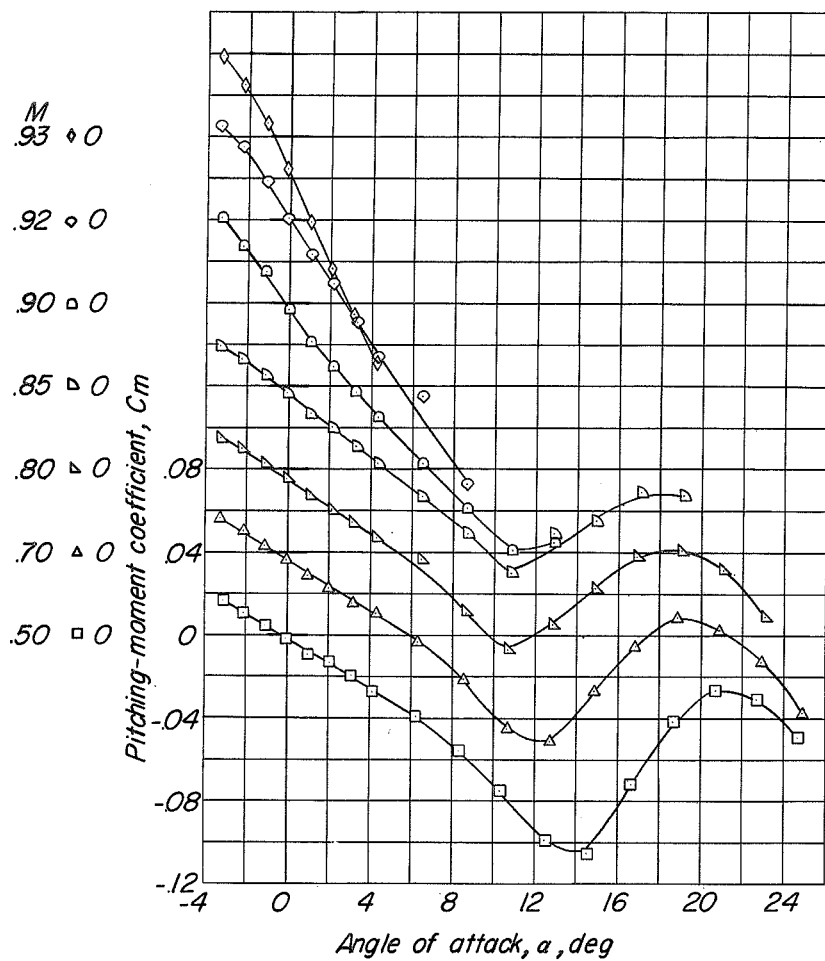
(a) Lift.

Figure 12.- Aerodynamic characteristics in pitch of the enlarged-vertical-tail configuration (modification 10).  $\beta = 0^\circ$ ;  $i_t = 0^\circ$ .



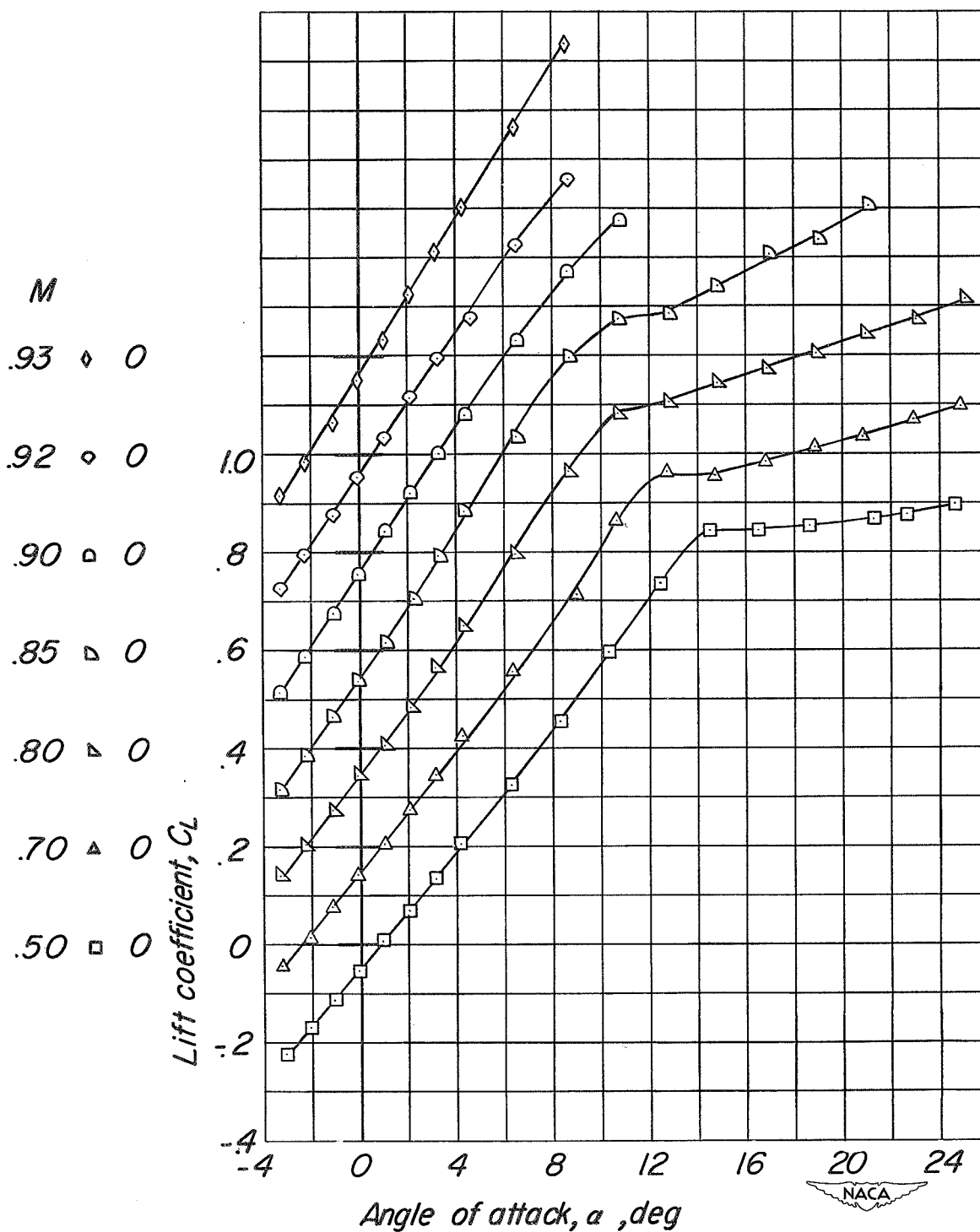
(b) Drag.

Figure 12.- Continued.



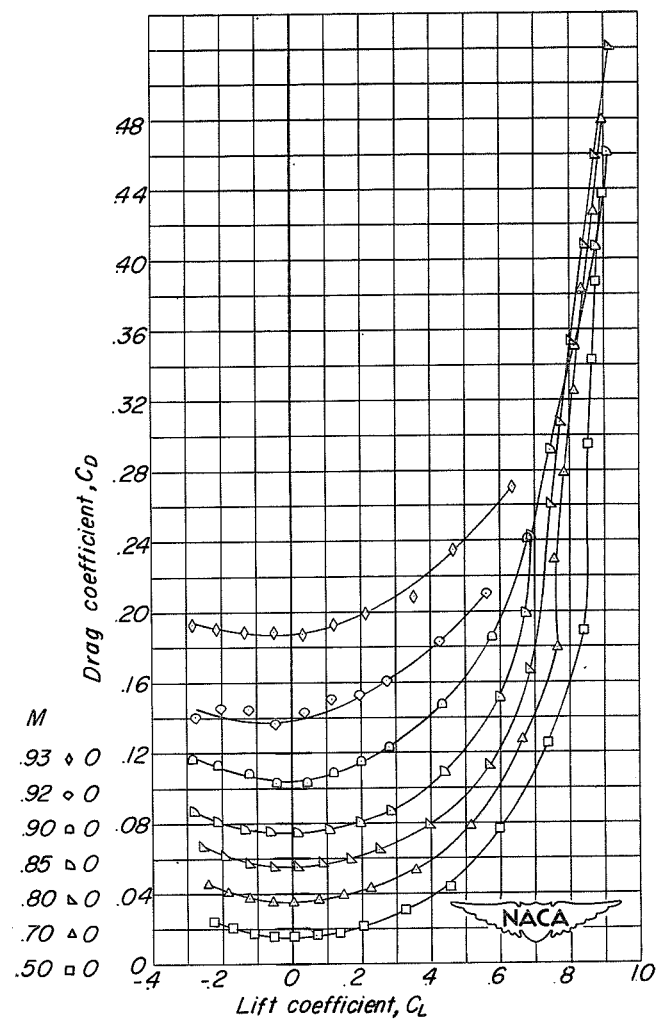
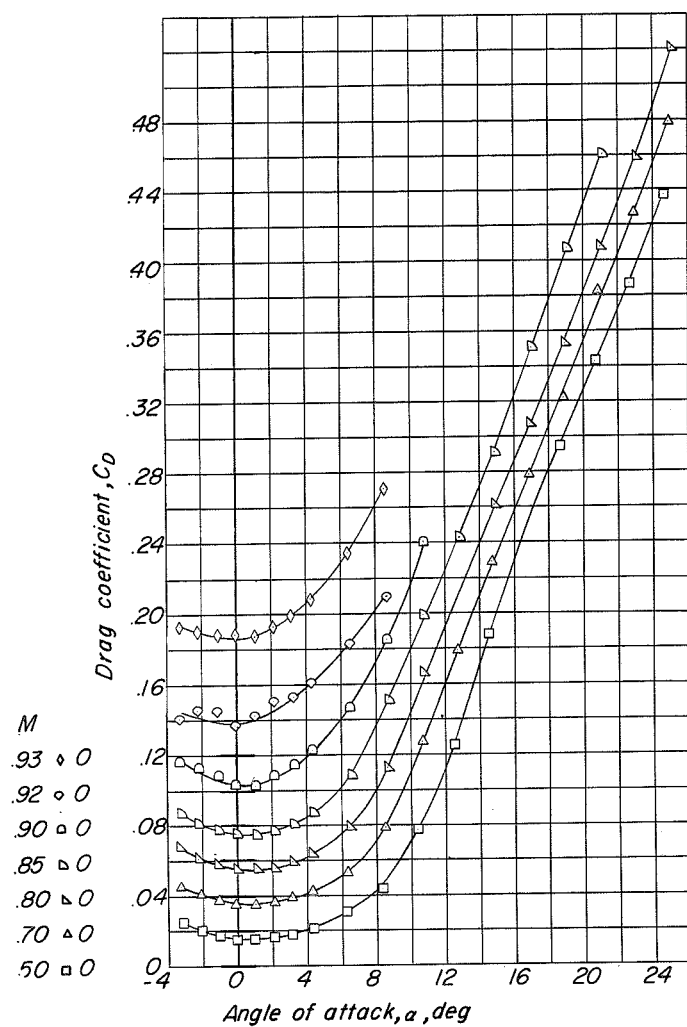
(c) Pitching moment.

Figure 12.- Concluded.



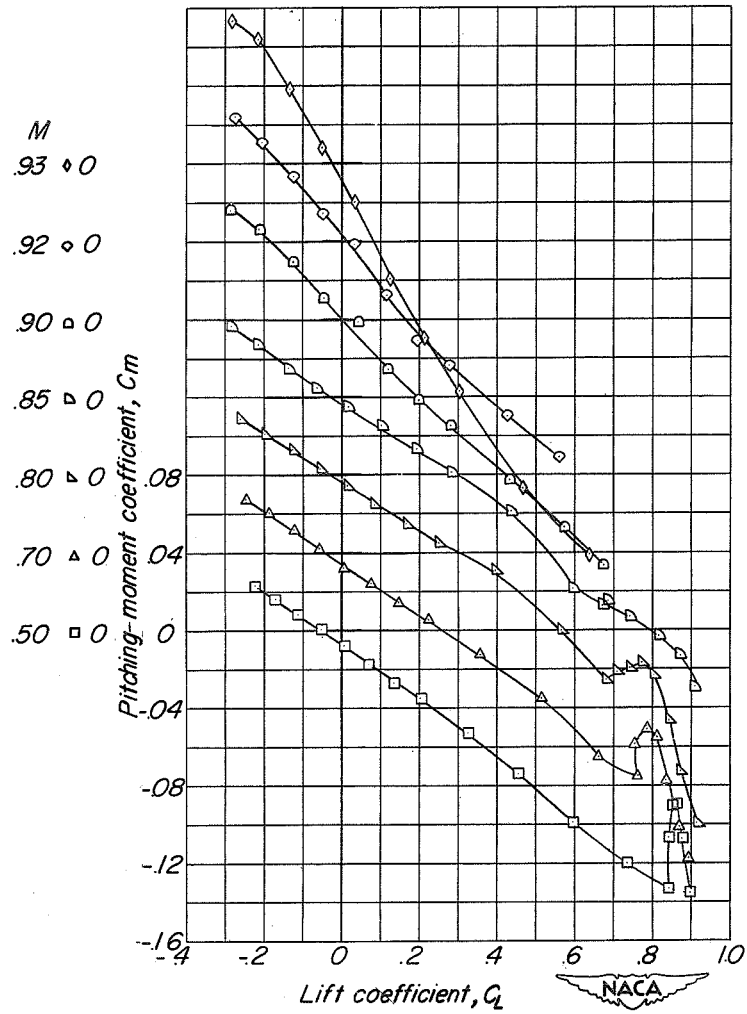
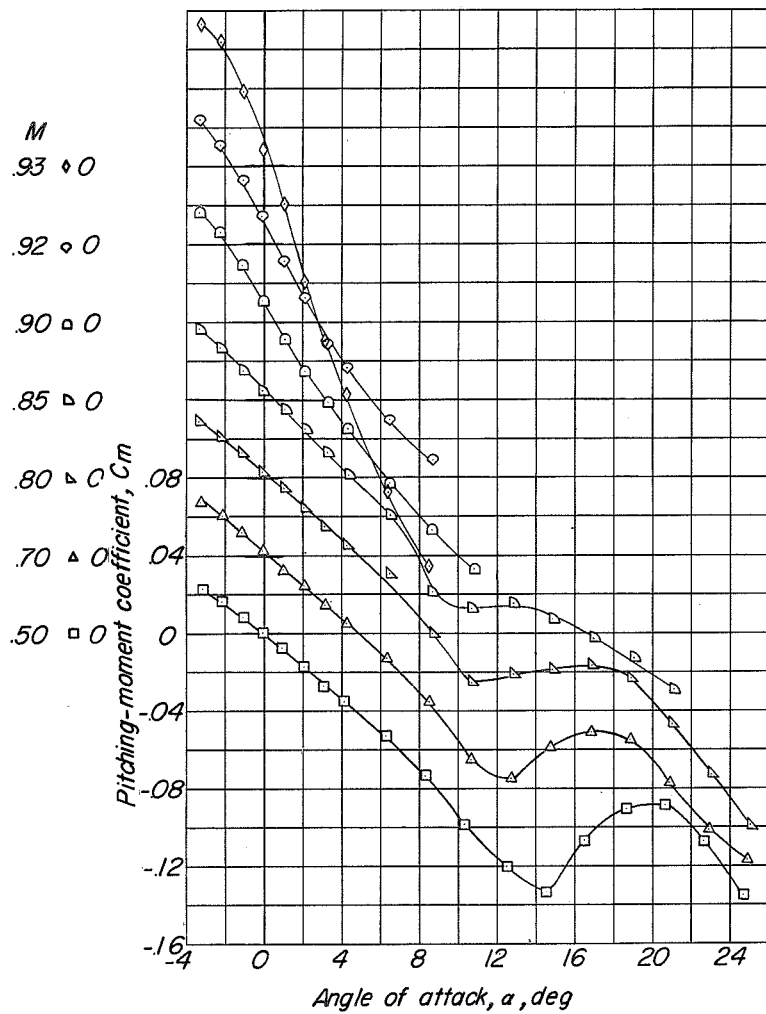
(a) Lift.

Figure 13.- Aerodynamic characteristics in pitch of the enlarged-vertical-tail configuration with fuselage side fins (modification 11).  $\beta = 0^\circ$ ;  $i_t = 0^\circ$ .



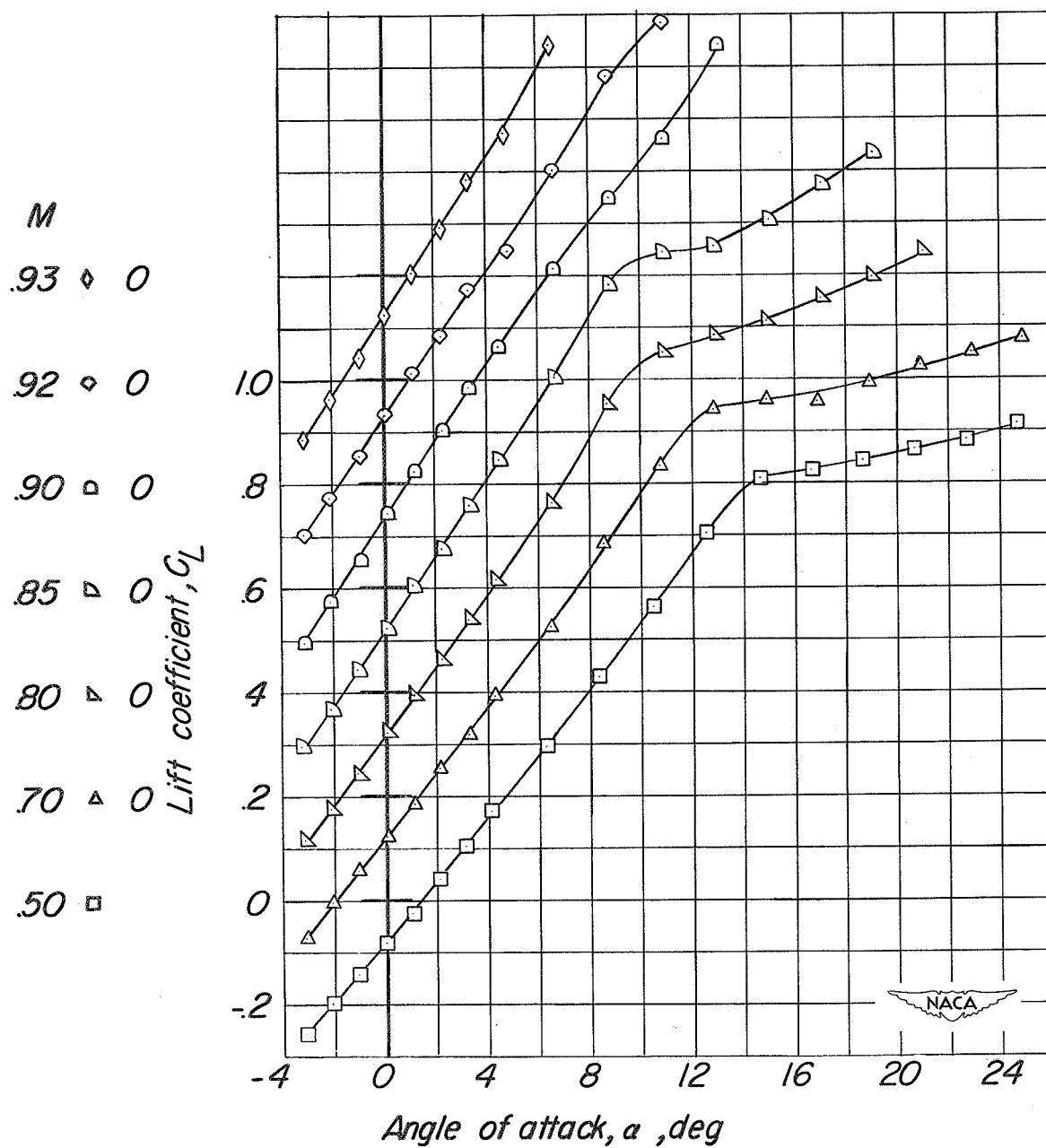
(b) Drag.

Figure 13.- Continued.



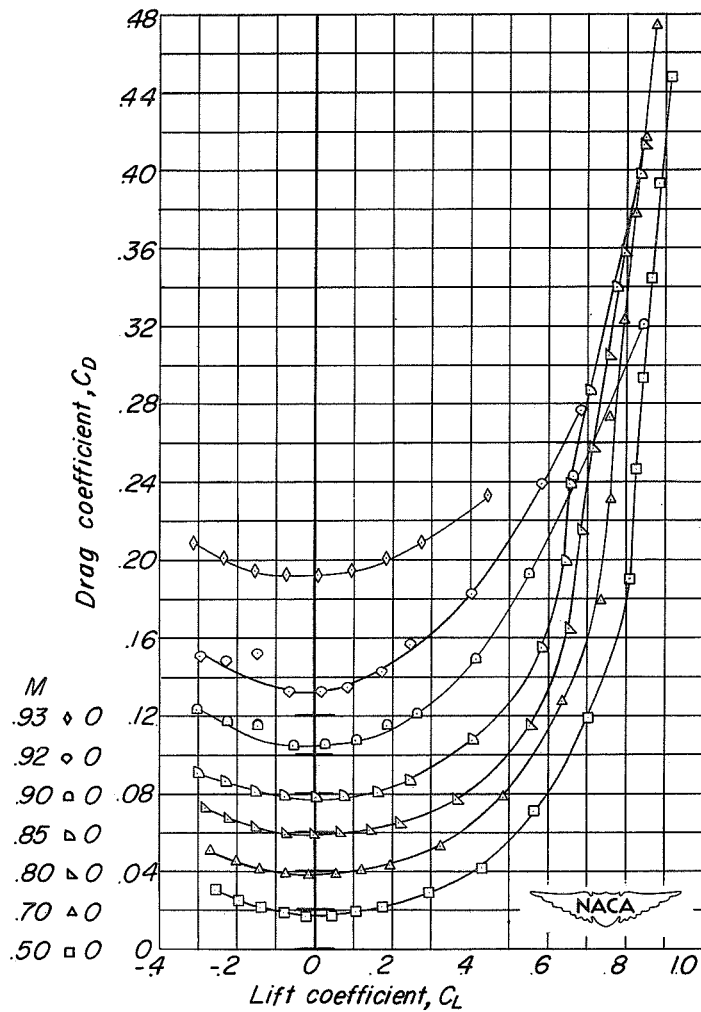
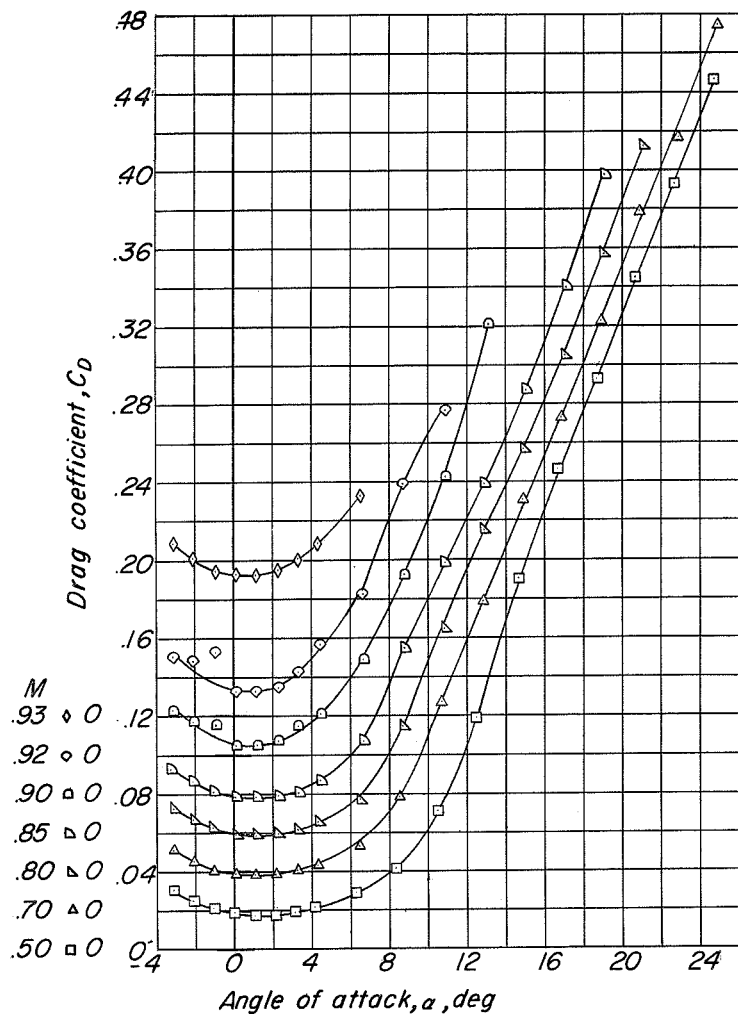
(c) Pitching moment.

Figure 13.- Concluded.



(a) Lift.

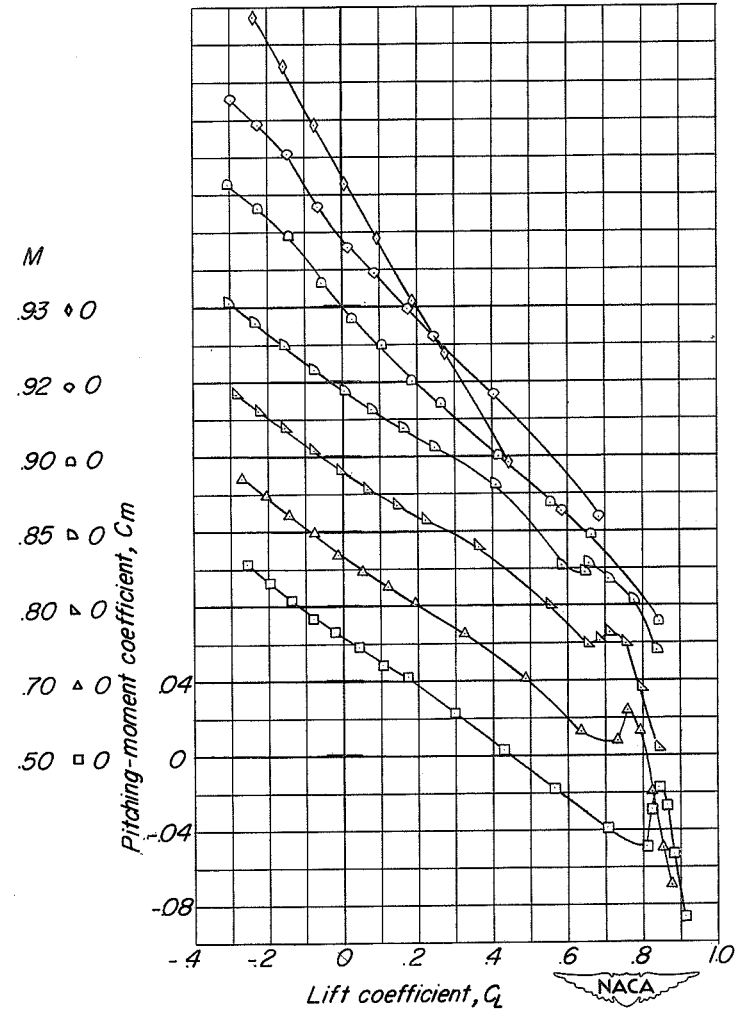
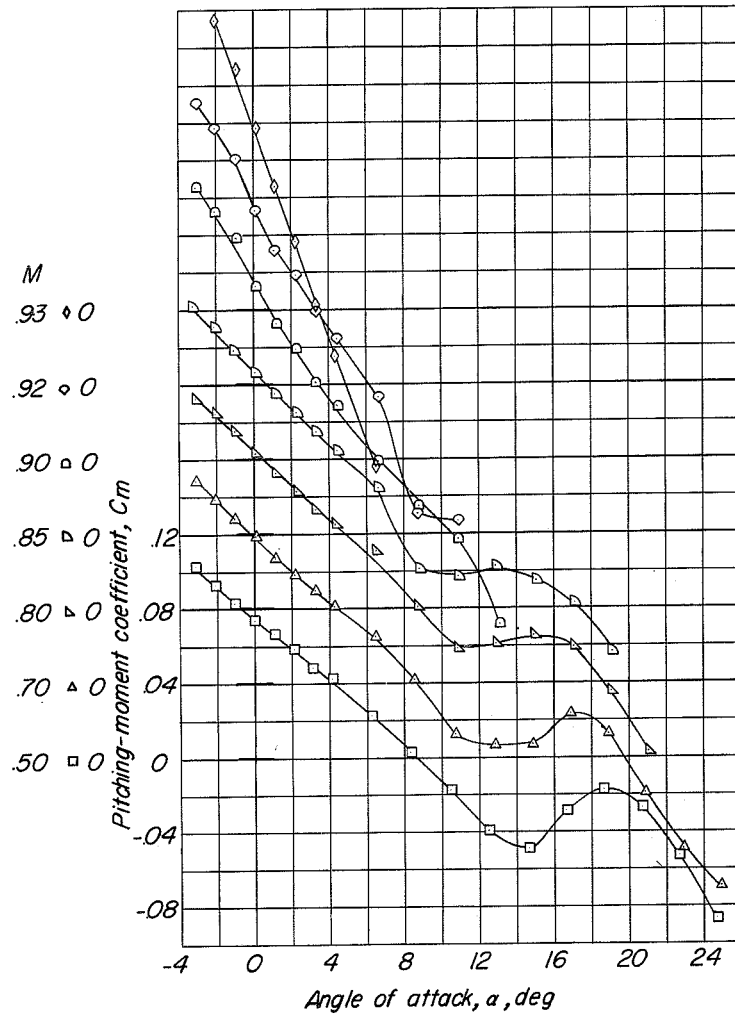
Figure 14.- Aerodynamic characteristics in pitch of the enlarged-vertical-tail configuration with fuselage side fins (modification 11).  $\beta = 0^\circ$ ;  $i_t = -4^\circ$ .



(b) Drag.

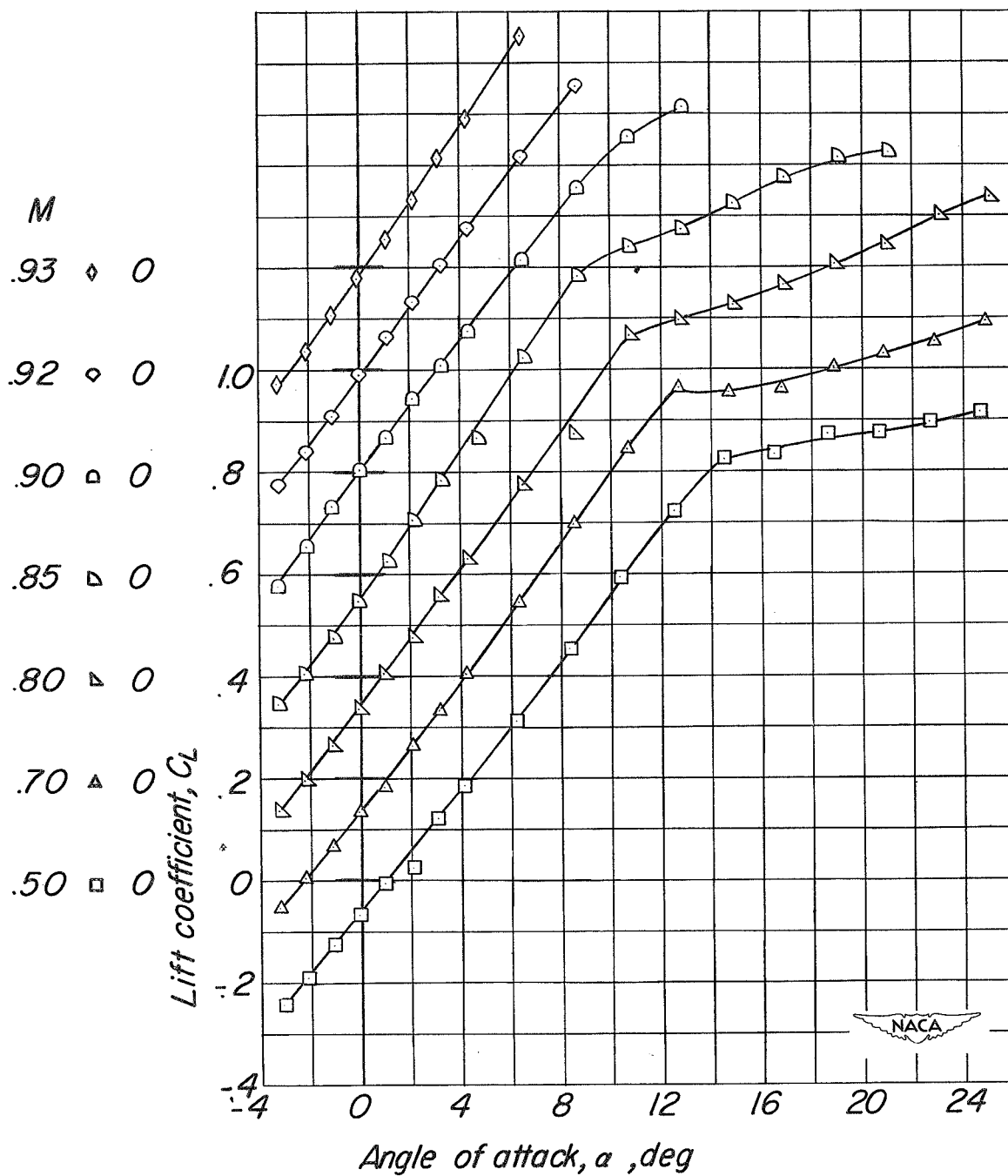
Figure 14.- Continued.





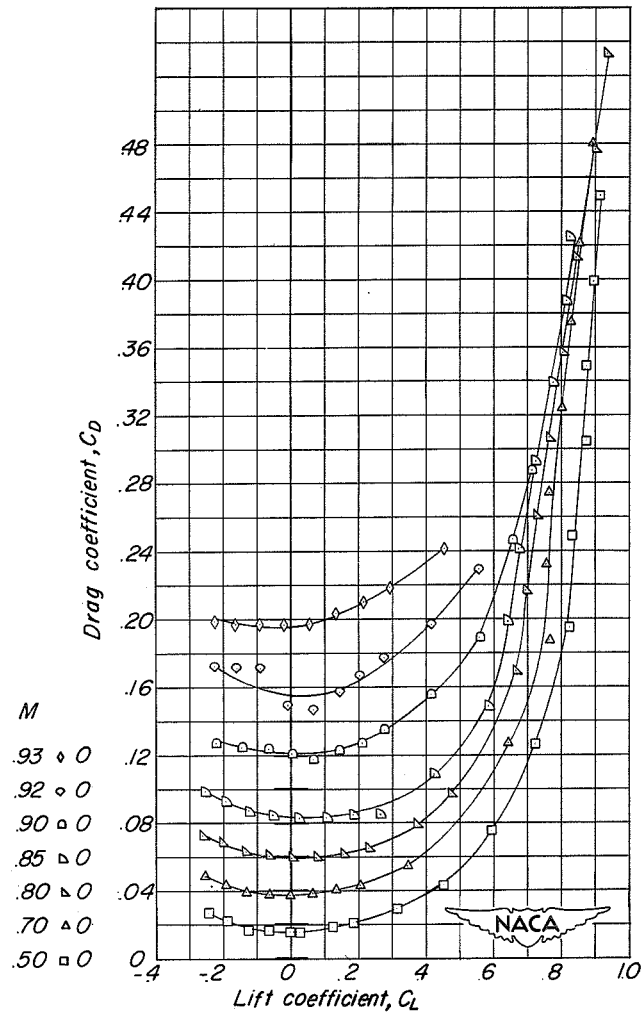
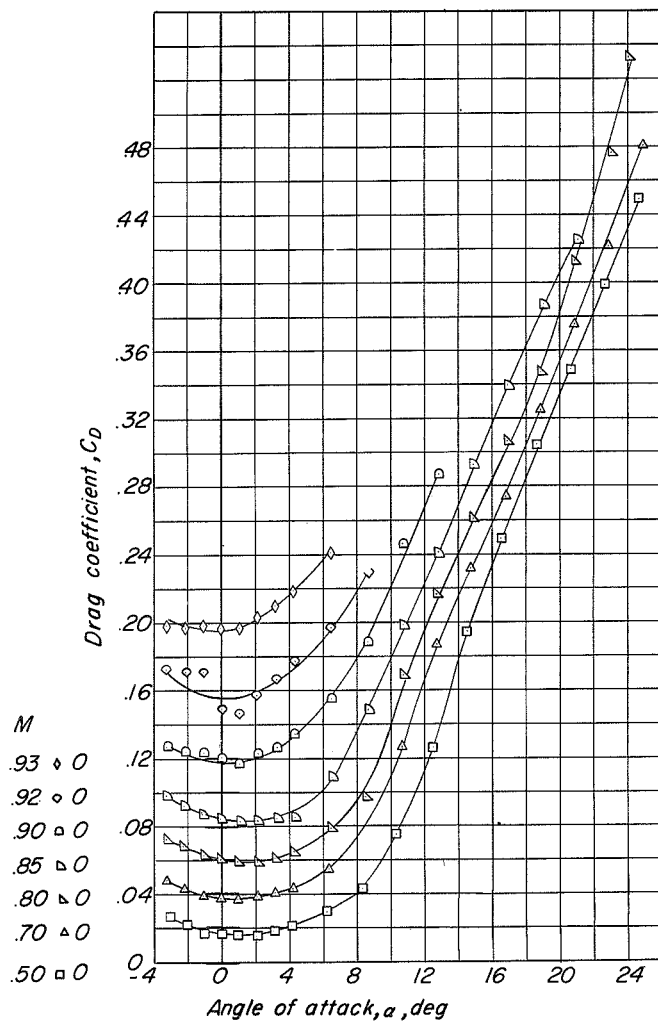
(c) Pitching moment.

Figure 14.- Concluded.



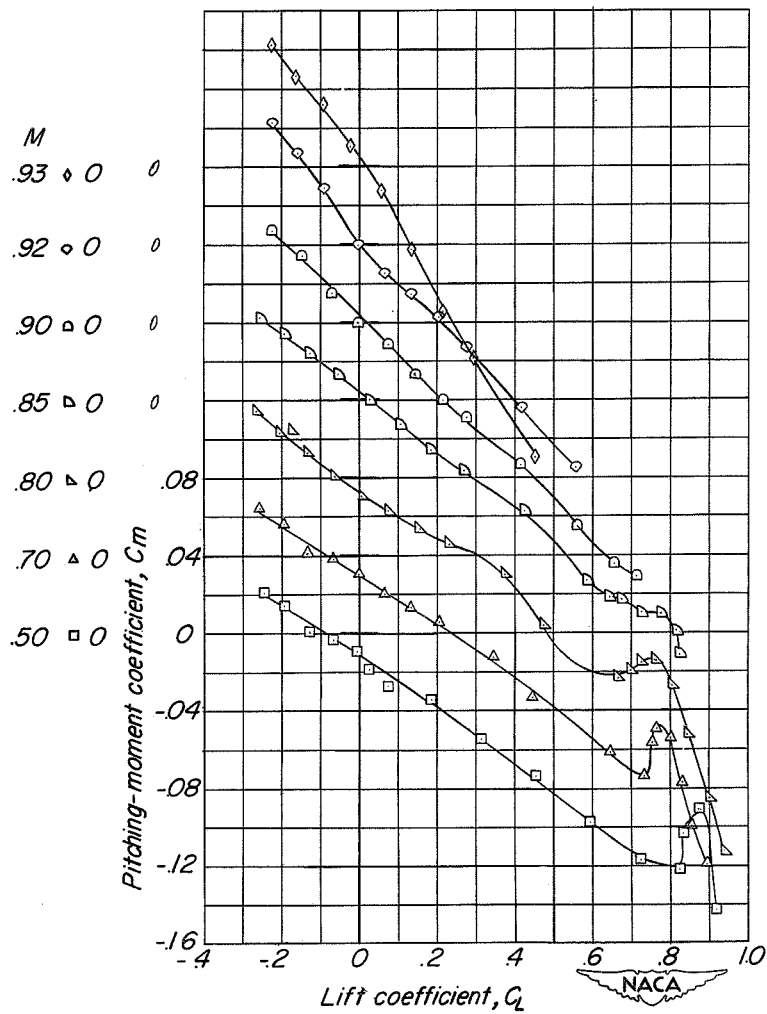
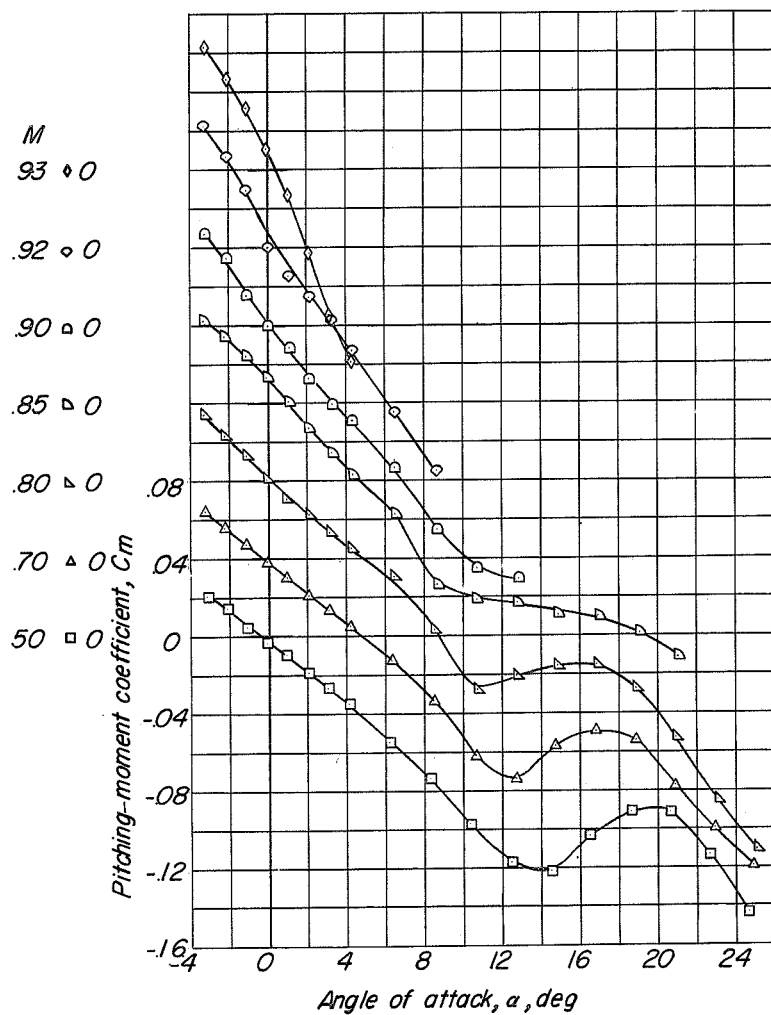
(a) Lift.

Figure 15.- Aerodynamic characteristics in pitch of the enlarged-vertical-tail configuration with fuselage side fins and wing stores (modification 12).  $\beta = 0^\circ$ ;  $i_t = 0^\circ$ .



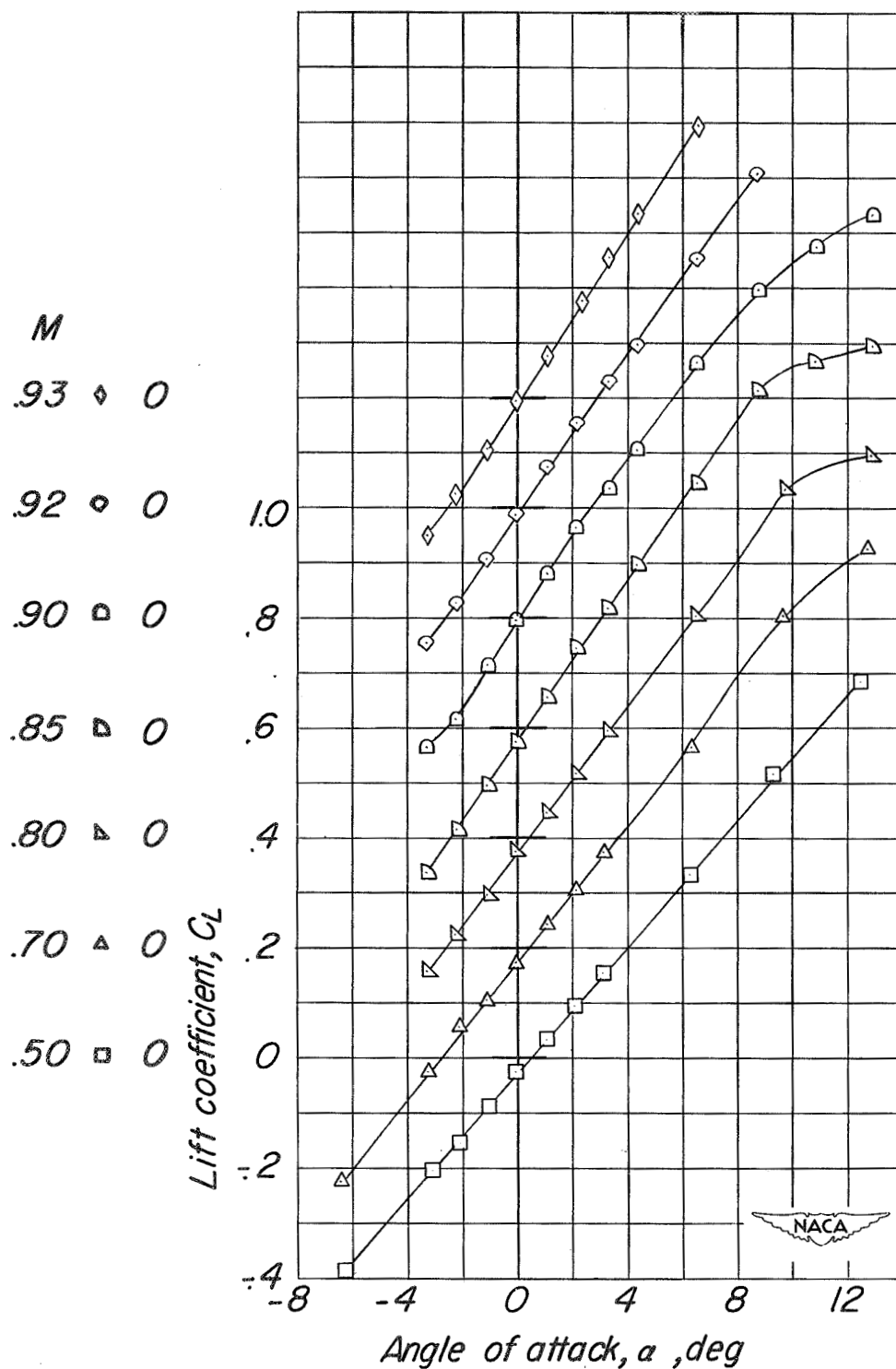
(b) Drag.

Figure 15.- Continued.



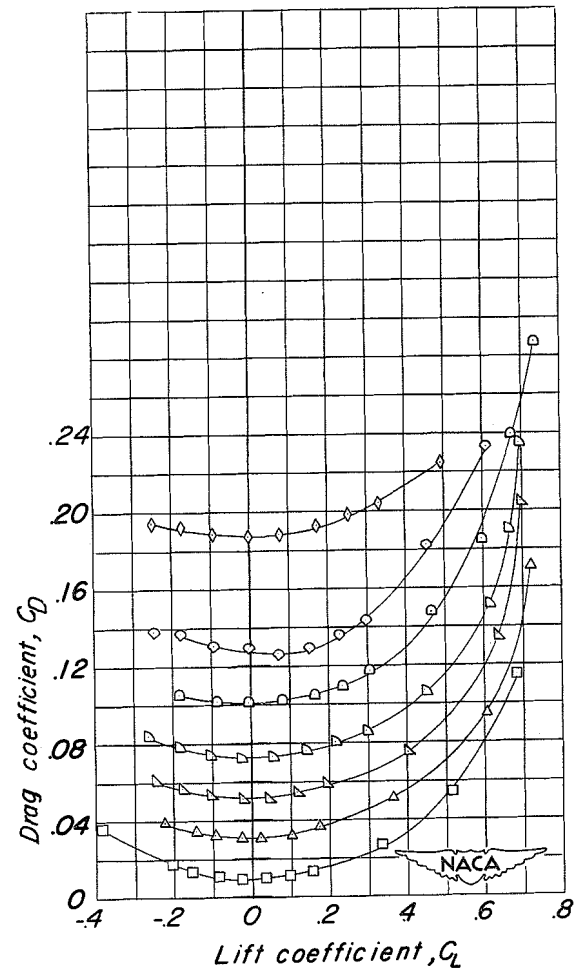
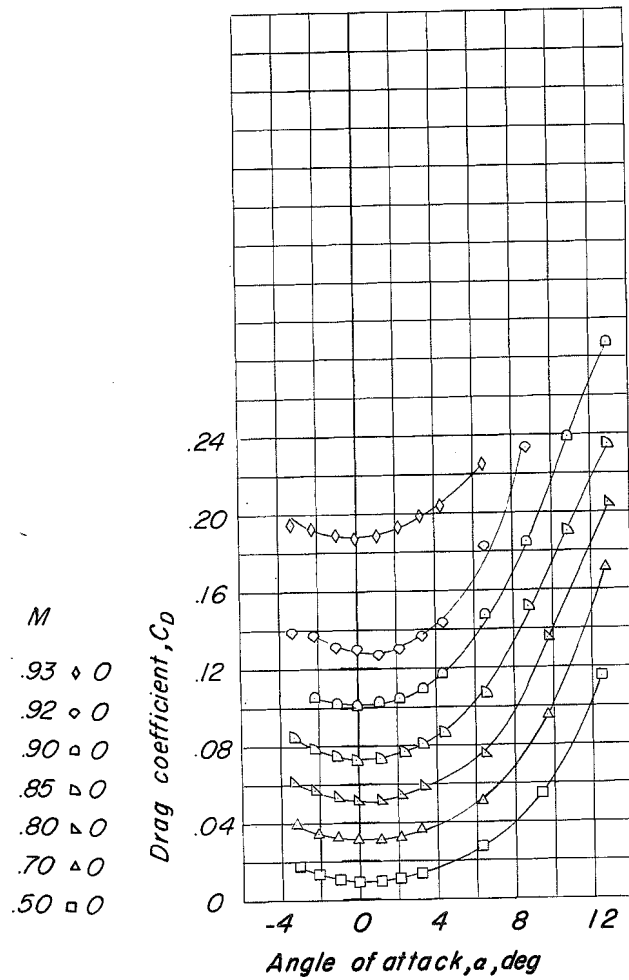
(c) Pitching moment.

Figure 15.- Concluded.



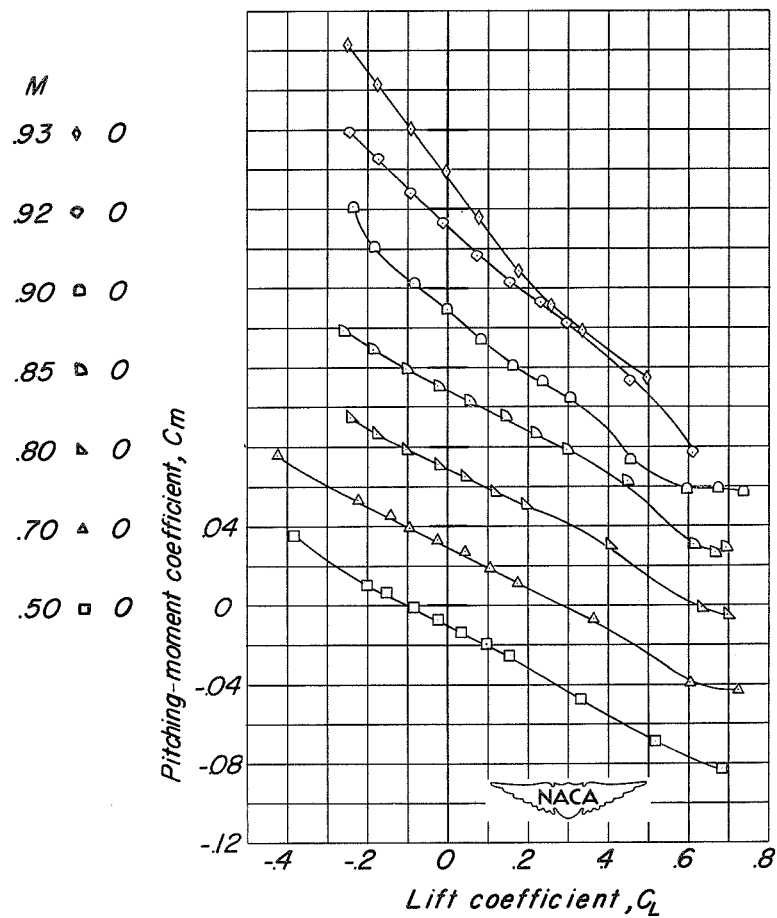
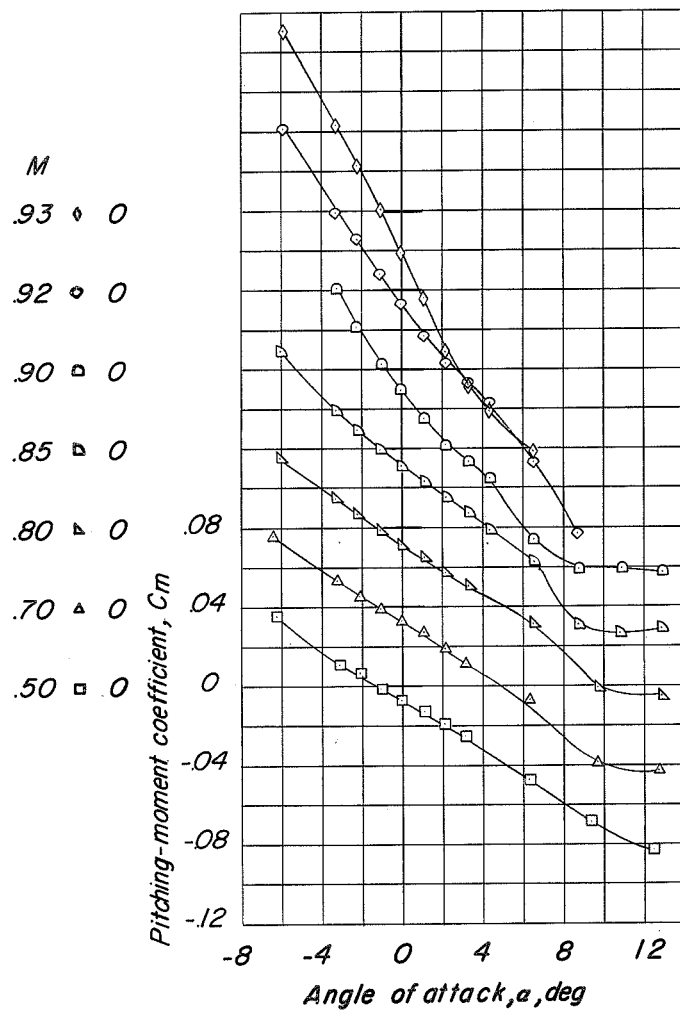
(a) Lift.

Figure 16.- Aerodynamic characteristics in pitch of the enlarged-vertical-tail configuration (modification 11).  $\beta = 6^\circ$ ;  $i_t = 0^\circ$ .



(b) Drag.

Figure 16.- Continued.



(c) Pitching moment.

Figure 16.- Concluded.

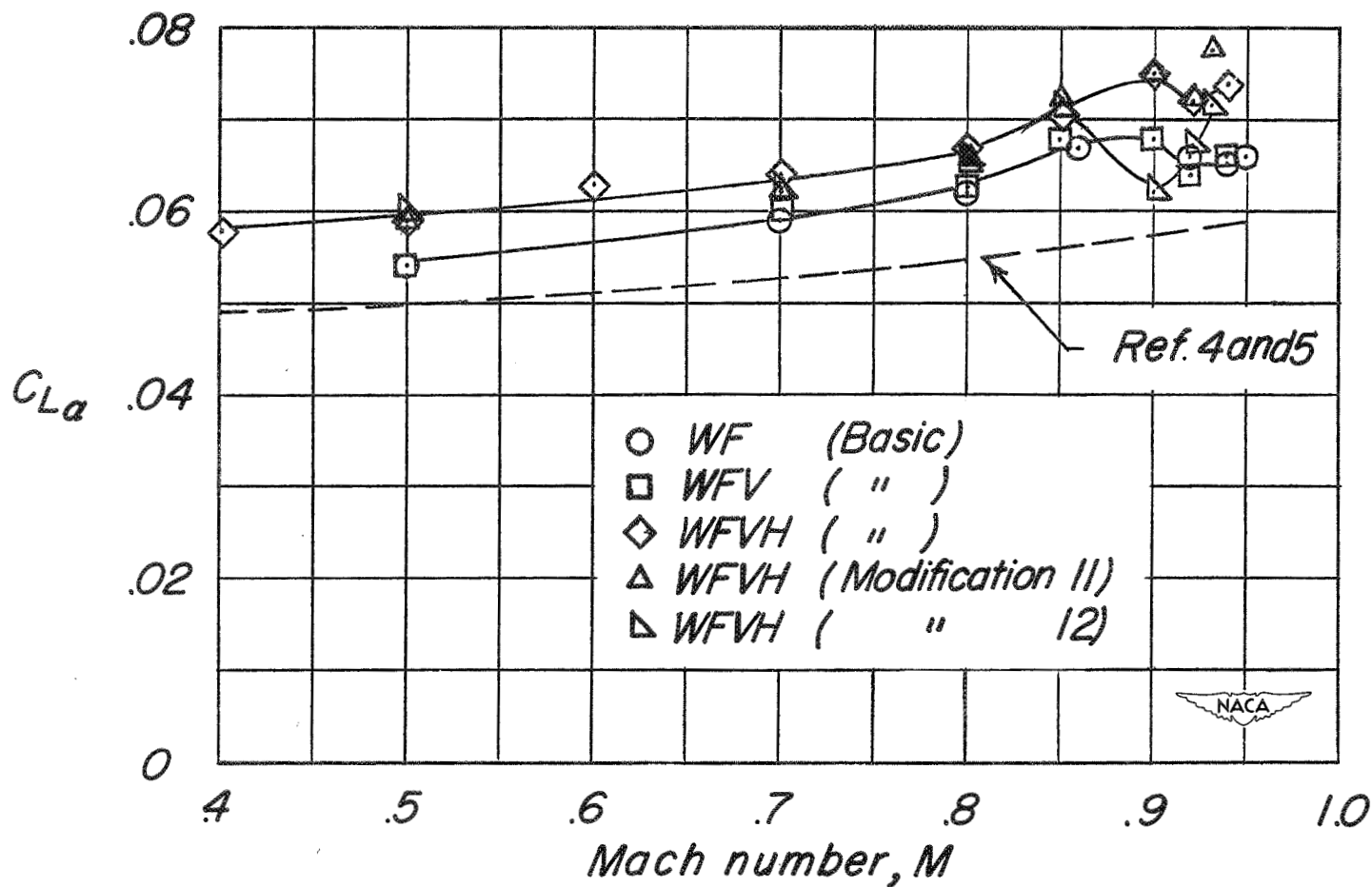


Figure 17.- Variation of the lift-curve slope for several configurations with Mach number and a comparison with wing alone theory.  $\alpha = 0^\circ$ .



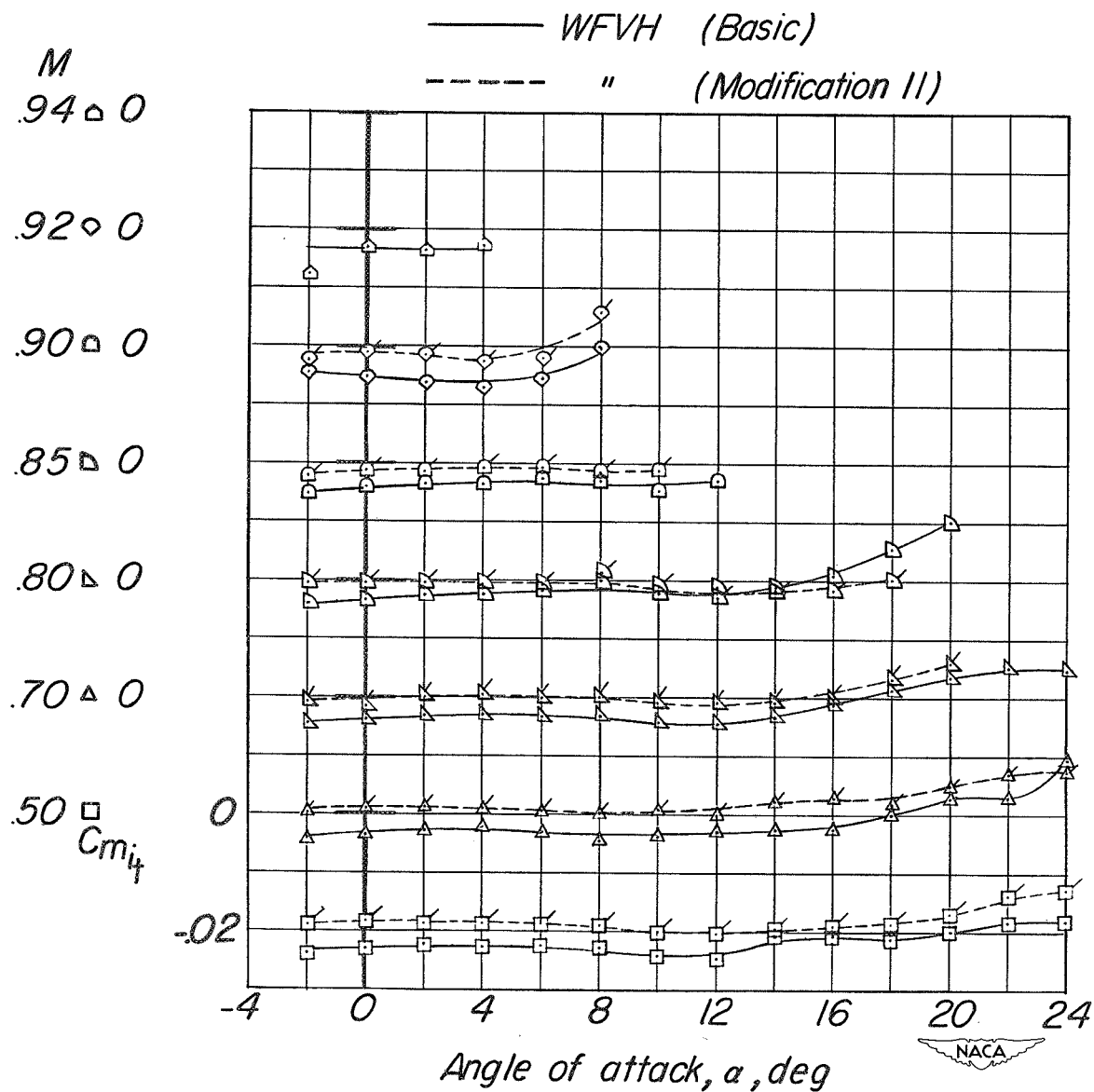


Figure 18.- Variation of stabilizer effectiveness with angle of attack for the basic and modification II configurations.  $\beta = 0^\circ$ .

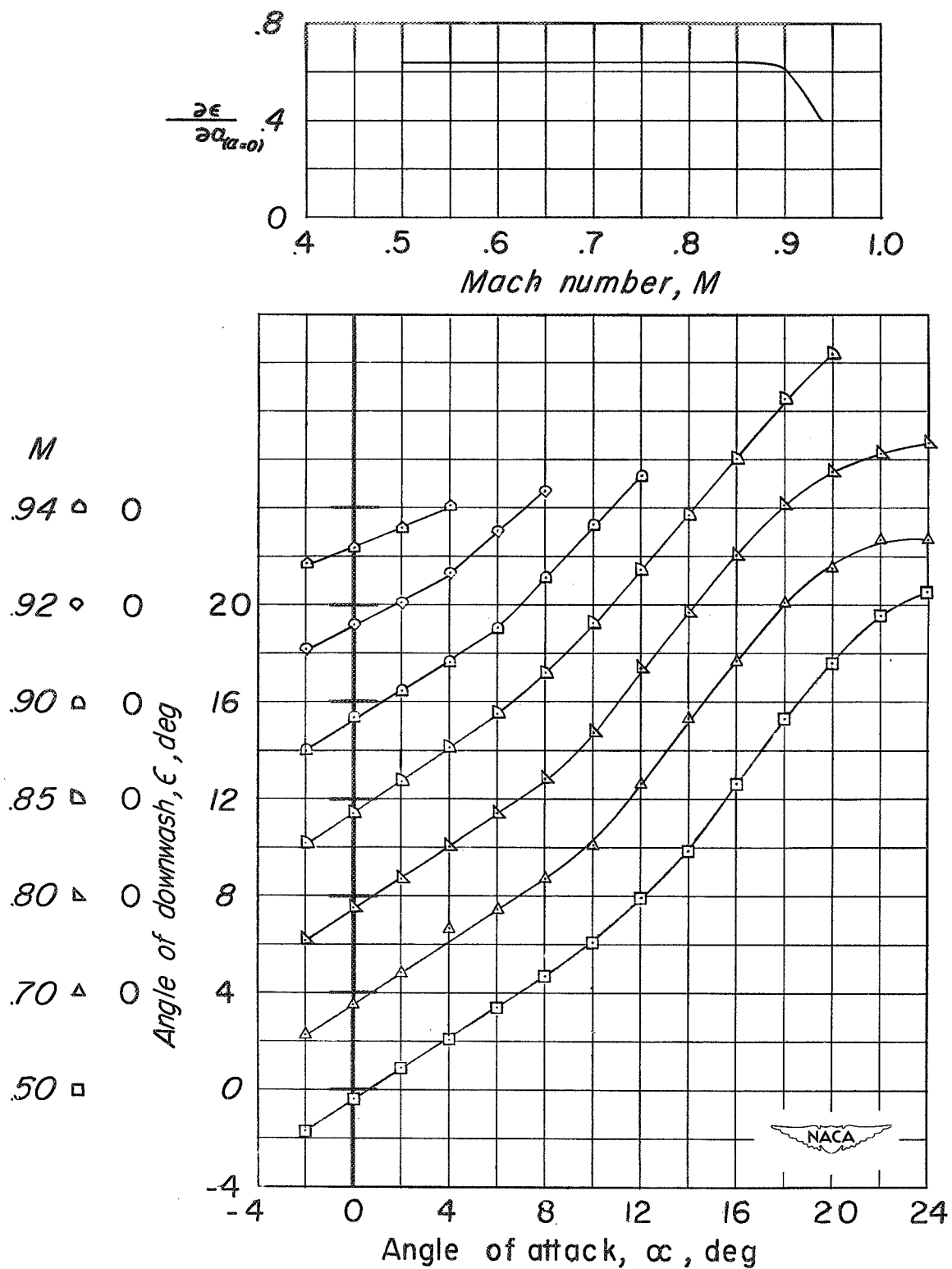


Figure 19.- Variation of downwash angle  $\epsilon$  at the horizontal-tail position of the basic model.

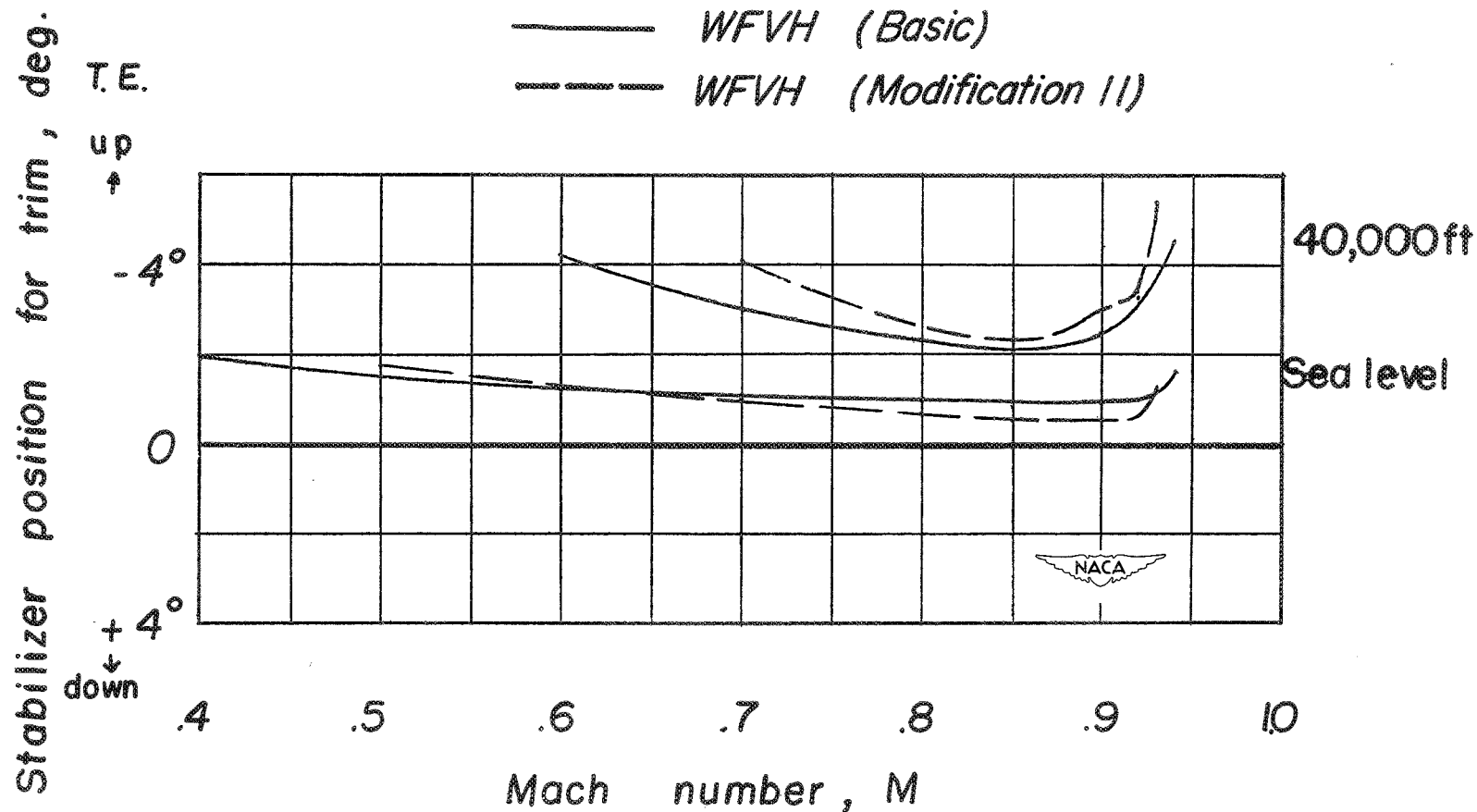


Figure 20.- Variation of stabilizer position required for trim flight through the Mach number range for the basic and modification 11 configurations at sea level and at an altitude of 40,000 feet.  $W/S = 60$  pounds per square foot.

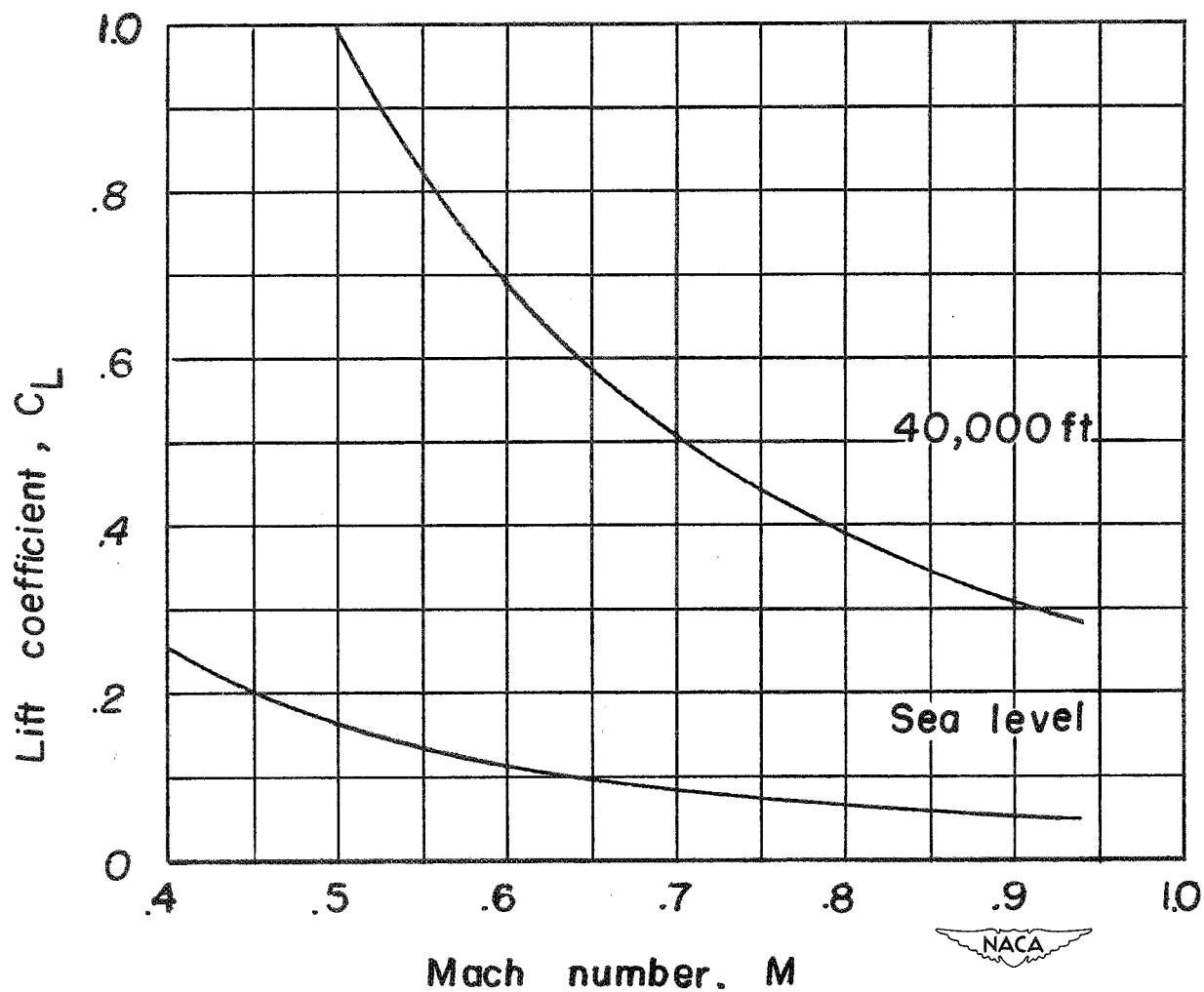


Figure 21.- Lift coefficient required for level flight through the Mach number range for  $W/S = 60$  pounds per square foot at sea level and at an altitude of 40,000 feet.

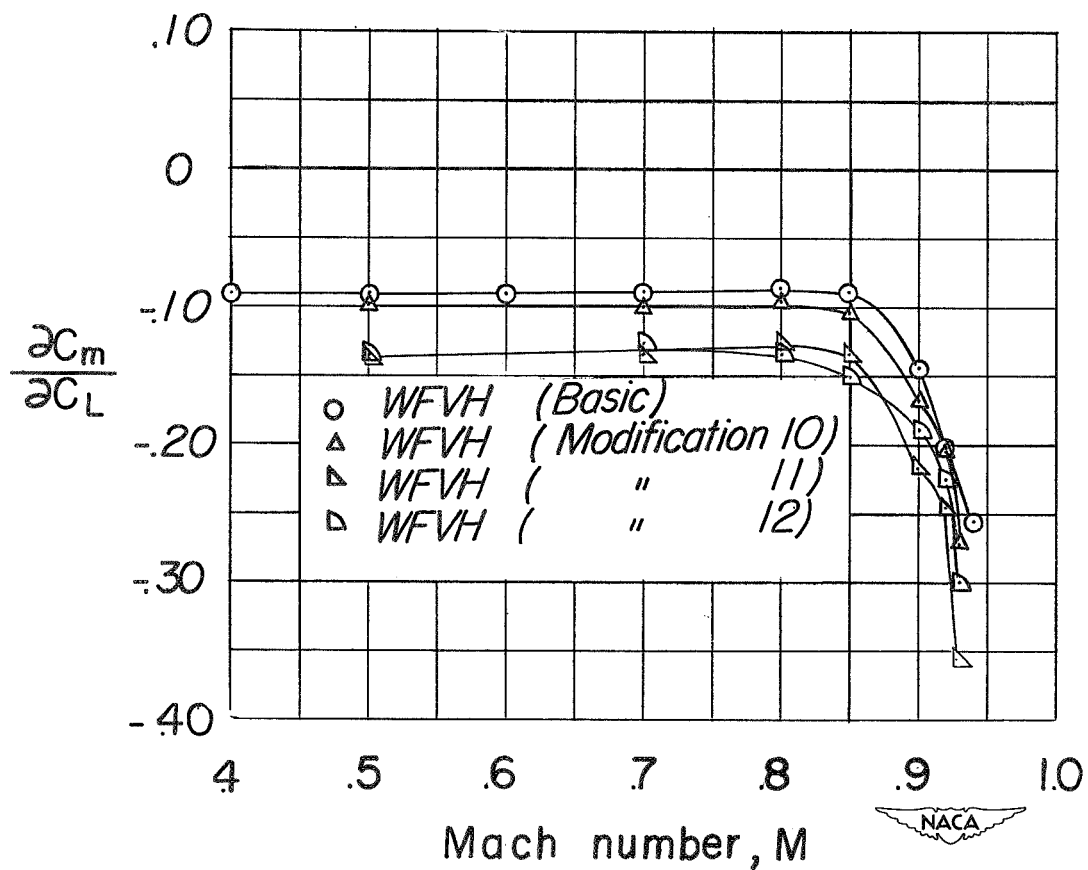
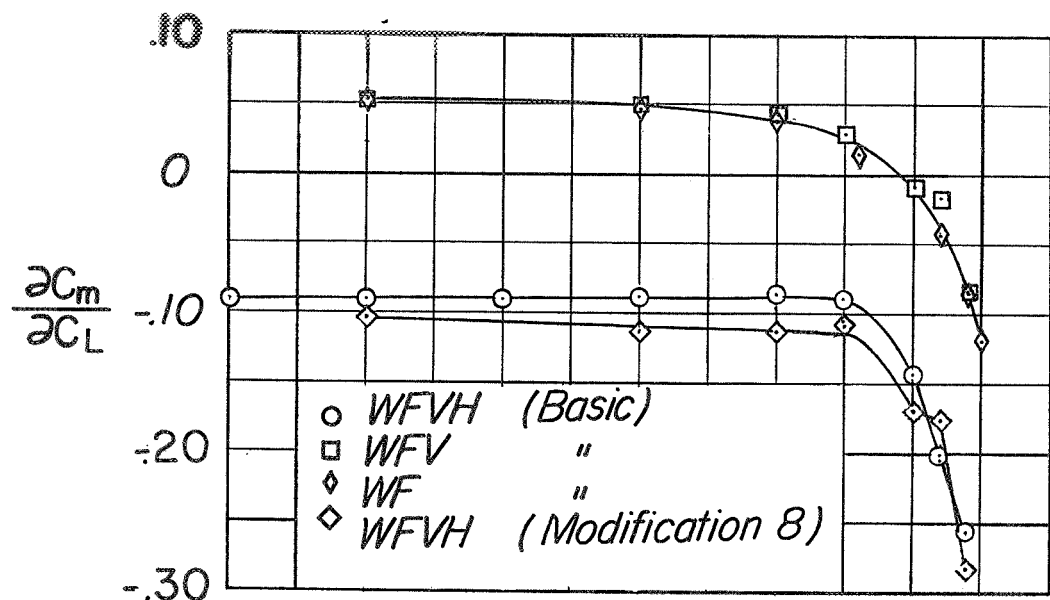


Figure 22.- Variation of  $\frac{\partial C_m}{\partial C_L}$  with Mach number for several configurations of the model.  $\alpha = 0^\circ$ .

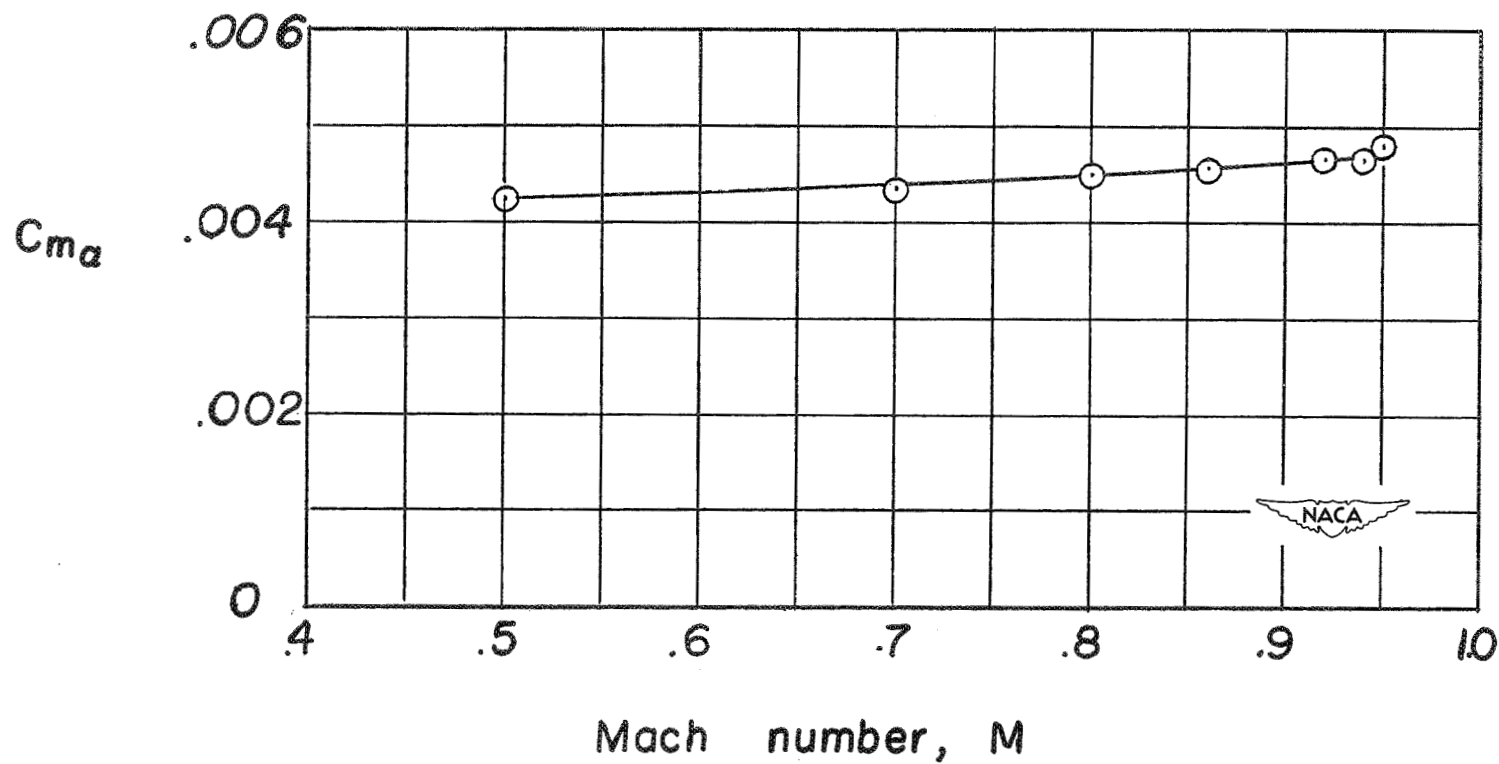


Figure 23.- Slope of the pitching-moment curve with angle of attack for the fuselage alone.  $\alpha = 0^\circ$ .

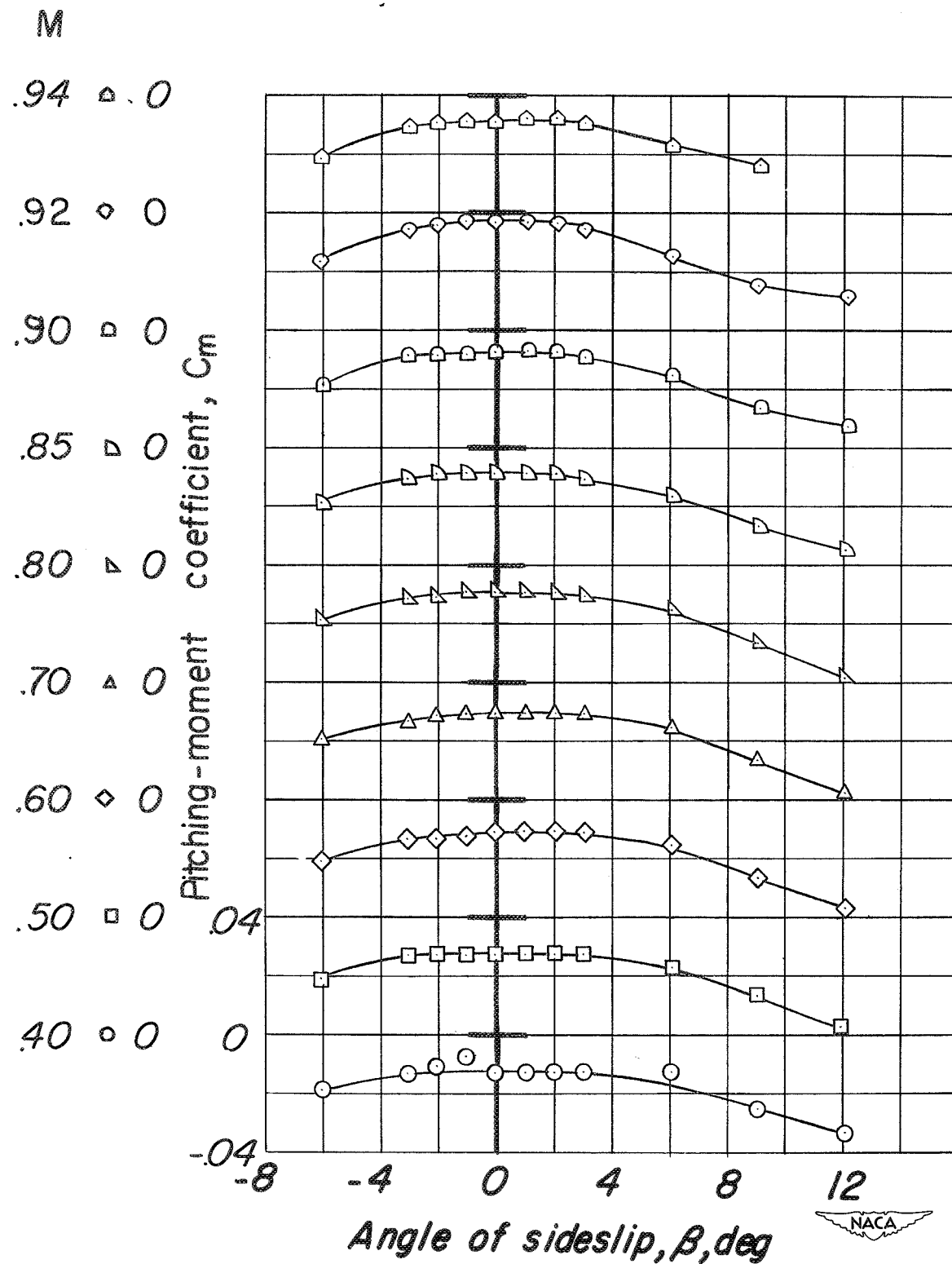


Figure 24.- Variation of pitching moment with sideslip for the basic model (WFBH).  $\alpha = 0^\circ$ .

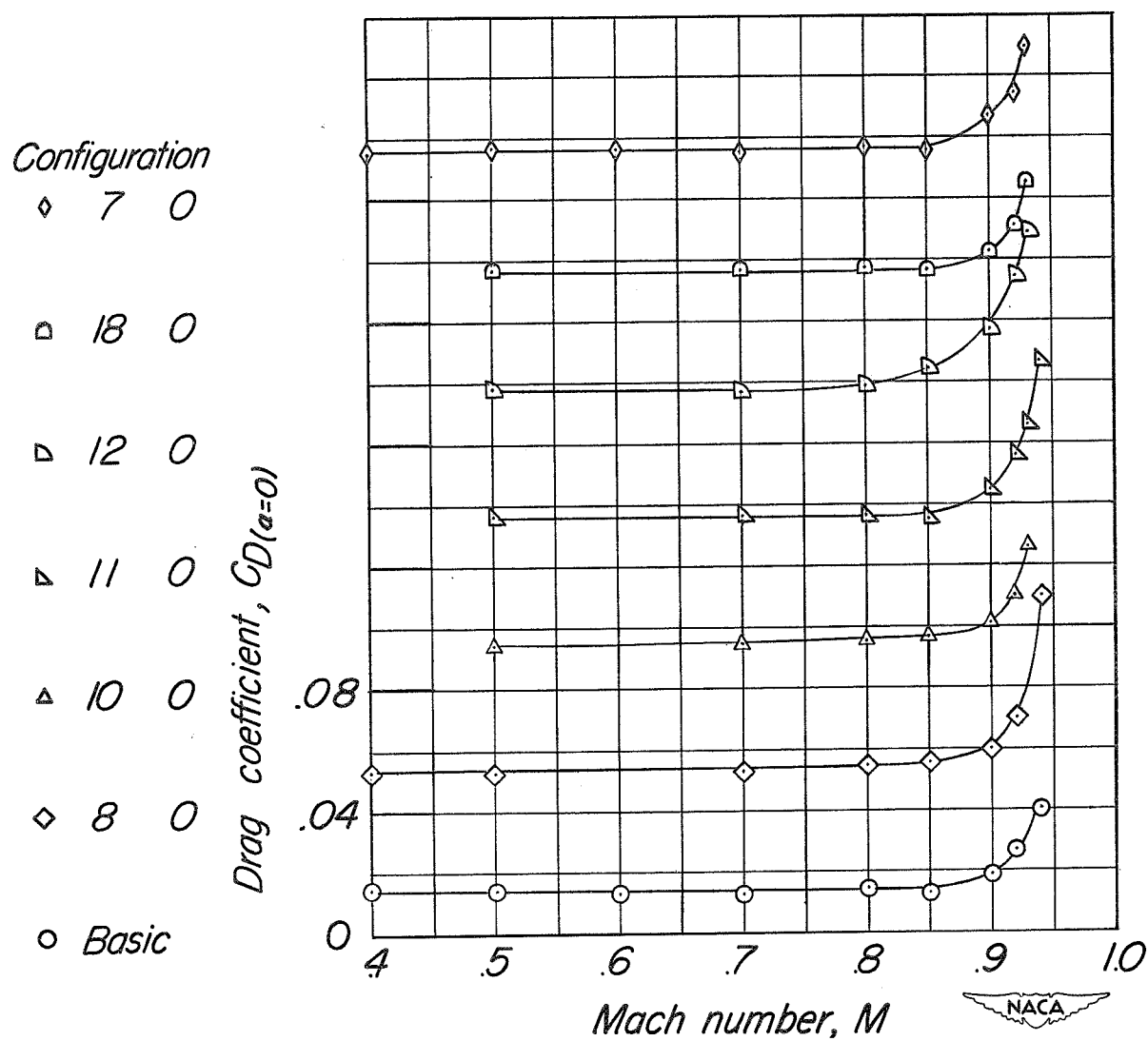


Figure 25.- Drag for several configurations of the complete model.  $\alpha = 0^\circ$ .



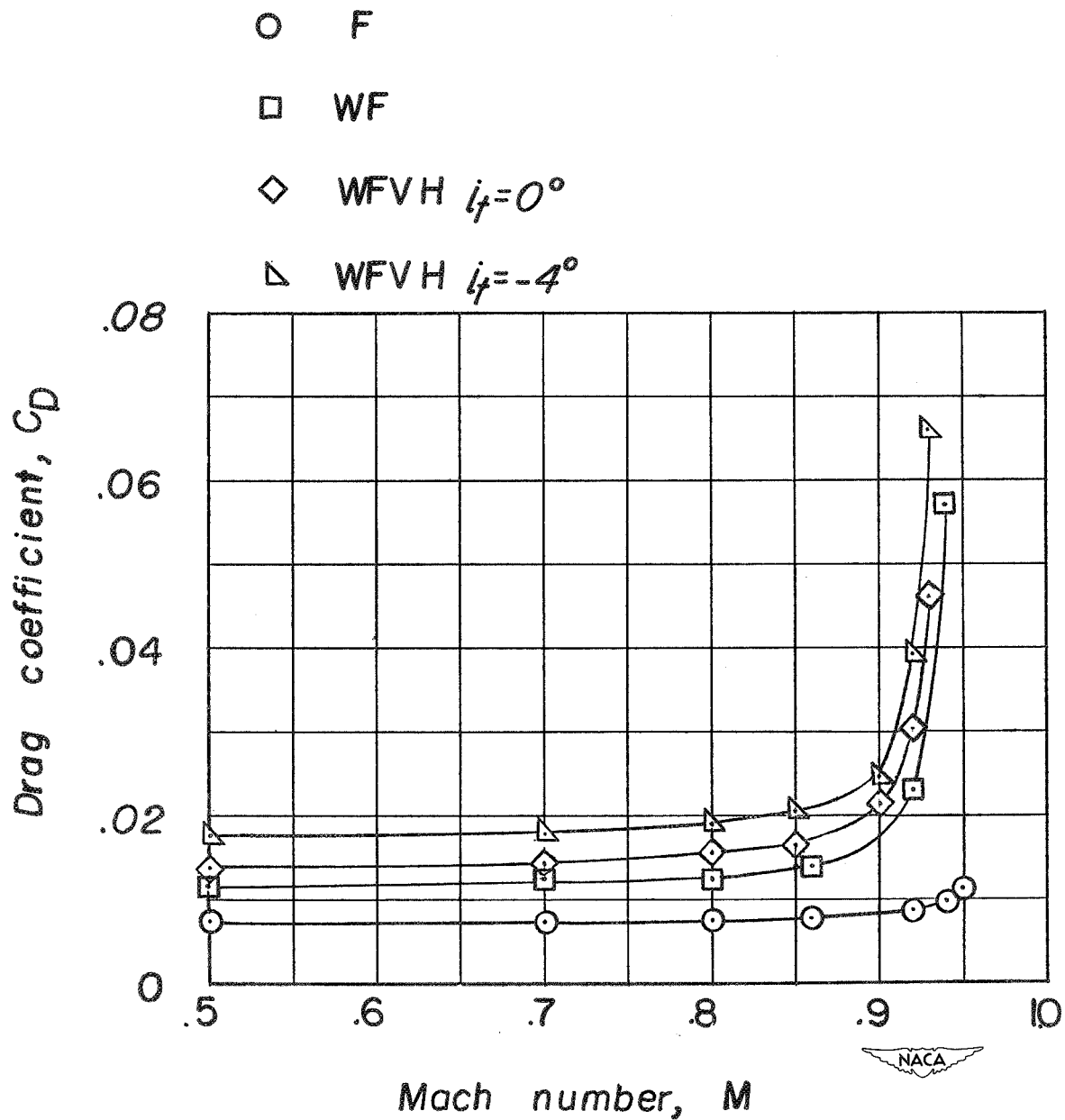


Figure 26.- Minimum drag for various components of modification 10 configurations.  $\alpha = 0^\circ$ .

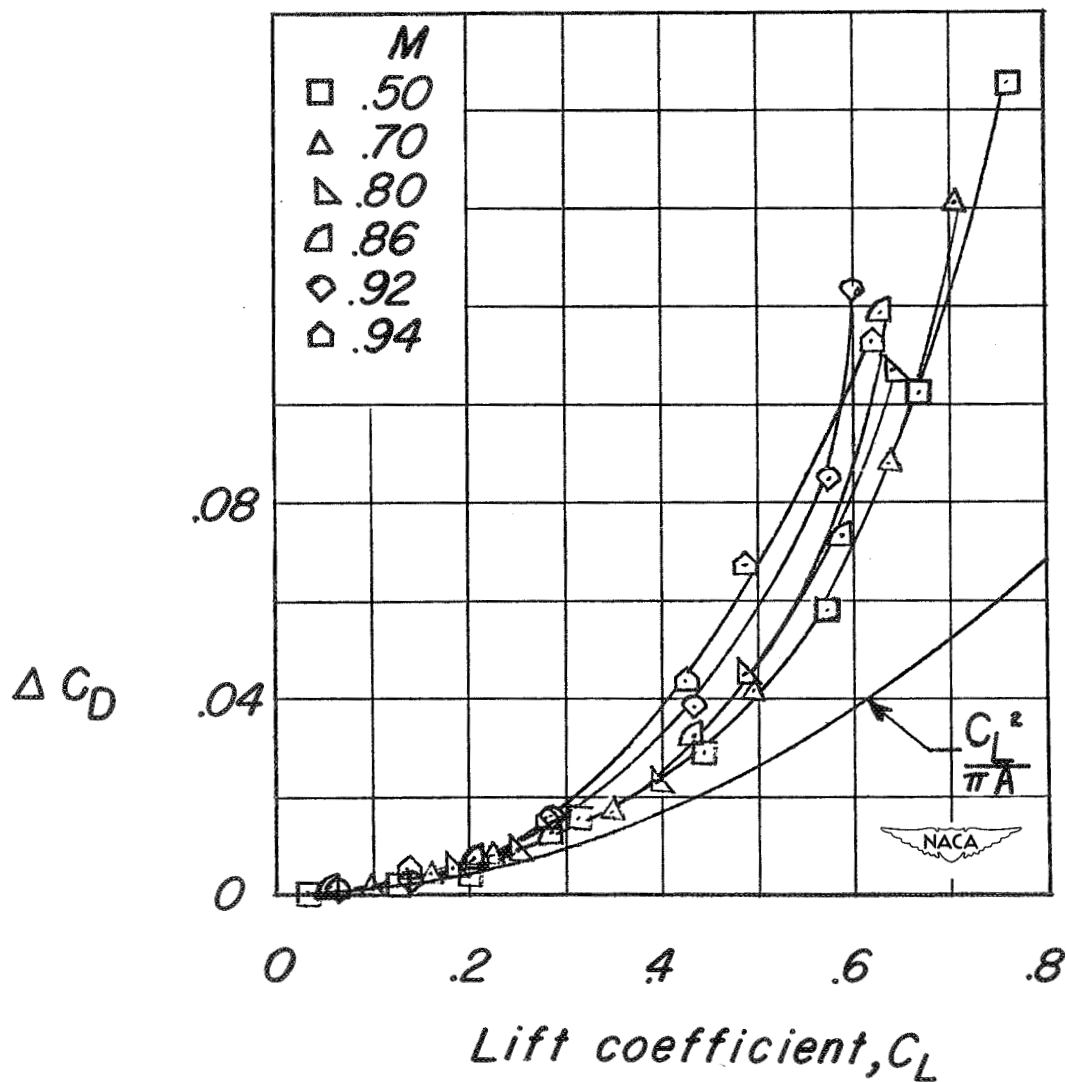


Figure 27.-- Drag due to lift for the Mach number range tested for the wing-fuselage configuration.

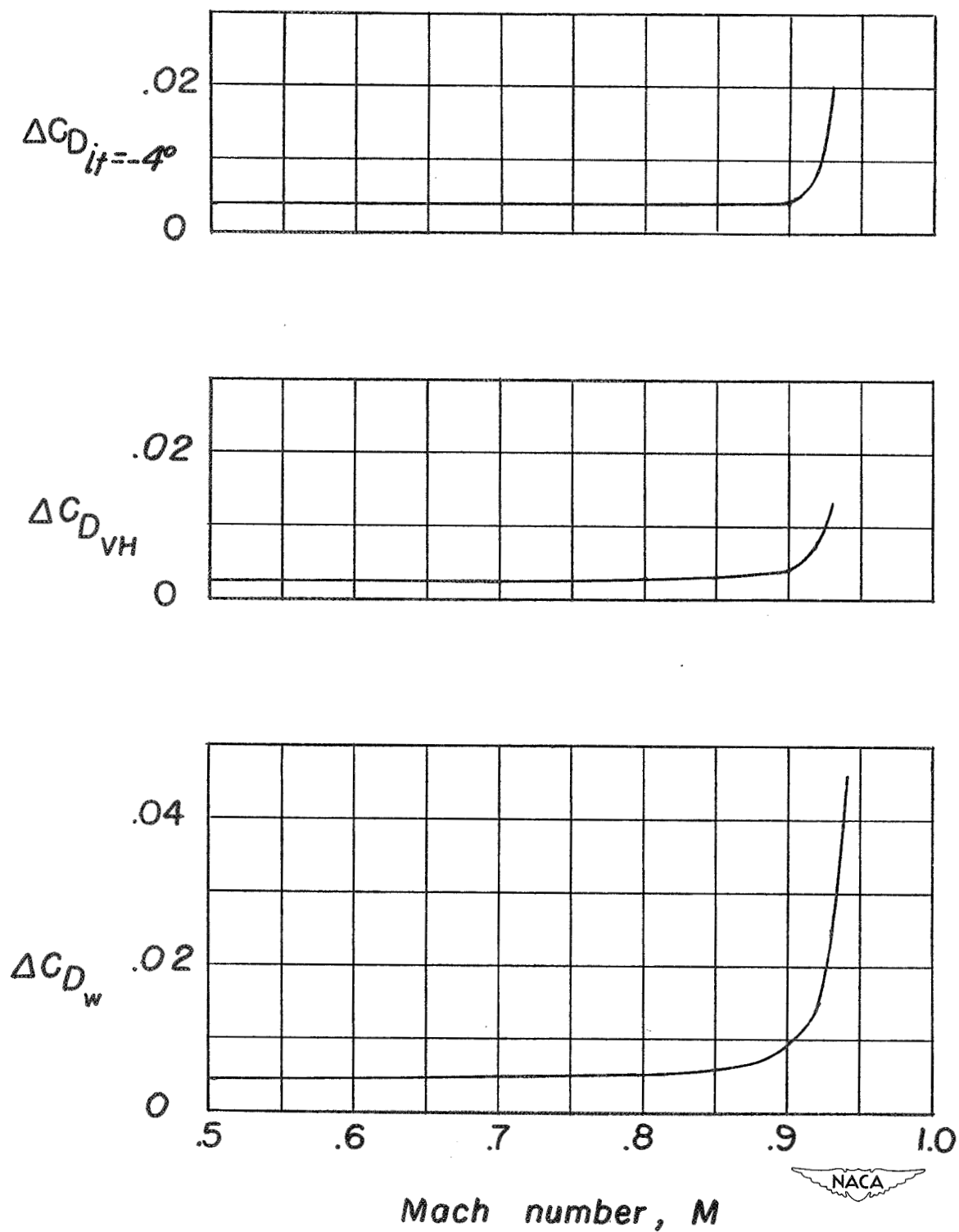


Figure 28.-- Drag increments on the basic model due to stabilizer deflection, vertical and horizontal tails, and wing.  $\alpha = 0^\circ$ .

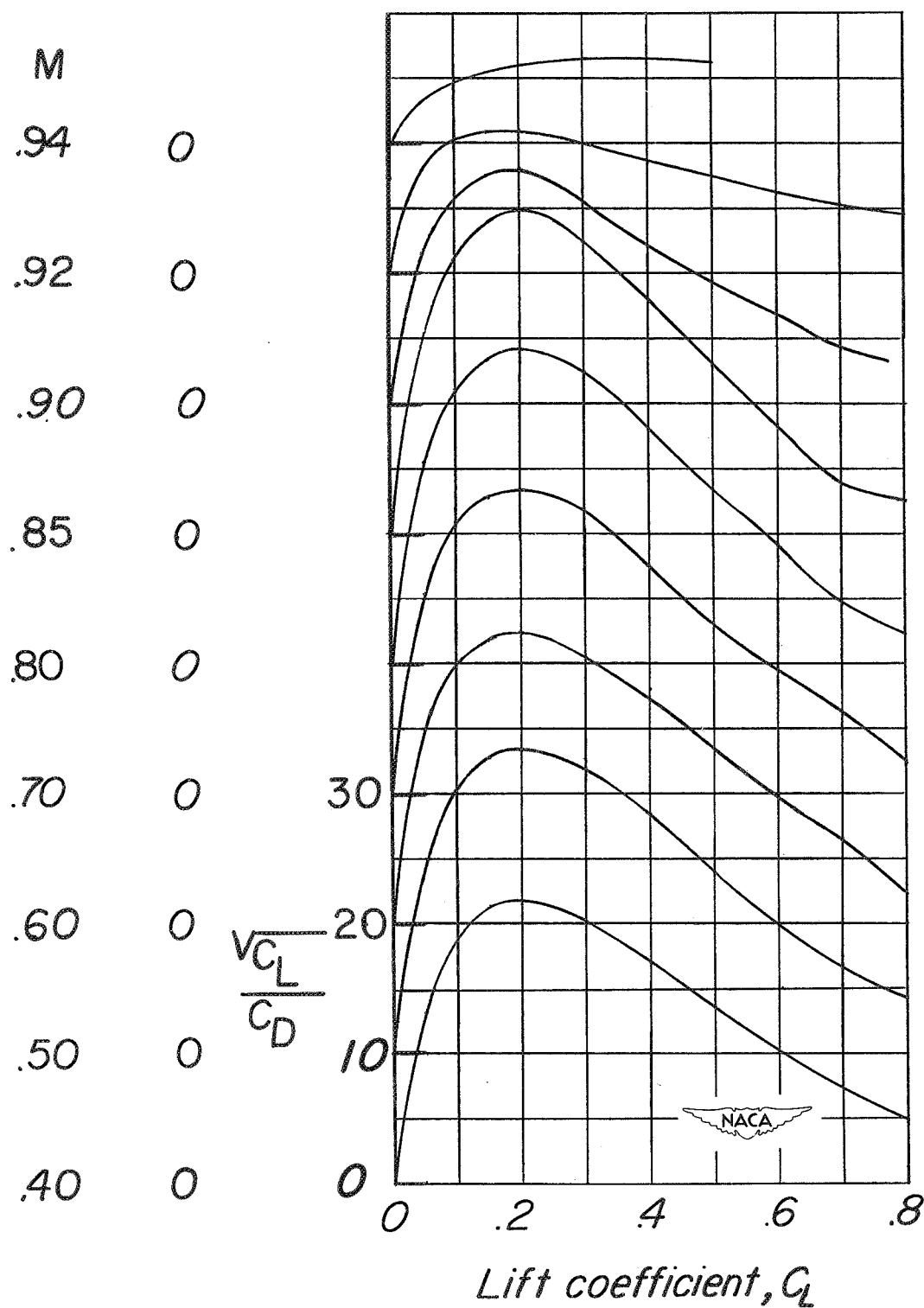


Figure 29.- Variation of the  $\sqrt{C_L/C_D}$  portion of the jet-airplane range parameter through the lift and Mach number range.  $i_t = 0^\circ$ .

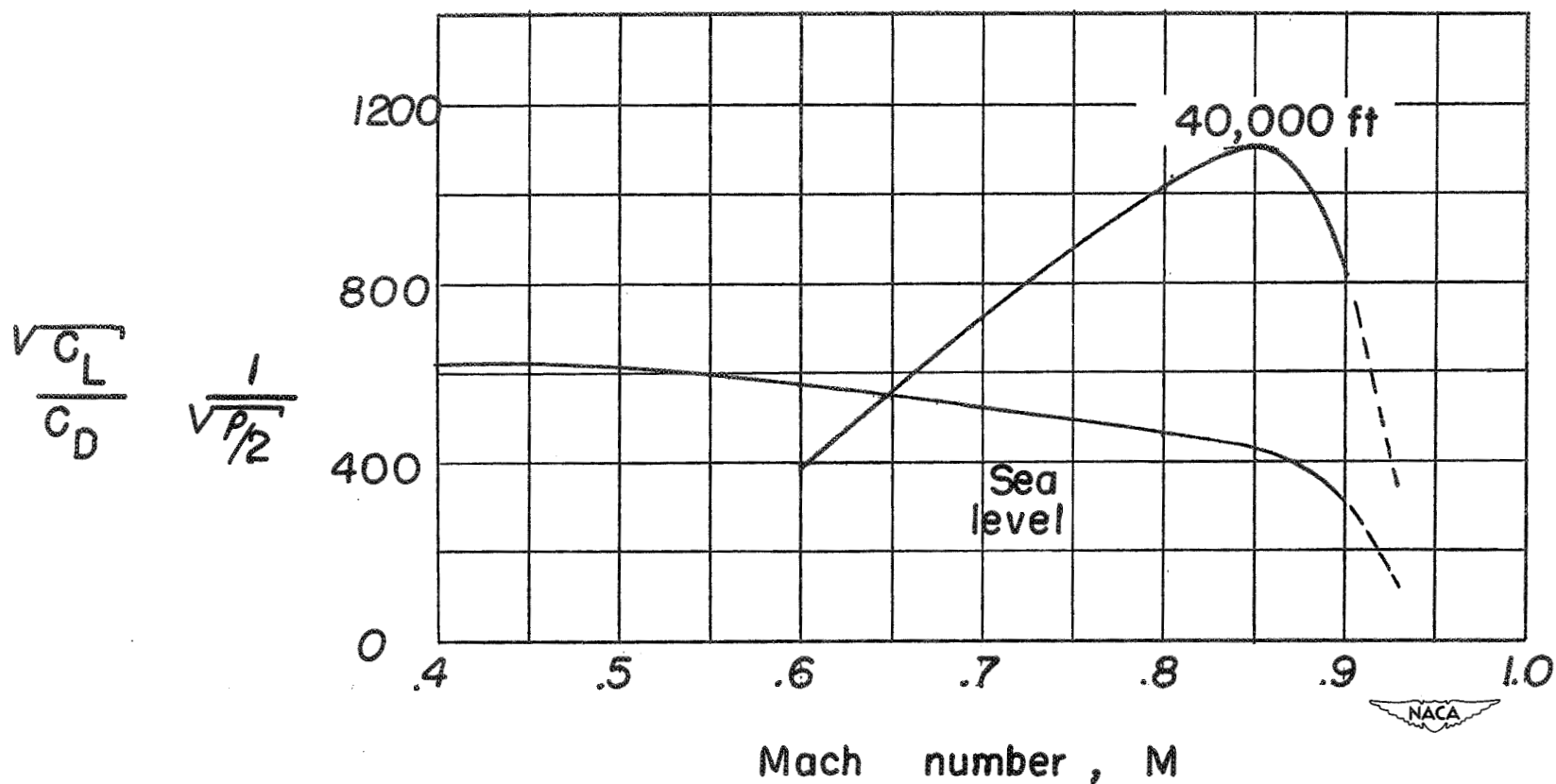
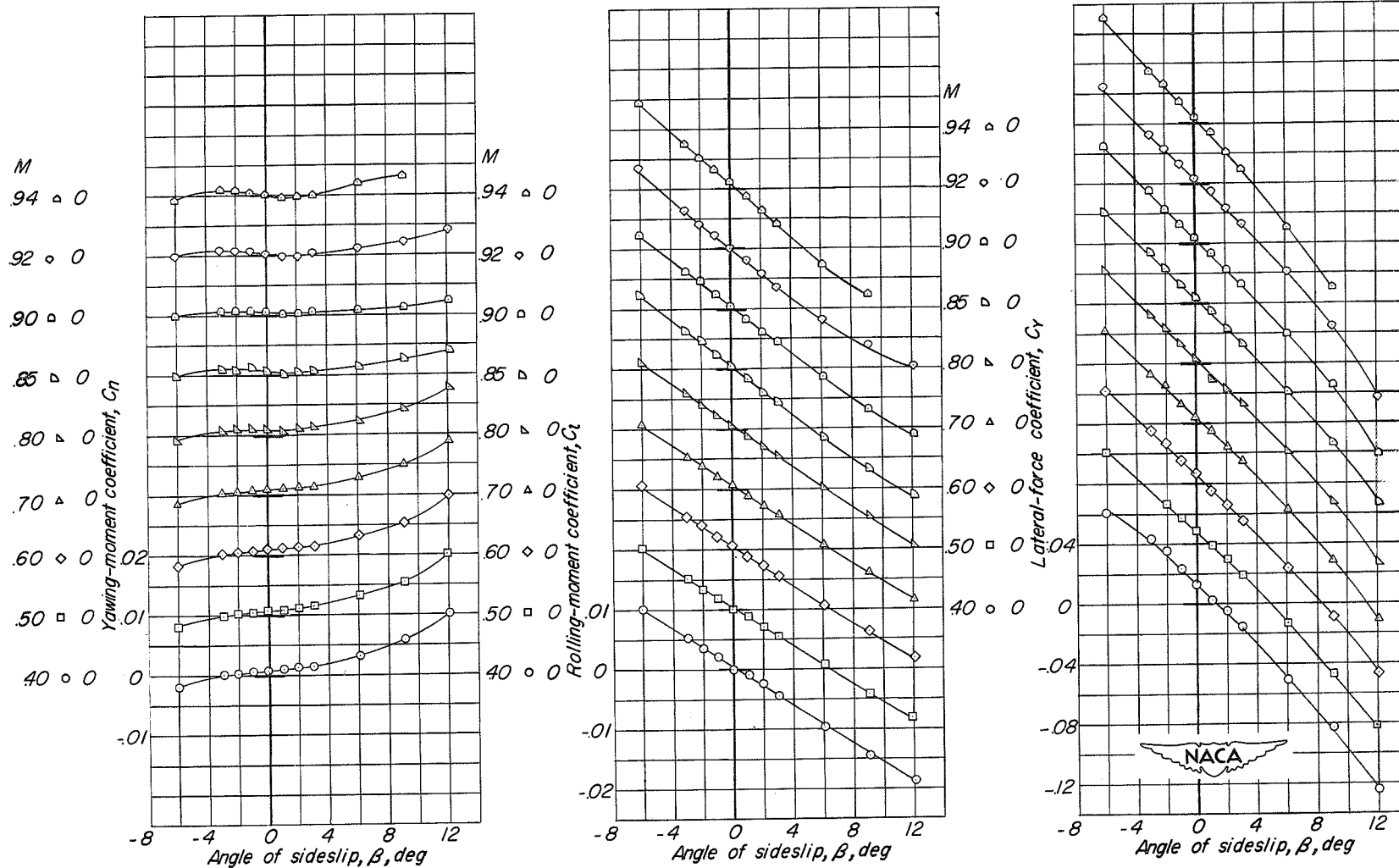
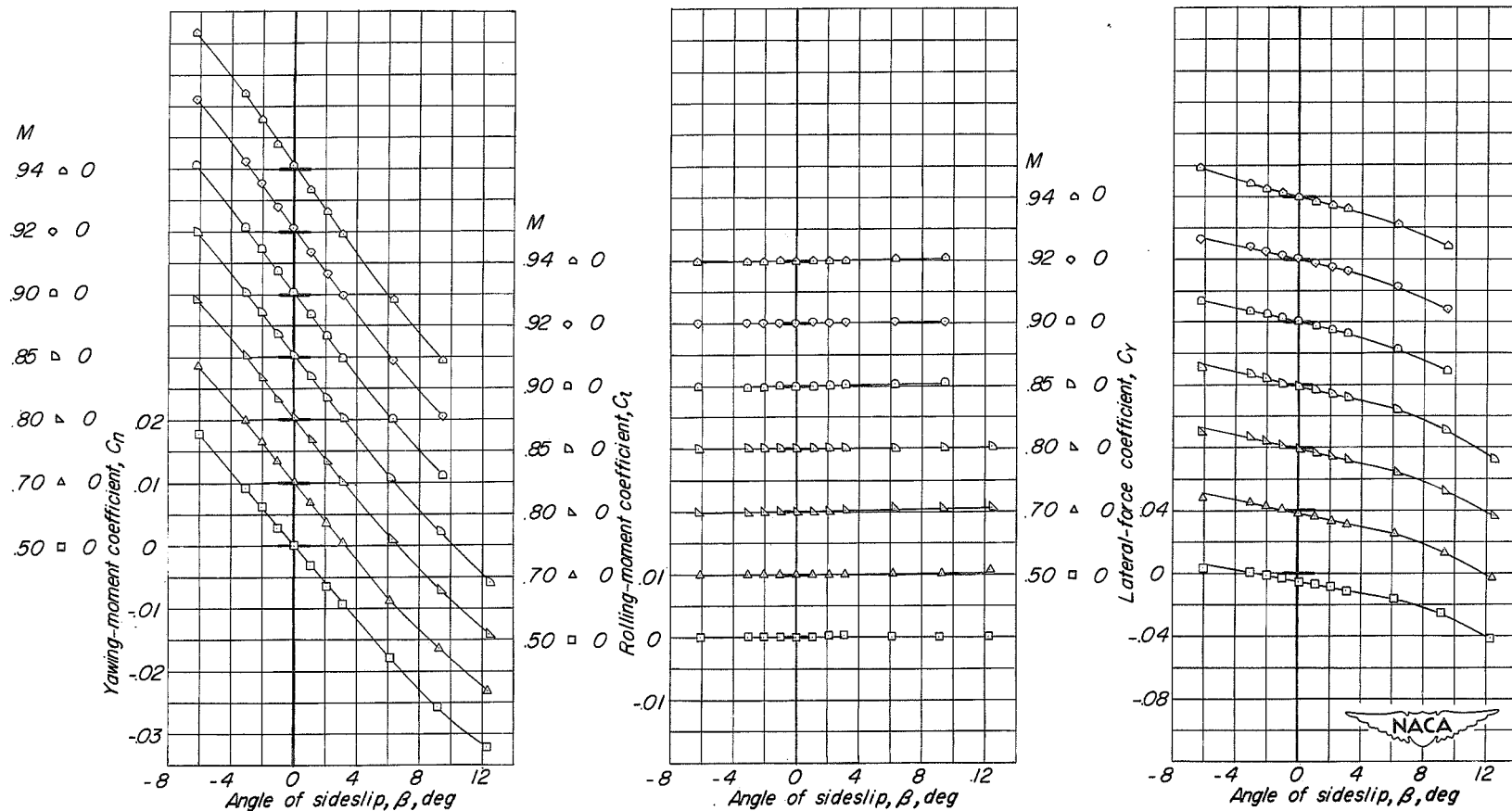


Figure 30.- Jet-airplane range parameter  $\sqrt{\frac{C_L}{C_D}} \frac{1}{\sqrt{\rho/2}}$  at sea level and at an altitude of 40,000 feet through the Mach number range, trimmed flight.  $W/S = 60$  pounds per square foot.



(a) Complete model.

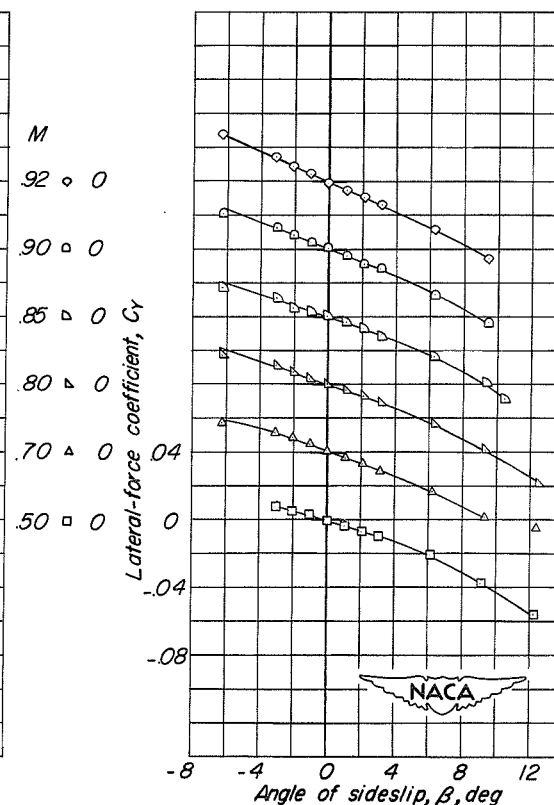
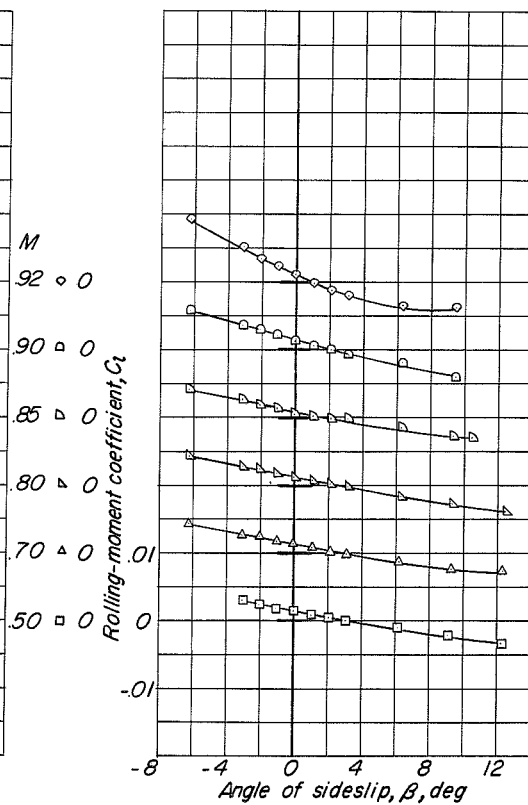
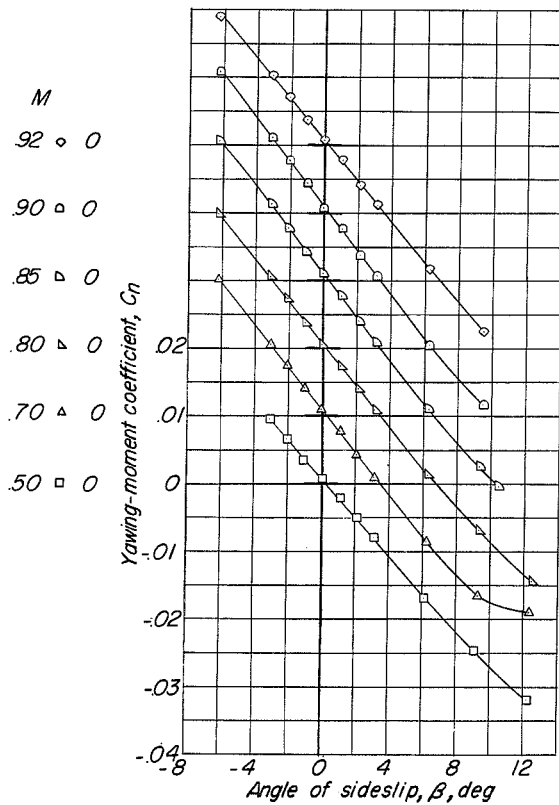
Figure 31.- Lateral characteristics of the basic model.  $\alpha = 0^\circ$ ;  $i_t = 0^\circ$ .



(b) Fuselage alone.

Figure 31.- Continued.

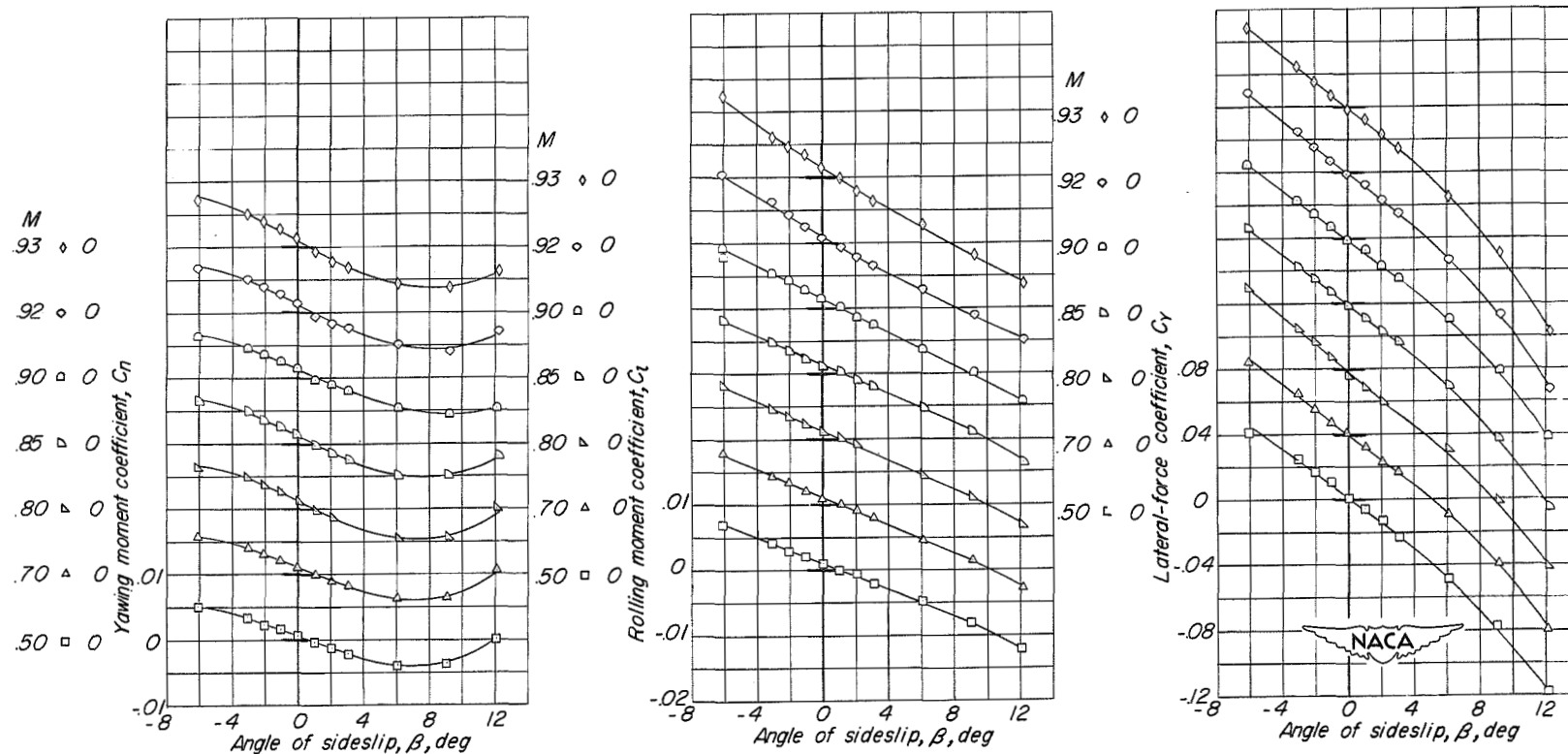
CONFIDENTIAL



(c) Wing and fuselage.

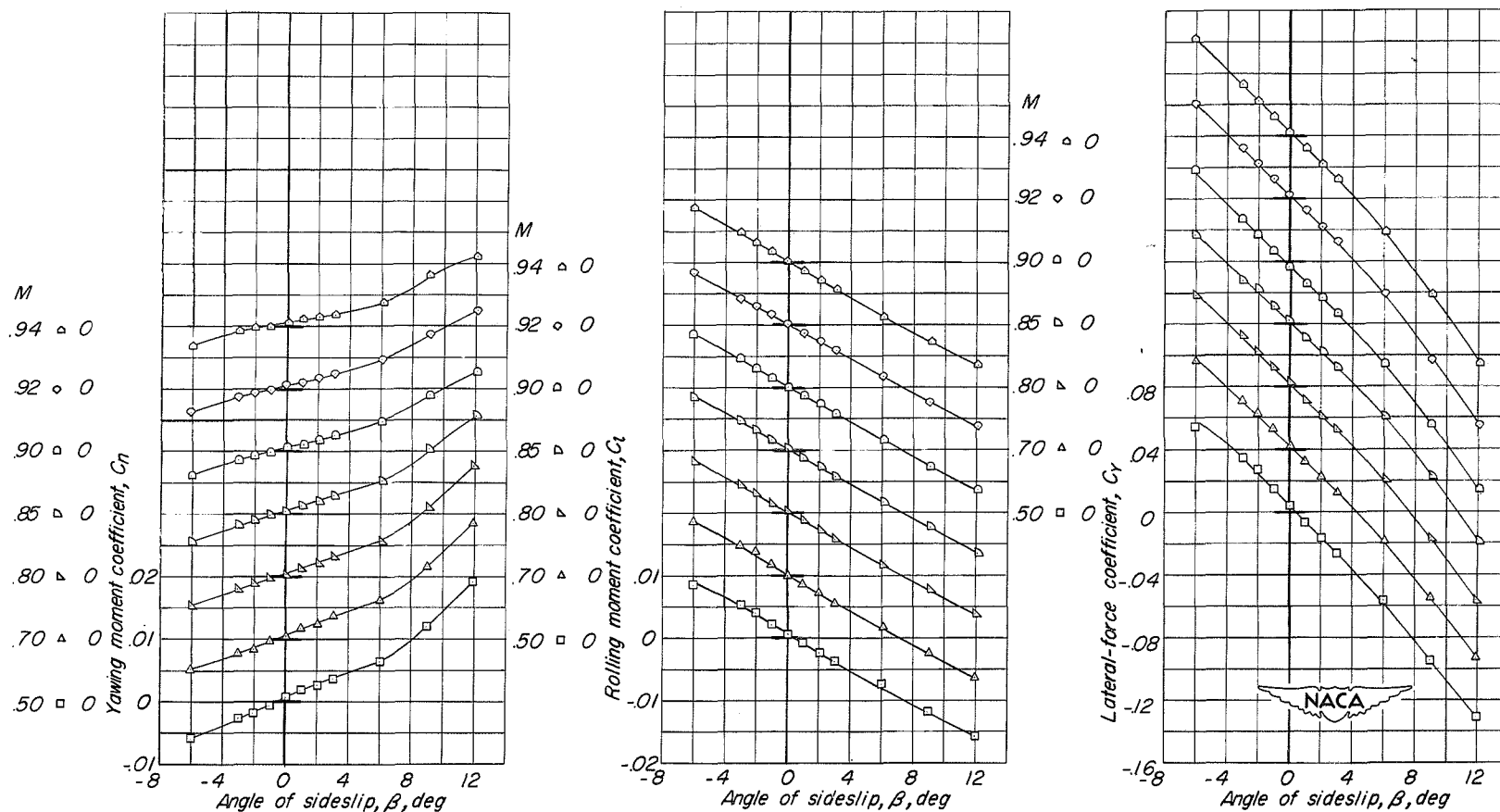
Figure 31.- Continued.





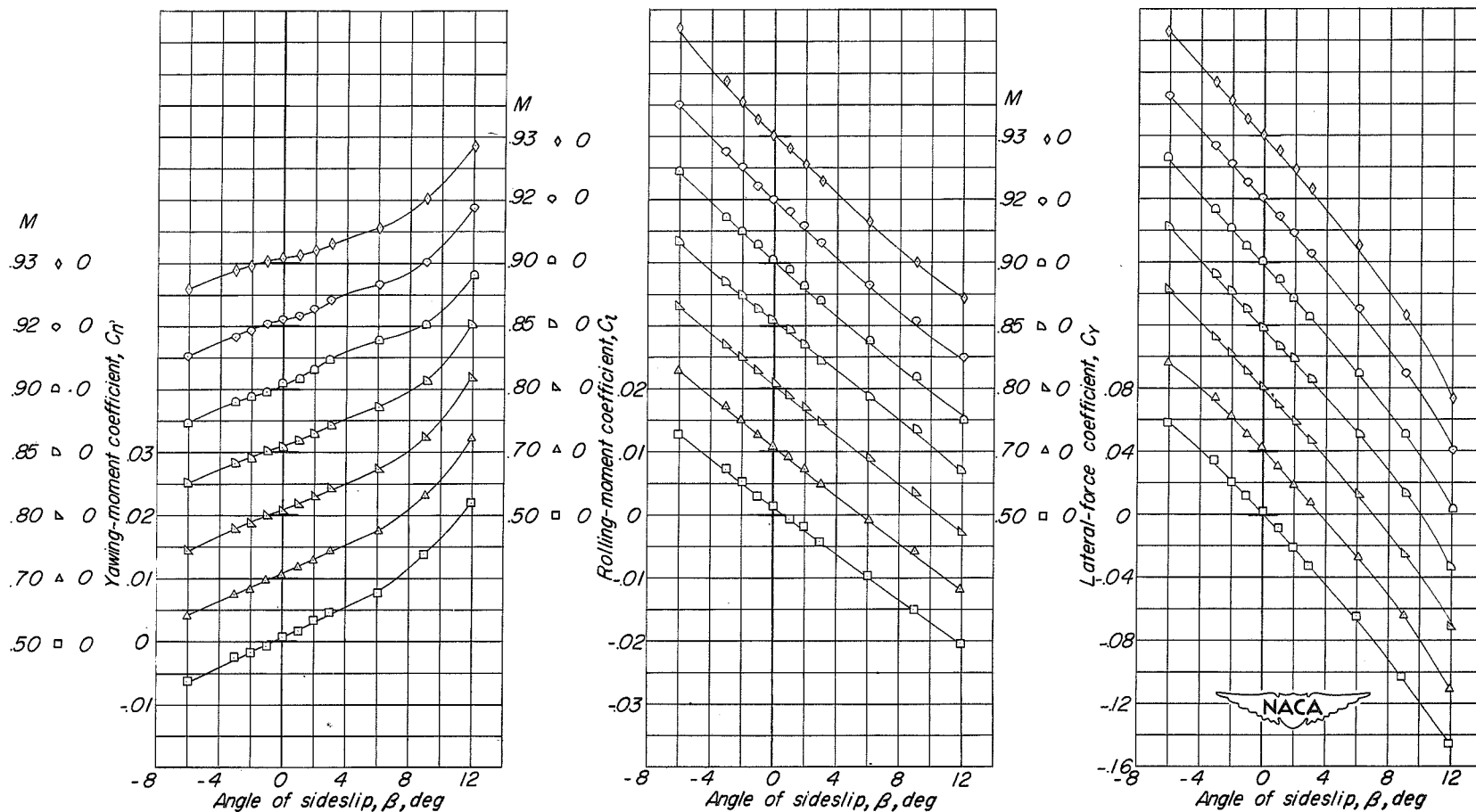
(d) Wing, fuselage, and vertical tail.

Figure 31.- Continued.



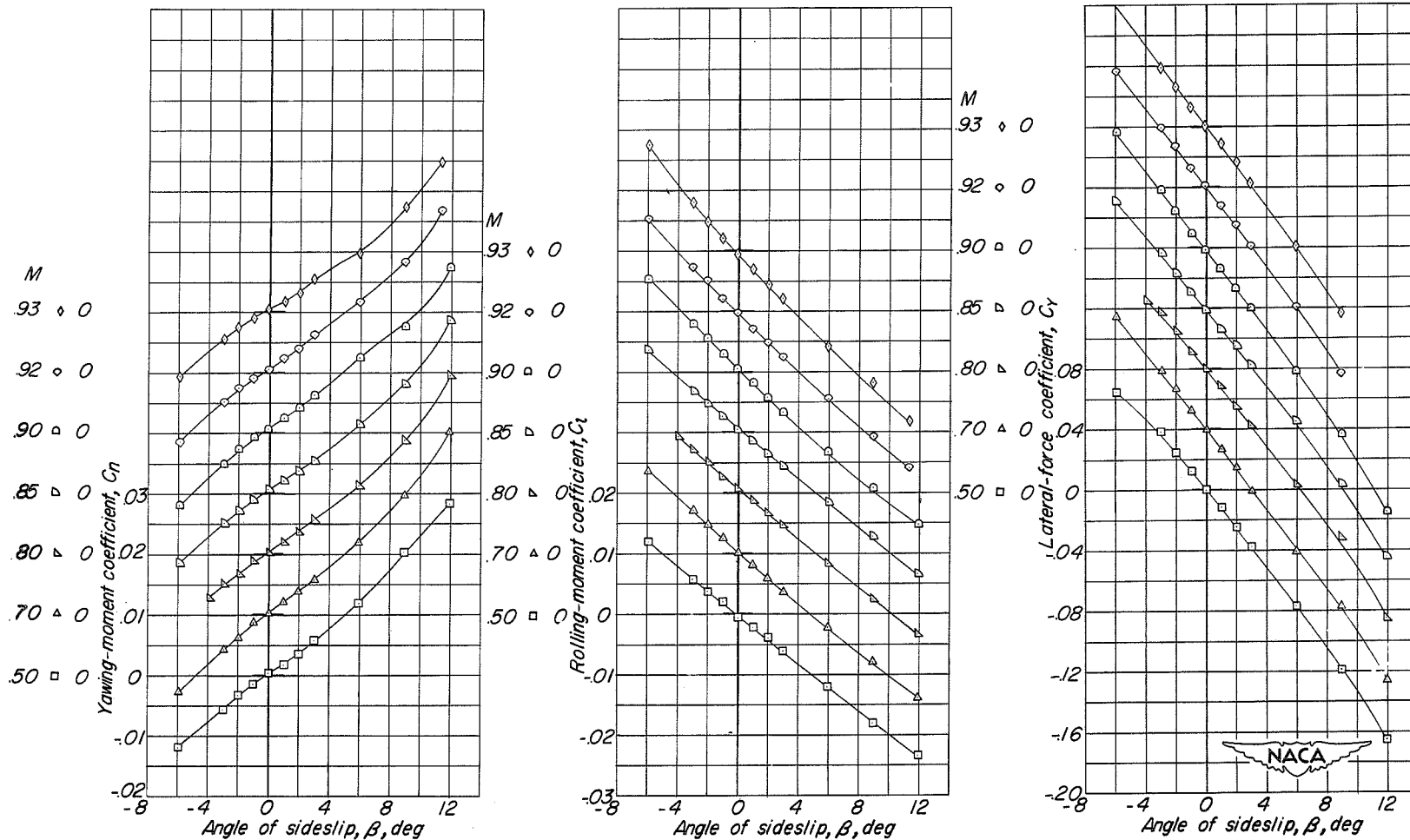
(e) Fuselage, vertical tail, and horizontal tail.

Figure 31.- Concluded.



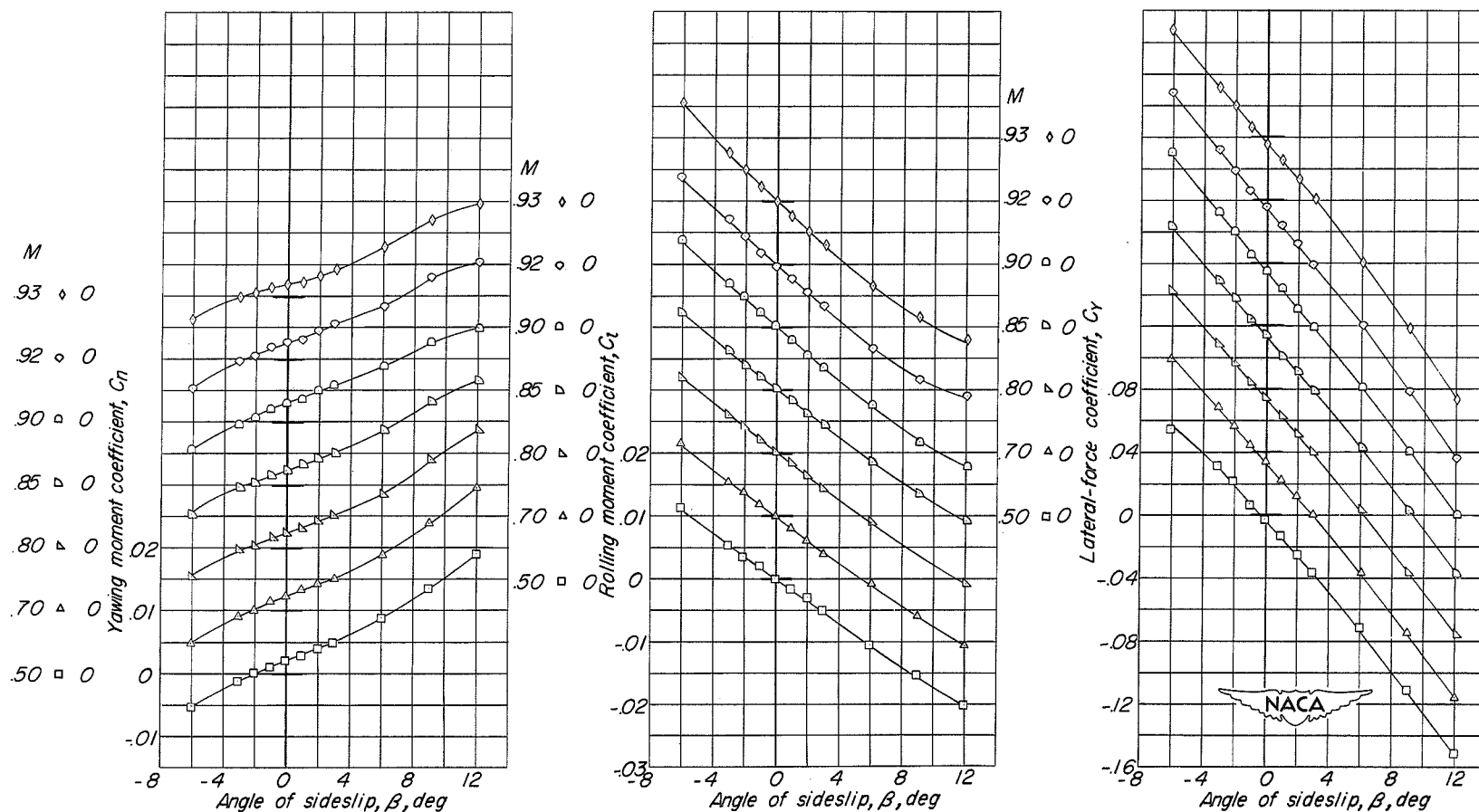
(a) Modification 1; vertical-tail extension.

Figure 32.- Lateral characteristics of modifications to the basic model (modifications 1 to 10).  $\alpha = 0^\circ$ ;  $i_t = 0^\circ$ .



(b) Modification 2; vertical-tail extension with straight-base fuselage extension.

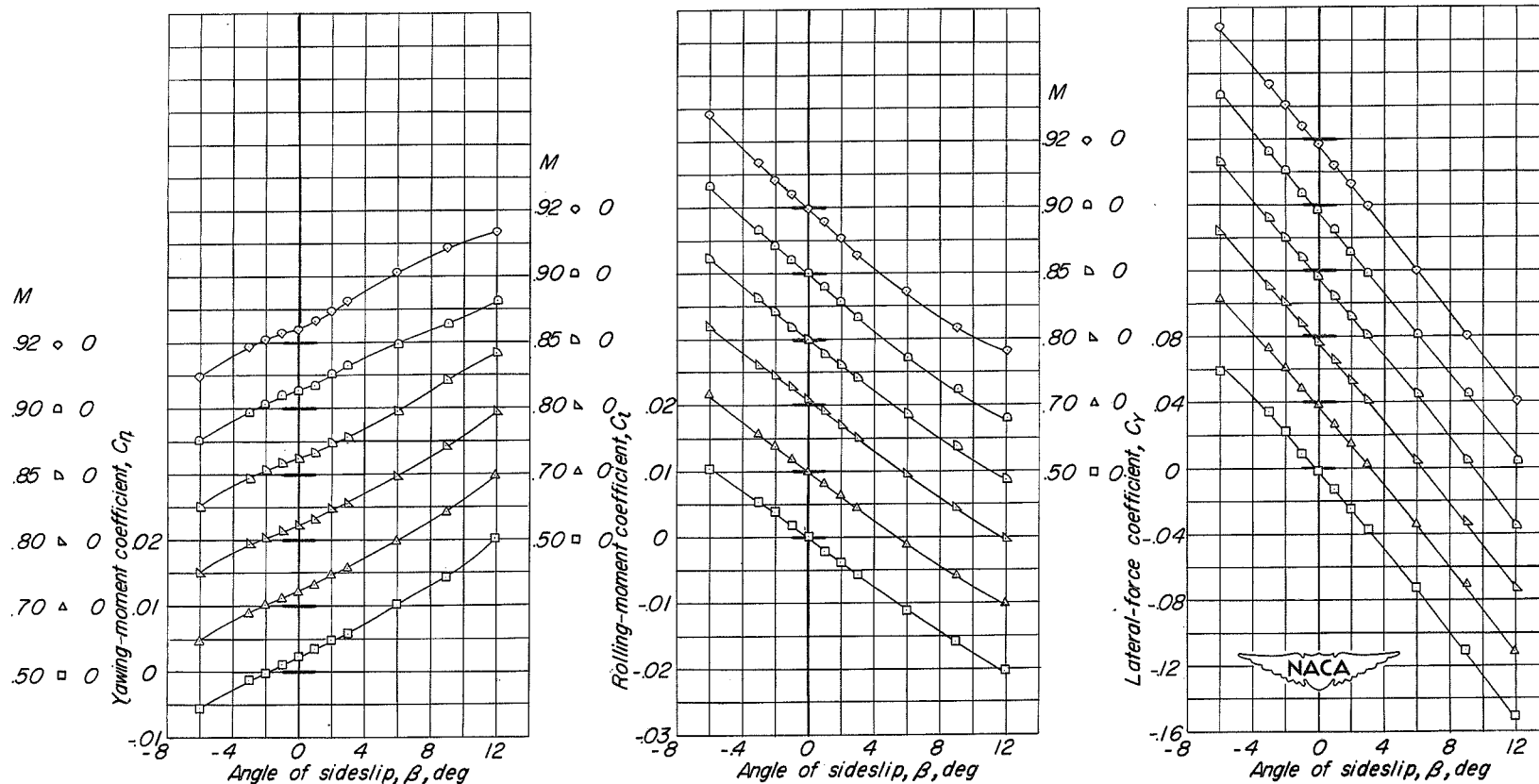
Figure 32.- Continued.



(c) Modification 3; straight-base fuselage extension.

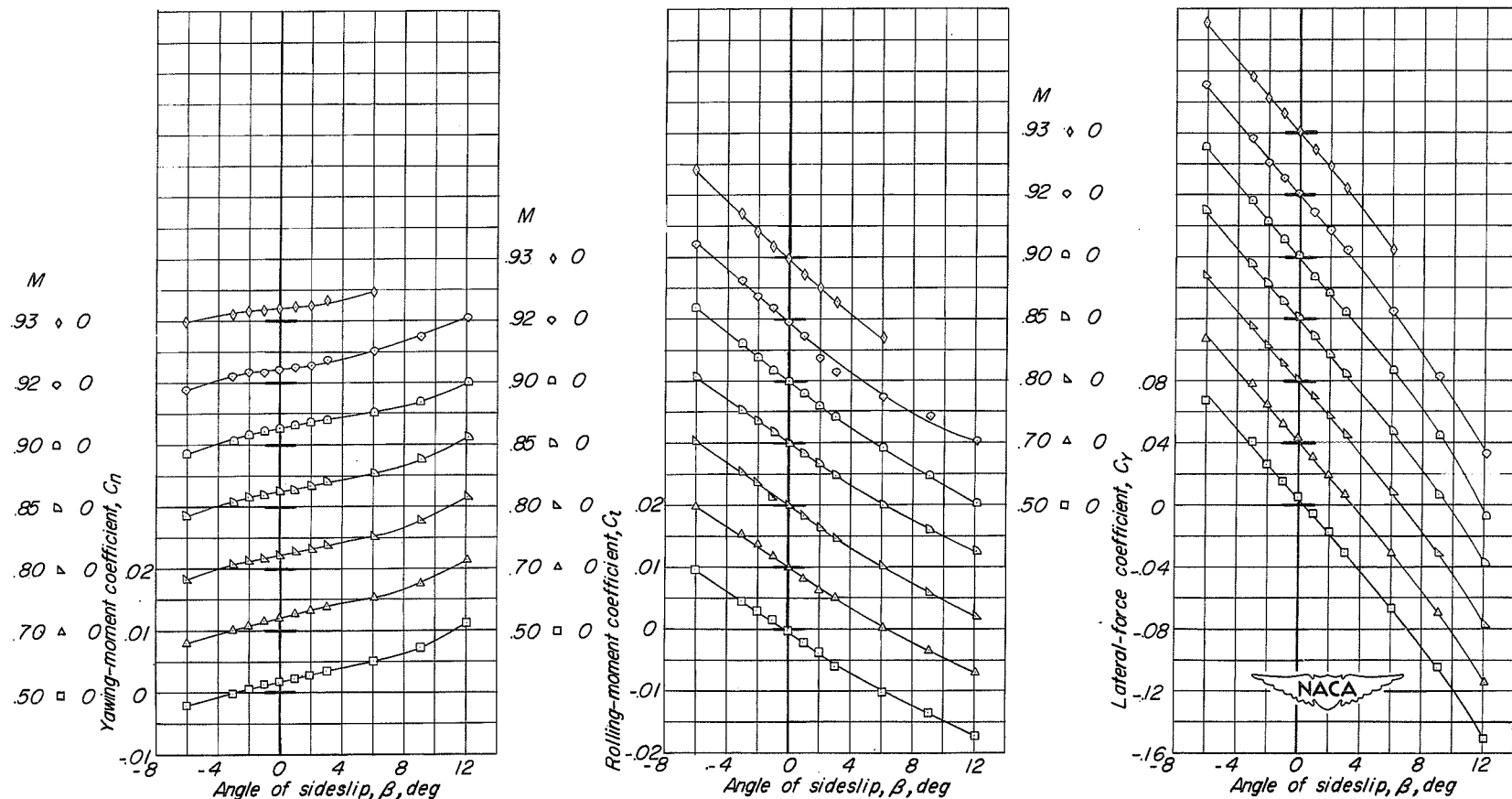
Figure 32.- Continued.

CONFIDENTIAL



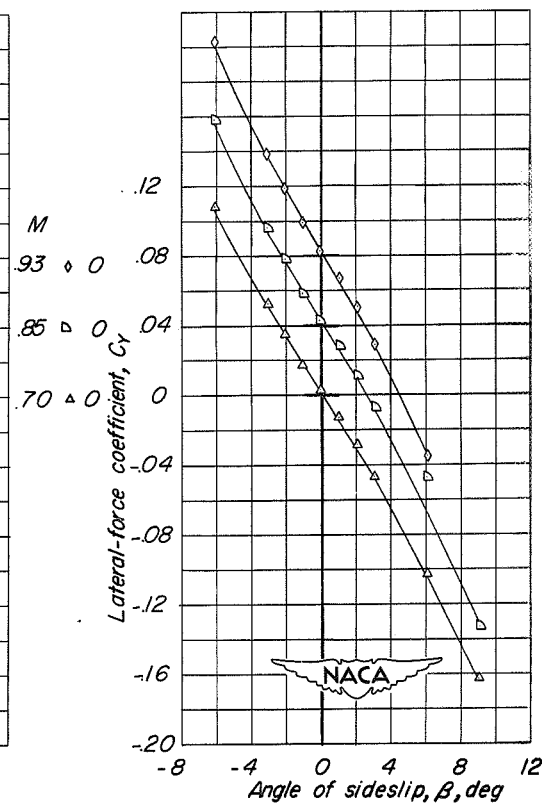
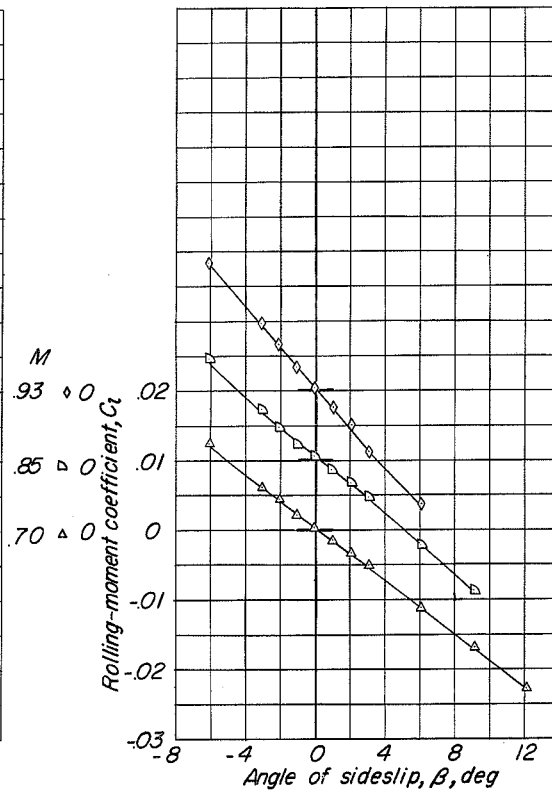
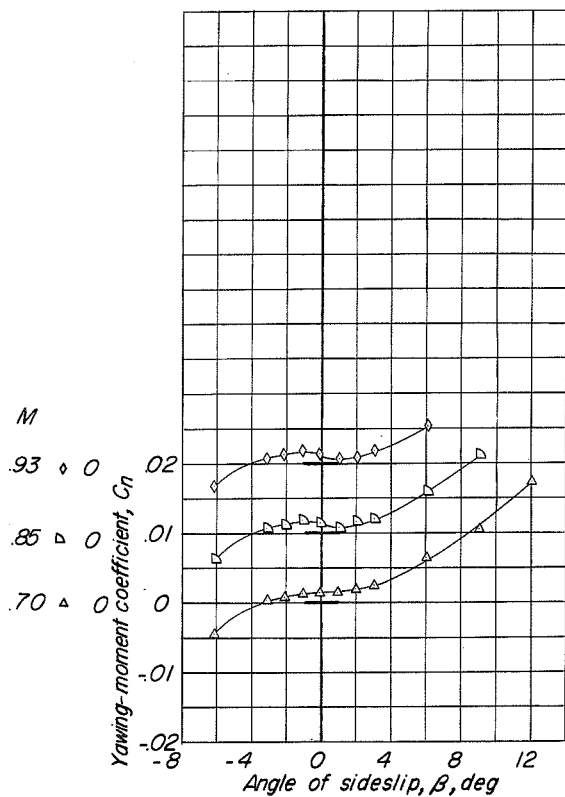
(d) Modification 4; slant-base fuselage extension.

Figure 32.- Continued.



(e) Modification 5; straight-base fuselage extension with dorsal fin.

Figure 32.- Continued.



(f) Modification 6; ventral fin.

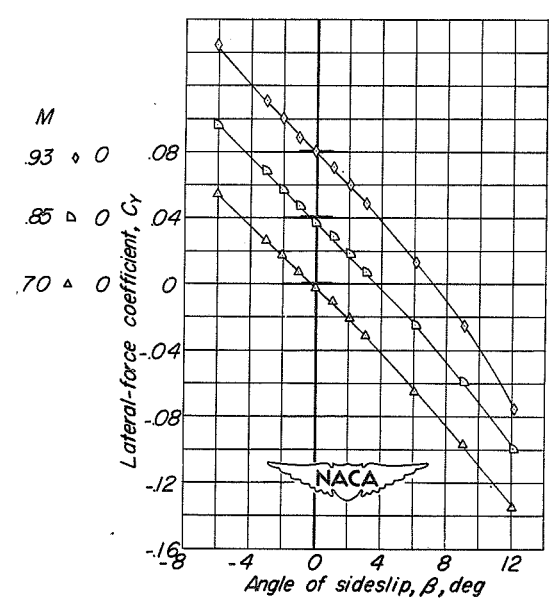
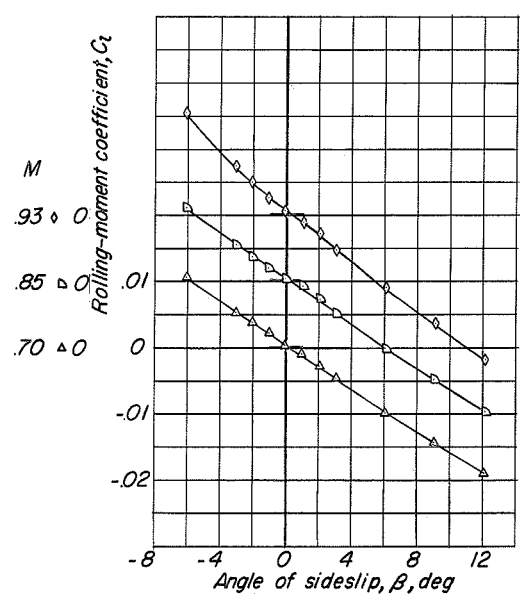
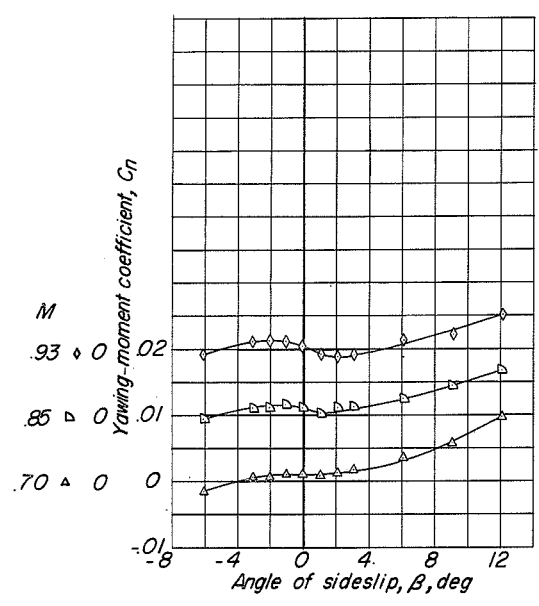
Figure 32.- Continued.



CONFIDENTIAL

NACA RM SL53G20

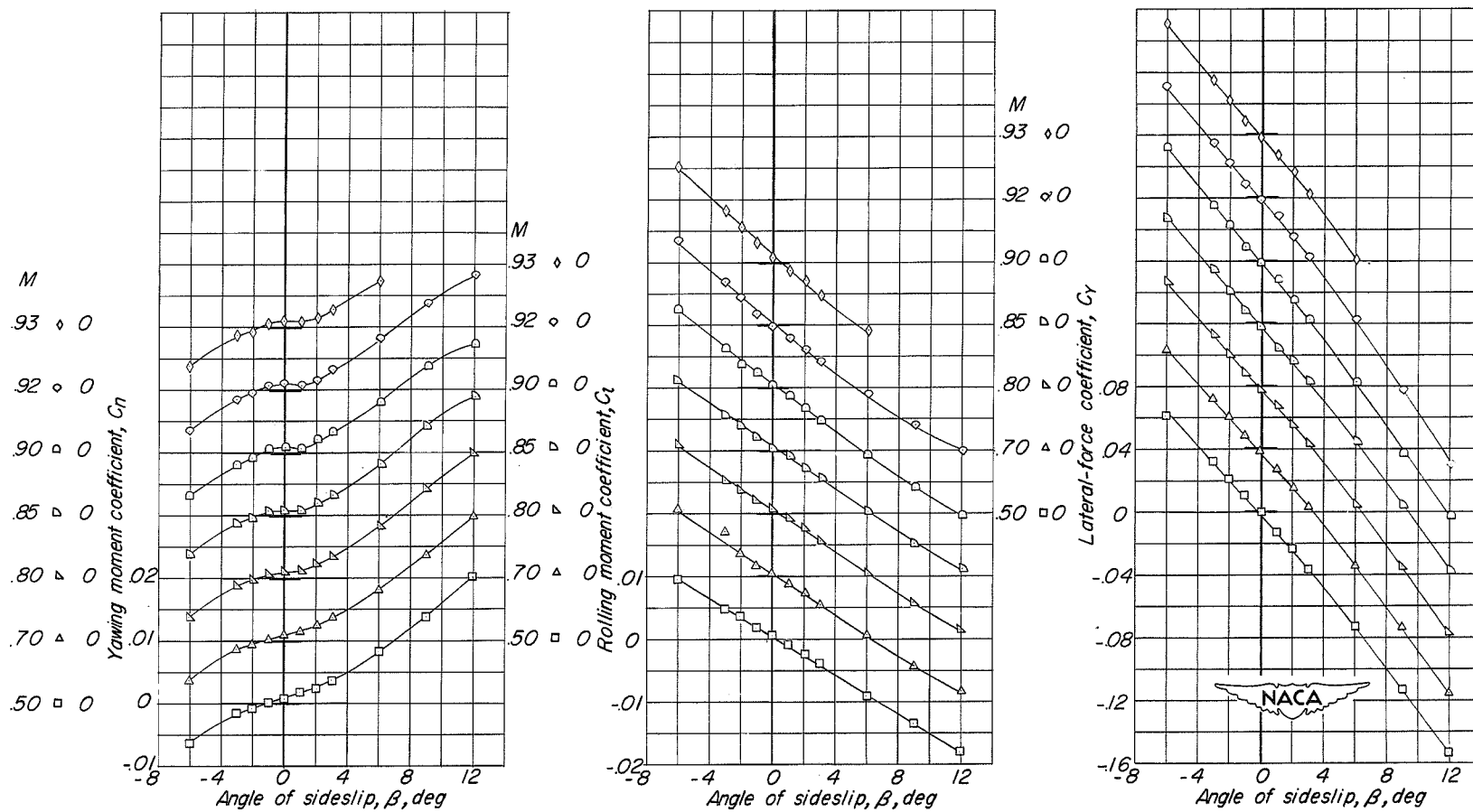
CONFIDENTIAL



(g) Modification 7; wing fillet.

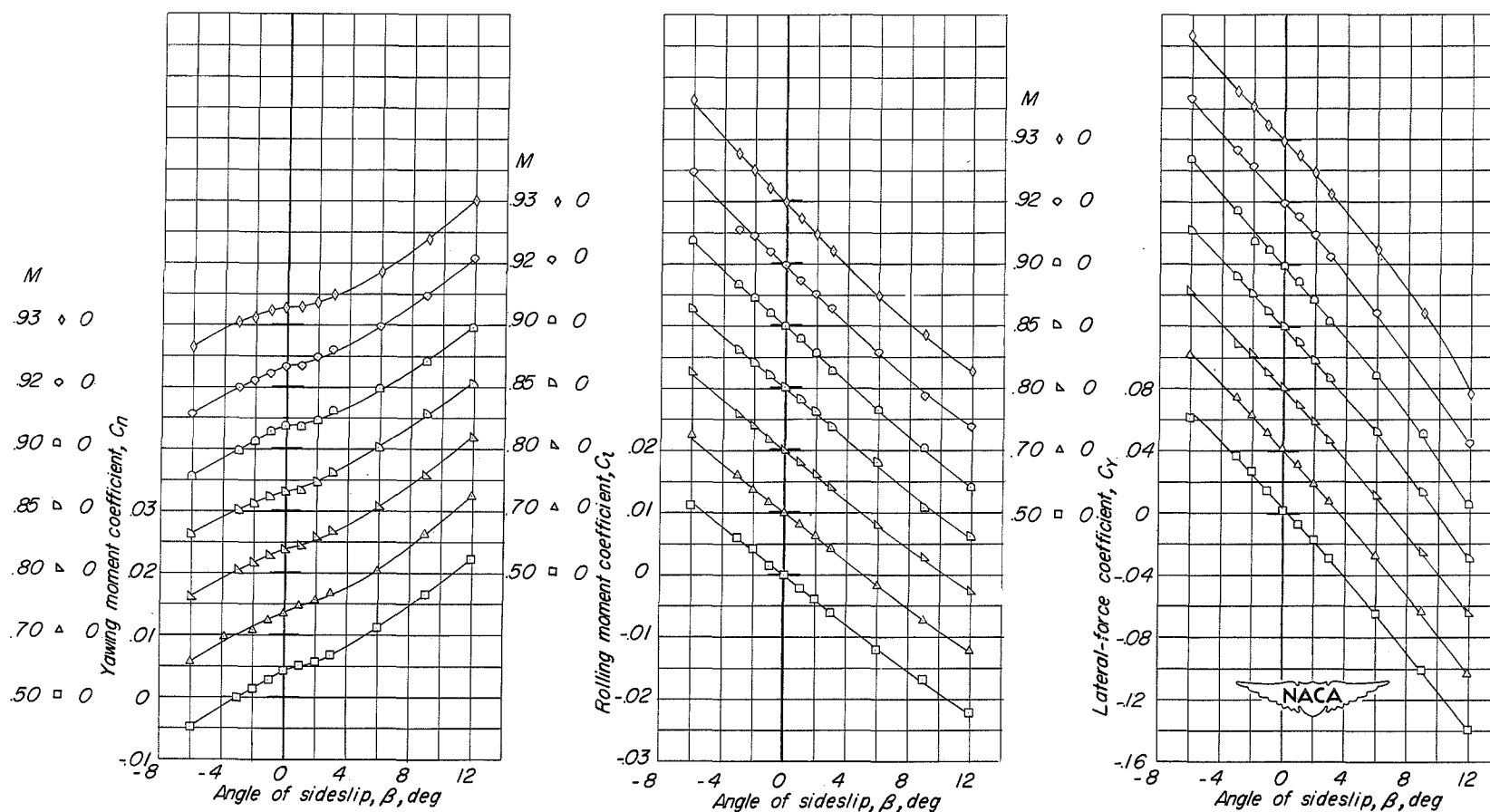
Figure 32. Continued.

CONFIDENTIAL



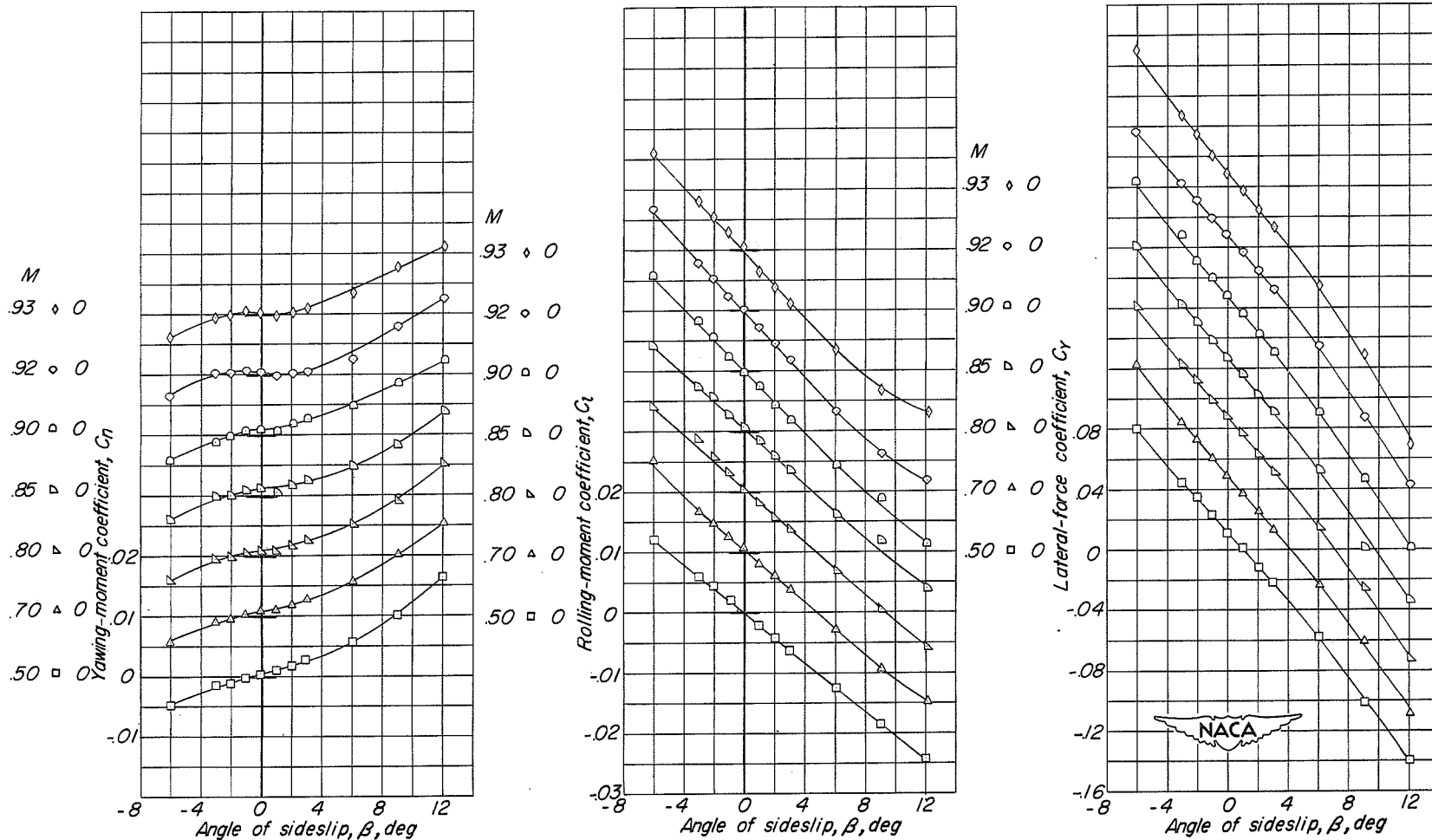
(h) Modification 8; fuselage side fins.

Figure 32.- Continued.



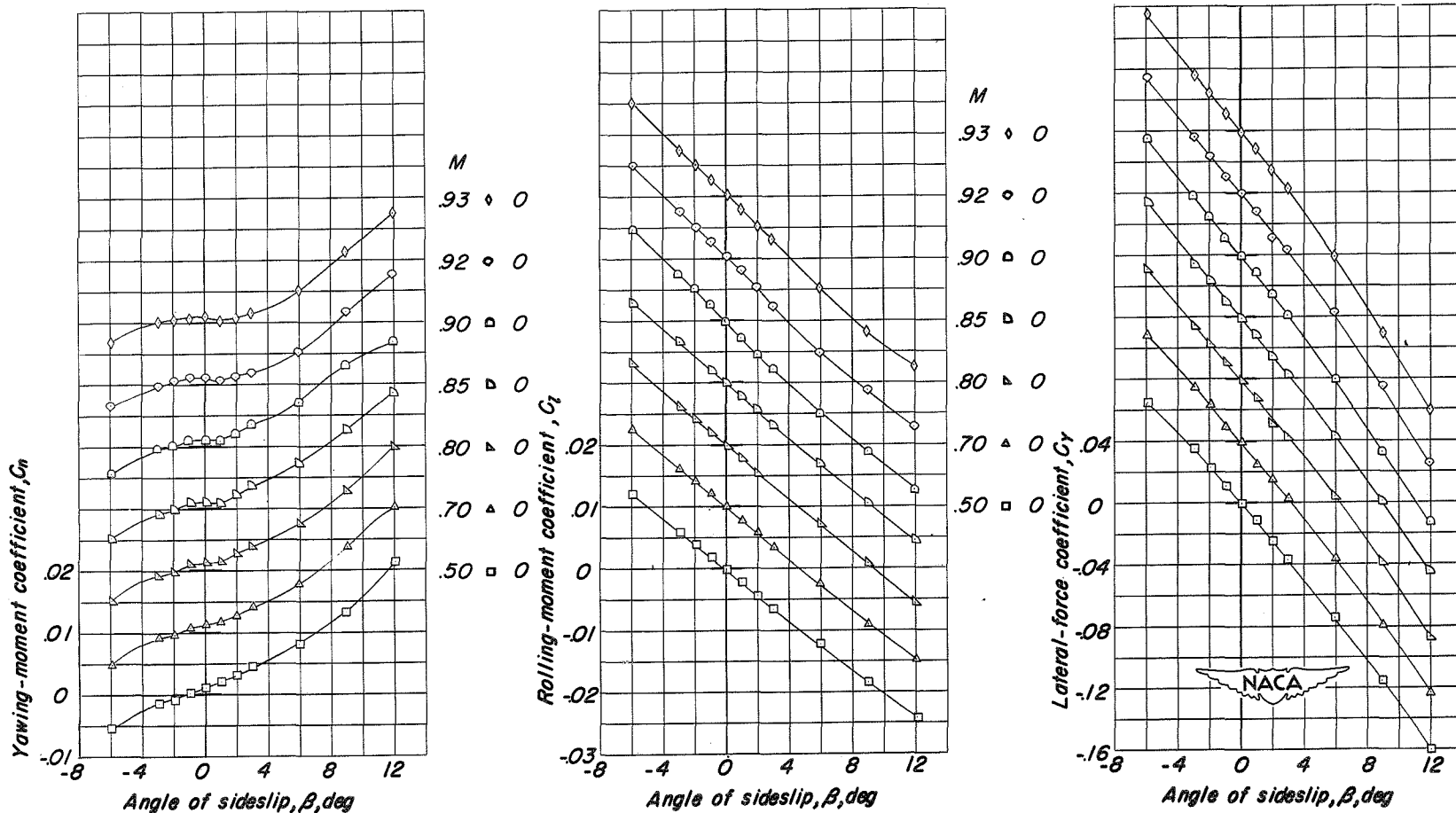
(i) Modification 9; tip fins mounted on the bottom surface of the horizontal tail.

Figure 32.- Concluded.



(a) Complete model.

Figure 33.- Lateral characteristics of modification 10. Enlarged vertical tail;  $\alpha = 0^\circ$ ;  $i_t = 0^\circ$ .

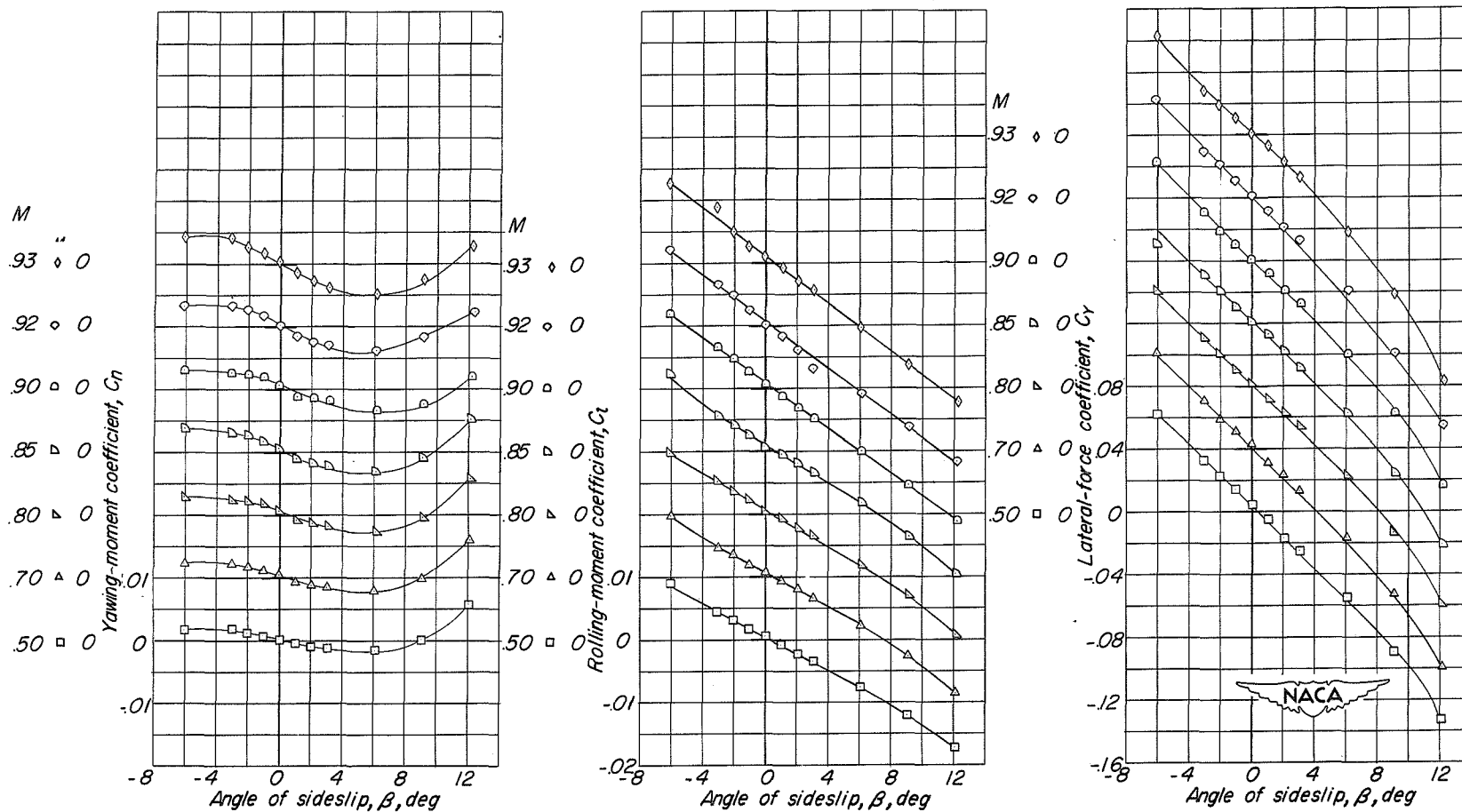


(b) Complete model;  $i_t = -4^\circ$ .

Figure 33.- Continued.

CONFIDENTIAL

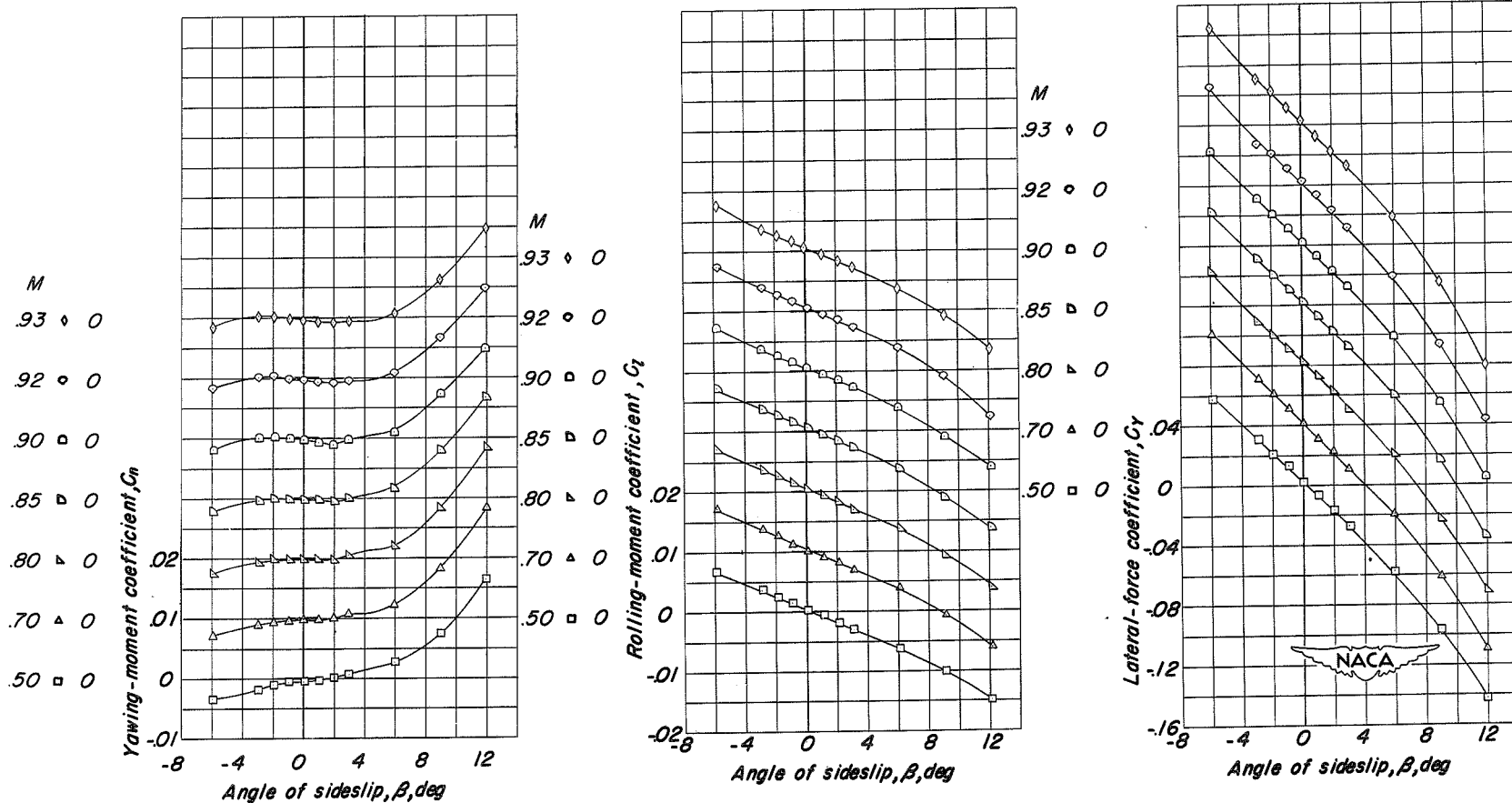
CONFIDENTIAL



(c) Wing, fuselage, and vertical tail.

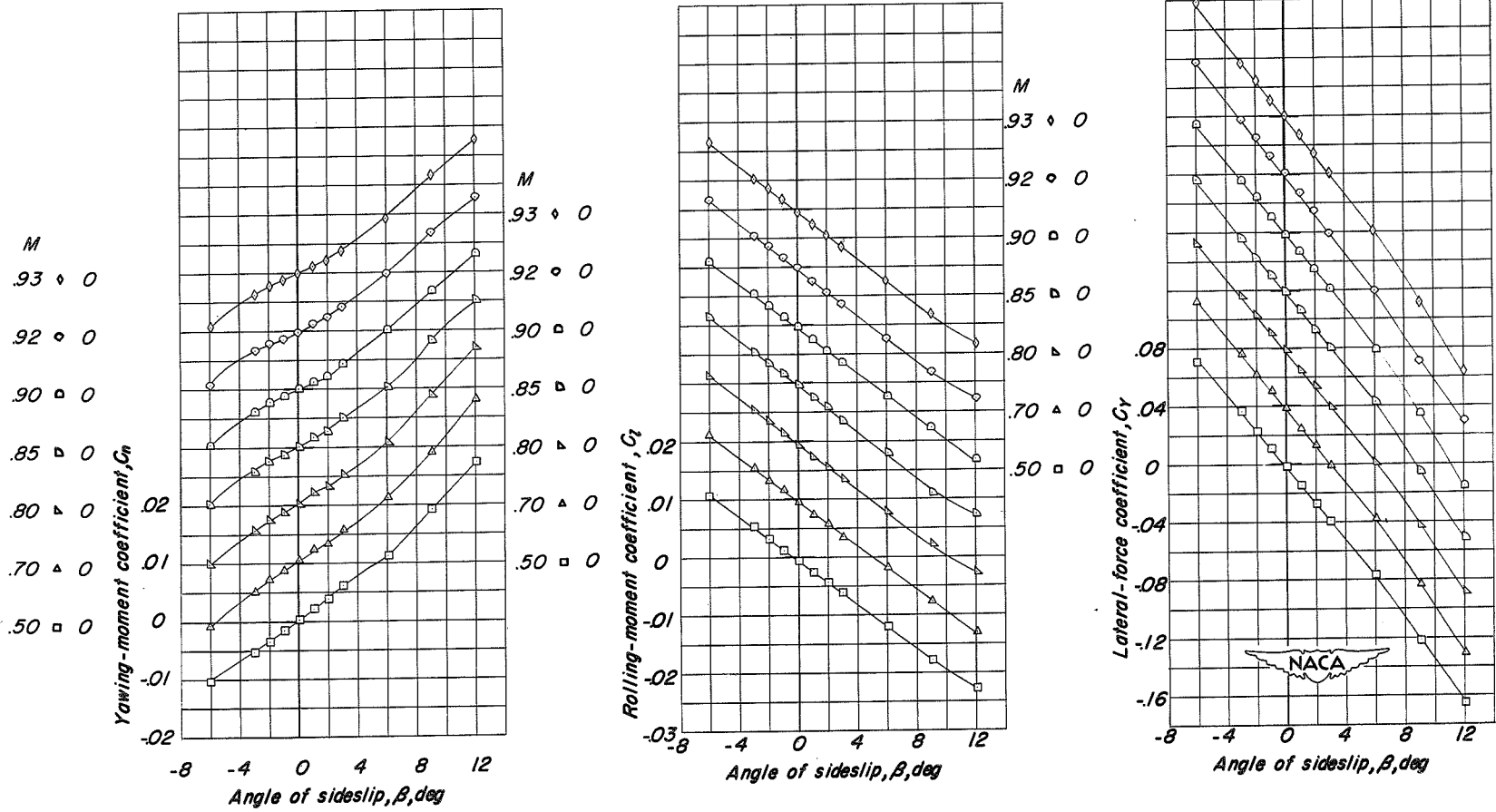
Figure 33.- Continued.

CONFIDENTIAL



(d) Fuselage and vertical tail.

Figure 33.- Continued.

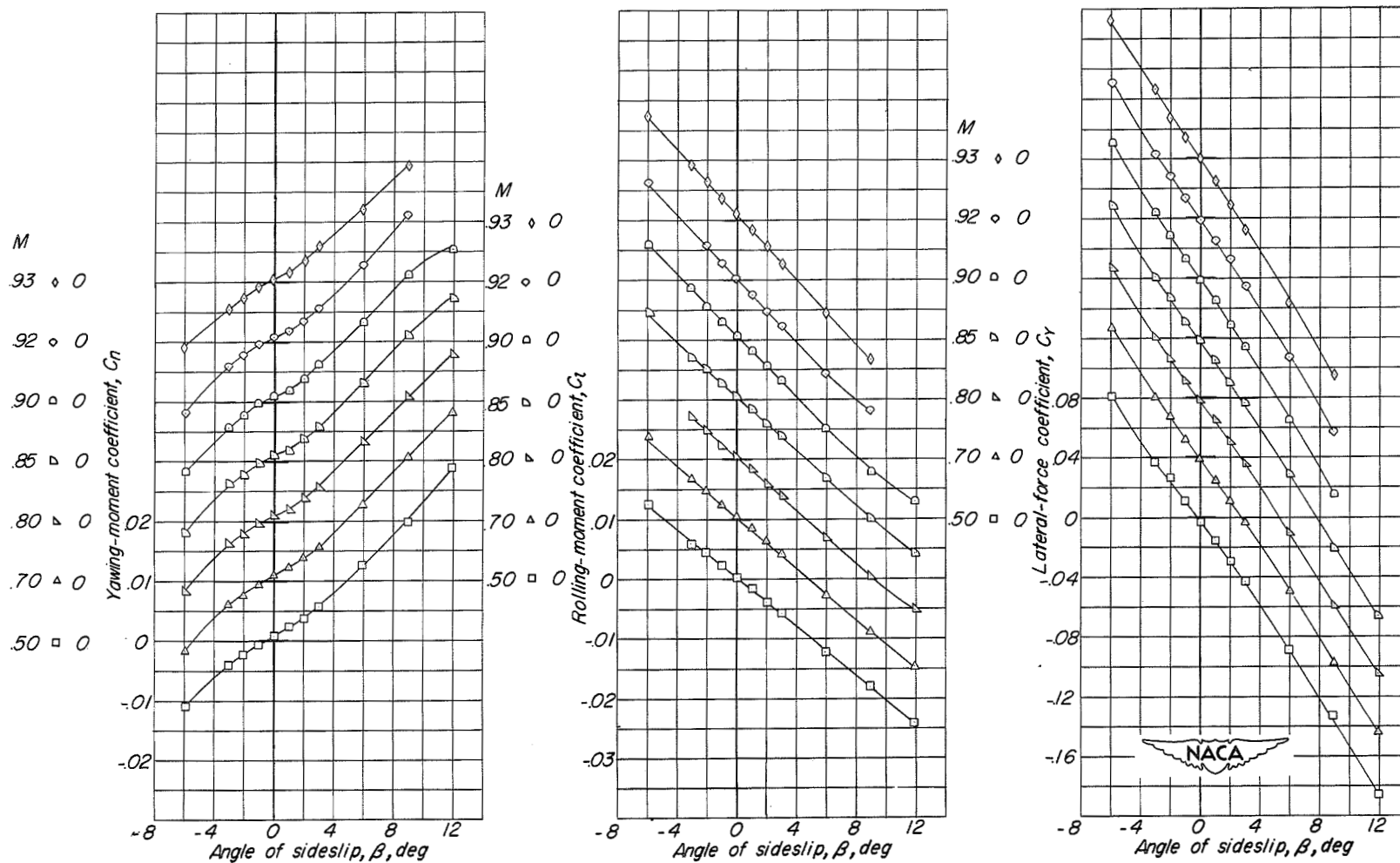


(e) Fuselage, vertical tail, and horizontal tail.

Figure 33.- Concluded.

CONFIDENTIAL





(a) Modification 11, fuselage side fins;  $\alpha = 0^\circ$ .

Figure 34.- Lateral characteristics of modifications to the enlarged-vertical-tail configuration (modification 10).  $i_t = 0^\circ$ .

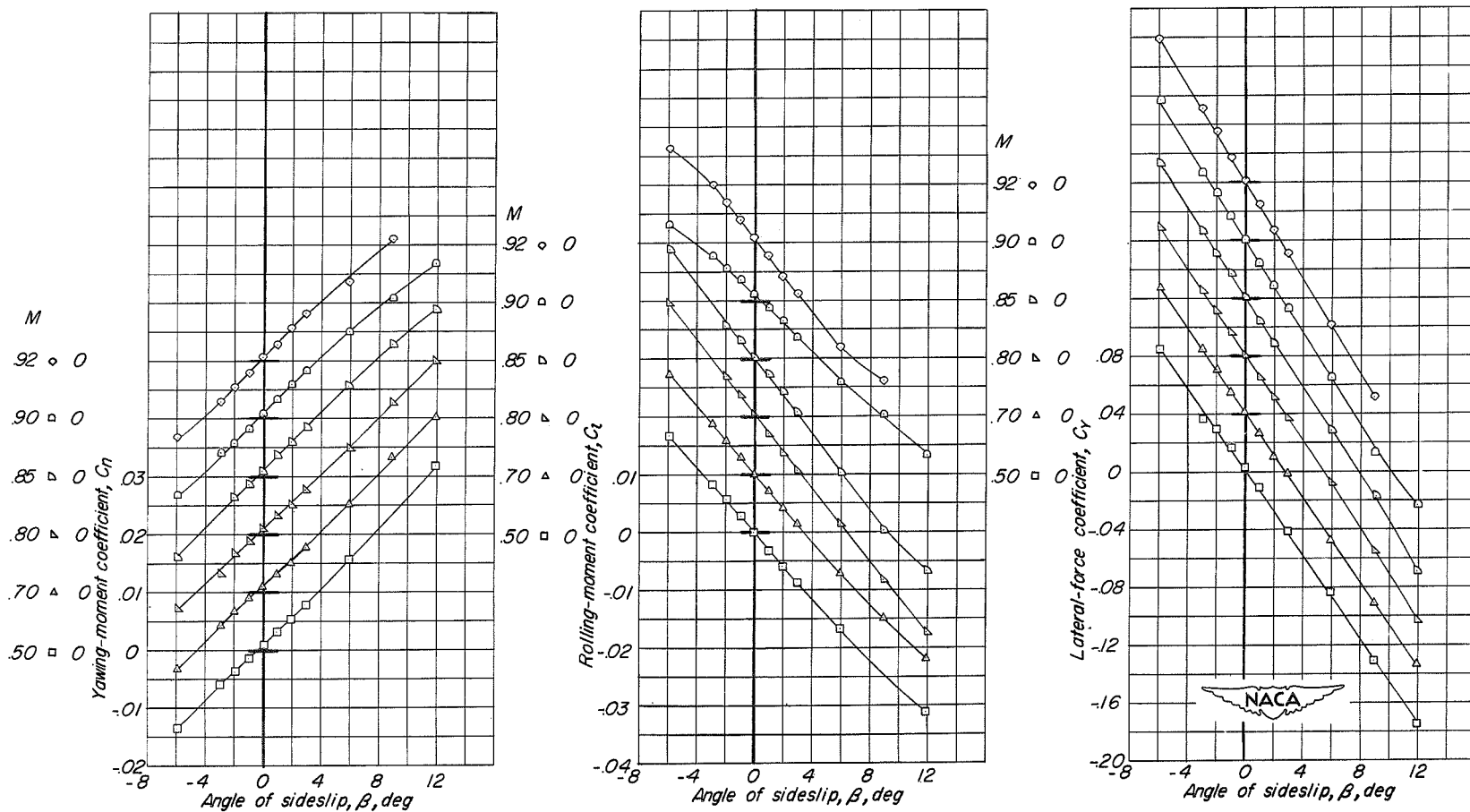
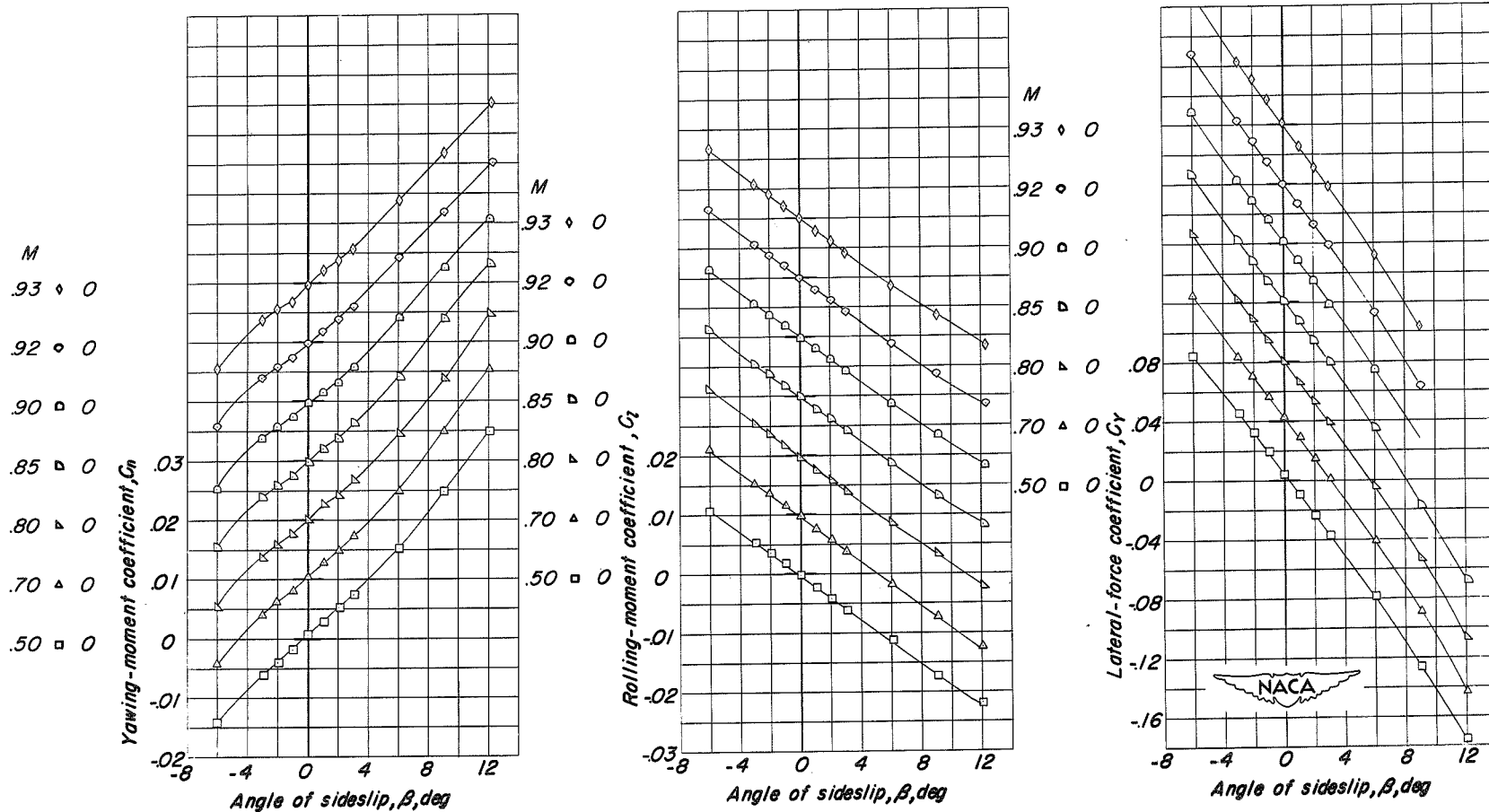
(b) Modification 11, fuselage side fins;  $\alpha = 6^\circ$ .

Figure 34.- Continued.

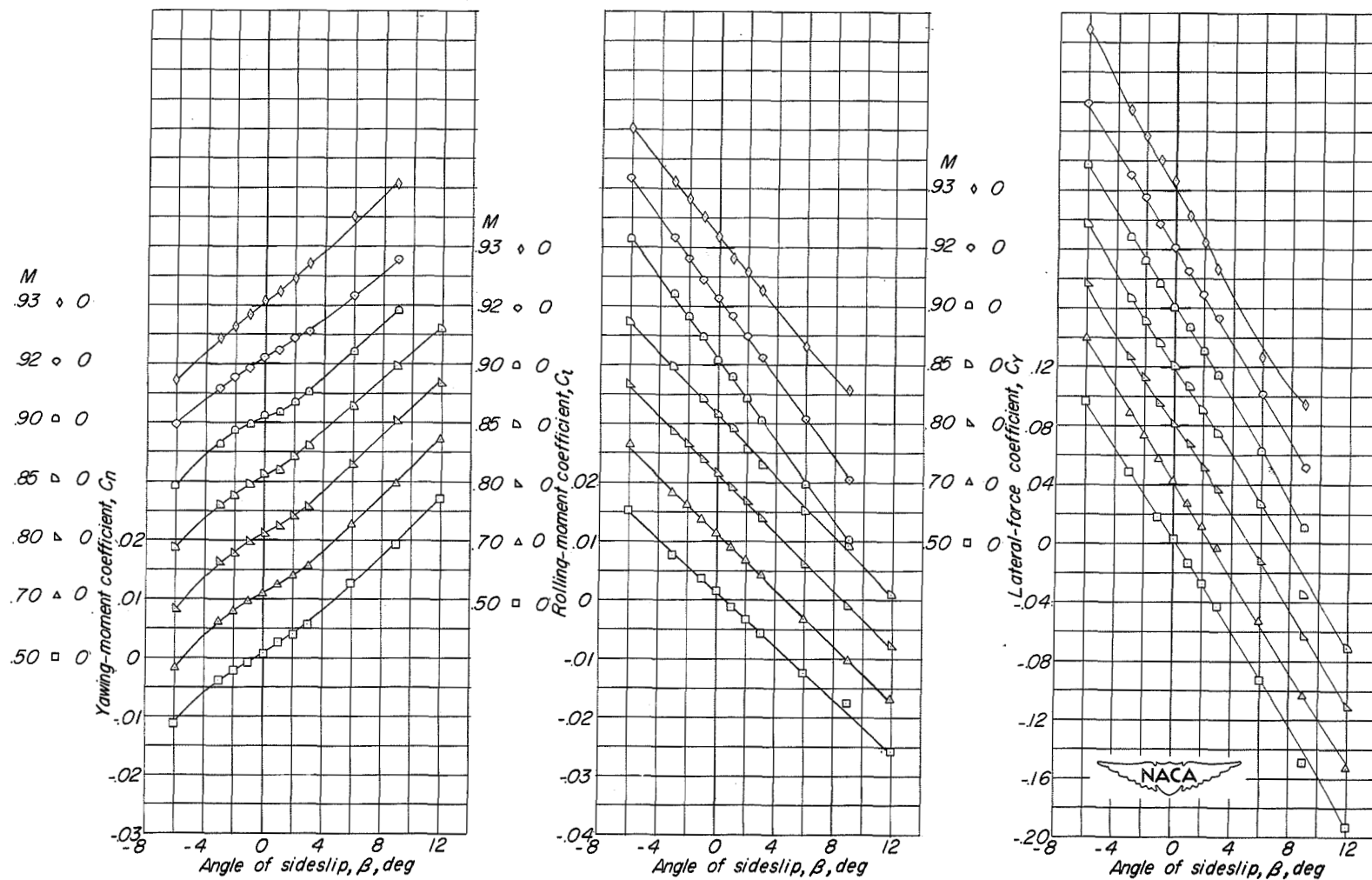
CONFIDENTIAL

CONFIDENTIAL



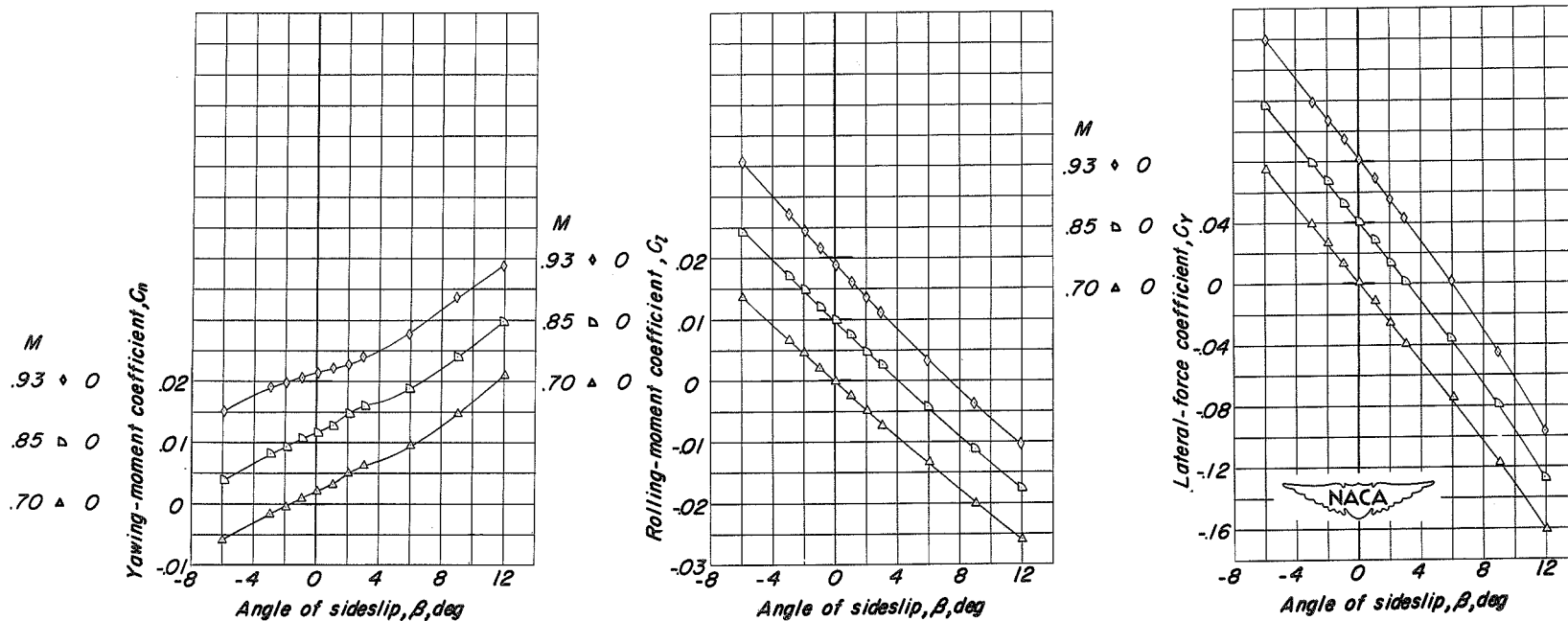
(c) Modification 11, wing removed;  $\alpha = 0^\circ$ .

Figure 34.- Continued.



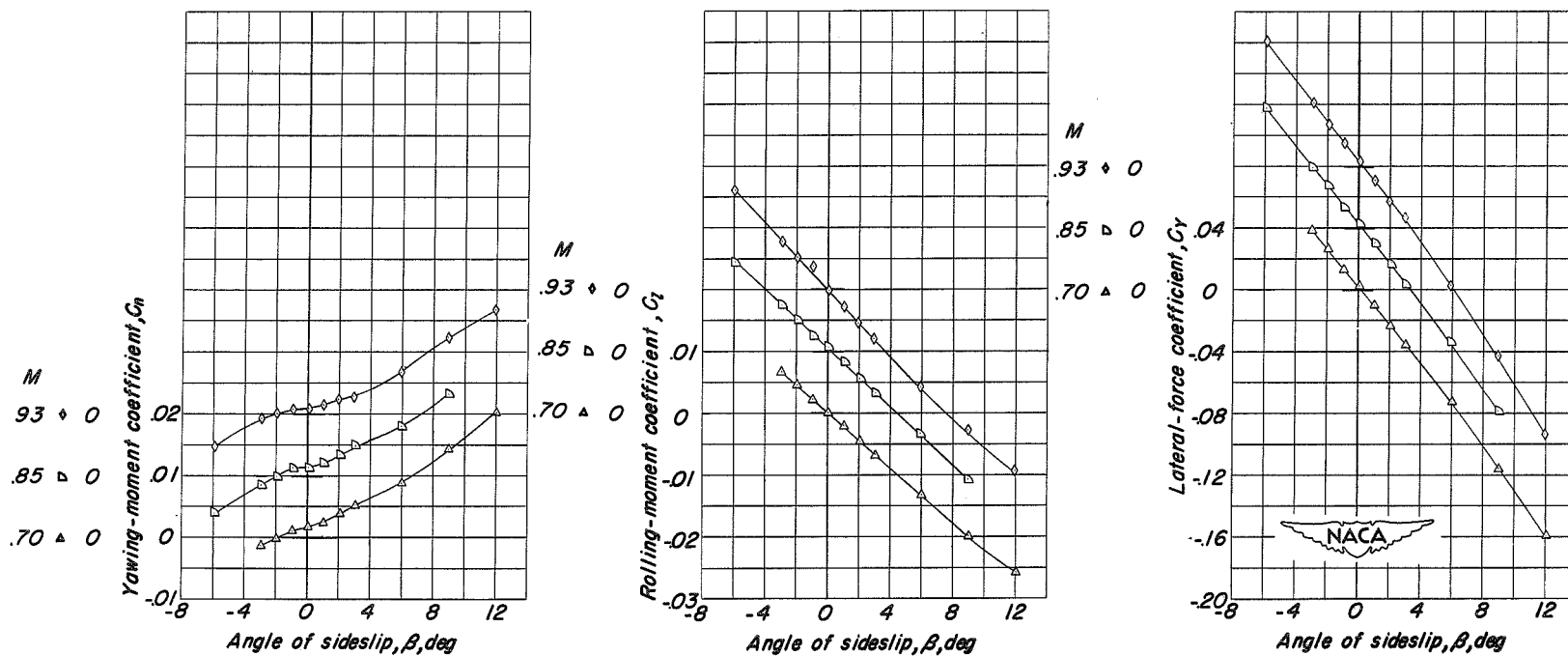
(d) Modification 12 (modification 11 with wing stores);  $\alpha = 0^\circ$ .

Figure 34.- Continued.



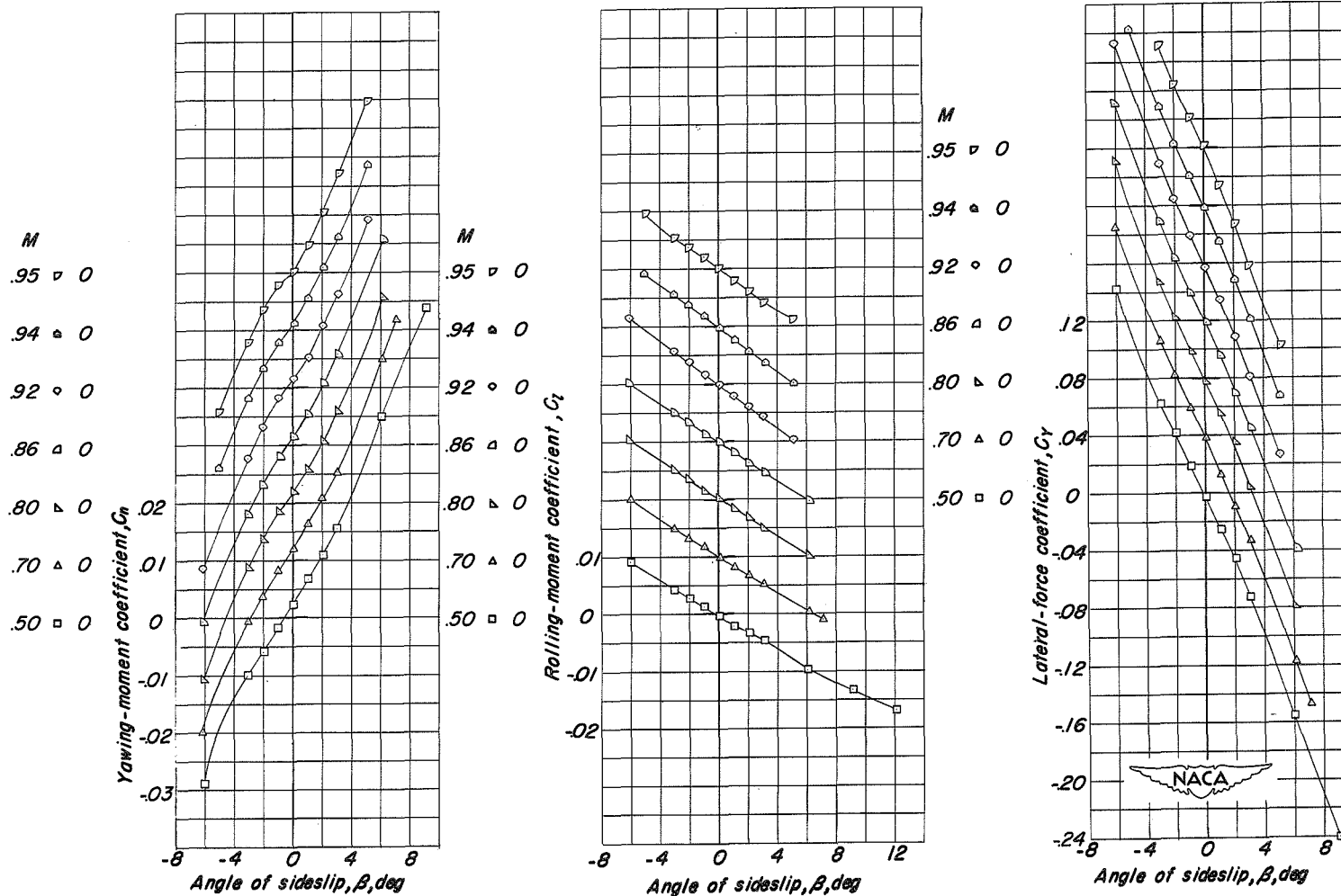
(e) Modification 13; vertical tail end plate;  $\alpha = 0^\circ$ .

Figure 34.- Continued.



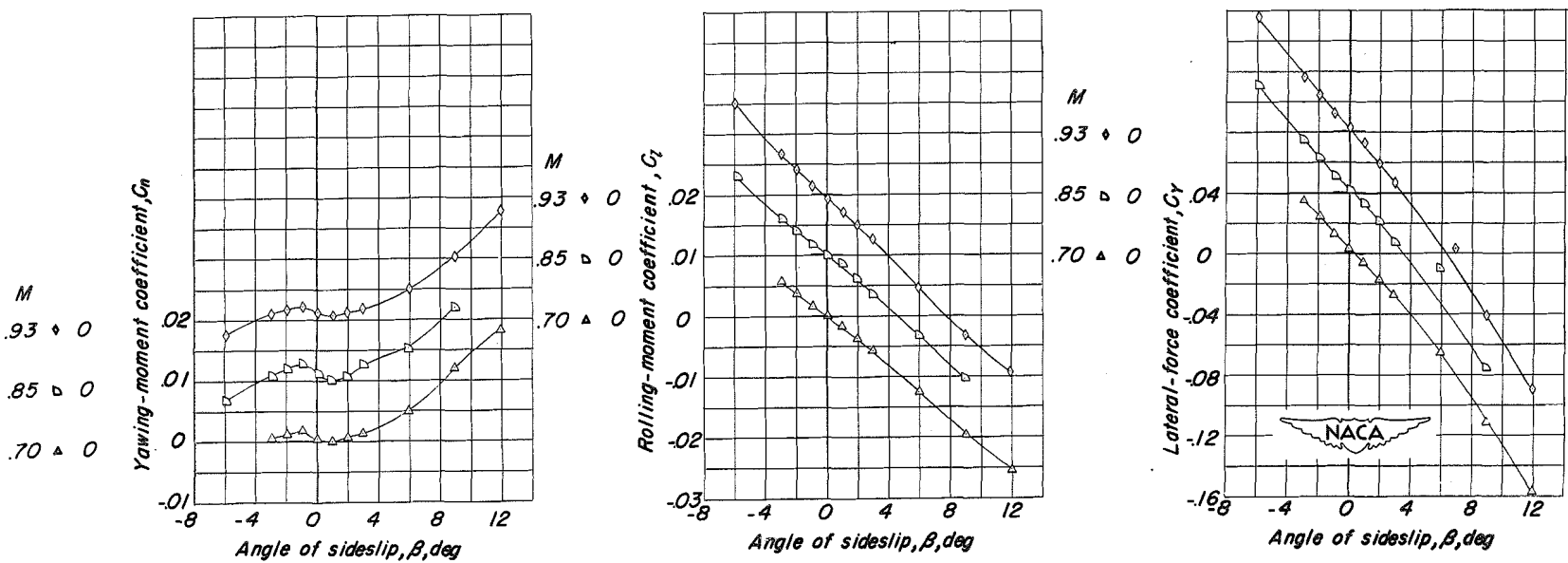
(f) Modification 14; vertical tail fence;  $\alpha = 0^\circ$ .

Figure 34.- Continued.



(g) Modification 15; large ventral fin for rocket model;  $\alpha = 0^\circ$ .

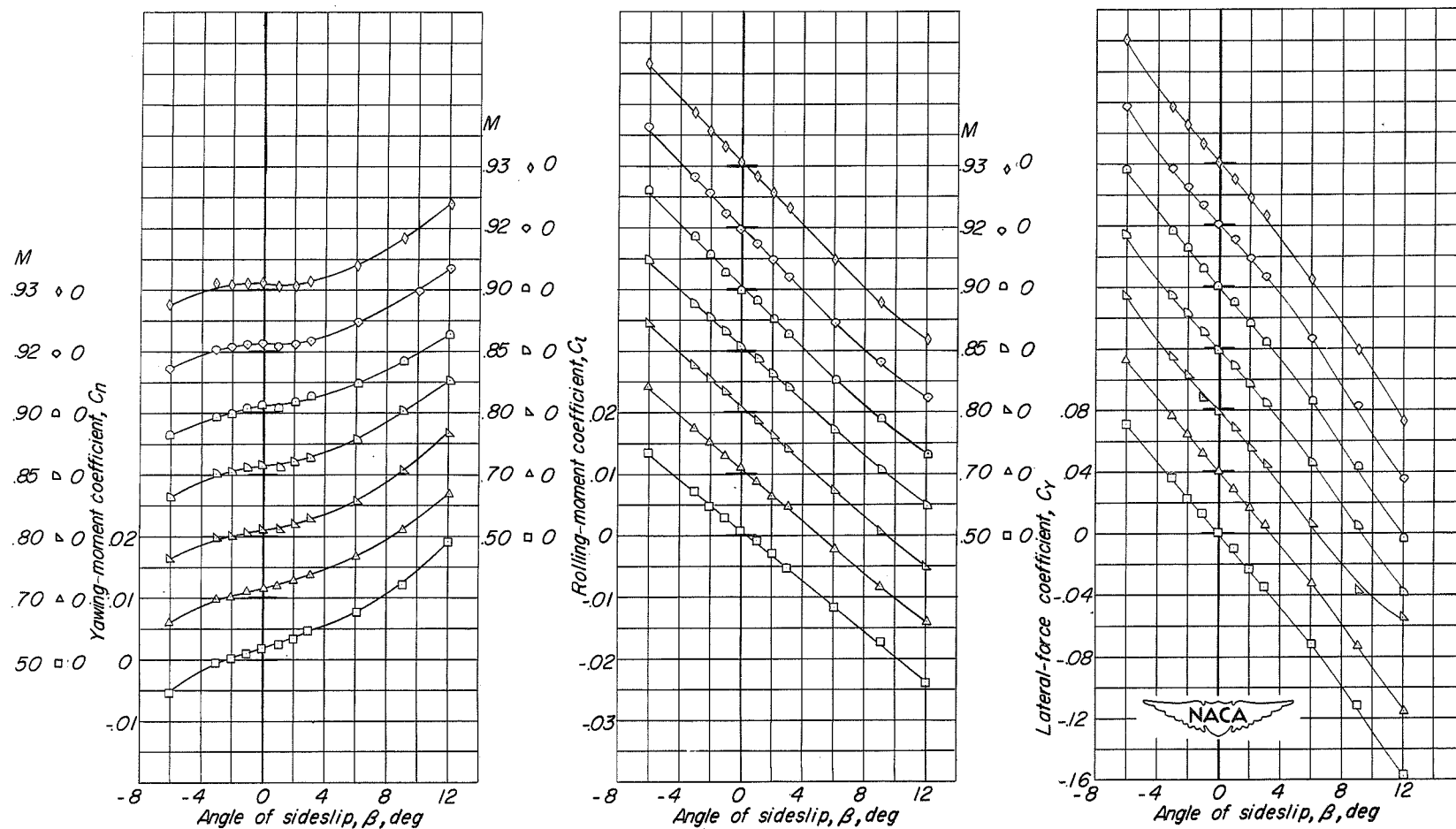
Figure 34.- Continued.



(h) Modification 16; separated rocket model booster;  $\alpha = 0^\circ$ .

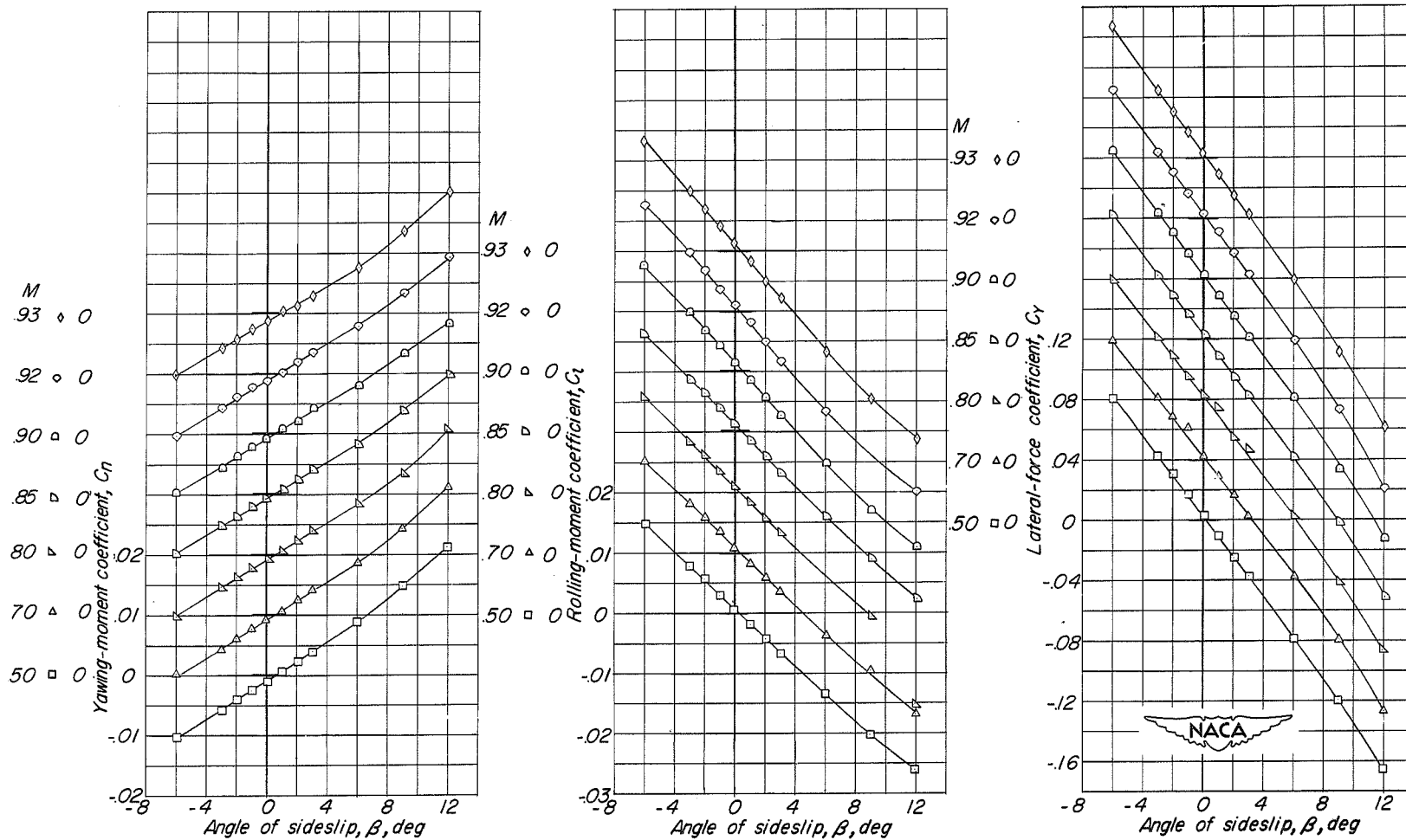
Figure 34.- Continued.





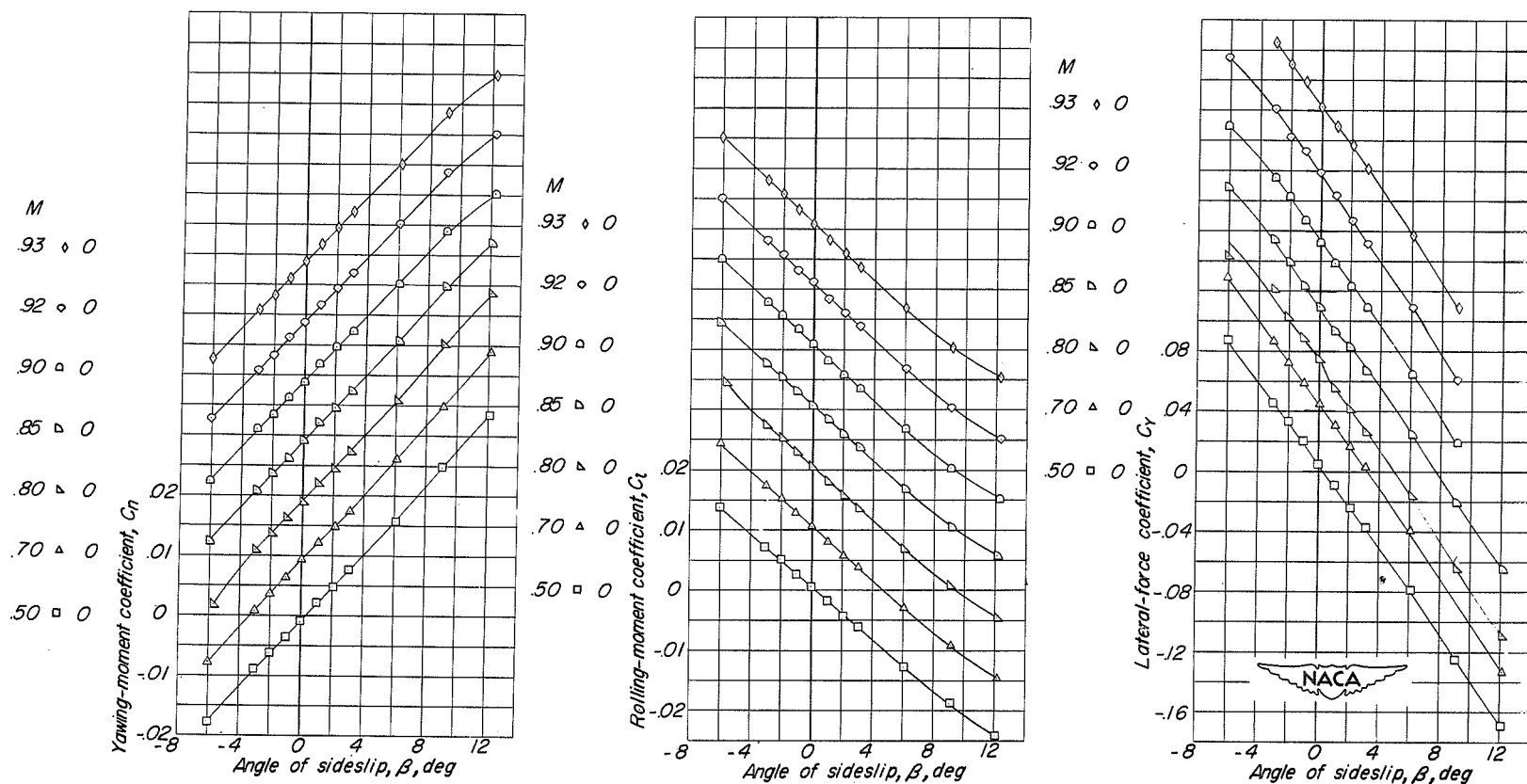
(1) Modification 17; vertical tail - horizontal tail junction tunnel faired and sealed.  $\alpha = 0^\circ$ .

Figure 34.- Continued.



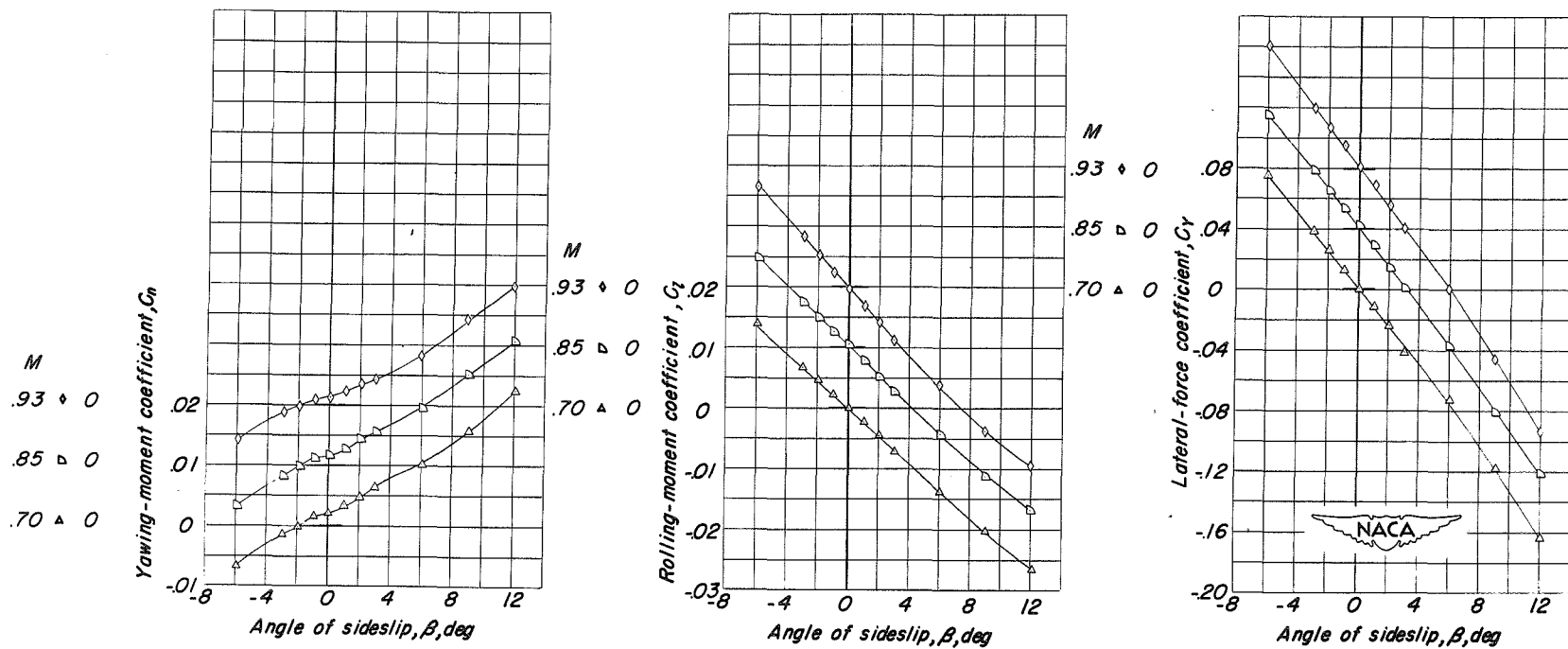
(j) Modification 18, thick trailing edge on vertical tail;  $\alpha = 0^\circ$ .

Figure 34.- Continued.



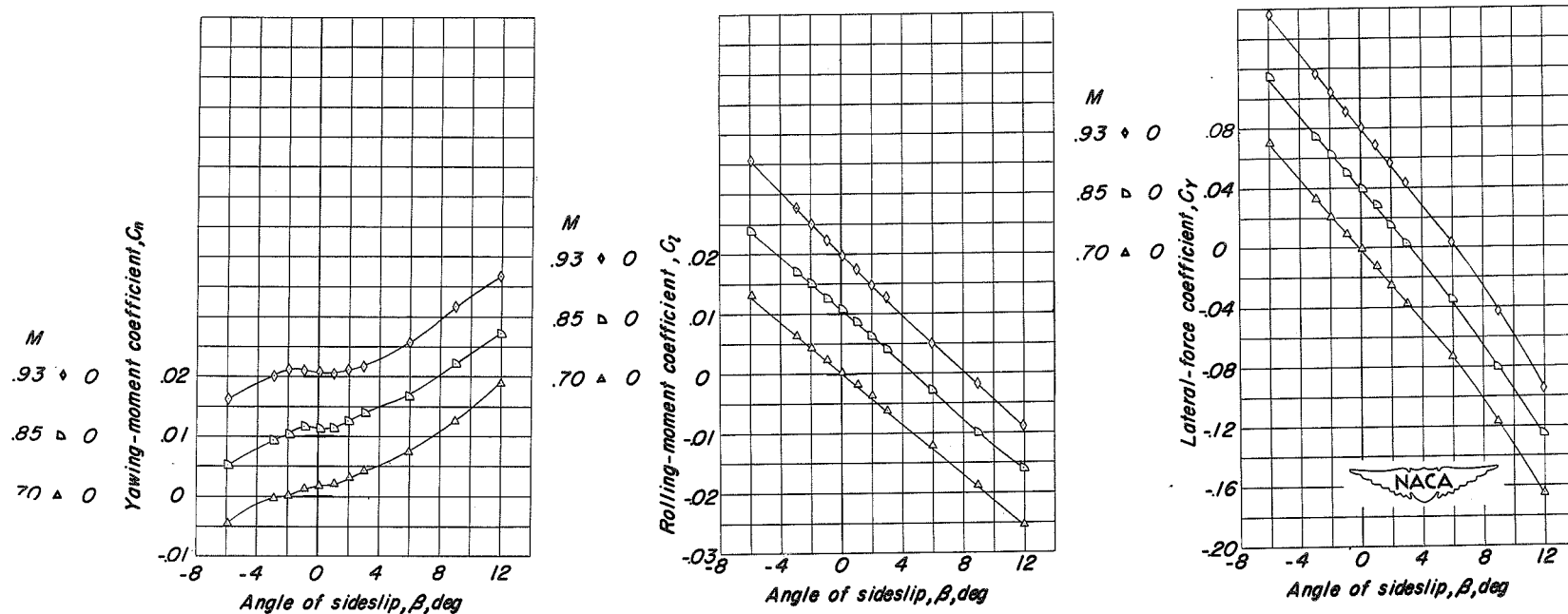
(k) Modification 18, thick trailing edge on vertical tail, wing removed;  
 $\alpha = 0^\circ$ .

Figure 34.- Continued.



(1) Modification 19; trailing-edge strips on vertical tail;  $\alpha = 0^\circ$ .

Figure 34.- Continued.



(m) Modification 20, fixed transition on vertical tail;  $\alpha = 0^\circ$ .

Figure 34.- Concluded.

CONFIDENTIAL

NACA RM SL53G20

CONFIDENTIAL

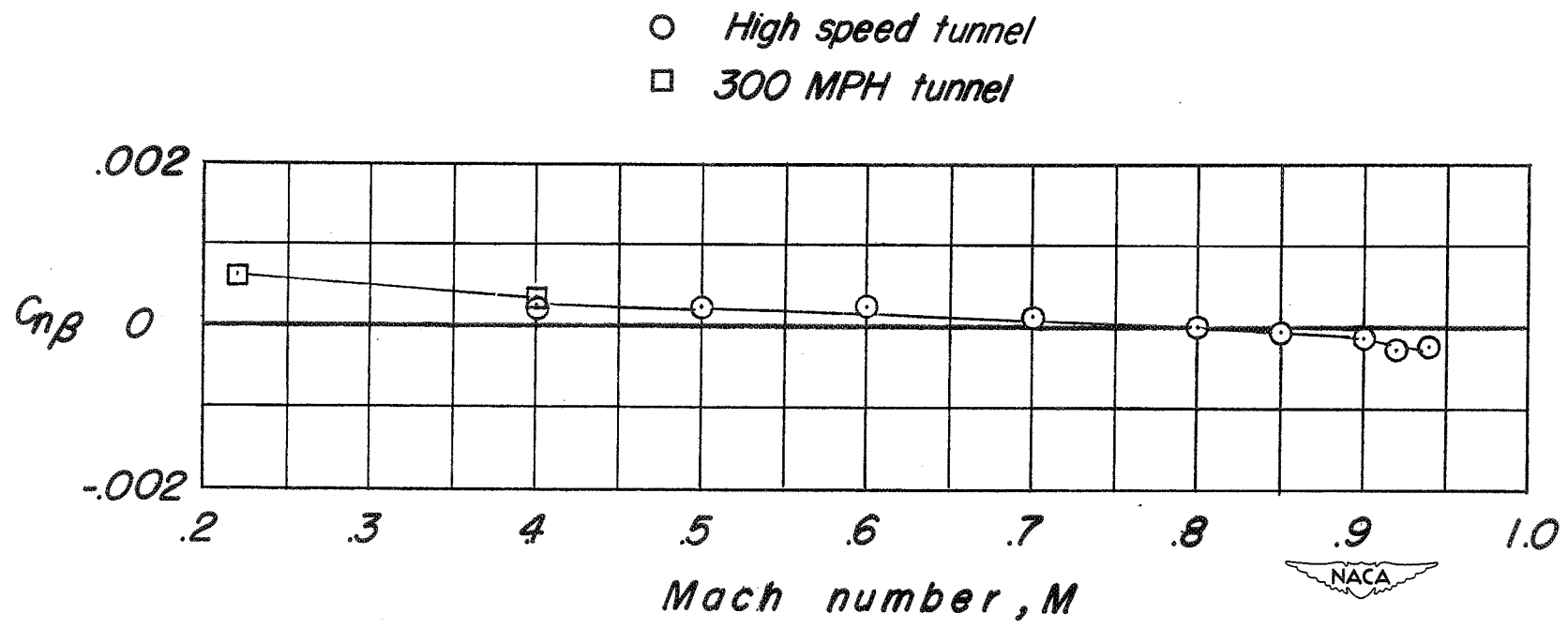


Figure 35.- Comparison of the directional stability characteristics of a 1/7-scale model tested in the 300 MPH tunnel and a 1/14-scale model tested in the high-speed tunnel.  $\alpha = 0^\circ$ ;  $i_t = 0^\circ$ .

CONFIDENTIAL

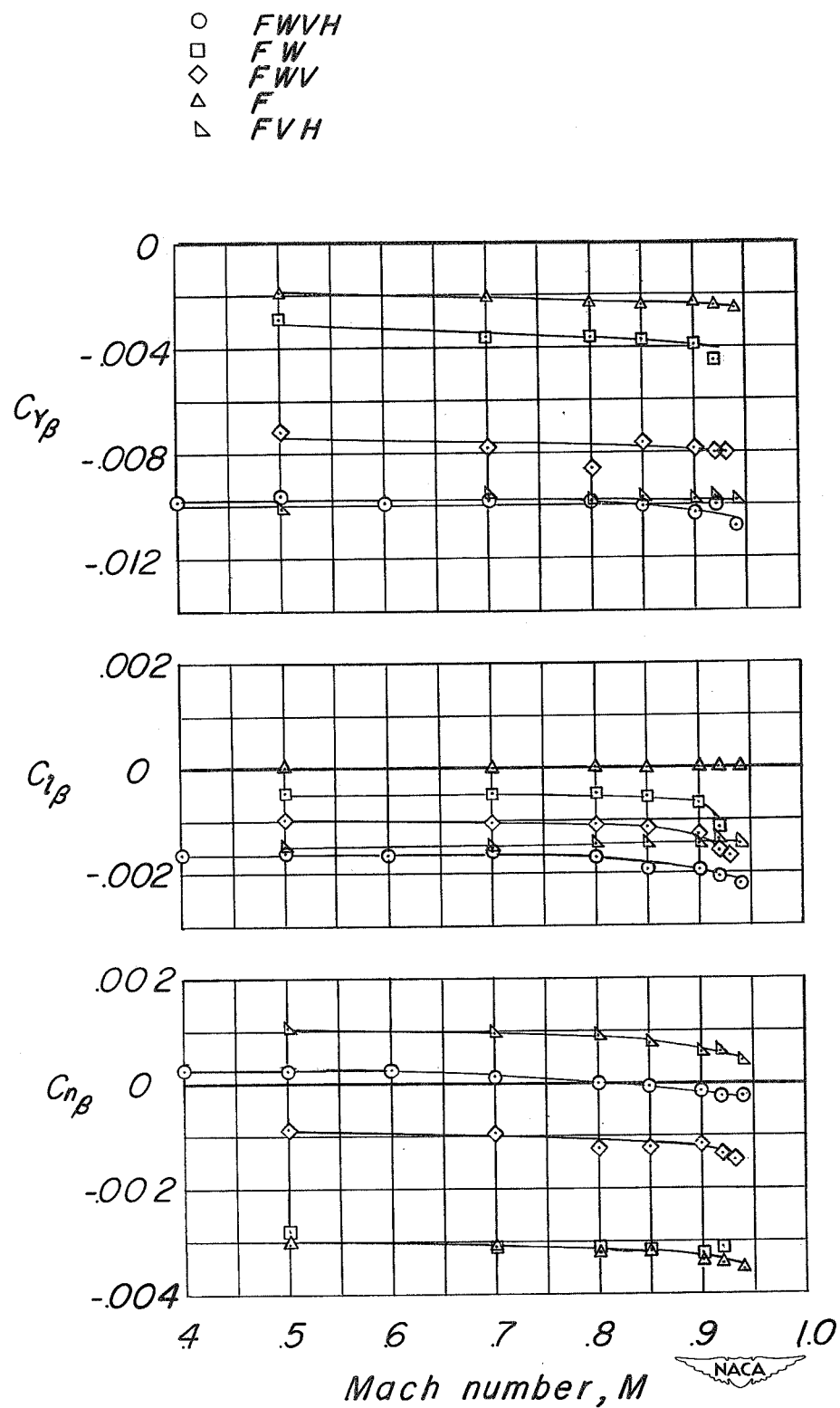
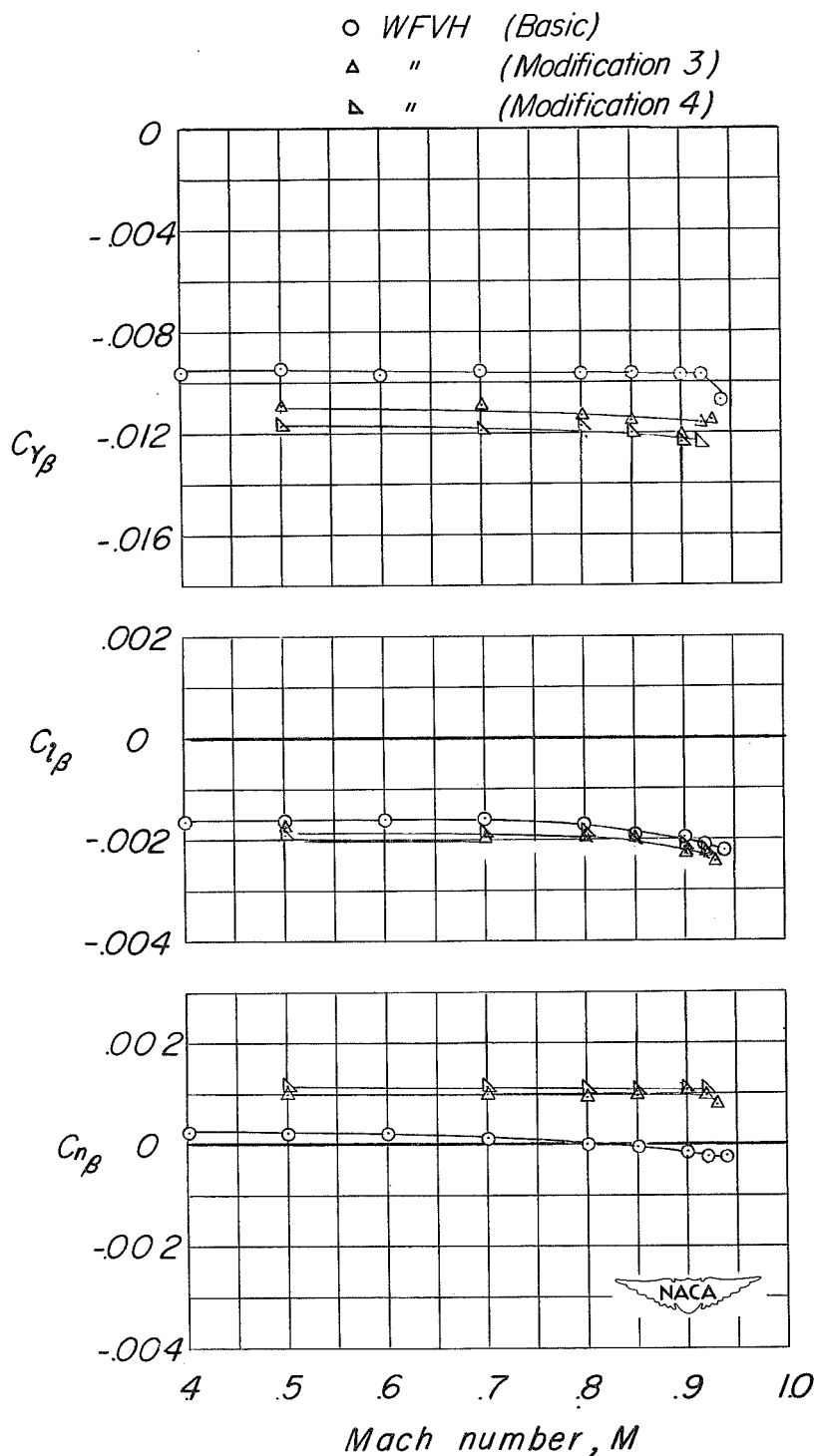


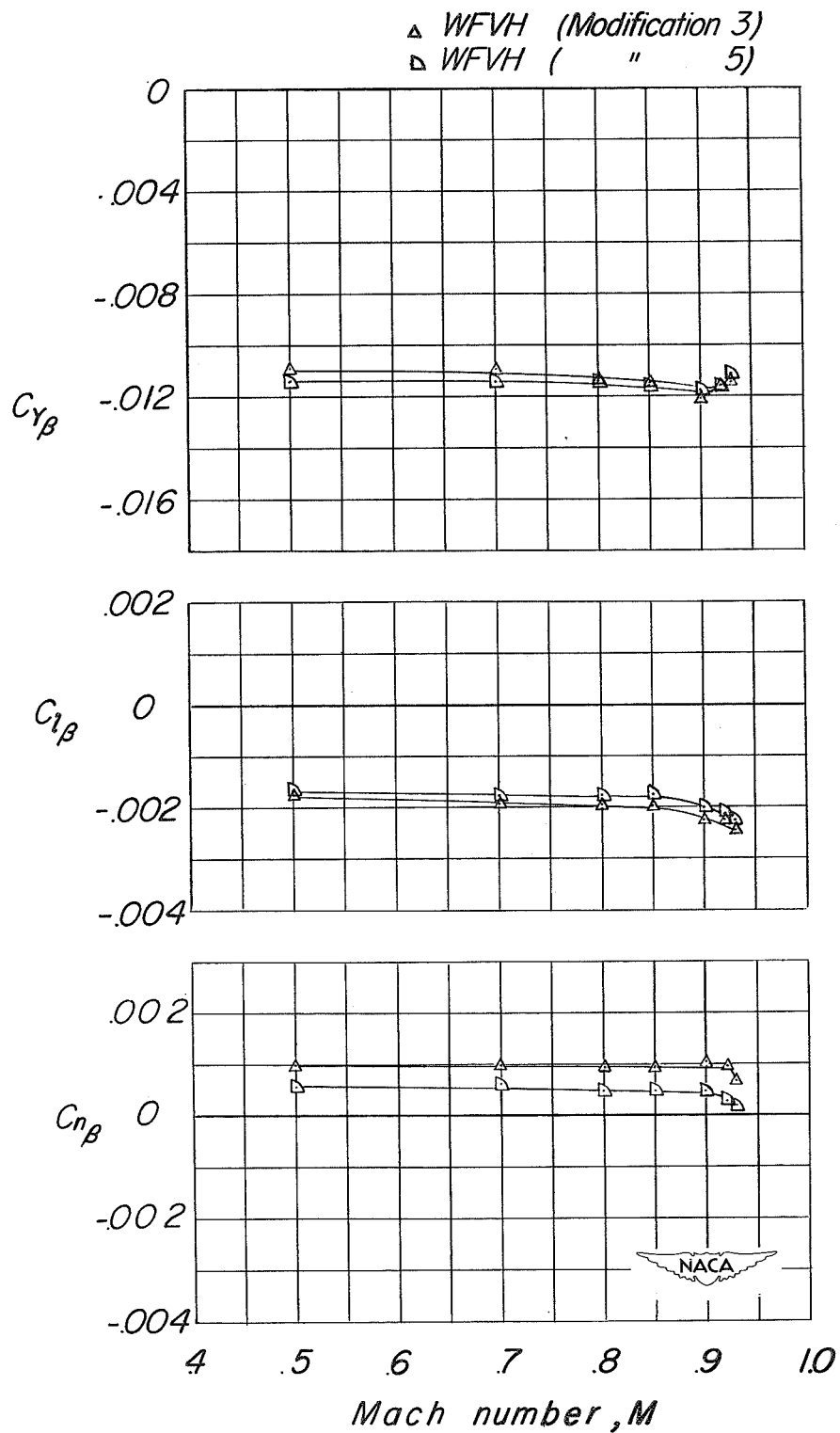
Figure 36.- Lateral stability characteristics of components of the basic model.  $\alpha = 0^\circ$ ;  $i_t = 0^\circ$ .



(a) Fuselage extensions.

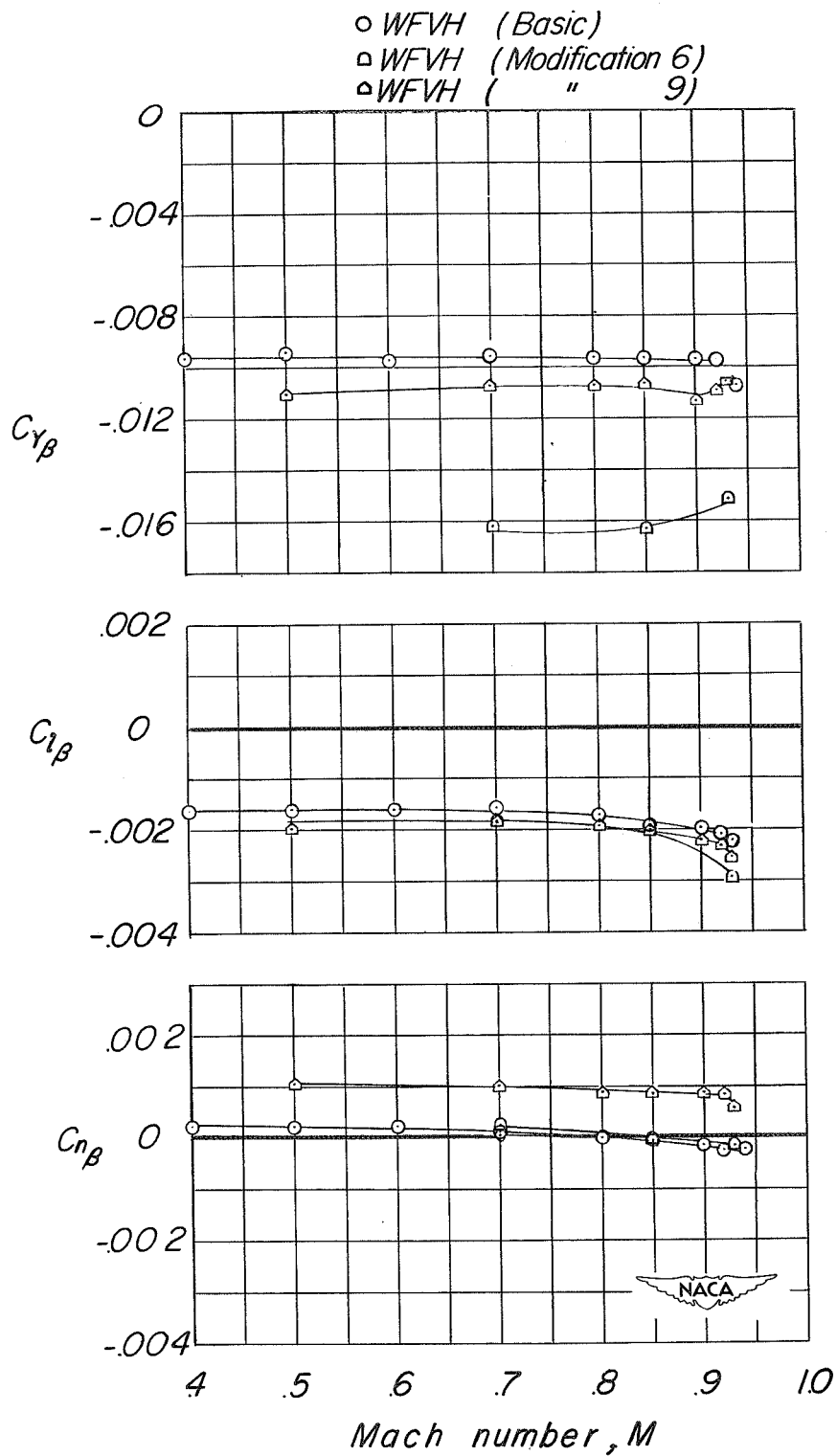
Figure 37.- The effects of modifications on the lateral stability characteristics of the basic model with original vertical tail.  $\alpha = 0^\circ$ ;  $i_t = 0^\circ$ .





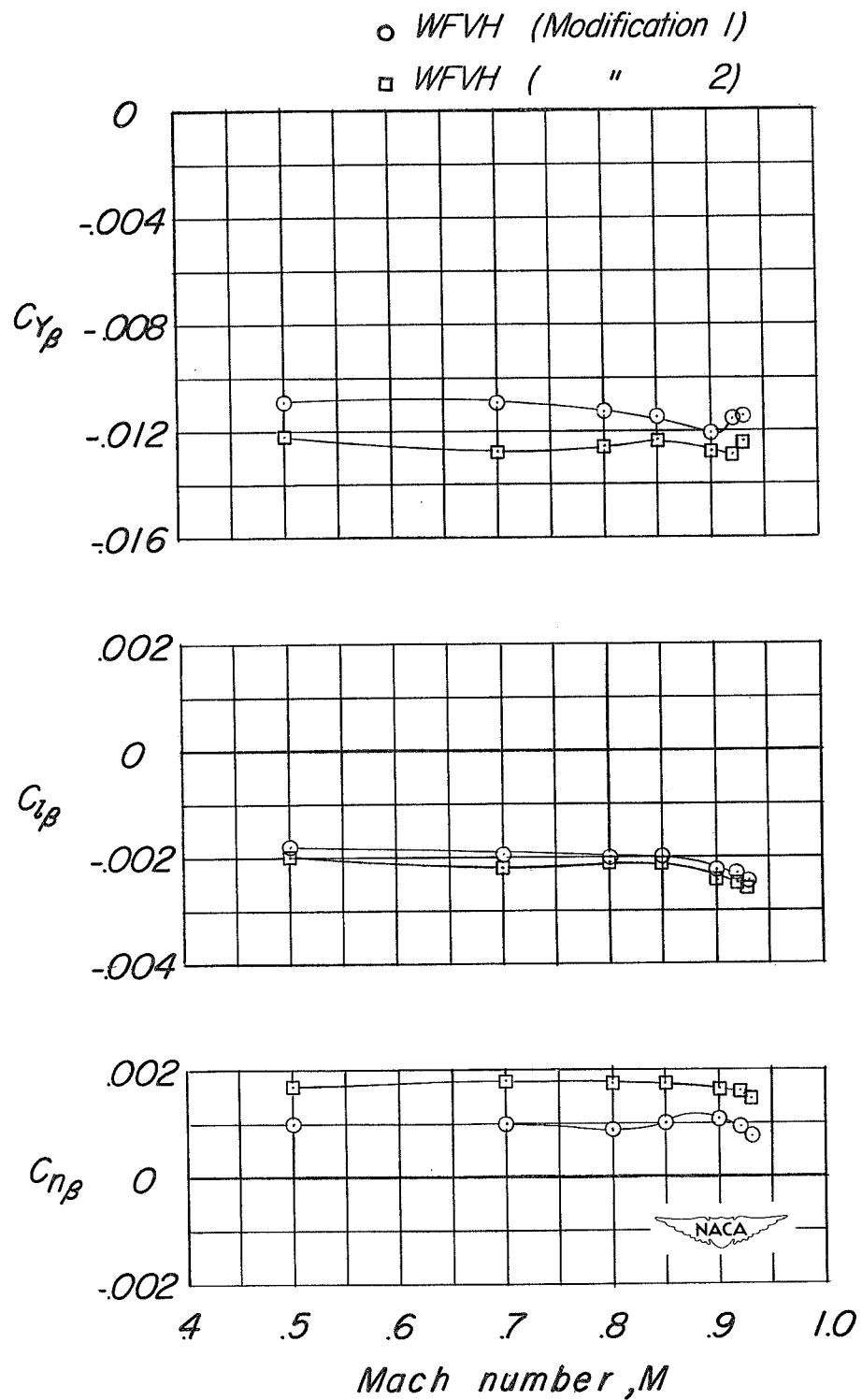
(b) Dorsal fin.

Figure 37.- Continued.



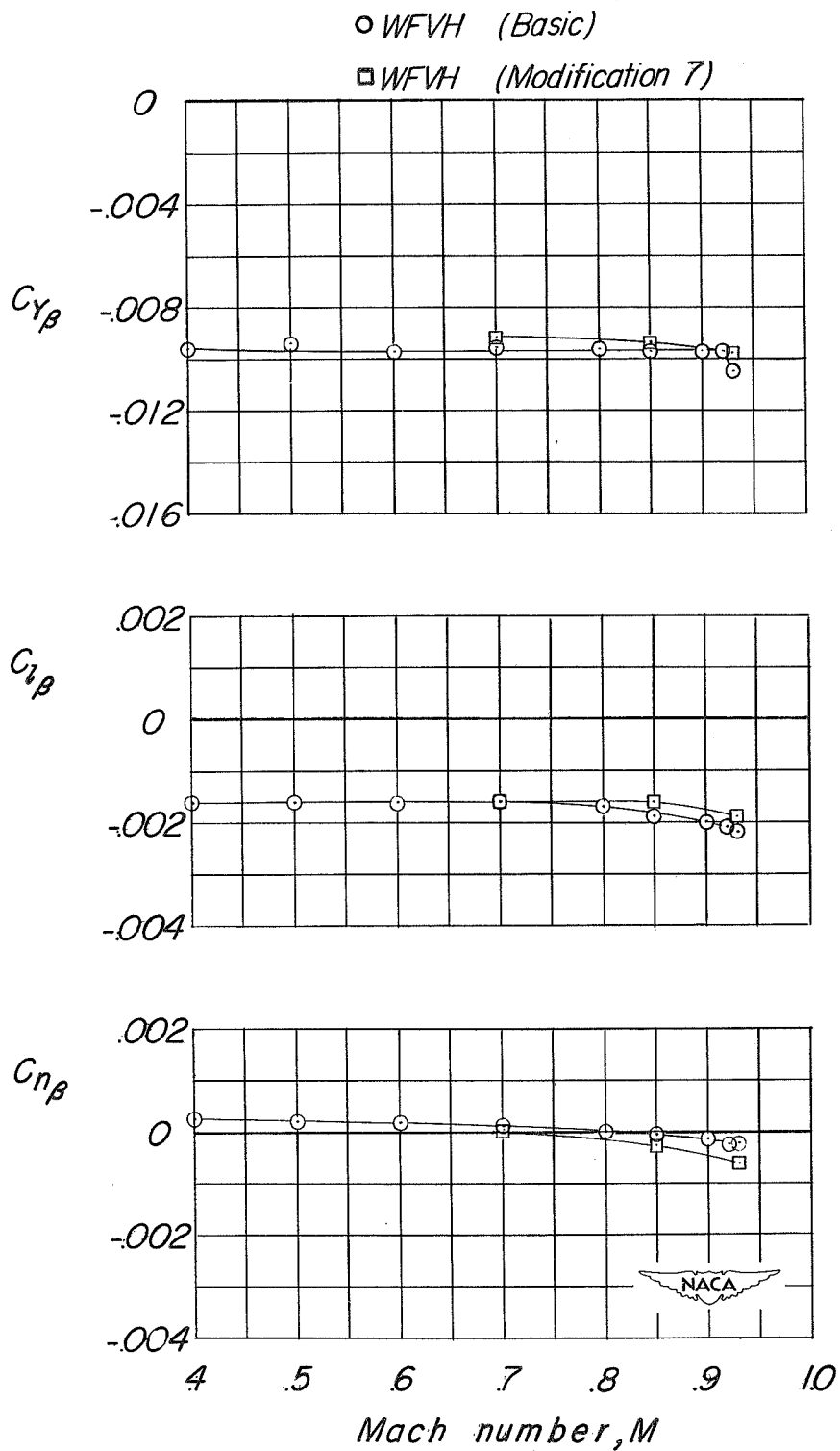
(c) Ventral fin; horizontal tail tip fins.

Figure 37.- Continued.



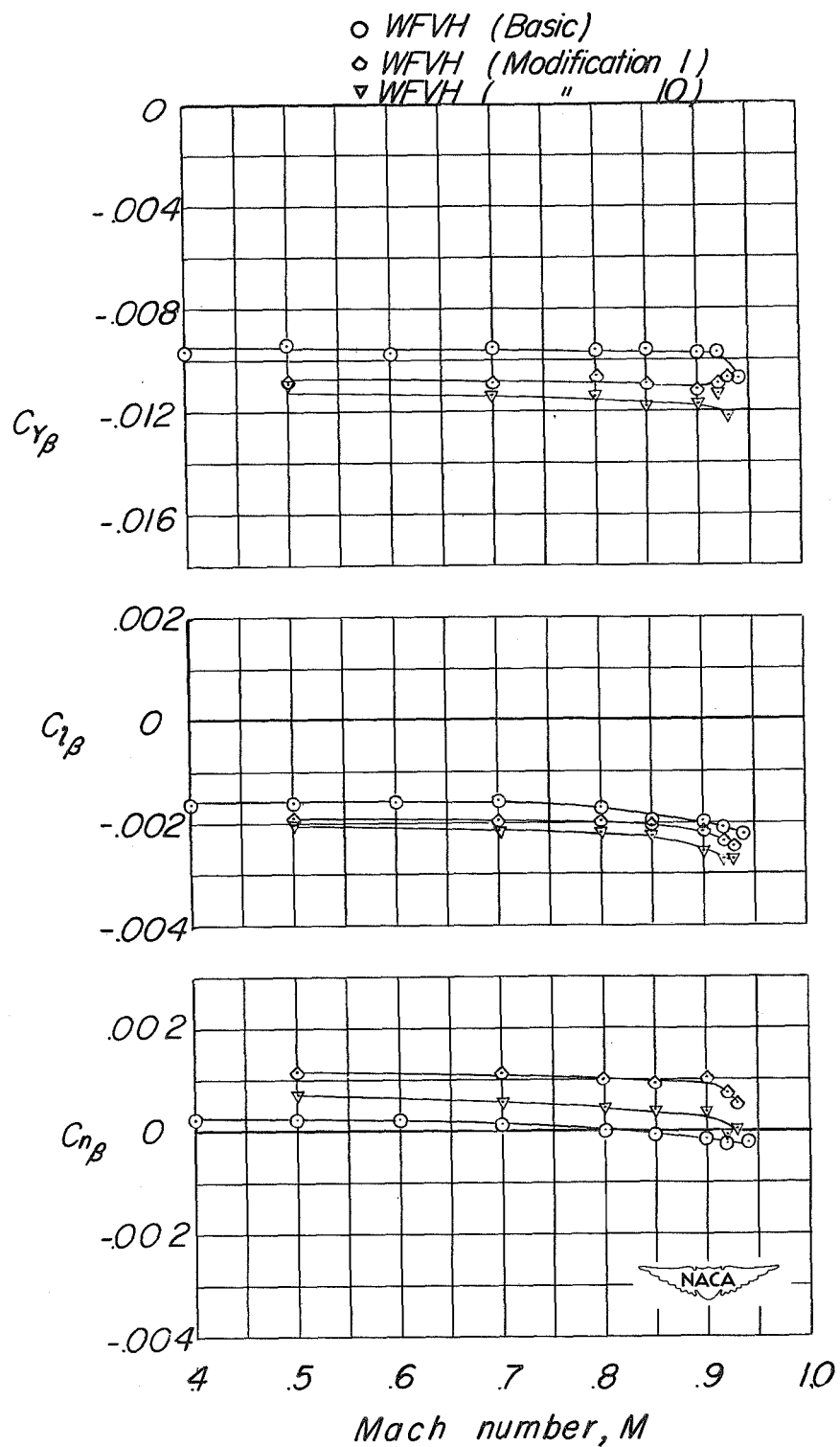
(d) Vertical tail extension.

Figure 37.- Continued.



(e) Wing fillets.

Figure 37.- Continued.



(f) Vertical tail size.

Figure 37.- Concluded.

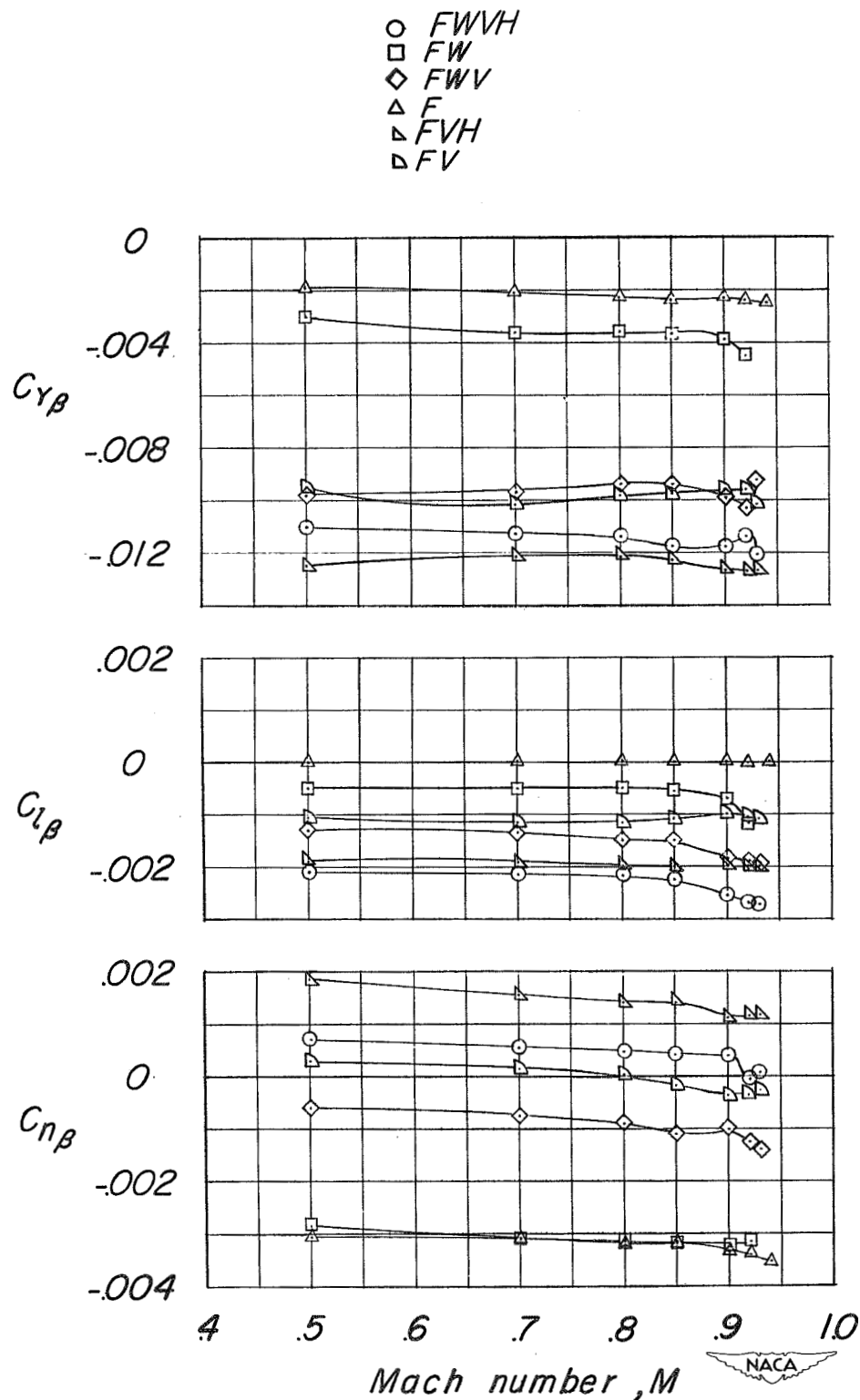
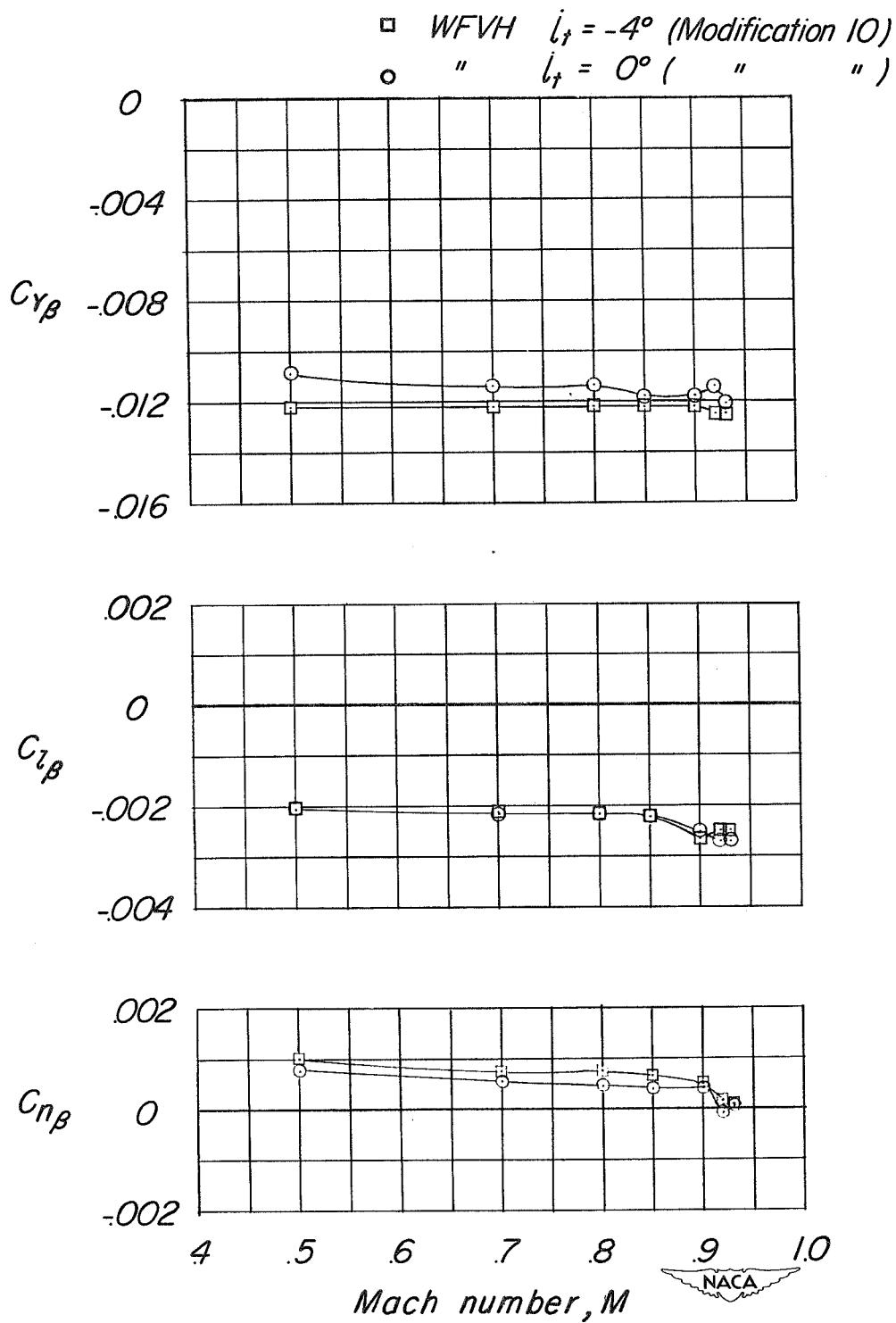


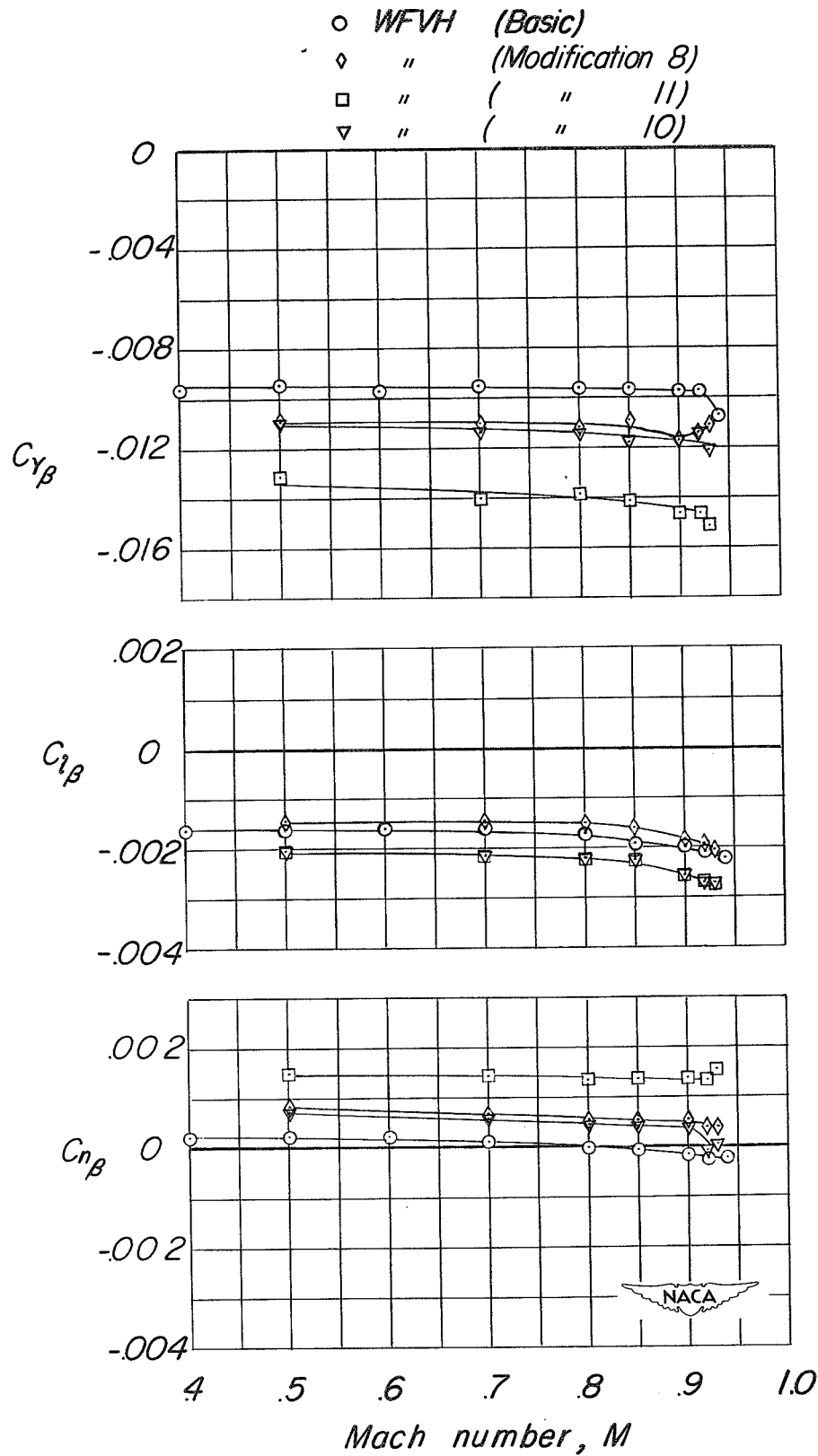
Figure 38.- Lateral stability characteristics of components of the large vertical tail configuration (modification 10).  $\alpha = 0^\circ$ ;  $i_t = 0^\circ$ .



(a) Stabilizer incidence.

Figure 39.- The effect of modifications on the lateral stability characteristics of the model with enlarged vertical tail.

CONFIDENTIAL



(b) Fuselage side fins.

Figure 39.- Continued.

CONFIDENTIAL



CONFIDENTIAL

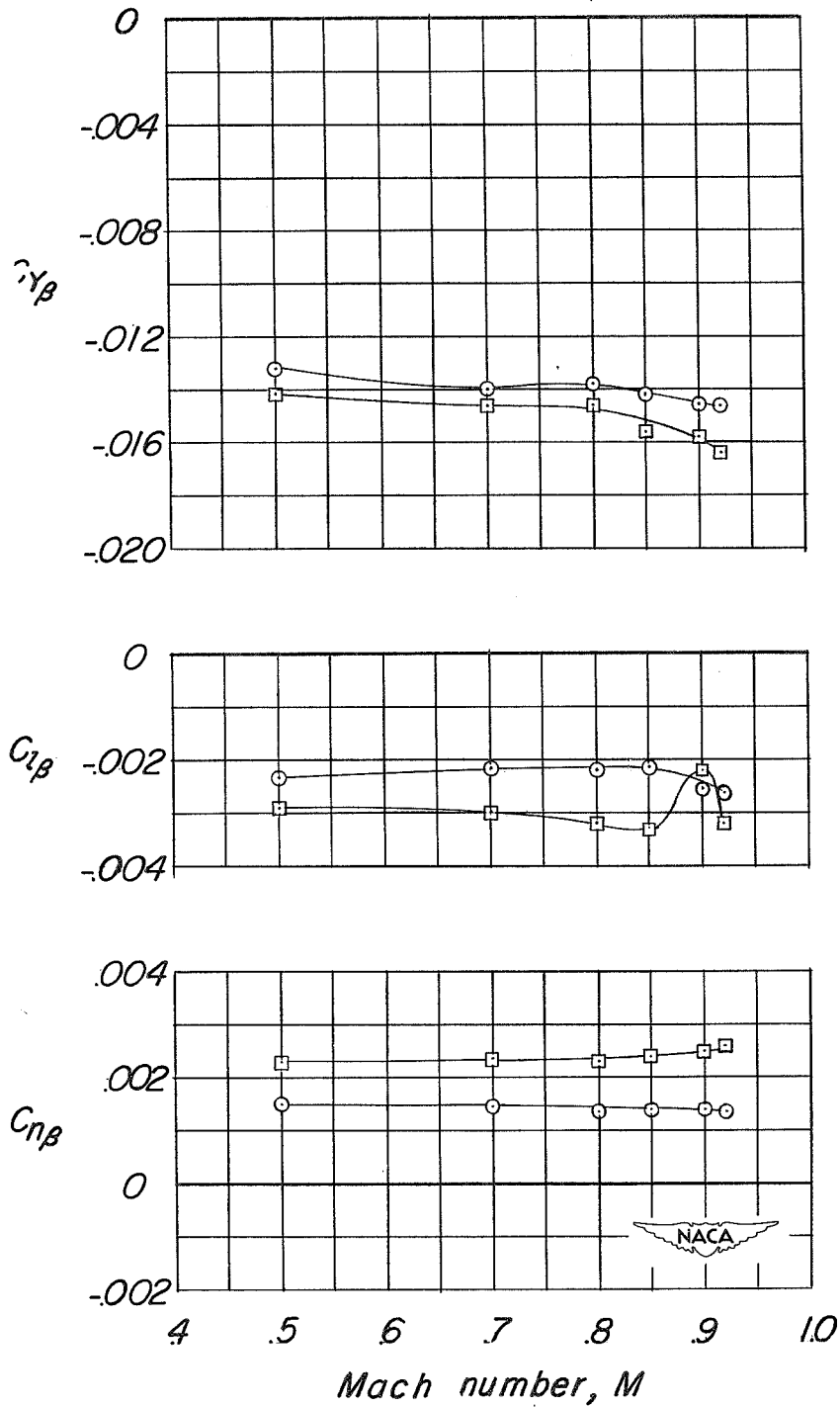
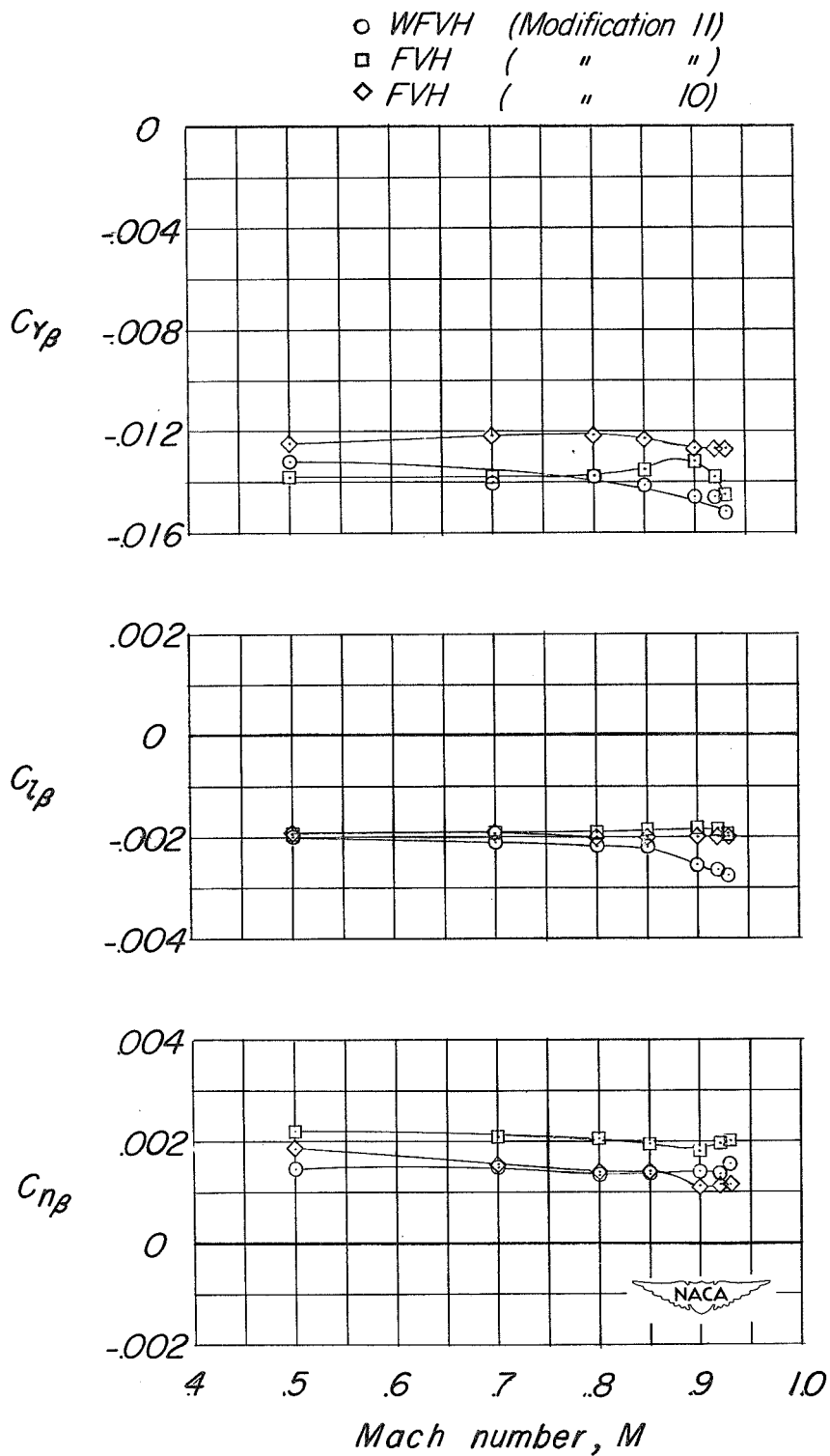
○ WFVH  $\alpha = 0^\circ$  (Modification II)□ WFVH  $\alpha = 6^\circ$  ( " " )(c) Fuselage side fins;  $\alpha = 0^\circ$  and  $\alpha = 6^\circ$ .

Figure 39.- Continued.

CONFIDENTIAL

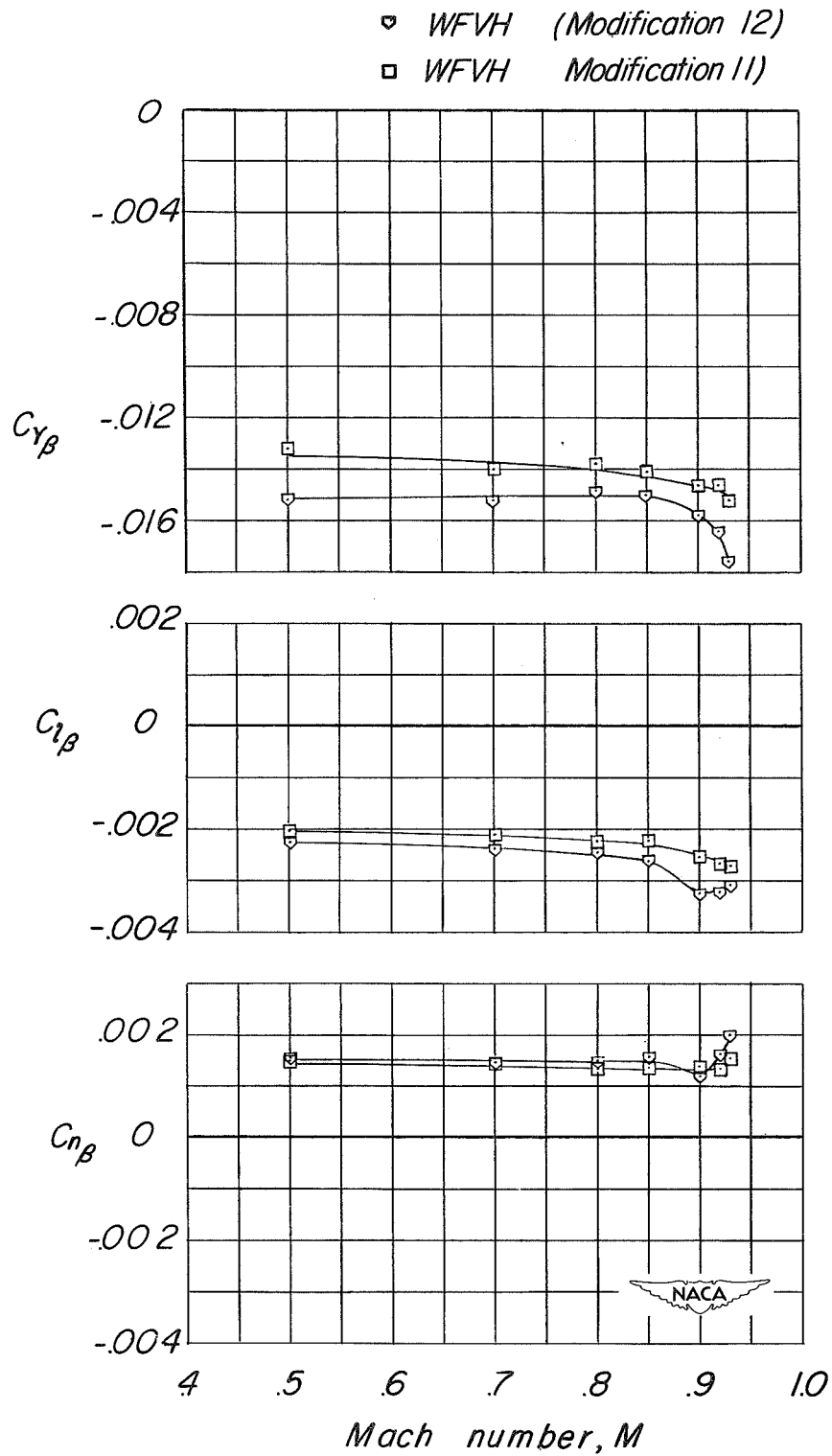
CONFIDENTIAL



(d) Wing and fuselage side fins.

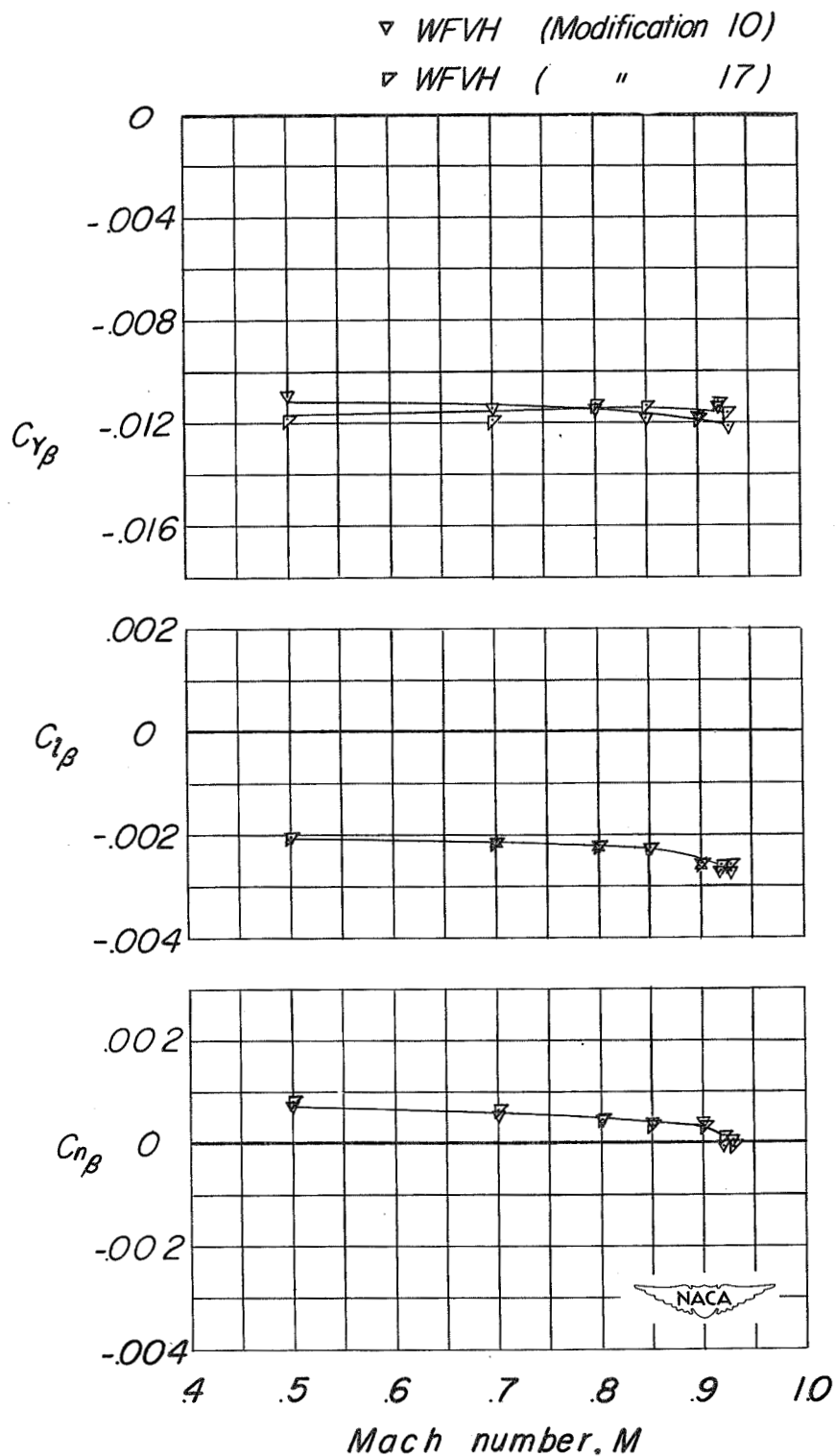
Figure 39.- Continued.

CONFIDENTIAL



(e) Wing stores.

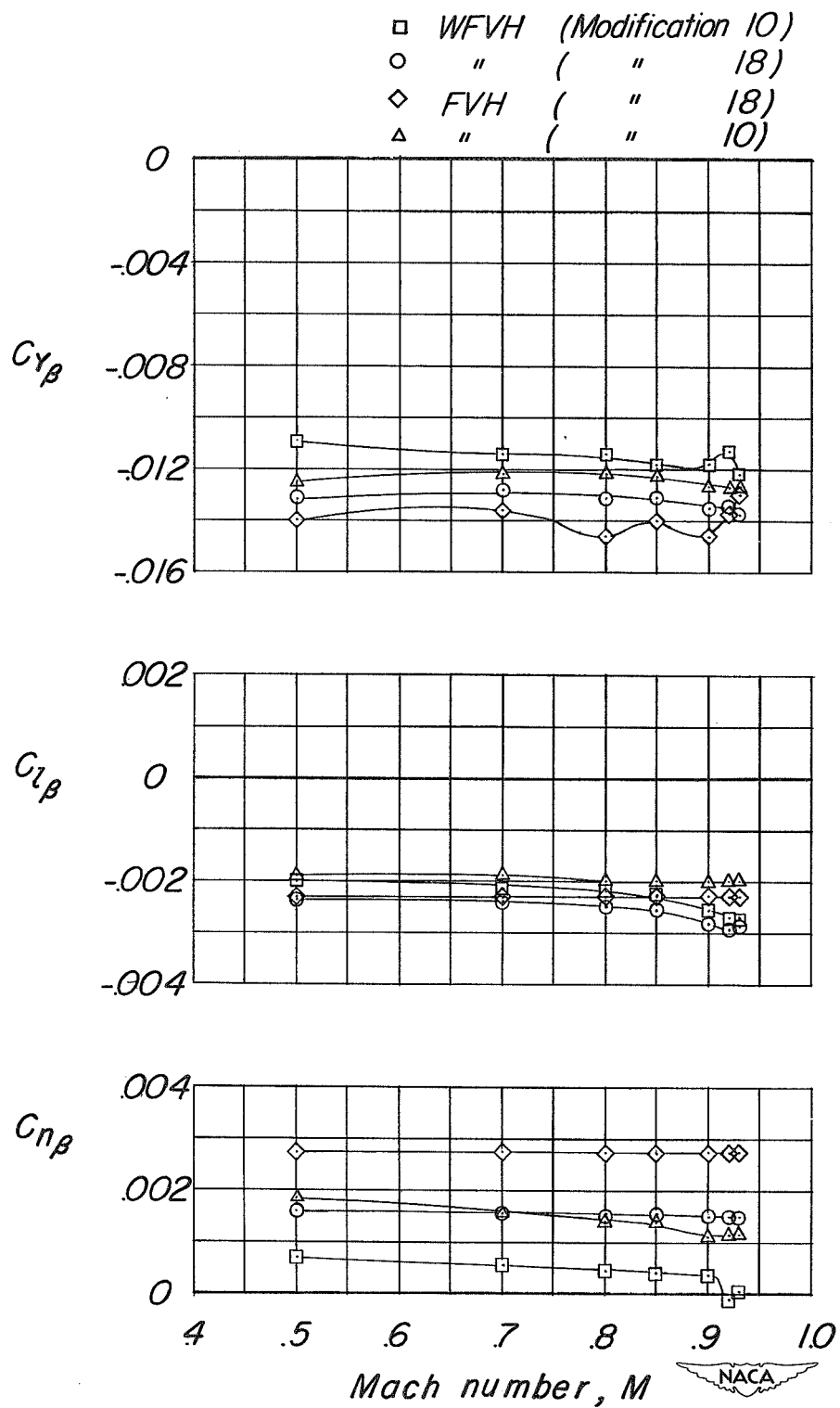
Figure 39.- Continued.



(f) Closed tunnel at intersection of vertical and horizontal tail.

Figure 39.- Continued.

CONFIDENTIAL



(g) Increased trailing edge thickness of vertical tail.

Figure 39.- Concluded.

CONFIDENTIAL

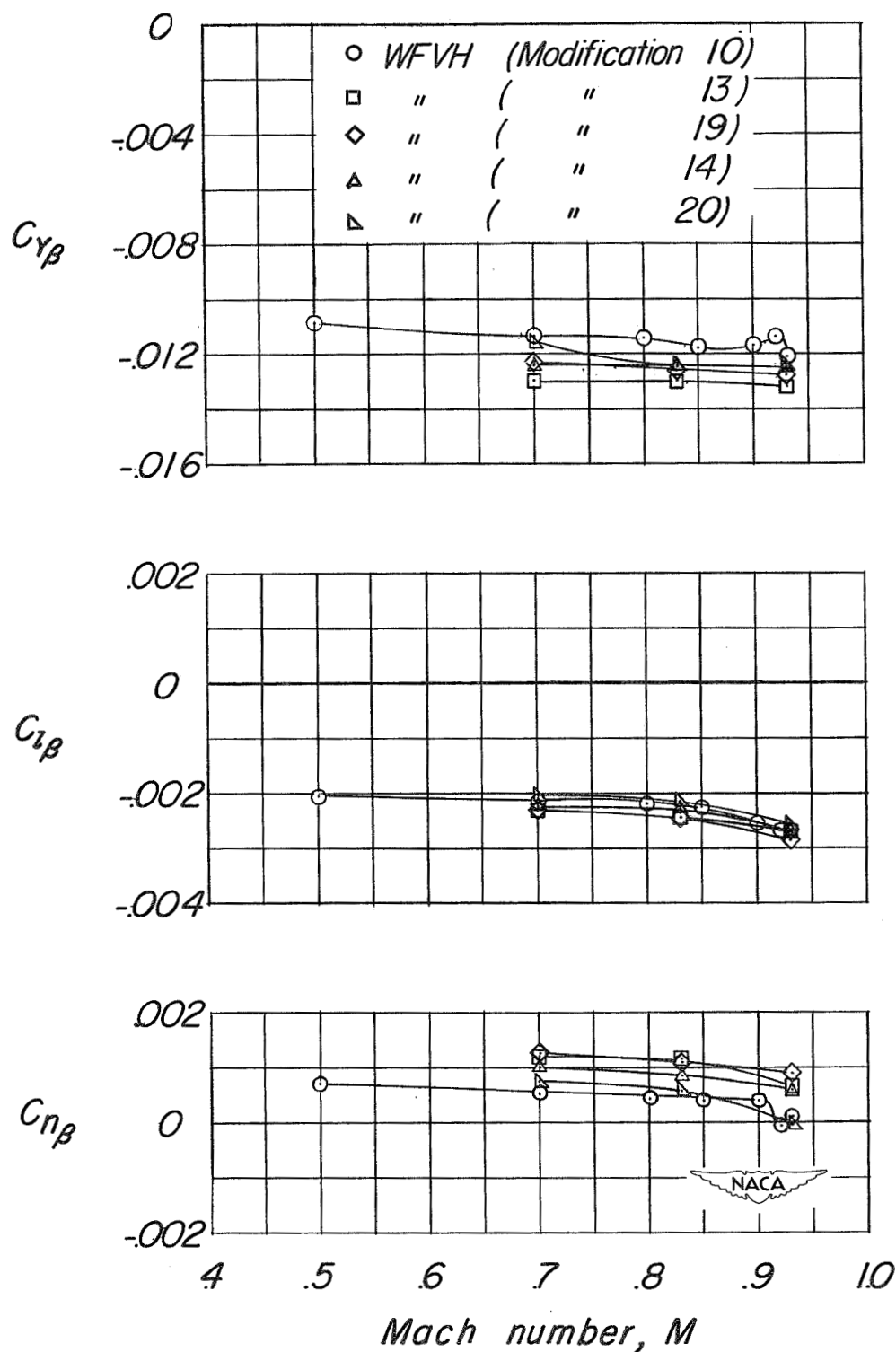


Figure 40.- Lateral stability characteristics of modifications to the enlarged vertical tail: end plate, trailing edge strips, fin fences, and fixed transition on the vertical tail.  $\alpha = 0^\circ$ ;  $i_t = 0^\circ$ .

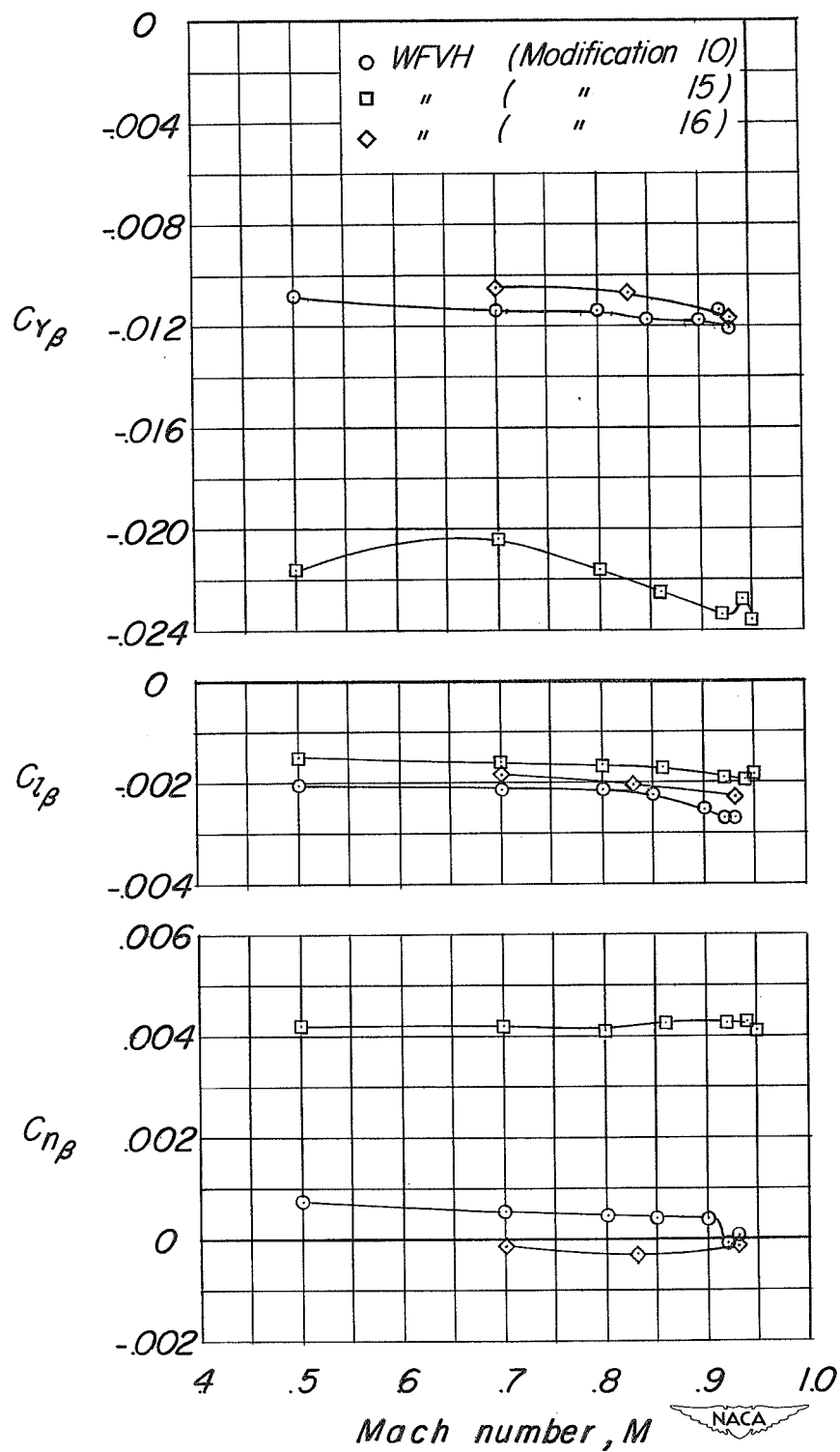


Figure 41.- Lateral stability characteristics of the complete model with a large ventral fin and with the rocket booster at separation.  $\alpha = 0^\circ$ ;  $i_t = 0^\circ$ .

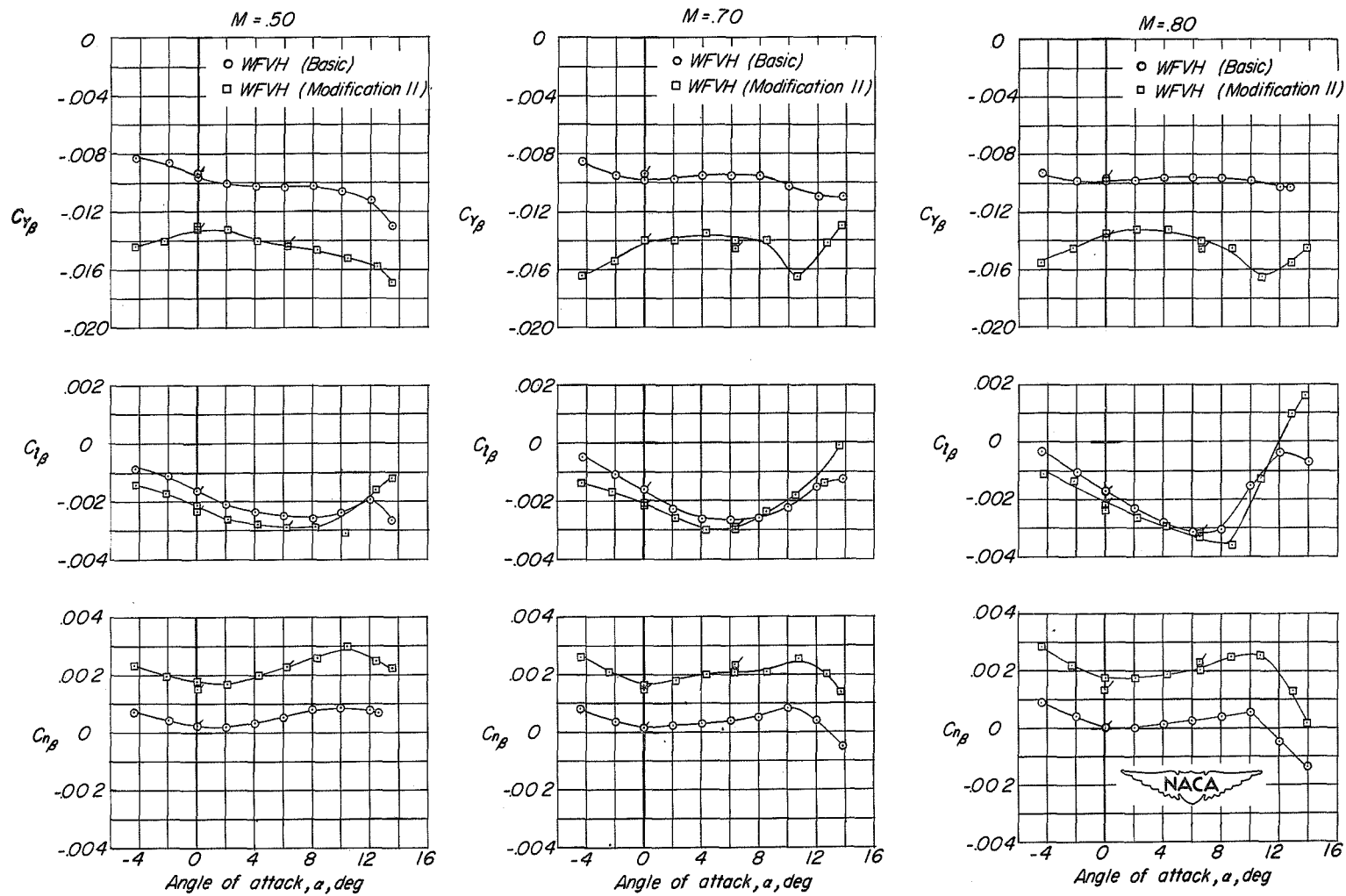


Figure 42.- Lateral stability characteristics of the basic model and modification 11 through the angle-of-attack range. Flagged symbols indicate data presented in figures 36 and 39(c).



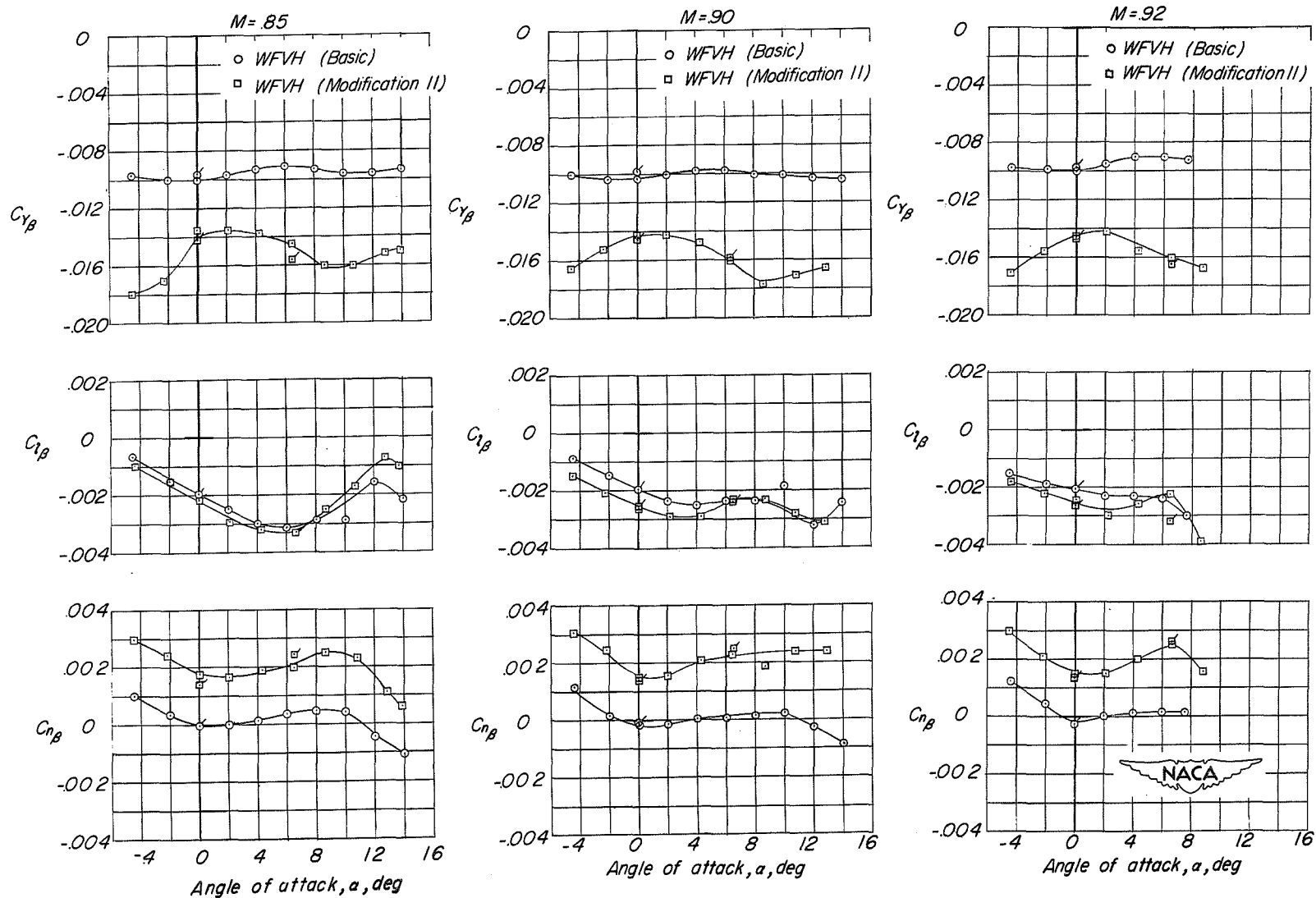


Figure 42.- Concluded.

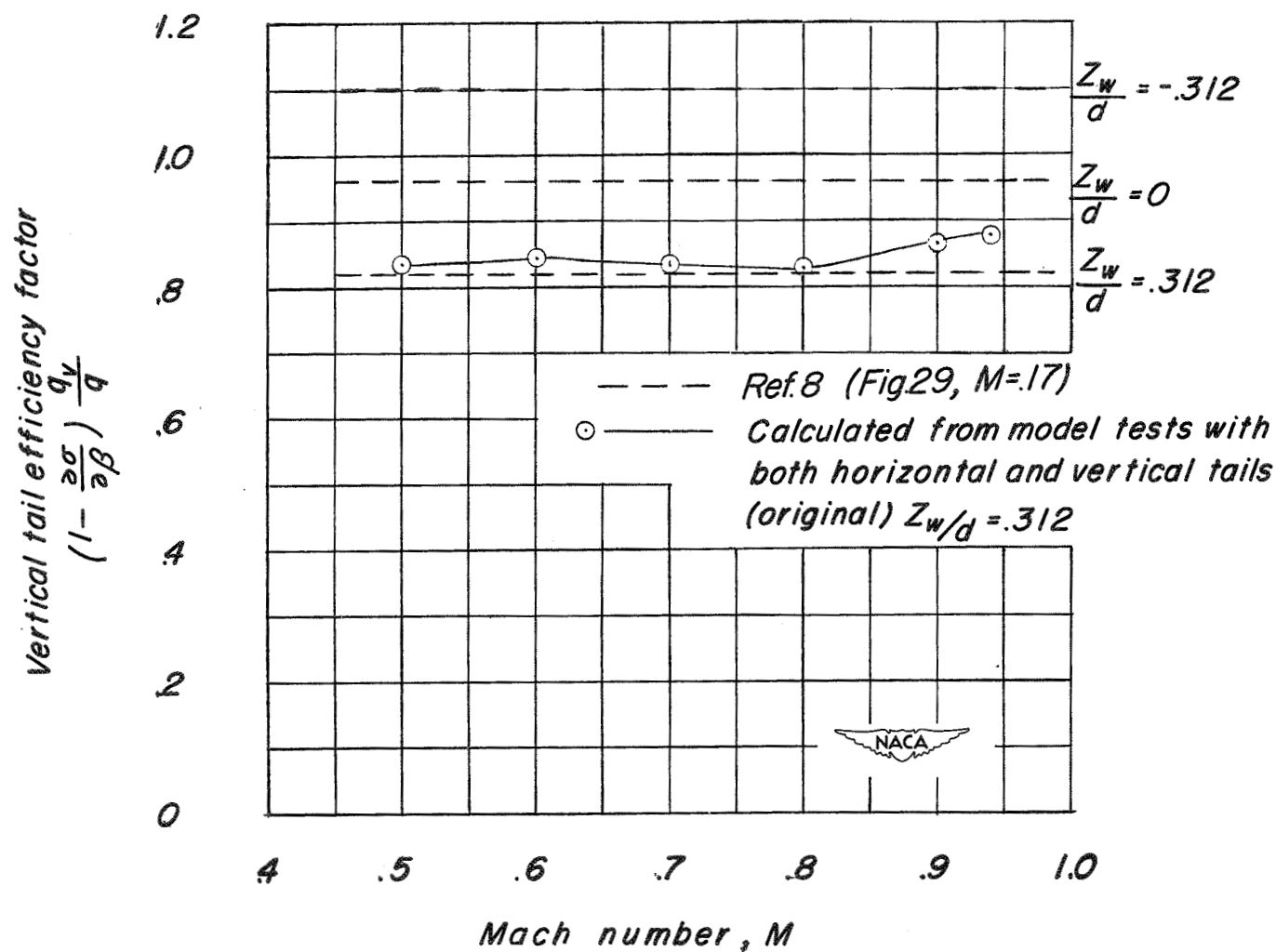


Figure 43.- Variation of vertical tail efficiency factor with Mach number as calculated for the basic model configuration by the method of reference 8.  $\alpha = 0^\circ$ .

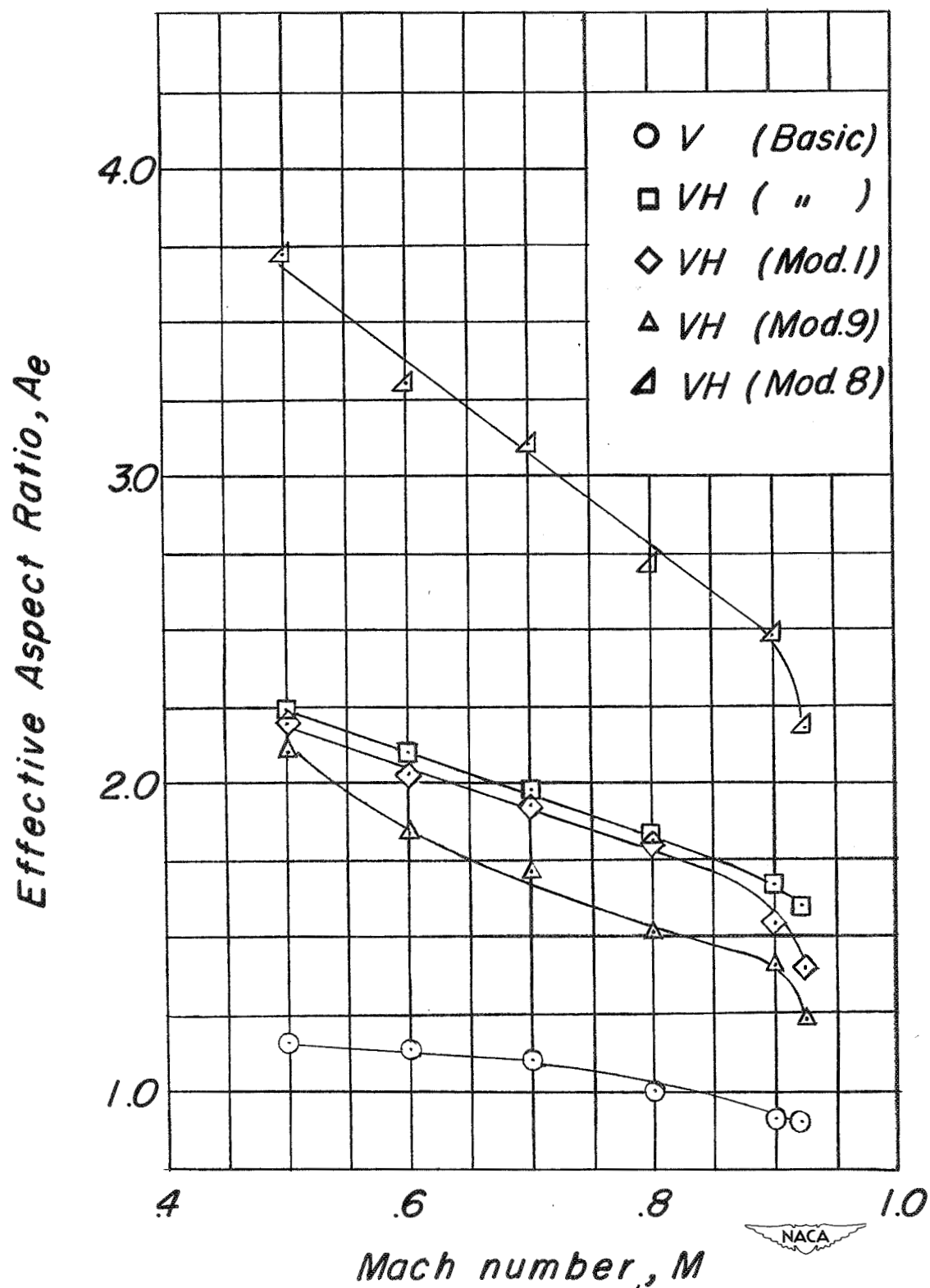


Figure 44.- The effective aspect ratio of the basic vertical tail with some modifications, calculated for the wing-off configuration.  $\alpha = 0^\circ$ .

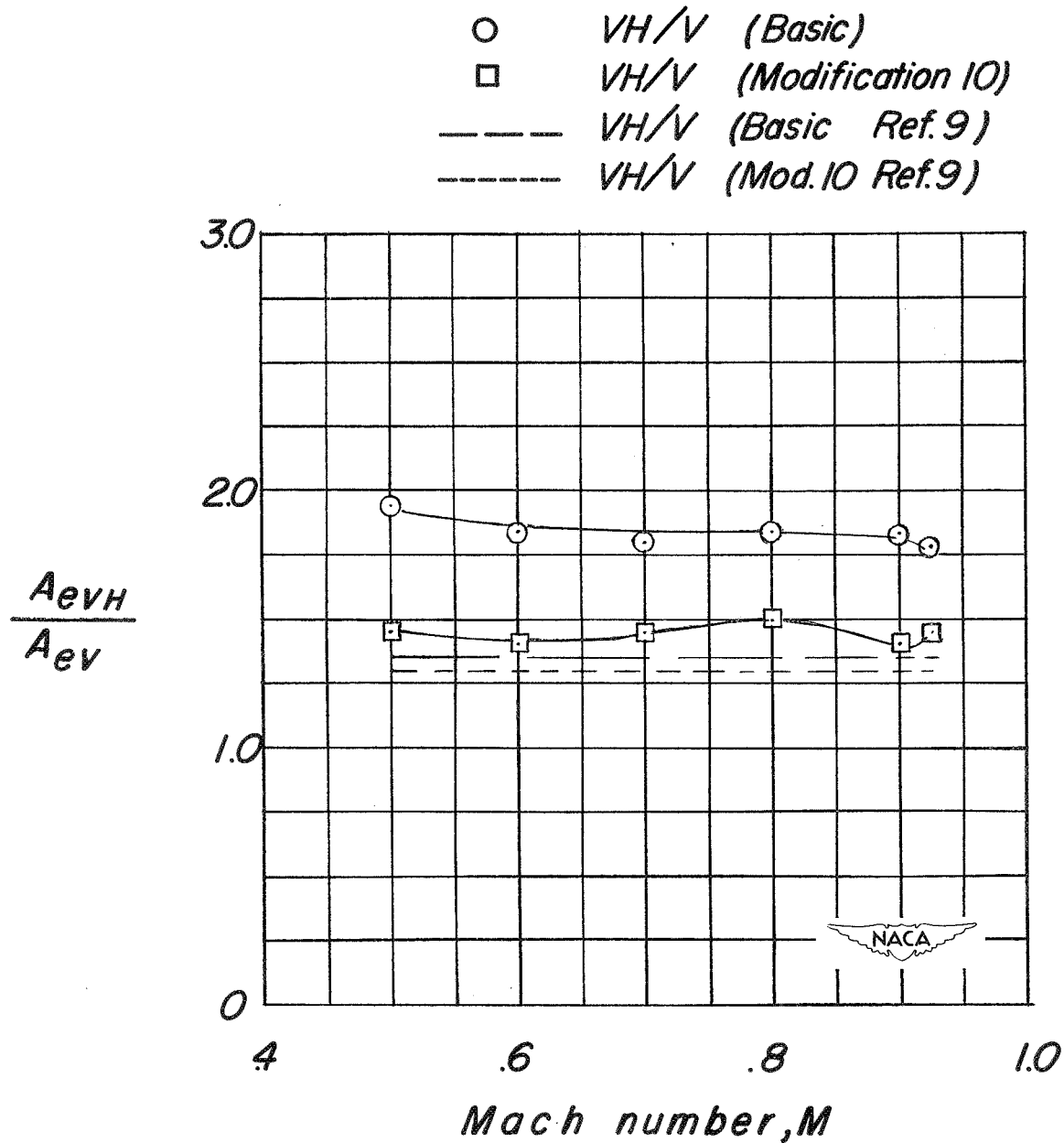


Figure 45.- The effect of the horizontal tail on the effective aspect ratio of the basic and modification 10 vertical tails.  $\alpha = 0^\circ$ .

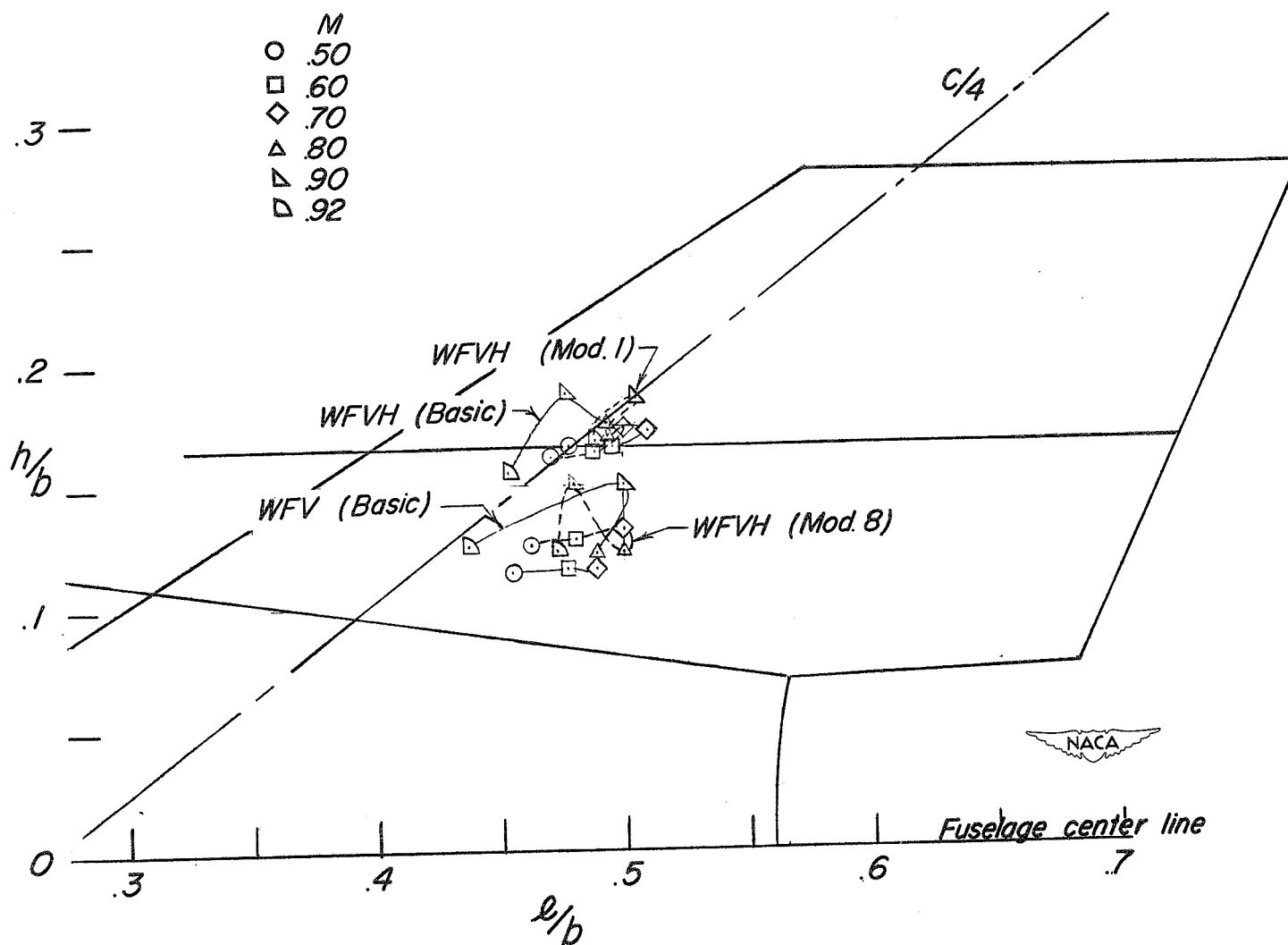


Figure 46.- Center-of-pressure location on the vertical tail for the vertical tail configurations.  $\alpha = 0^\circ$ ;  $i_t = 0^\circ$ .

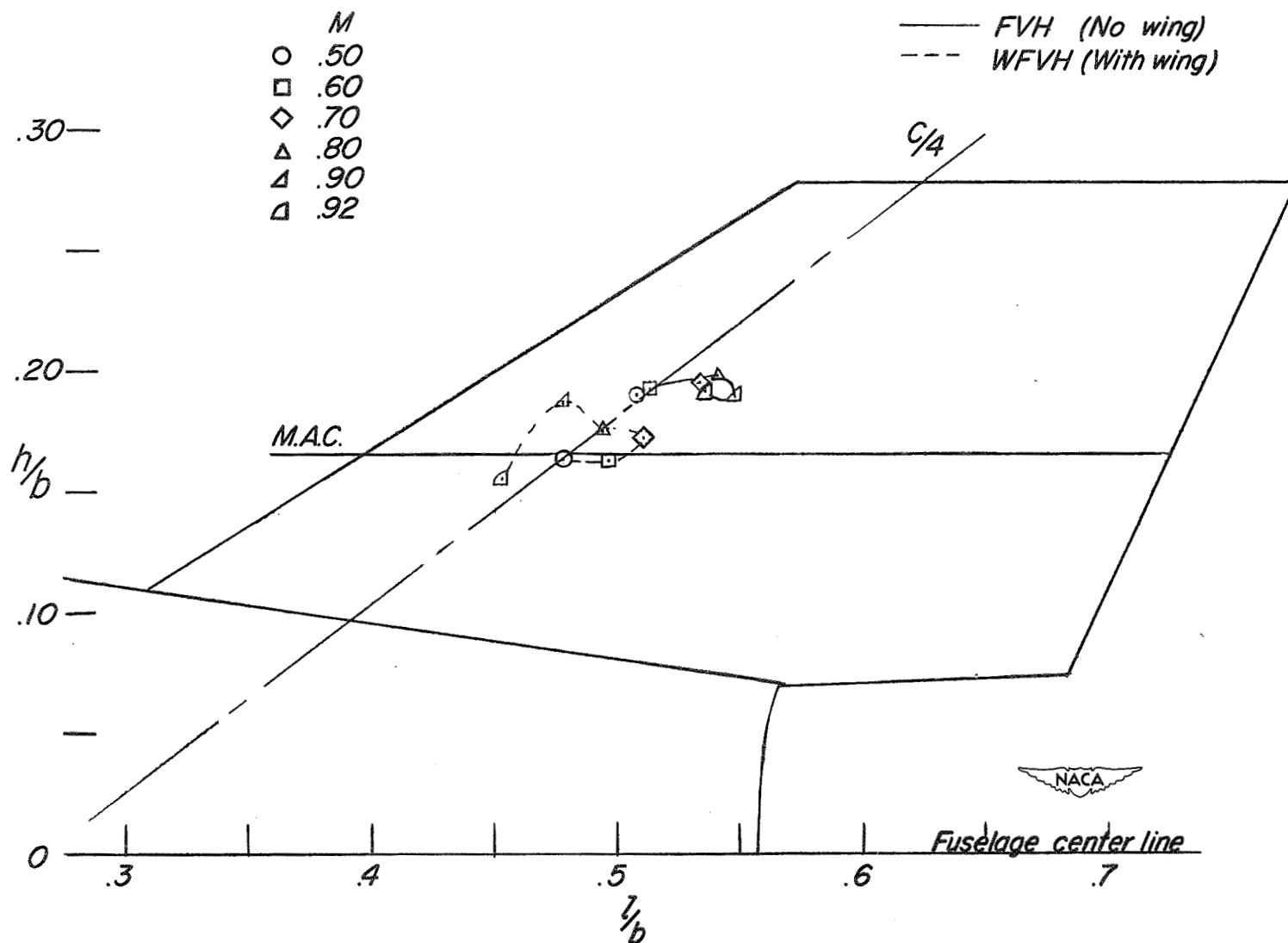


Figure 47.- The effect of the wing on the center-of-pressure location of the vertical tail of the basic model.  $\alpha = 0^\circ$ ;  $i_t = 0^\circ$ .

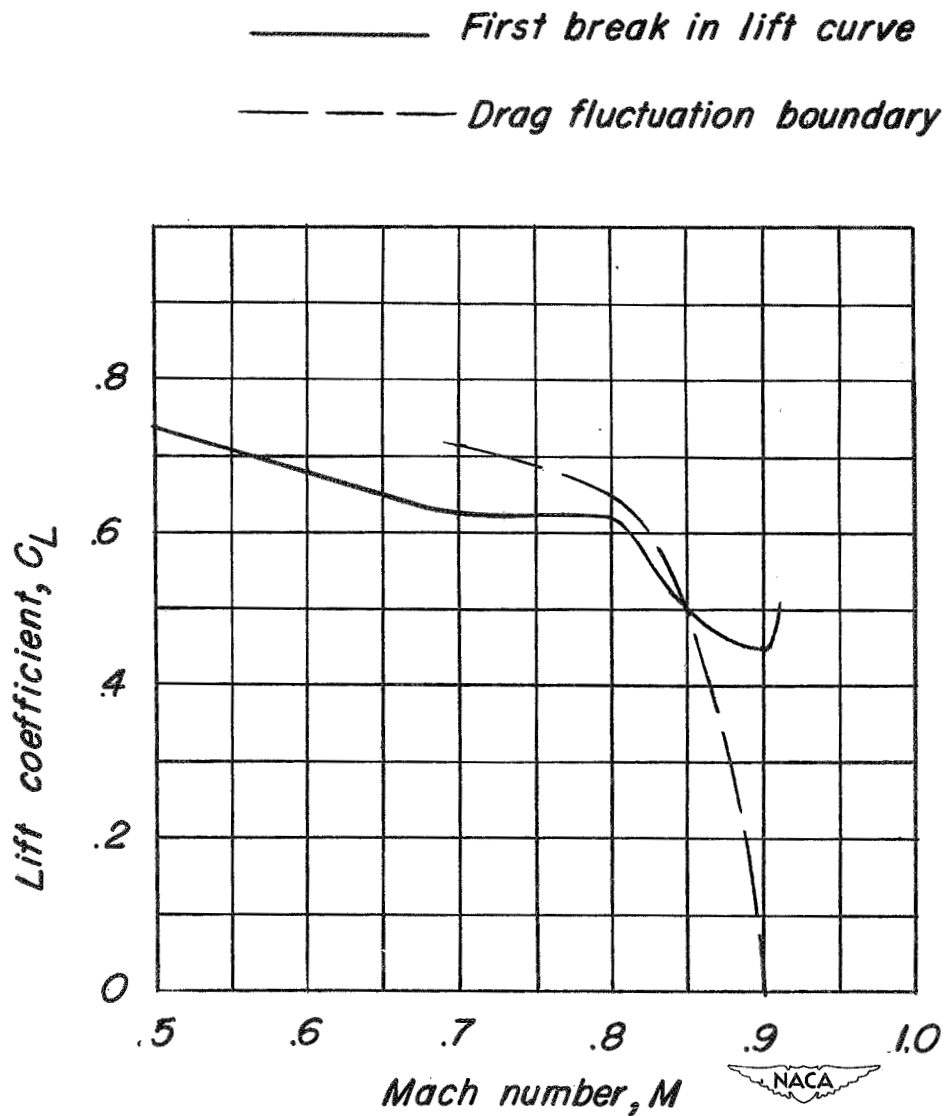


Figure 48.- Comparison of the lift coefficient corresponding to the first break in the lift curve and lift coefficient above which unsteady drag forces were observed.